Development of a Novel Method for the Fabrication of Nanostructured Complex Oxide $Zr_{(x)}Ni_{(y)}$ Catalyst for Improving the Hydrogen Storage Properties of MgH_2

Gracia Nshokano, BSc/MSc/MRes

A dissertation submitted in fulfilment of the requirements for the degree of

Doctor of Philosophy

College of Engineering, Design and Physical Sciences

Supervisory team (1st) Dr Zahir Dehouche

(2nd) Dr George Fern

Research Advisor: Dr Jan Wissink

-----October 2023-----

DECLARATION OF AUTHORSHIP

I hereby declare that the work presented in this thesis is wholly my own and that all material extracted from other sources is clearly stated and referenced in the text accordingly.

I grant powers of discretion to the University librarian to allow this thesis to be copied in whole or part without further references to me. This permission covers only single copies made for study purposes, subject to normal acknowledgement conditions.

This thesis was carried out by myself for the degree of Doctor of Philosophy at Brunel University London, Uxbridge, UK.

Signature

Gracia Shokano

Gracia Nshokano

London, October 2023

PhD Thesis College of Engineering, Design and Physical Sciences Brunel University London, Uxbridge, UB8 3PH, UK

ABSTRACT

The present study involves the development of a novel method for the fabrication of zirconium/nickel-based nanocatalysts to improve the hydrogen storage properties of the Magnesium/Magnesium Hydride (Mg/MgH_2) system. Three novel methods were implemented for fabricating the catalysts.

Method 1: ***Step 1 - "Synthesis of ZrO_2/Ni Nanocatalyst" Step 1 – High-Pressure Reactor and Catalyst Activation.*** The catalyst ZrO_2/Ni was synthesized using a high-pressure reactor and calcinated under the flow of hydrogen before being mechanically milled with the MgH_2 for 20 hours under Argon (Ar) in a SPEX High-Energy Ball Mill**.** ***Step 2 – Ball Milling - SPEX High-Energy Ball Mill.*** The synthesized catalyst was activated under hydrogen before being mechanically milled with the MgH_2 for 20 hours under Ar in a SPEX High-Energy Ball Mill**.**

Method 2: : "*High-Pressure Reactor, Catalyst Activation and Ball Milling - Planetary Ball Mill PM 100".*The catalyst ZrO_2/Ni was synthesized using the high-pressure reactor utilized in method 1, calcinated under the flow of hydrogen, and activated under hydrogen before being mechanically milled with the MgH_2 for 5 hours under Ar in a Planetary Ball Mill PM 100.

Method 3: "***Synthesis of ZrO_2/Ni Vs ZrO_2/$NiCl_2$ Nanocatalyst. High-pressure reactor, Catalyst Activation, and Ball Milling - Planetary Ball Mill PM 100".*** The catalyst prepared in **Method 2** (ZrO_2/Ni) was compared with a new catalyst, ZrO_2/$NiCl_2$.The ZrO_2/$NiCl_2$ was synthesized via the high-pressure reactor and calcinated under the flow of 95%Ar /5%H_2 before being mechanically milled with the MgH_2 for 5 hours under Ar in a Planetary Ball Mill PM 100.

For all the 3 methods, the hydrogenation and dehydrogenation properties of hydrogen storage materials in MgH_2 were measured from the plots of the PCT (Pressure-Composition Temperature) with the help of a Manometric Gas Sorption Analyser. The synthesized catalysts and composites were characterized by the XRD (X-Ray Diffraction), FE-HRTEM (Field Emission High-Resolution Transmission Electron Microscopy), and SEM-EDX (Scanning Electron Microscope) to determine the microstructure of the prepared powder. The desorption characteristic of the nanocomposite was determined via TPD (Temperature-Programmed Desorption).

The outcome of the experiment from **Method 1** shows that the milling of the powder via the SPEX ball mills resulted in particle agglomeration of the nanostructured composite MgH_2/10wt%ZrO_2/Ni mainly in the range of 2000 nm to 4000nm, as well as in a high level of impurities, and oxide formation, which significantly affected the absorption property of the MgH_2, 4.4wt.% at 250°C after 1 minute. On the other hand, **Method 2** shows that the nanostructured MgH_2 powder milled with 10 wt.% of ZrO_2/Ni-based nanocatalyst resulted in a wide range of MgH_2 particle size distribution below 1000 nm. A faster hydrogen release of 5.9 wt.% at onset temperature 210 °C/peak temperature 232 °C was recorded.

Lastly, **Method 3** shows that the nanocomposites MgH_2 powder milled with 10 wt.% of ZrO_2/Ni have a high percentage of hydrogen 5.4 wt.% at 250ºC with a fast kinetic of hydrogen uptake at 1 minute, and a maximum absorption capacity of 7.3 wt.% was achieved in less than 10 minutes. Whereas the composite MgH_2/10wt.% ZrO_2/$NiCl_2$ shows moderate improvement of hydrogen uptake, 4.0 wt.% at 250ºC, with a maximum uptake of 5.3wt.%, which may be due the presence of a high percentage of chloride catalyst on the surface of the Mg/MgH_2. The PCT plot of the MgH_2/10 wt.% of ZrO_2/Ni resulted in significant thermodynamic improvement, with the enthalpy value of -57.17KJ/mol which is approximately 20% when compared to the commercial MgH_2.

Alloying ZrO_2 and Ni significantly enhanced the hydrogenation and dehydrogenation properties of the MgH_2.The observed significant improvement in the hydrogen sorption properties may be due to the impact of the highly dispersed catalyst on the surface of the Mg/MgH_2 system as well as due to the reduction in particle size during the ball milling process and the formation of $Mg_{0.996}Zr_{0.004}$ phase during the milling process. Furthermore, the significant reduction in particle size and homogenous distribution of the catalyst in the MgH_2 was probable the result of the catalyst activation prior to the milling process with the MgH_2.

ACKNOWLEDGEMENT

I dedicate this work to my parents – Thank you for your kind words of encouragement and for always believing in me even when I did not believe in myself at times. You have been my role model all my life and continue to play a massive part in it.

A big thank you to my supervisor Dr Zahir Dehouche, for having believed in me enough to offer me the opportunity to work alongside him, for his support, all through my time at the university and for his guidance and understanding when things did not go accordingly. My gratitude goes to Dr George Fern and Dr Jan Wissink for their technical advice and support throughout my PhD. Mr Eamon Wyse and Mr Costas Xanthos for their assistance in the laboratory. My sincere thank you must also go to the Experimental Techniques Centre (ETC) members at Brunel University. Thank you for providing me with helpful training and assistance on the SEM/ TEM and XRD - Dr Uchechukwu Onwukwe, Dr Ashley Howkins, Dr Lorna Anguilano and Dr Nicholas Nelson.

I acknowledge Dr Gina Postole and Dr Basile Galey; thank you for your collaboration. And thank you to the members of the panel for taking the time to examine me.

I would also like to thank all those who have helped me through highs and lows – To my husband and my baby girl, thank you for your patience.

Thank you for being there! To my sisters and brothers, thank you for your encouragement and for believing in me. To friends and to all those I did not mention by name, I had tremendous help and enjoyed my time as a PhD candidate at the university because of you.

G. Nshokano

TABLE OF CONTENTS

LIST OF FIGURES

LIST of TABLES

GLOSSARY

Absorption

Is it a physical or chemical process in which atoms, molecules or ions penetrate a metal hydride material. The *present study* refers to hydrogen's absorption process in the metal hydride matrix.

Alloy

It refers to a substance that combines a mixture of metals. The *present study* refers to the formation of catalysts, which involves the combination of metallic Nickel and metal oxide Zirconium.

Catalyst

It is a substance that increases the rate of a reaction without itself being consumed in the reaction. In the *present study*, the catalyst is used to improve the rate of hydrogen absorption in the metal hydride.

Charging

Refer to SEM analysis: the sample has a charging effect when it is non-conductive. Therefore, the surface of the non-conductive material acts as an electron trap. The electron accumulates on the sample's surface, resulting in the creation of extra white region affection the image formation during the SEM analysis. The most common way to decrease the sample's charging effect is by coating it with gold before analysis to make it conductive.

Desorption

It is a physical process involving releasing a substance (Hydrogen previously adsorbed) from the surface (metal hydride). This process can only occur if the molecule acquires enough energy to overcome the activation barrier.

Endothermic

The product has high energy than the reactant. Therefore, the enthalpy of the reaction is positive (+ΔH).

Enthalpy(ΔH)

It is a property of a thermodynamic system which refers to the difference between the potential energy of the product and the reactant where the pressure is constant (kJ/mol). (It is the product – the reactant). The system favours minimum enthalpy.

Entropy (ΔS)

It is a property of a thermodynamic system which refers to the measure of a disorder in a system's thermal energy per unit temperature that is unavailable for doing practical work (J/mol/K). A good system generally favours maximum entropy.

Exothermic

It is a reaction when the heat is released from the system into its surroundings. In the exothermic process, the product has less energy than the reactant. Therefore, the enthalpy of the reaction is negative (-ΔH).

Metal hydride

Refer to a class of materials containing metal or metalloids bonded to hydrogen.

Precursor

It is the starting material (compound) of a chemical reaction that produces another compound. The present work is referring the sol-gel formation from the precursor of $ZrCl_4$ and $Ni(NO_3)2.6H_2O$.

Kinetics

Refer to the rate of a chemical reaction, how fast a reaction occurs and factors that may affect the chemical pathway.

Thermodynamic

The study deals with the relative between heat, work, temperature and energy states of reactants and products. Lowing the thermodynamic (ΔH) means the system will require less energy. Therefore, it will be more likely for the system to have significant results at lower temperatures. In the *present study*, this refers to the sorption property of metal hydride.

Pressure

The force of the gas particle applied/wall collisions over the area of the wall (surface) defines as 1 newton per square meter (N/m^2). The SI unit for pressure is the pascal (Pa). The higher the pressure, the faster the reaction occurs, and vice versa.

NOMENCLATURE

E_a: Activation Energy, J/mol

Ea_R: Reverse activation energy, J/mol

Ea_F: Forward activation energy, J/mol

M: Molar mass, g/mol

P: pressure, bar

P: Total Pressure, bar

P_{abs}: Hydrogen Absorption Pressure, bar

P_{des}: Hydrogen Desorption Pressure, bar

E: Energy, J

PE: Potential energy

ΔS: Entropy, J/mol/K

T: Temperature, K or °C

wt.%: weight percentage

w/v: weight /volume

ΔH: Enthalpy, kJ/mol

Acronyms

BCC: Body-Centered Cubic

BM: Ball-Milling

Cyc: Cycle

DOE: Department of Energy

HRTEM: Field Emission High-Resolution Transmission Electron Microscopy

H: hydrogen

MOF: Metal-Organic Frameworks

TEM: Transmission Electron Microscopy

TPD: Temperature-Programmed Desorption

PCT: Pressure-Composition-Temperature

SEM-EDX: Scanning Electron Microscope–Energy-Dispersive X-Ray Spectroscopy

LHV: Lower Heating Value

HHV: Higher Heating Value

Mg: Magnesium

MgH_2: Magnesium Hydride

Ni: Nickel

P: Product

Ref: Reference

R: Reactant

rxn: Reaction

SEM: Scanning Electron Microscope

TS: Transition state

T_{abs}: Hydrogen Absorption Temperature

T_{des}: Hydrogen Desorption Temperature

T_{abs}: Hydrogen Absorption Time

T_{des}: Hydrogen Desorption Time

t: time, minutes

time: h: Hours

XRD: X-Ray Diffraction

Zr: Zirconium

% mass: Mass Percentage

List of Publications

Some of the work presented in this thesis has given rise to the following publications and conference proceedings.

Publications and conference proceedings

- Article Title: ''Development of a Novel Method for the Fabrication of Nanostructured ZrO_2/Ni Catalyst to Enhance the Desorption Properties of MgH2'' Catalysts 2020, 10(8), 849; https://doi.org/10.3390/catal10080849 Received: 8 June 2020 / Revised: 18 July 2020 / Accepted: 22 July 2020 / Published: 30 July 2020
- Book Title: ''Development of Metastable Catalysts to Improve the Hydrogen Sorption Characteristics of Nanostructured Magnesium Hydrides for Hydrogen Storage''. Chapter Published on the 28 December 2020. Prime Archives in Chemistry: 02nd Edition https://videleaf.com/product/prime-archives-in-chemistry-2nd-edition/ https://videleaf.com/development-of-a-novel-method-for-the-fabrication-of nanostructured zrxNiy-catalyst-to-enhance-the-desorption-properties-of-mgh2/

Conferences and Posters Presentations

- Poster Title: Development of a novel method for the fabrication of nanostructured $Zr_{(x)}Ni_{(y)}$ catalyst to enhance the sorption characteristics of MgH_2. H2FC Supergen Research Conference: Nottingham university 17/18th February 2020. https://www.h2fcsupergen.com/events/h2fc-supergen-research-conference-2020-presentations-posters-photos/
- Poter Title: Innovative method for the fabrication of nanostructured ZrO_2/Ni catalyst to enhance the hydrogenation/dehydrogenation properties of MgH_2. H2FC SUPERGEN Research Conference, Hydrogen and Fuel Cells Powering the Future: 19 March 2019, NEC Birmingham University.
- Poster Title: Development of a novel method for the fabrication of nanostructured $Zr_{(x)}Ni_{(y)}$ catalyst to enhance the sorption characteristics of MgH_2. 3MT competition challenges research on the 19th of March 2019. And Poster conference Brunel University May 2018

- Poster Title: “Innovative Method for Improving the Development of Catalysts and Nanostructured Magnesium Hydrides for Hydrogen Storage” Calorimetry School, Ecole de calorimétrie, Lyon University, 16th June 2019 - presented poster

Reader Guide

Chapter I: General Introduction

Chapter II: Literature

Chapter III: Methodology

Chapter IV: Establishing an Innovative Method for the Synthesis of ZrO_2/Ni Nanocatalyst for Improving the Sorption Property of MgH_2 in the Field of Solid-State Hydrogen Storage

20 hours milling time/ SPEX high energy ball mill MgH_2+10wt.%ZrO_2/Ni

Introduction Recap

Experimental

- Catalyst-ZrO_2/Ni synthesis
- Composite (MgH_2+10wt.%ZrO_2/Ni) ball mill: 5 hours via Planetary
- Characterisation

Results/ Discussion

- XRD
- SEM
- TPD
- Kinetics

Conclusion

References

Chapter V: Development of a Novel Method for the Fabrication of Nanostructured ZrO_2/Ni Catalyst to Enhance the Desorption Properties of MgH_2

5 hours milling time/ Planetary ball mill - MgH_2+10wt.%ZrO_2/Ni

Introduction Recap

Experimental

- Catalyst-ZrO_2/Ni synthesis
- Composite (MgH_2+10wt.%ZrO_2/Ni) ball mill: 20 hours via SPEX
- Characterisation

Results

- XRD
- SEM
- TPD

Discussion

Conclusion

References

Chapter VI: Comparing the Novel Catalysts ZrO_2/Ni and ZrO_2/$NiCl_2$ Storage Behaviour of Hydrogen Sorption Properties of MgH_2 Powder

5 hours milling time/ Planetary ball mill (ZrO_2/$NiCl_2$) catalyst

Introduction Recap

Experimental

- Catalyst-ZrO_2/Ni synthesis
- Composite (MgH_2+10wt.%ZrO_2/$NiCl_2$) ball mill: 5 hours via Planetary
- Characterisation

Results / Discussion

- XRD
- SEM
- Kinetics
- PCT

Conclusion

References

Chapter VII: General conclusion

References

Appendices

CHAPTER I: GENERAL INTRODUCTION

1.1. Background

Throughout the recent years, researchers and scientists have grown their concerns over the rapid increase in demand for global energy resulting from the faster human population growth and the heavy industrial sectors expansion. [1] The concerns over the global energy demand have led to an increased pressure on governments and businesses to promote sustainable energy efficient developments, to preserve economic growth and to reduce the effect of climate change. The primary energy consumed worldwide is from combusted fuel, half biomass and half coal. [2], [3] The transport sector accounts for approximately 40% of total fuel consumption, contributing to around 23% of global greenhouse gas emissions. [3]

According to the Energy Information Administration (EIA) report, fossil fuels account for approximately 79% of the primary energy consumption in the U.S. in 2021. The remaining 21% of U.S. primary energy consumption for 2021 came from renewables and nuclear energy sources. [4]

The depletion in oil and fossil fuel consumption was reported by B.P.'s World Energy Outlook 2018 Edition' to account for approximately 75% of the world's energy supply by 2035, as the growth of natural gas will exceed coal and oil [5], (Figure 1.1). B.P. has predicted that from 2015 to 2035, the global energy demand would increase by 30%, making an average annual increase of 1.3%. [1], [6]

The first decline in primary energy consumption - was reported in 2020 by 4.5% since 2009, where oil accounted for almost three-quarters of the decrease. Although, this decline did not affect the consumption of renewables and hydro energy. From the B.P.'s report 2021, fossil fuels continue to hold the largest share of energy in the world, where oil and coal account for 31.2% and 27.2% of total primary energy consumption, respectively. The percentages of natural gas, nuclear and renewable energy in 2021 were reported as 24.7%, 4.3% and 5.7%, respectively.[7] The depletion of fossil fuels and global climate change have captivated the attention of researchers to introduce

the idea of building hydrogen-based energy infrastructure. The U.S. Department of Energy proposed the importance of hydrogen storage for hydrogen-powered light-duty vehicles in 2005.[8]

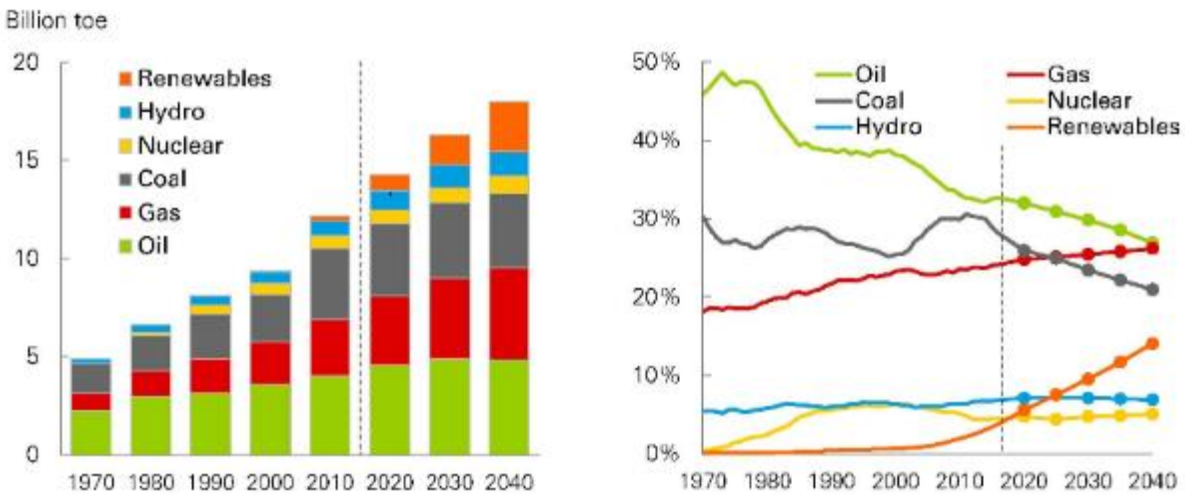

Figure 1. 1: B.P. prediction 'World Energy Outlook 2018 Edition [1]

The U.S. Department of Energy (DOE) has set their parameter for selecting the best storage method for lightweight mobile applications, presented in Table 1.1. According to the 2020 onboard hydrogen-storage applications' requirements, the minimum hydrogen-storage capacity should be at a gravimetric and volumetric capacity of 6.5 wt.%/ 0.05 kg H_2L^{-1} (successively), and at a decomposition temperature ranging from 60 ºC to 120 ºC for commercial viability. [9] A standard hydrogen tank should: Have a low operating temperature range between -40 and 85°C for hydrogen desorption; Operate at a maximum delivery pressure of 12 bar, with a filling time between 3 and 5 minutes; Have a controllable reversibility with long cycle life; Produce a prolonged charge and discharge cycle with a faster reaction time and affordable cost; Have some tolerance for impurities such as humidity and carbon monoxide. [9]

Researchers have proposed alternative options, such as solar, wind, nuclear, hydro, biofuels, and geothermal energy, for future energy demand. [10], [11] However, what is needed is an effective secondary source of energy, renewable, abundantly available,

specifically for the transportation sector. Among all, hydrogen is the most appropriate candidate in the field of secondary energy due to its potential to be stored securely for transportation applications.

Table 1. 1: U.S. department of energy (DOE) target requirement for onboard Hydrogen Storage for Light-Duty Fuel Cell Vehicles versus Mg/MgH_2 storage properties, adapted from [2]

Storage Parameter	**Units**	**2020**	**2025**	**Ultimate**	**Mg/MgH_2**
DOE requirements					**Present work achievement**
System Gravimetric Capacity					
Specific energy from H_2 (net valid energy/max system mass)	kWh/kg (wt.% H_2)	1.5 (4.5)	1.8 (5.5)	2.2 (6.5)	7.6
System Volumetric Capacity					
Energy density from H_2 (net practical energy/max system volume)	kWh/L (kg H_2 L^{-1})	1.0 (0.03)	1.3 (0.04)	1.7 (0.05)	1.4
Durability/Operability					
Operating ambient temperature	°C	-40/85	-40/85	-40/85	>250
Operational cycle life (1/4 tank to full)	cycles	1,500	1,500	1,500	1500
System fill time	min	3–5	3–5	3–5	-
Storage system cost	($/kg H_2)	333	300	266	Meet target

Hydrogen is one of the highly abundant elements in the universe, produced on earth from diverse domestic resources, including fossil fuels and from renewable sources such as biomass and water electrolysis. It is environmentally friendly and releases water vapour into the environment during combustion. [12]

The transition to the hydrogen economy is still an area of research. There is a long road ahead before the consideration of a marketing technology using hydrogen as an energy vector for vehicular applications is put into plan. Hydrogen is not a natural source, such as coal and oil. Hydrogen is often considered an energy carrier. [13]

Scientists and researchers are focused on developing an efficient and cheap way of storing hydrogen. [14] There are two keys to be considered when referring to hydrogen storage. The gravimetric capacity (density), known as the amount of hydrogen to be adsorbed (stored) per unit mass of a vessel, expressed as a weight percentage (wt. %) kg H_2/kg or MJ/kg. And the volumetric capacity, which determines the amount of hydrogen to be adsorbed (stored) per unit volume of the tank, expressed in kg H_2/ L or MJ/L. [12] Hydrogen has an energy density between 120 MJ/kg lower heating value (LHV) and 142 MJ/kg higher heating value (HHV), which is roughly three times higher than the energy density of gasoline 43 MJ/kg. [12], [15] Refer to Figure 1.2.

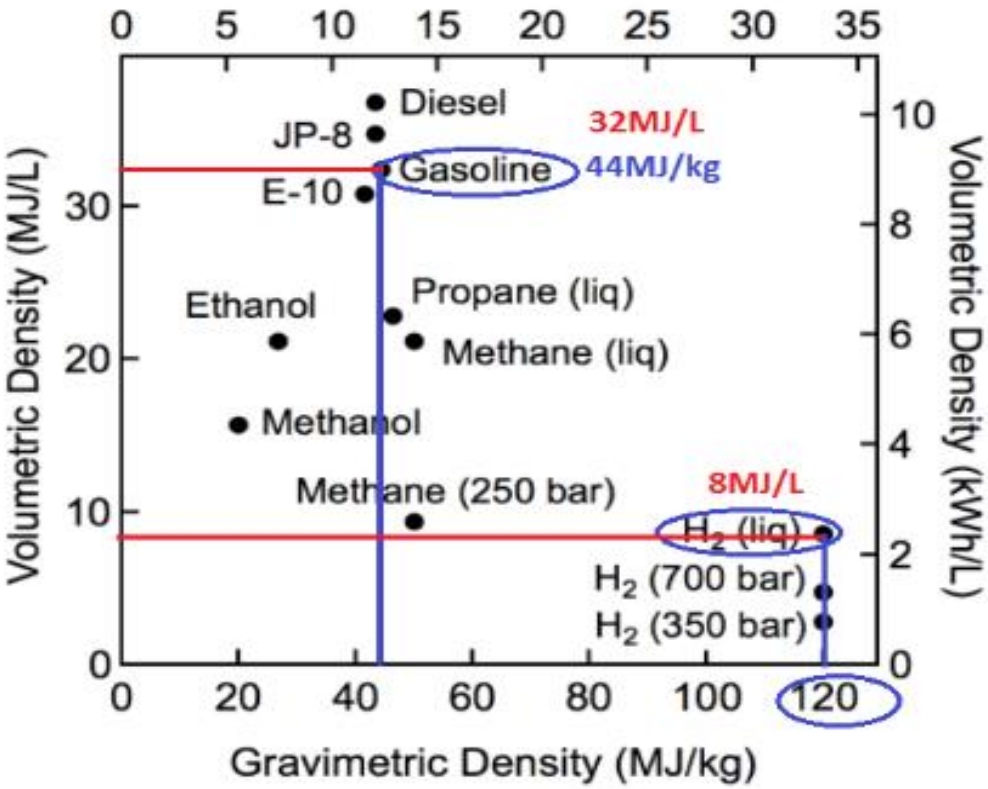

Figure 1. 2: Plot illustrating the gravimetric and volumetric densities of fuels, such as diesel, gasoline, ethanol, propanol, methane, methanol, methane, and hydrogen. Adapted from. [3]

Magnesium/magnesium hydride (Mg/MgH_2) is one of the metal hydride systems that serve as a solid-state hydrogen storage system, which has captivated the attention of researchers due to its high volumetric and gravimetric (110 g/L H_2, and 7.6 wt.%

respectively) hydrogen capacities. [16]–[20] Among the different metal hydride types, MgH_2 is the most promising. However, the practical applications of the Mg/MgH_2 system have drawbacks in terms of poor kinetic and thermodynamic properties. [21]

1.2. Proposed Approaches and Existing Solutions

Several approaches are proposed in the literature to overcome the problem of the poor hydrogen sorption kinetic and low thermodynamics stability of Mg/MgH_2. Approaches such as the doping of the Mg/MgH_2 with a catalyst and the reduction of the particle size via nano-scaling are highlighted below. [22]

1.2.1. Doping Mg/MgH_2 with a Catalyst

The addition of catalysts is the simplest and most promising method to enhance the hydrogen storage performance of the Mg/MgH_2. [22] The transition metal catalysts intensively studied in the past are Nickel (Ni), Titanium (Ti), Vanadium (V), Ruthenium (Ru), Niobium (Nd), Copper (Cu), Cobalt (Co), Zirconium (Zr), and Iron (Fe). [20], [23] Ni has shown high catalytic activity compared to other transition metal catalysts, in improving the sorption/ desorption properties of MgH_2 after mechanical milling. [24], [25] Ni, ZrNi, and $Zr_{70}Ni_{20}Pd_{10}$ are examples of transition metal catalysts proven in the literature to release hydrogen at a temperature below 350°C under 50 bar. [26]–[29] In addition, metal oxides such as Fe_2O_3, ZrO_2, and TiO_2 have also shown remarkable progress in past studies, in enhancing the hydrogen storage properties of MgH_2. [26]

Furthermore, in the literature, recent data states that alloying metal chloride with a Ni catalyst could improve the hydrogen storage properties of the Mg/MgH_2. Galey *et al*.[30], [31] have presented two studies where the authors compared the effect on the thermal stability of 20wt.% Ni Hydride $[NiCl_2(P(C_6H_{11})_3)_2]$, and $NiHCl(P(C_6H_{11})_3)_2$ addition to MgH_2 consecutively. The presence of two chlorine atoms ($NiCl_2$) negatively impacted the decomposition kinetics of MgH_2. Doping MgH_2 with 20wt.%NiHCl improved the desorption rate by 5.2wt.% of H_2 at a peak temperature of 255ºC, whereas the $NiCl_2$ released 5.4wt.% of H_2 at a peak temperature of 285°C.[30] It is vital to consider the ratio of the hydride to the Mg/MgH_2 as a more significant percentage of heavy elements will affect the amount of Hydrogen

absorption by approximately 1 to 3%. [31] Though the state of the metal chloride catalyst and its addition in metal hydride catalysts requires further investigation, as there is not much data available on the addition of chloride in metal hydride when compared to other catalysts such as metal oxides.

1.2.2. Reduction of the Particle Size/ Nano-scaling

Another approach involves the reduction of the particle size by nano-scaling. The most used method is the ball milling technique. The advantages of the ball milling technique are listed as follows: It allows the reduction in the grain size from micrometre to nanometre of approximately 500 nm to about 5 nm and plays a significant part in creating oxide-free surfaces. Magnesium is a pyrophoric material that reacts when exposed to air, resulting in the formation of MgO. A compact, non-permeable layer of oxide on the Mg surface significantly reduces the sorption rate of hydrogen molecules into the Mg matrix, which facilitates hydrogen chemisorption. [32]

On the other hand, a thin layer of MgO can be beneficial. A thin oxide layer only forms a patch, allowing hydrogen diffusion into the Mg. [33] For example, doping MgH_2 with a transition metal, nano-oxide catalysts, has dramatically decreased hydrogen desorption temperatures in past studies. It is crucial to avoid increased heat during the powder milling, as cold welding (C.W.) favours plastic deformation and prevents powder aggregation. [32] In addition, ball milling allows the plastic deformation of the Mg lattice and forms the β-MgH_2 phase, which later tends to transform into a metastable γ-MgH_2 phase. [24], [34]

The X-ray technique is the characterisation approach proposed in the literature to study the effect of the composite after milling. An un-milled Mg generally displays sharp Bragg-diffraction peaks related to hexagonal close-packed (hcp). After milling the composite Mg/MgH_2 plus the addition of the catalyst, the formation of high-intensity Bragg lines β-MgH_2 phase resulted. After that, the aggregated Mg fragments form smaller grains with new active surfaces, which as a result, allows a formation of a reactive MgH_2 phase whilst improving the gas-solid reaction. [36]

In addition, the cyclic stability of metal hydride is a crucial point for selecting an ideal alloy for stationary applications. According to the DOE's criterion set for hydrogen storage materials, the hydrogen kinetics and the absorption/desorption properties of

the metal hydride should not degrade after undergoing approximately 1000 cycles.[37] The degradation of hydrogen capacity may result from structure modification during cycling or the presence of impurities, which results in changes in the PCT shape and a decrease in hydrogen storage capacity. [6] Therefore, the PCT analysis is necessary to study the kinetics and thermodynamics of the analysed materials and determine the stability of the hydride after different cycles. Hence, SEM and TEM analysis are required to determine the change in particle size and surface morphologies consecutively.

N B. Please note that the PhD thesis will often be referred to as "the present study" all throughout the text.

1.3. Work Motivation

The motivation for the *present study* comes from a personal interest on pollution's health impacts. The interest rapidly grew after conducting research in the past, on the health effect of lung surfactants associated with exposure to the secondary pollutant ozone during inhalation. [38] Therefore, the *present study* comes as a personal challenge and dedication to focus on working on a solution to tackle the current pollution problem by finding the best approach to the use of renewable energy.

The *present study* follows previous work on doping Mg/MgH_2 with nanostructured transition metal complexes and metal oxide catalysts to improve the hydrogen storage properties of the Mg/MgH_2 system. [39]–[41]

However, the *present study* reports a novel method for fabricating ZrO_2/Ni based nano-catalyst via a high-pressure reactor. Examples of Zr/Ni-based catalysts reported in past studies to improve the dehydrogenation storage properties of solid-state hydrogen storage are 5 wt.%Ni+5 wt.%ZrO_2 [39], $ZrNi_5/Nb_2O_5$ [42], $Zr_{0.67}Ni_{0.33}$ [40], Zr_9Ni_{11}, $Zr_{43}Ni_{57}$, and Zr_8Ni_{21} [41]. Refer to Figure 1.3 for the desorption kinetics plot of different Mg/MgH_2 doped with various Zr/Ni-based nanocatalysts where the catalysts were synthesised by arc-melting under an Ar atmosphere.

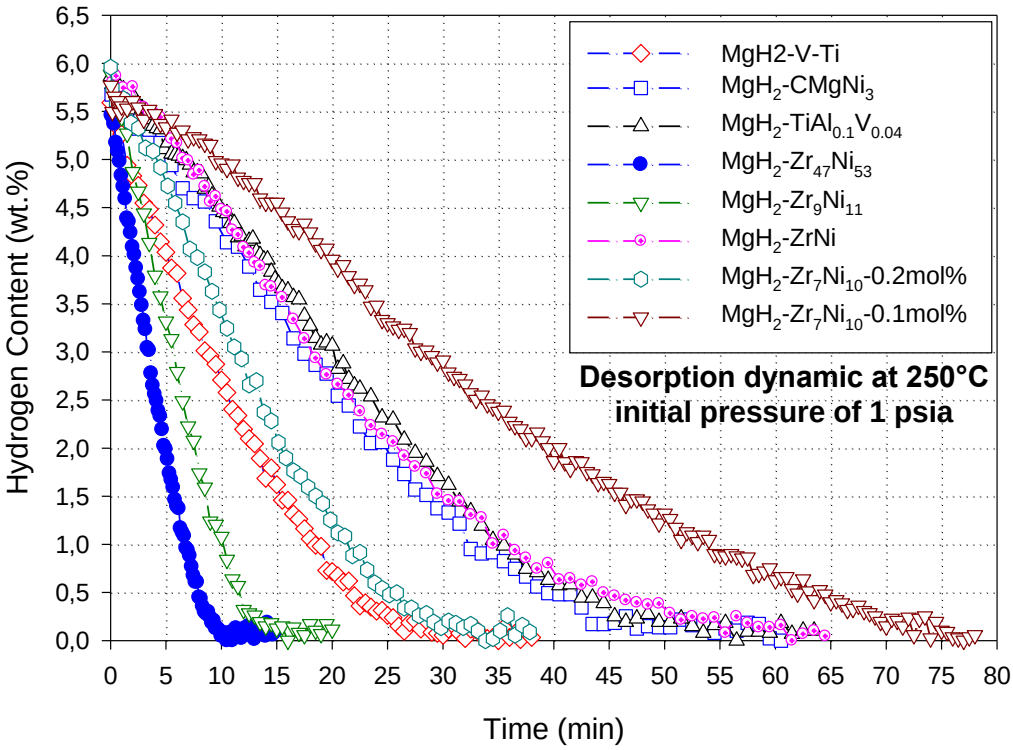

Figure 1. 3: Desorption kinetics of selected Mg-nanocomposites at 250 ◦C. [41]

The more promising results were achieved with the eutectoid $Zr_{47}Ni_{53}$ fully desorbed at 10 minutes, at a desorption rate of 5.5wt%, and the catalyzed Mg-hydride with activated Zr_9Ni_{11} fully desorbed after 15 minutes, at a desorption rate of 6.0 wt%. Moreover, it is worth noticing that the results demonstrated that the composition of dispersed Zr_xNi_y catalysts strongly influences the amount of accumulated hydrogen and desorption rate of Mg-nanocomposite.

1.4. Aim and Objectives of the *present study*

The *present study* aims to improve hydrogen economy research by enhancing the dehydrogenation hydrogen storage capacity of MgH_2. To content this aim, the objectives are listed below.

- **Objective 1**. Developing a great understanding of the importance of hydrogen economy for future energy storage. Refer to Chapter I.
- **Objective 2**. Understanding how to overcome the drawback of Mg/MgH_2 as the ideal storage system in terms of slow Kinetic and poor thermodynamics. E.g.,

by alloying, implementing a nano-catalyst, and nano-sizing with ball milling. Refer to Chapter II.

- **Objective 3**. To understand the importance of analytical techniques used for characterising the powder – catalysts and composites prepared in the *present study*. And how the results correlate to the improvement of hydrogenation and dehydrogenation of hydrogen in Mg/MgH_2. Refer to Chapter III.
- **Objective 4**. Establish the best approach for the novel catalyst synthesis method to produce nanosized metastable catalysts. Refer to Chapter IV.
- **Objective 5**. To enhance the sorption kinetics by catalysing the surfaces of the Mg/MgH_2. To improve the pathway of hydrogen diffusion and sorption thermodynamics and allow Mg to form new compounds or phases. To improve the slow dissociation of the hydrogen on the Mg surface by milling Mg/MgH_2 with nanostructure catalyst additive. The aim is to produce nanocomposite powder whilst breaking the oxide layer, which inhibits hydrogen penetration into the material. Refer to Chapters V, and VI
- **Objective 6**. To understand the importance of the characterisation techniques. XRD to quantify the compositions of the crystalline phases of the composite after the milling process with MgH_2 powder. SEM to determine the distribution of the catalyst on the surface of Mg and the size of the particles. TEM determines the surface morphologies of the catalyst ZrO_2/Ni and the nanocrystal structures. Refer to Chapters IV, V and chapter VI.
- **Objective 7**. TPD/ and PCT analysis for the nanocomposites' hydrogen absorption/desorption kinetics. To understand how the novel ZrO_2/Ni-based catalyst impacts the dehydrogenation properties of MgH_2. Refer to Chapters IV, V and chapter V.

1.5. Thesis Outline

The *present study* comprises **seven chapters** discussed comprehensively below.

Chapter I: The *present study* starts with an introduction, motivation, and a summary of the research conducted on solid-state hydrogen storage with Mg/MgH_2. Moreover, it shows the potential of nano-catalysts to enhance the kinetics and the thermodynamics of the hydrogen sorption to Mg/MgH_2.

Chapter II: Literature – This Chapter covers the overview of Mg-based materials for hydrogen storage, where the hydrogen economy and its challenges are covered, methods for storing hydrogen, and the advantages and disadvantages of using Mg/MgH_2 for storing hydrogen are highlighted.

Furthermore, Chapter II covers the importance of the fabrication of nanostructure material – Ball milling, the use of a catalyst reduction of particle size to nano size is considered. This section covers past experimental studies of the synthesis of the catalyst to improve the sorption of hydrogen storage with Mg/MgH_2.

Chapter III: Methodology – This section elaborates on the techniques used to synthesise and characterise the catalysts and composites prepared in the *present study*:

- The high-pressure reactor was used for synthesising nanosized catalysts, and the ball mill instrument, for the milling of the composite. The composites were milled via two different milling systems – via the SPEX High-Energy Ball Mill, refer to **Chapter IV**, and the Planetary Ball Mill PM 100, refer to **chapter V and chapter VI.**
- The microstructure characterisation of the samples was analysed via XRD (X-ray diffraction), FE-HRTEM (field emission high-resolution transmission electron microscopy), and SEM-EDX (scanning electron microscope analysis–energy-dispersive X-ray spectroscopy).
- The desorption characteristic of the nanocomposite was measured via the TPD (Temperature-Programmed Desorption), and the kinetics/ thermodynamics PCT (pressure-composition-temperature) was determined via a Manometric Gas Sorption Analyser.

Chapter IV: " Title: *Establishing an Innovative Method for the Synthesis of ZrO_2/Ni Nano-catalyst for Improving the Sorption Property of MgH_2 in the Field of Solid-State Hydrogen Storage".* This Chapter focuses on determining the best approach for catalyst fabrication. The catalyst was synthesised via the high-energy ball miller, doped with Mg/MgH_2, and milled for 20 hours via the *SPEX High-Energy Ball Mill*. This Chapter comprises a brief introduction, a methodology, results/ discussion, and a conclusion.

Charter V: Title: "*Development of a Novel Method for the Fabrication of Nanostructured ZrO_2/Ni Catalyst to Enhance the Desorption Properties of MgH_2*". This Chapter aims to resolve the problem of poor sorption, which may result from milling the composites via the SPEX High-Energy Ball Mill for 20 hours. In this Chapter, an alternative method of milling is proposed, via the *Planetary Ball Mill PM 100*, for 5 hours. This Chapter covers a brief introduction to the importance of using catalysts to enhance hydrogen sorption in the Mg/MgH_2 matrix. This Chapter comprises a brief introduction, a methodology, results/ discussion, and a conclusion.

Chapter VI: Title: "*Comparing the Novel Catalysts ZrO_2/Ni and $ZrO_2/NiCl_2$ Storage Behaviour of Hydrogen Sorption Properties of Mg/MgH_2 Powder"*

This Chapter looks closely at the impact of chlorine-based catalysts on the hydrogen storage properties of MgH_2. The formation of nano-structuring material via Planetary ball mills is covered—the reduction in crystallite size. This Chapter comprises a brief introduction, a methodology, results/ discussion, and a conclusion.

Chapter VII: This Chapter englobes the comprehensive discussion of the results achieved through the *present study*. It covers the conclusion of the work, highlighting the main findings of the *present study* and advice on various suggestions for future work.

REFERENCES: Comprise a series of carefully selected references used concerning the *present study*. It includes references from books, journal papers as well as conference papers. It also contains a list of carefully selected internet websites helpful for the *present study*.

APPENDICES: Contains a series of remaining graphs, tables, figures, and photographs used during the *present study*

Reader Guide

Chapter I: General Introduction

Chapter II: Literature

Chapter III: Methodology

Chapter IV: Establishing an Innovative Method for the Synthesis of ZrO_2/Ni Nanocatalyst for Improving the Sorption Property of MgH_2 in the Field of Solid-State Hydrogen Storage

20 hours milling time/ SPEX high energy ball mill MgH_2+10wt.%ZrO_2/Ni

Introduction Recap

Experimental

- Catalyst-ZrO_2/Ni synthesis
- Composite (MgH_2+10wt.%ZrO_2/Ni) ball mill: 5 hours via Planetary
- Characterisation

Results/ Discussion

- XRD
- SEM
- TPD
- Kinetics

Conclusion

References

Chapter V: Development of a Novel Method for the Fabrication of Nanostructured ZrO_2/Ni Catalyst to Enhance the Desorption Properties of MgH_2

5 hours milling time/ Planetary ball mill - MgH_2+10wt.%ZrO_2/Ni

Introduction Recap

Experimental

- Catalyst-ZrO_2/Ni synthesis
- Composite (MgH_2+10wt.%ZrO_2/Ni) ball mill: 20 hours via SPEX
- Characterisation

Results

- XRD
- SEM
- TPD

Discussion

Conclusion

References

Chapter VI: Comparing the Novel Catalysts ZrO_2/Ni and ZrO_2/$NiCl_2$ Storage Behaviour of Hydrogen Sorption Properties of MgH_2 Powder

5 hours milling time/ Planetary ball mill (ZrO_2/$NiCl_2$) catalyst

Introduction Recap

Experimental

- Catalyst-ZrO_2/Ni synthesis
- Composite (MgH_2+10wt.%ZrO_2/$NiCl_2$) ball mill: 5 hours via Planetary
- Characterisation

Results / Discussion

- XRD
- SEM
- Kinetics
- PCT

Conclusion

References

Chapter VII: General conclusion

References

Appendices

CHAPTER II: LITERATURE REVIEW

This Chapter covers an overview of hydrogen storage with Mg/MgH_2 systems research completed prior to the research undertaken in the *present study*. The critical points elaborated are – the kinetics and thermodynamics of metal hydrides for solid-state hydrogen storage and published results in the literature on Mg-based materials for bibliographic review.

2.1. Hydrogen Storage

Hydrogen storage comes with several challenges due to its low volumetric energy density, resulting in its limitation for mobile applications. Hydrogen storage can be parted into two broad categories: Physical-based storage comprising; Compressed gas and Liquid hydrogen storage, and Material-based storage, as shown in Figure 2.1.

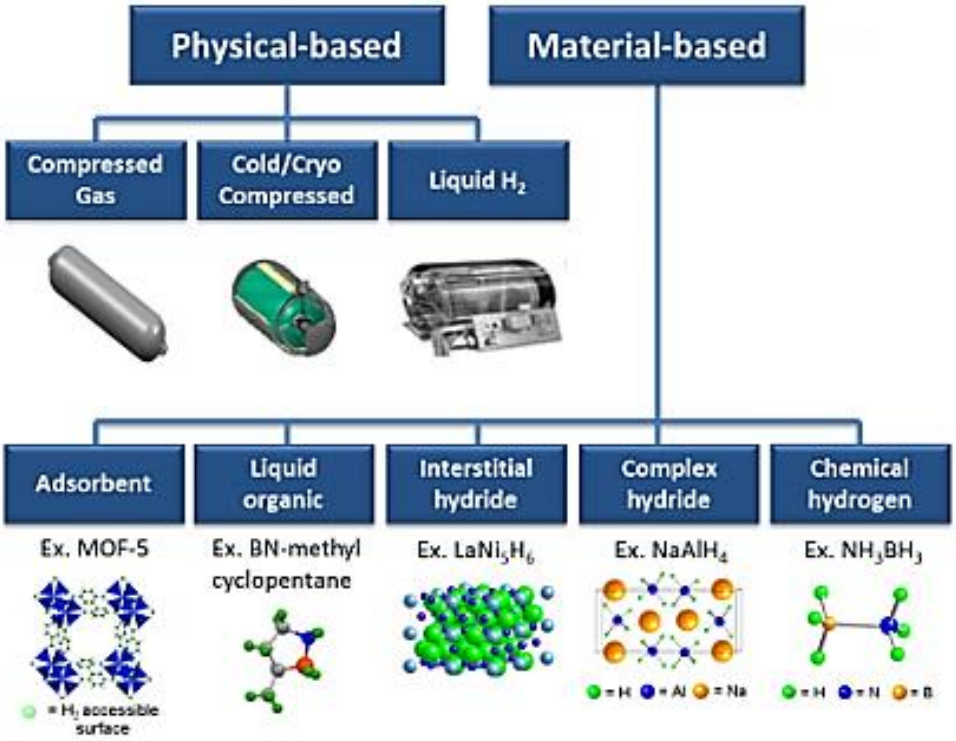

Figure 2. 1: Potential Hydrogen Storage Technologies.[43]

2.2. Physical Based Storage

2.2.1. Compressed Gas and Liquid Hydrogen Storage

Compressed gas is the conventional hydrogen storage system; it has several limitations regarding safety concerns, cost wise and transportation. This system has a low volumetric hydrogen storage density of 4.5MJ/L and requires a higher pressurise tank to store hydrogen at 350-700 bar at room temperature. The conventional gas storage technology was proven effective in various prototype vehicles and was demonstrated in a prototype fuel cell vehicle with a pressure tank of 700 bar (10,000 psi). [44] The high capacity of the tank resulted from the low energy density of hydrogen gas of approximately 26 g/L. The lower density was due to the thickness of the tank's wall and the additional protective liner. [44]

A liquid storage system comes with a slightly higher volumetric density at 8.7 MJ/L; however, it requires a cryogenic tank to store hydrogen at -253ºC with a pressure of 5 to 10 bar. This temperature is crucial to maintain hydrogen in a liquid state. (12) The cooling technology at low temperatures results in a loss of approximately 30% of the total energy. [12] About 7 kg/day for a 725 kg tank size of hydrogen is lost daily due to irreversibility during refilling, pumping, and cooling transfer lines. [9] Both physical base storage systems require expensive and lightweight materials to construct the vessel tank, with high resistance in the event of an explosion resulting from a vehicle collision. [15]

2.2.2. General Principles of the Solid-State Hydrogen Storage

Solid-state hydrogen storage has two categories: physisorption and chemisorption, as shown in Figure 2.2. The solid-state storage method involves storing hydrogen in a metal hydride or a chemical hydrogen storage material. The solid-state hydrogen storage method involves bonding hydrogen atoms to other metal or semimetal atoms through ionic, covalent, or metallic-type bonds. [43] On the other side – hydrogen can be adsorbed on carbon surfaces or bonded organic or inorganic compounds to form different hydrides. [13], [14], [16], [17] The solid-state hydrogen method offers numerous advantages, such as high energy efficiency, good cycle stability, and low cost. [16]

Additionally, the safety concern reported for the gas and Liquid storage (boils off/ explosion during a vehicle collision) is not a concern regarding the solid-state hydrogen storage method.

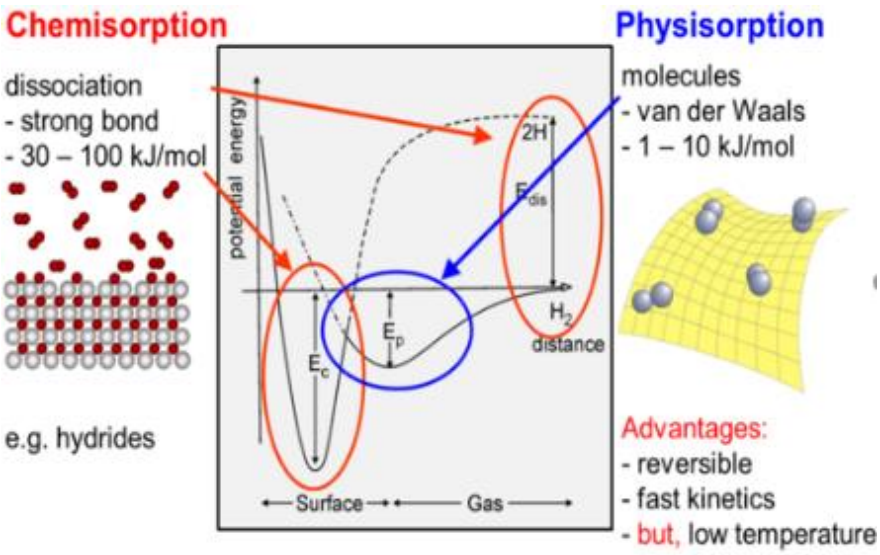

Figure 2. 2: Potential energy diagram- Hydrogen sorption on a metal surface via chemisorption and physisorption. [45]

2.2.2.1. The physisorption

Physisorption refers to the adsorption of hydrogen atoms or molecules on the surface of the adsorbent material without forming a chemical bond". [19] The physisorption process comes with several drawbacks. Physisorption has a weaker absorption enthalpy (DH_a) of 1 to 10 kJ/mol, as shown in Figure 2.2, with binding energy ranging from 0.04 to 0.1eV. This reaction occurs via van der Waals interactions. When an element undergoes physisorption, the materials drop the hydrogen storage capacity below 1 wt.% at ambient temperature and pressure range of 50 to 100 bar. Therefore the binding ability of the hydrogen on the surface of the materials becomes ineffective. [46] The attention is on porous materials such as zeolites, carbon nanostructures, and metal-organic frameworks (MOFs). [18]

Adsorption capacity strongly depends on the surface area, pore volume, working pressure, and temperature. Porous materials such as MOFs require a larger surface

area to increase their capacities to store a larger volume of hydrogen at cryogenic temperature. However, due to the weak van der Waals type of interaction, they have a low ability to store hydrogen at room temperature (physisorption).

2.2.2.2. Chemisorption

Chemisorption is generally for storing hydrogen metal and chemical hydride material. It involves a more substantial binding energy, with an enthalpy of formation (ΔH_f) ranging from 50 to 100 kJ/mol H_2, as shown in Figure 2.2, and binding energy ranging from 2 to 4eV. [47] Therefore, it requires a large amount of heat, which gets released during the charging process, and extra energy to enable the release of hydrogen for its applications. [46] Chemisorption is the absorption process, where a dissociation reaction of hydrogen molecules occurs on the surface, followed by diffusion of the hydrogen atoms into the metal host lattice, as shown in Figure 2.3. This process generally occurs under ambient conditions but requires costly absorbent materials. [20] The complex hydrides involve the interaction of hydrogen with light elements of groups 1, 2, and 3 of the periodic table, e.g. Li, Na, Mg, Ti, alloys or intermetallic compounds, to form stable metal hydrides or complex metal hydrides. [19] The drawback of complex hydride is the slow kinetics of hydrogen desorption. [24]

Intermetallic hydrides are generally found in the groups IIA to IVA of the periodic table. The intermetallic compounds intensively investigated in the literature are such as TiFe and LaNi5. Though TiFe is extremely sensitive to impurities, it quickly deactivates upon oxidation. $LaNi_5$-based hydrides are advantageous as they can store hydrogen reversibly close to ambient conditions and at low pressures. Although the advantageous, $LaNi_5$-based hydrides are not only costly, however they also suffer from an insufficient hydrogen storage capacity, refer to Table 2.1

Chemical hydrogen storage, such as Metal-boron hydrides – $LiBH_4$, $NaBH_4$ and NaB_3H_8, are of interest in the field of hydrogen storage, as they possess high gravimetric hydrogen capacities. And they have a high hydrogen storage capacity of 10.8 wt.%, which agrees with the DOE's criterion set for hydrogen storage materials. However, they require very high temperatures exceeding 500 °C for the hydrogenation process and have a very complex decomposition process involving forming intermediate phases such as NaH and $Na_2B_{12}H_{12}$. [48]

In hydrogen storage with metal hydrides, the hydrogen creates a chemical band with the metal host. It physically gets adsorbed on the surface of the metal host, unlike porous and high surface area materials. In addition, the storage with metal hydride results in high volumetric and mass densities and long-term stability after 1000 cycles. [15] The hydrogenation and dehydrogenation processes occur via an exothermic and endothermic reaction, respectively. Absorption of hydrogen with many metals and alloys forming metals generally occurs at high temperatures and relatively low pressure for a response. [24]

The storage of hydrogen with complex hydrides involves the interaction of Light elements, e.g., Li, Mg, B, and Al, with hydrogen to form stable compounds. Complex hydrides form an ionic or covalent band with hydrogen atoms. The strong nature of the bonds results in a decrease in kinetics capacity and requires high temperature to achieve hydrogen desorption. [49] The use of lightweight metals results in high gravimetric and volumetric densities due to their capability of usually storing two hydrogen atoms per metal atom. e.g. the metal hydrides most published in the literature are such as alanates (AlH_4), amides (NH_2), Ammonia borane (BH_6N) has been suggested as a storage medium for hydrogen and borohydrides (BH_4). [15]

Figure 2.3 illustrates the comparison of the plot of the volumetric over the gravimetric hydrogen capacities of the hydrogen storage materials presented in the literature. The top right corner of Figure 2.3. shows the ideal hydrogen storage system with higher volumetric and gravimetric capacity.

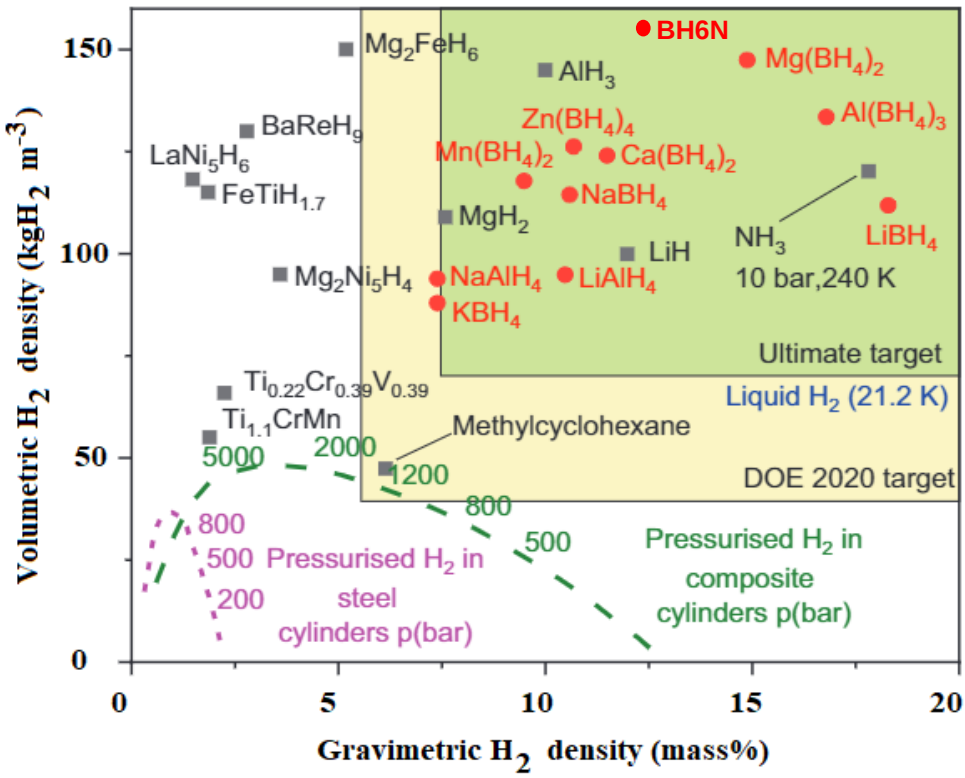

Figure 2. 3: The plot of the hydrogen volumetric capacity over the gravimetric capacity of a few hydrides, adapted from. [6]

2.2.3. Criteria for the selection of an ideal solid hydrogen storage system

There are a few key points to be considered for an ideal solid state hydrogen storage system: favourable kinetics for the sorption of hydrogen system, high gravimetric and volumetric hydrogen storage capacity, temperature ranges, operating pressure, reversibility, cost-wise, and safety concerns. [34] The kinetics strongly depends on the materials' properties, considering the material's surface compositions and morphology, grains sizes, microstructural properties, additives, and catalyst concentration. [50] In this regard, the Kubas interaction is an explored option to enhance Hydrogen sorption. Refer to Figure 2.4; the Kubas interaction is at a mid-point of the physisorption and chemisorption binding. It has an enthalpy value of 20–30 kJ/mol H_2 and a bonding energy range of 0.1 to 0.8eV. Kubas binding.

enthalpy values are ideal for creating a strong interaction between hydrogen and the material whilst minimising heat management. [46]

Kubas binding involves the interaction between the H-H bonding to a metal, where the H-H s-bonding orbital donates one of the electrons to the empty d-orbital of the transition metal. However, this binding interaction only occurs when the supplied energy, defined as temperature and pressure present in the system, exceeds the activation energy barrier of the system. [51]

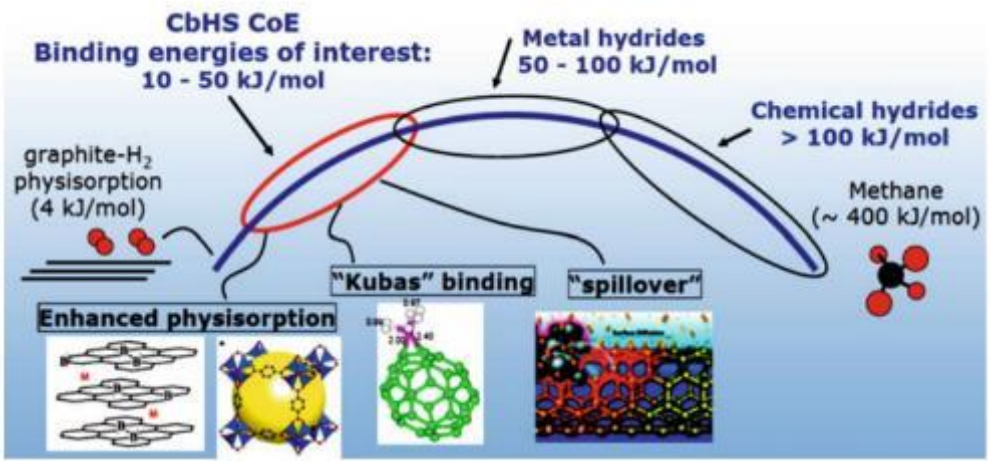

Figure 2. 4: Illustrates the Kubas interaction of the physisorption chemisorption process. [46]

The approach of the Kubas interaction for enhancing hydrogen storage capacities is still under development in terms of practical application, as most results are limited to computational studies. [52]

Table 2. 1: List of a hydride of interest for solid hydrogen storage

Family type	Metal hydrides	$-\Delta H^{\theta}$ (kJ mol^{-1} H_2)	H_2 capacity wt.%	Dehydrogenation temp(ºC)	Disadvantages	Ref
Metal hydride	MgH_2	-74	7.6	300ºC/15bar	Kinetics/ Thermodynamic	[53]
Intermetallic compounds	AB-TiFe	-31.7	1.2	20ºC/10bar	Poor storage capacity	[54]
Intermetallic compounds	AB5-LaNi5	-30	1.37	28ºC/ 10bar	Poor storage capacity	[55]
Microporous	MOF-5	7.9	2.27	149ºC /25bar	Poor adsorption capacity	[56]
Hydrides Borohydrides	LiBH4	-177	13.5	453ºC	High desorption temperatures/ Poor reversibility	[49]
Complex	LiAlH4	140	10.6	385ºC 260ºC	High decomposition temperature/ Slow dehydrogenation kinetics and irreversibility.	[57]

2.3. Mg/MgH_2 Storage Material

As mentioned in the previous Chapter, the metal hydride system is ideal for storing hydrogen, more precisely, the Mg-based metal hydride. Mg has been reported in the literature as one of the promising hydrogen storage materials, as it possesses several desirable characteristics for automobile applications. [23]

Mg is a lightweight metal, abundantly available, and relatively low cost. Due to the solid ionic bonds between Mg-H, Mg reacts reversibly with hydrogen to form a stable MgH_2 compound. MgH_2 is especially advantageous due to its high hydrogen storage gravimetric capacity of 7.6 wt. %; with potential reversibility, and Mg is environmentally friendly. [58]–[60] Nonetheless, the practical application of MgH_2 for automobile applications is still under development. – A temperature of approximately 350ºC is required to achieve hydrogen desorption at a pressure > 1atm. The high operating temperature results from the high thermodynamic stability and shows an enthalpy

value of 74.5 kJ/mol, an entropy value of 130 J/mol/K, and kinetic barrier of Ea = 160 kJ/mol. [58] The slow kinetics resulted from the poor decomposition of hydrogen into the bulk of the MgH_2/Mg. [60] Refer to Table 2.2. for the summary of the properties of the storage of MgH_2.

Table 2. 2: Properties of the hydrogen storage of commercial MgH_2

Gravimetric capacity	**Hydrogenation**			**Dehydrogenation**		
Wt.%	Temp (°C)	ΔH° kJ/mol	Ea kJ/mol	Temp (°C)	ΔH° kJ/mol	Ea kJ/mol
7.6	>250	-74	160	>300	74	200-240

The hydrogen absorption into the Mg is known as a hydrogenation process. The hydrogenation is an exothermic reaction involving the formation of the α–MgH_2 tetragonal crystal structure compound. The α-phase characterises a relatively low hydrogen concentration. The interactions between hydrogen atoms are weak, and mobility is generally very high. [61] In the high pressure of approximately 2 to 8 GPa, at a temperature of 250–900°C, a mutual interaction between dissolved hydrogen atoms results in the α–MgH_2 undergoing a polymorphic transformation. There is a formation of α-β transition, which is transformed into a total β–MgH_2 with a tetragonal crystal structure at a later stage. Later, the β–MgH_2 gets converted to a metastable phase known as the γ–MgH_2 with an orthorhombic shape. Refer to Figure 2.5. [62]

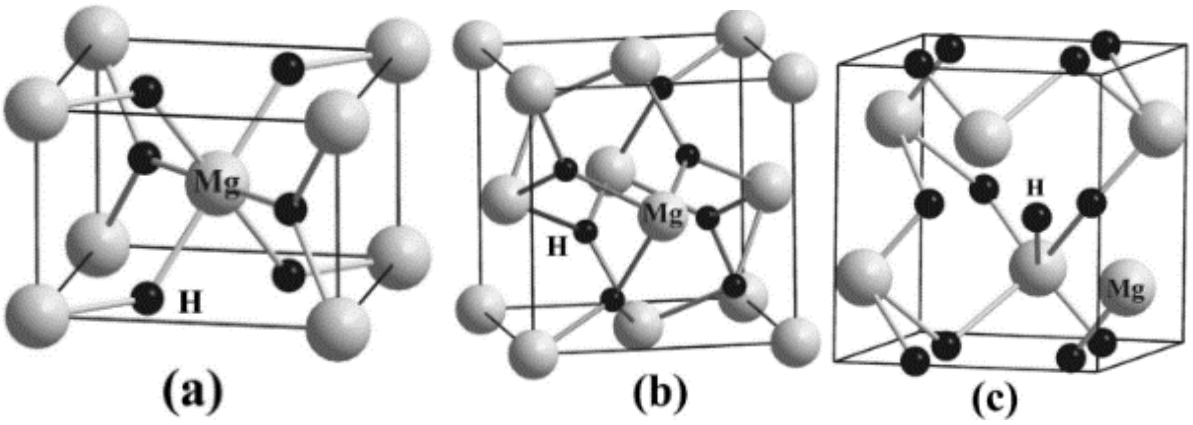

Figure 2. 5: (A) Crystal structure of α-(MgH_2), (B) β-(MgH_2), (c) γ-(MgH_2). Picture adapted form [59]

Mg is a pyrophoric metal that reacts when exposed to air and forms the MgO compound. The oxide layer decreases the permeability of the hydrogen molecules into the Mg matrix. Therefore, the Mg surface must be perforated or cracked to initiate the hydrogenation process. The oxide layers which cover Mg particles hindering hydrogenation can be cracks with annealing Mg at a high temperature exceeding 400ºC under vacuum. [63] As a result, the hydrogen becomes exposed to the metal surfaces, allowing more absorption inside the Mg matrix. Another method is the activation process, which involves cycling the oxidised Mg at a high temperature exceeding 400ºC. [64] In addition, mechanical milling hydrogen in a MgH_2 matrix to reduce the particle size, which contributes to breaking the oxide layer on the surface of the Mg particles.

Although, it is stated in the literature that a thin layer of MgO can be beneficial. [63] A thin oxide layer only forms a patch, allowing hydrogen diffusion into the Mg. [64] Hence a compact, non-permeable layer of oxide on the Mg surface significantly reduces the sorption rate of hydrogen. [33]

Summary of the problem associated with Mg/MgH_2/ affecting the sorption property:

- High thermodynamic stability
    - High-temperature requirement for desorption

- Slow kinetic
    - Oxide layer formation
    - By product formation
- Poor decomposition of hydrogen on the Mg surface
    - Slow diffusion of hydrogen through MgH_2
- Slow absorption and desorption process of hydrogen molecules on the Mg surface
    - The dissociation process of the hydrogen on the Mg surface requires a high level of energy.
- Hydrogen molecules easily dissociate with low activation potential barriers on transition metals, such as Ni.
- MgH_2 is very stable, so it requires a very high temperature for decomposition; the decomposition reaction is slow, requiring a large amount of energy to extract hydrogen from Mg matrix.

2.3.1. Hydrogenation and Dehydrogenation Principal in Metal Hydride

The storage of hydrogen in a solid form is a convenient method for storing hydrogen. Mg-based metal hydride is the storage material of interest for storing hydrogen at specific pressure and temperature conditions. Figure 2.5 represents the diffusion steps of the hydrogen gas into the metal hydride. [6] First: The hydrogen molecule is absorbed through a Physisorption reaction into the metal surface via the Van der Waals interactions.

Second: The absorbed hydrogen molecules dissociate via a chemisorption - $E_{chem(H)}$ reaction. There is a binding interaction of the hydrogen on the host surface and electron sharing between the dissociated hydrogen and metal atoms.

Third: The hydrogen atom penetrates the subsurface $E_{Pen(H)}$ as the hydrogen reaches the point below the critical temperature (Tc). There is a formation of two-phase between the solid solution known as the α phase and the hydride β phase (α+β), as shown in Figure 2.6. [65], [66]

Four: Involves the separation of hydrogen into two hydrogen atoms. Next is the chemical absorption and diffusion of hydrogen into the sub-surface of the metal. When the reaction reaches the critical temperature (T_c.), the formation of the two-phase

region disappears. A flat plateau isotherm is formed as the two-phase coexist, prior to a total transformation of the α-phase into the β-phase – a more stable metallic hydride phase with a more significant concentration of hydrogen. The length of the flat plateau strongly determines the amount of hydrogen stored reversibly with slight pressure variations. (28)

Lastly: The nucleation ($E_{nuc/growth}$) process takes place. The hydrogen atoms get converted from the octahedral to the tetrahedral interstitial sites. [67], [68] In the desorption process, the hydrogen atoms get converted into molecules before being physically desorbed. [47]

Refer to Figure 2.6 for the five intermediate processes of the complex metal hydride thermodynamic reaction.

- Physisorption of hydrogen molecules
- Dissociation of hydrogen molecules and chemisorption
- Surface penetration of hydrogen atoms
- Diffusion of hydrogen atoms through the hydride layer
- Hydride formation at the metal/hydride interface

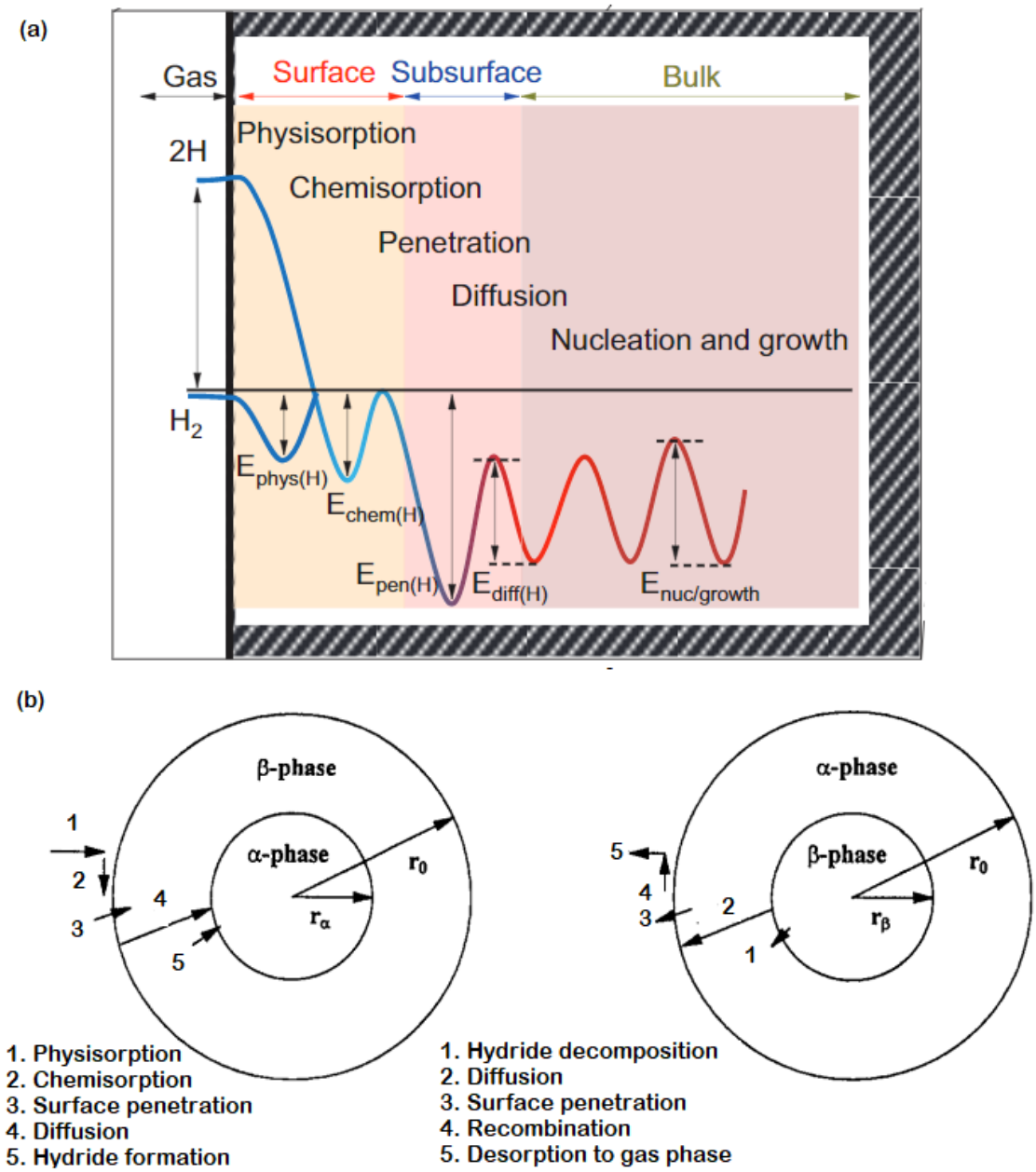

Figure 2. 6: (a) Energy barriers for the hydrogenation of metal and complex hydrides [47], (b)Diffusion steps of the hydrogen gas into the metal hydride. [6]

2.3.2. Kinetics and Thermodynamic Properties of Metal Hydrides

It is necessary to obtain the enthalpy (ΔH) and entropy (ΔS) to predict the plateau pressure (P) level. This pressure is related to the temperature (T) by van't Hoff's law – refer to Equation 2.1. [69]

The ΔH is the slope of the graph of the hydrogen gas pressure over the general operating temperature. The ΔS is the Y-intercept, representing the entropy of hydrogen gas lost during the hydrogenation process, which is approximately 130 J/mol/K H_2 for metal hydride material. [6]

$$ln\left(\frac{P_{eq}}{P_o}\right) = \frac{\Delta H}{RT} - \frac{\Delta S}{R} \qquad \text{Eq 2.1}$$

Where R is the ideal gas constant = 8.3145 J/K/mol

P_{eq} is the equilibrium pressure (bar)

P_o is the atmospheric pressure (bar)

One of the most critical characteristics of metal hydrides are the pressure–composition–temperature (PCT) isotherm, from which parameters such as enthalpy ΔH and entropy ΔS can be determined.

Refer to Figure 2. 7. (a) for the Isotherm curve, plot the equilibrium pressure (P) as a function of hydrogen concentration (C) and temperature (T). PCT curve provides information on the amount of hydrogen stored in the metal hydride at a specific temperature and pressure. The activation energy (Ea) gives the knowledge of the minimum energy required for the chemical reaction to take place. [70] The activation energy can be determined using the Kissinger method, with the use of a DSC (Differential Scanning Calorimetric) instrument. Refer to Equation 2.2. [71]

$$\mathrm{d}\left(\frac{ln\beta}{T_p^2}\right) / \, d\left(\frac{1}{T_p}\right) = -\frac{E_a}{R} \qquad Eq.\,2.2.$$

- Where β is the heating rate,
- T_p is the peak temperature,
- E_a is the activation energy,
- R is the gas constant

The E_a can be determined by analysing the metal hydride powder at different temperatures and calculating the slope of the fitted line from a plot of $ln\ (\beta/T^2_p)$ over $1000/T_p$. The activation energy of the commercial MgH_2 reported in the literature is 168 kJ/mol. And doping MgH_2 with nickel catalyst decreases the activation energy to 83 kJ/mol. [71]

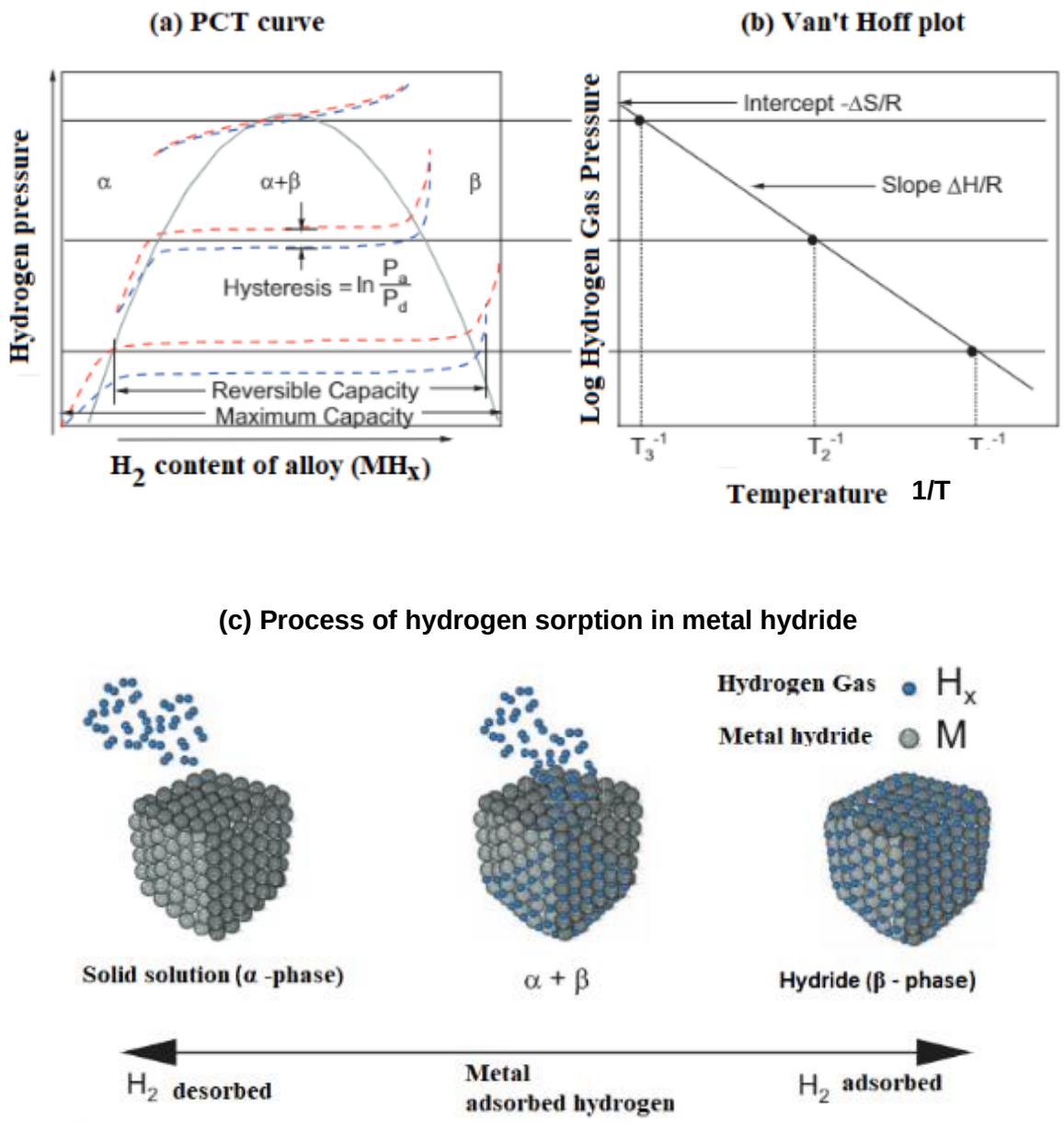

Figure 2. 7: (a) Plot of the pressure composite isotherms (PCT) of the metal hydride system, (b) Van't Hoff plot, (c) chemisorption of hydrogen in the metal hydride (α-phase), and diffusion into the bulk (β-phase), adapted from [6]

The higher desorption temperature is associated with increased ΔH at a given hydrogen pressure. The activation energy increase is related to a decrease in the reaction rate at a higher temperature. Therefore, the activation energy should be lower to improve the sorption kinetics of MgH_2 for a faster reaction rate. [23]

Figure 2.8 shows the kinetics represented by the reaction's activation energy (Ea) and the thermodynamics characterised by the formation enthalpy (ΔH) and entropy (ΔS) of metal hydride. Figure 2.8 (a) illustrates the exothermic reaction. Here the product has less energy than the reaction. The heat released from the system into its surroundings results in a negative reaction enthalpy, known as (ΔH). In this reaction, the ΔH is positive as the system gains energy. Although Figure 2.8. (b) illustrate the endothermic reaction. The product has high energy when compared to the reactant. [23]

The ΔH of a reaction is the difference between the potential energy (P.E.) of the product (P) and the reactant (R). For an exothermic reaction, the product has less energy when compared to the reactant, and the reaction results in a negative Enthalpy value. Refer to Equation 2.3.

$$\Delta H = P - R \qquad Eq. 2.3$$

The Forward activation energy (Ea_F) is the energy required to allow a reaction to start, which is the energy difference between the reactant (R) and the transition state (T.S.). As in the absence of the (Ea_F), the reaction will not occur. There are two ways to reach the activation energy and speed up the reaction rate.

- By subjecting the reaction to a high temperature
- Implementing a catalyst in the reaction

The Reverse activation energy (Ea_R) is the reverse reaction, known as the energy difference between the transition state (T.S.) and the product (P). Enough energy is needed to get to the T.S. for the reaction. Referring to Equation 2.4.-2.6, the second method to determine the ΔH of response is by subtracting the forward activation energy from the reverse activation energy.

$$Ea_F = Ts - R \qquad Eq.2.4$$

$$Ea_R = Ts - P \qquad Eq.2.5$$

$$\Delta H = Ea_F - Ea_R \qquad Eq.2.6$$

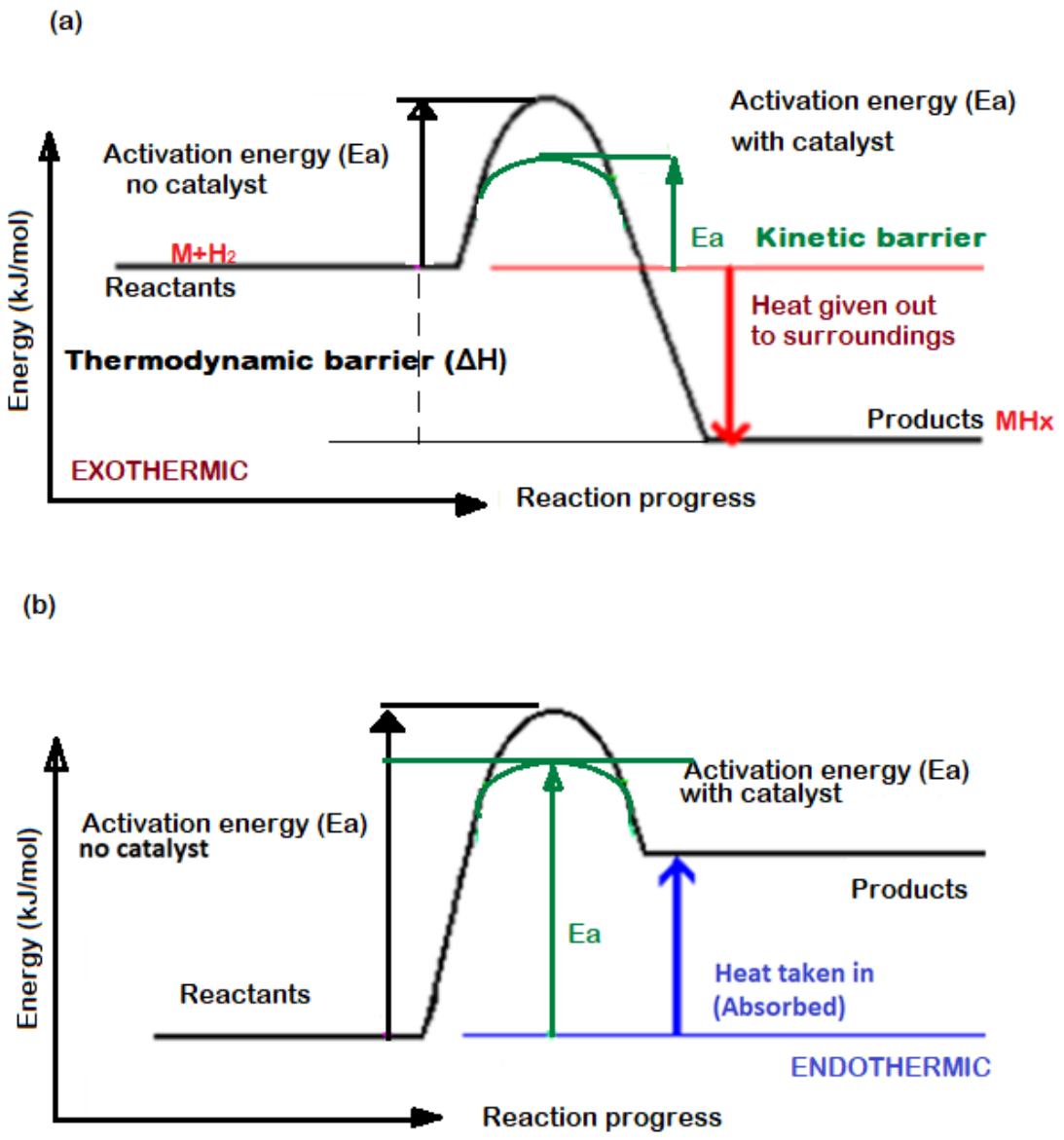

Figure 2. 8: Schematic illustration of a thermodynamic and kinetic barrier for sorption reactions of metal hydrides. Adding a catalyst to lower the activation Energy (E_a) (a) Exothermic reaction, (b) Endothermic reaction. Adapted from [72], [73]

2.4. Approaches to Enhance the Sorption Property of Mg/MgH_2

Methods proposed in the past to overcome the drawback of the thermodynamics and kinetics with the MgH_2 are: - catalysing, nanosizing–ball milling, additives doping, and alloying.

2.4.1. Addition of Catalysts

Implementing a catalyst was reported in the literature as one of the options to enhance the sorption property of Mg/MgH_2. [58]

Catalysts are substances that alter the rate of a chemical reaction without being permanently chemically changed in the reaction. Implementing a catalyst in a chemical reaction is beneficial, as the catalyst affects the activation barrier. Hence enhancing the kinetics – hydrogenation/ dehydrogenation rate of a metal/alloy. Refer to Figure 2. 8. The catalyst does not participate in the chemical reaction and does not affect the thermodynamics of the reaction. However, in some cases, the presence of a catalyst participates in the chemical reaction by changing its oxidation state or banding arrangement. Although, they remain intact at the end of the reaction after two or three catalytic cycles. [72] To date, the catalysts studies for different hydrogen storage materials are still a significant area of research, mainly regarding the reduction reactions and nanostructured catalysts for hydrogen storage materials.

The fabrication method of the Zr/Ni base nano catalysts reported in the literature is by Arc melting. Arc melting is a long process for catalyst fabrication. It requires melting the material up to five times in a repeated cycle, ensuring that the alloy's results to a uniform chemical composition. Followed by crushing the resulting material (spherical balls) into small pieces, milling the produced alloy powder under an Ar atmosphere for up to 950 hours. [69]

The *present study* focuses on the change in Ea, ΔH when catalysing the MgH_2 with nano-catalyst. The catalyst fabrication method in the *present study* is the novel method first reported in the literature for synthesising nano-catalysts Zr/Ni based metal oxide and Zirconium/Nickel-Chloride. This catalyst production follows the principle of the sol-gel process, previously proposed by Parayil *et al*. [74], to synthesise TiO_2 photocatalytic

hydrogen. The sol-gel method involves the hydrolysis reaction and gel formation via condensation. The drying process is the most critical step, where xerogel drying is a simple method that takes place under ambient conditions.

The novel method for the catalyst fabrication reported in the *present study* allows synthesising a powder on a nanoscale. As reported in the literature, the decrease in particle size results in a homogenous distribution of catalyst on the surface of the metal, which later increases the absorption and desorption process of the hydrogen in Mg/MgH_2. Among varieties of catalysts, Ni is the most published catalyst in the literature, as they possess a solid affinity for hydrogen due to its rapid kinetics, flat plateau and low hysteresis. [75] However, researchers recommended doping Ni with a transition metal such as Titanium (Ti), Iron (Fe), or Zr, as MgH_2 powder with Ni results in the aggregation of catalysts and the formation of an undesired Mg_2NiH_4 phase. [76], [77]

The hysteresis in metal hydrogen systems generally refers to the thermodynamic behaviour that occurs during hydrogen storage in metal hydride. [25], [40] In this phenomenon, the hydride absorption pressure (P_a) is higher than the hydride desorption pressure (P_d). Figure 2.9 illustrate the Hysteresis plot of the absorption, and desorption curve of hydrogen storage at different concentration, as a function of equilibrium pressure (y-axis) over a constant temperature (x-axis). The hydrogen pressure relates to energy applied in the system. At the end of the absorption process, the hydrogen pressure reaches an equilibrium point, meaning the concentration of hydrogen cannot longer increase in the absorbing material. From this stage, the decomposition of the hydrides should generally take place. One of the metal hydride's main challenges is obtaining a lower Hysteresis phenomenon (Pa/Pd), which known as the pressure difference between absorption and desorption for the exact temperature. [78], [79] The more rapid kinetics of the composite result in a fast decomposition and a significant decrease in the hysteresis gap. The main challenge of solid-state hydrogen storage is to decrease hydride decomposition pressure, which is related to the slow kinetics of metal hydrides.

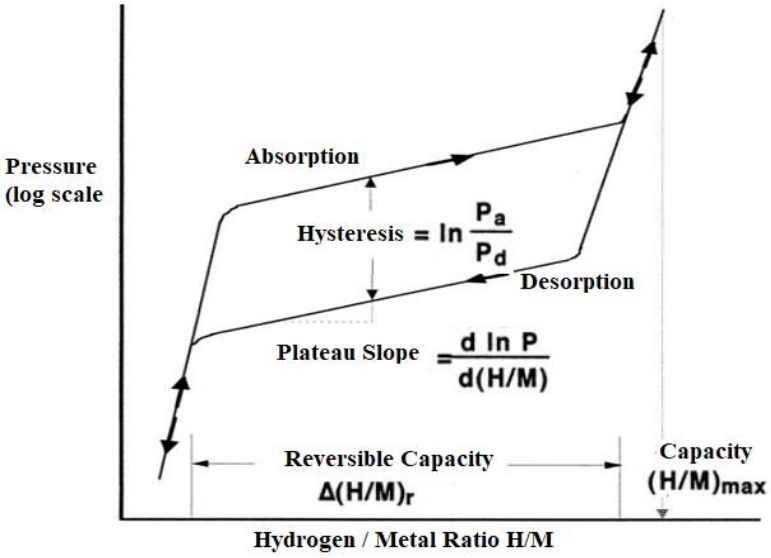

Figure 2. 9: Hysteresis plot to characterise the formation and decomposition of the hydride, adapted from [79]

2.4.2. Ball-milling Nanostructured Material

Decreasing the particle size is critical for enhancing the hydrogen sorption properties of hydride materials. The technique intensively reported in the literature is via a milling system. Ball mills is the method first discovered by Zaluska and Zaluski in 1999. [81] The ball-milling approach is advantageous for preparing Mg-based materials at low temperatures and for a short period. A short milling time, under 1 hour, does not show a significant change in the nanograin size – ranging from approximately 50 -60 nm, as shown in Figure 2.10. Whereas the increasing milling time for 10 hours and longer results in a decrease of grain–crystallite size below 20 nm—which results in the transformation of β-MgH_2 into the metastable γ-MgH_2. The metastable phase formation is due to the high pressure exerted by the contact impact of the milling balls and the milled powder MgH_2. Smaller crystal size enhances hydride materials' absorption/ desorption kinetics. [82]

Adding one or more catalysts in mechanical milled powder results in a remarkable improvement in hydrogenation and dehydrogenation of hydrogen in Mg/MgH_2. The milling metal hydride materials significantly create oxide-free surfaces and facilitate hydrogen chemisorption. [32] And this increases the interaction and distribution of the

catalyst on the surface of the hydrogen storage material – MgH_2.[32] Varin *et al*.[82] had reported a study on the correlation between milling time and particle size of MgH_2. The author had established the optimum milling time to be between five and ten hours as the increase in milling time generally results in powder agglomeration.

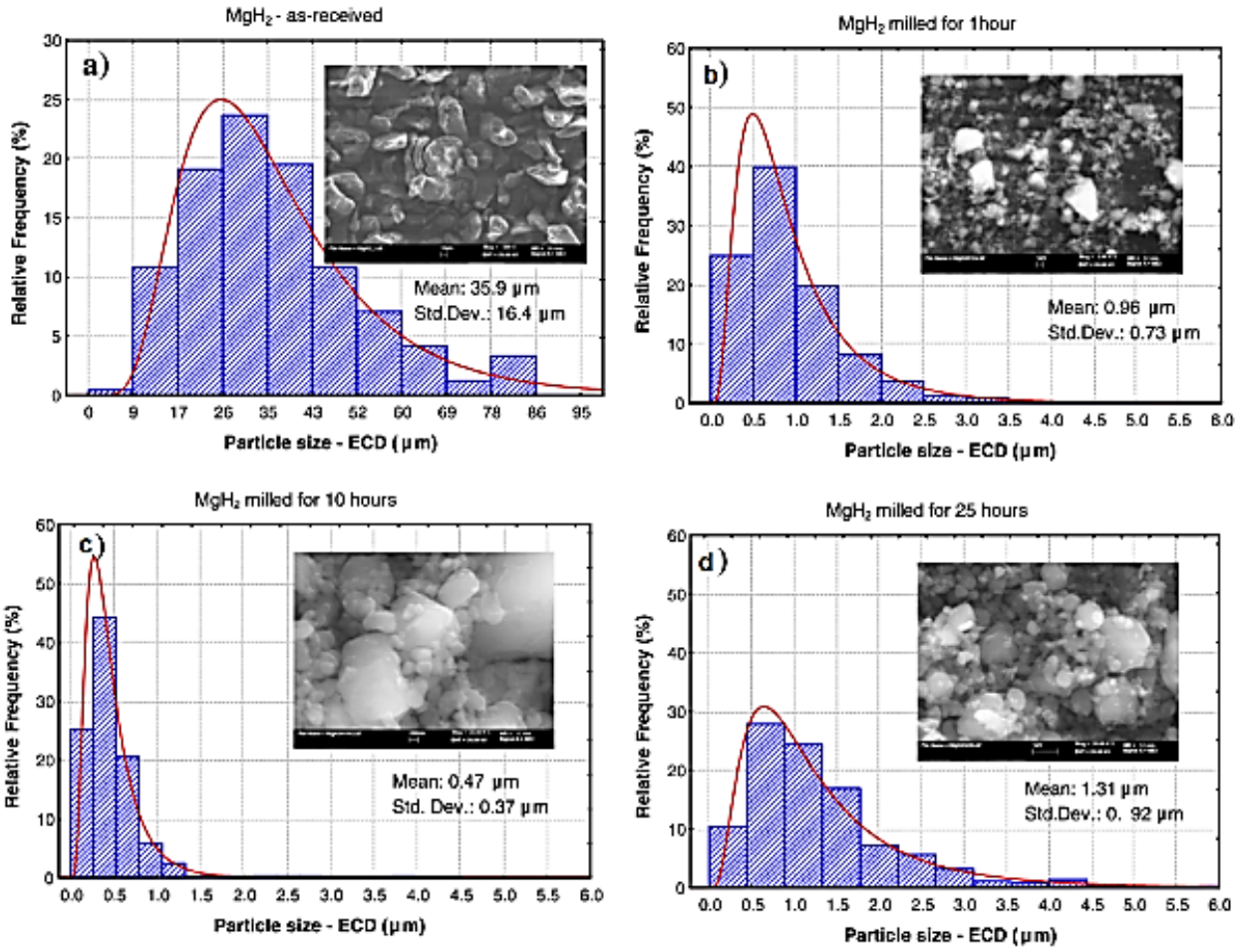

Figure 2. 10: An adapted image of particle size distributions and morphology of the as-received commercial MgH_2(a), 1 hour milling(b), 10 hours milling (c), and 25 hours milling of MgH_2.[82]

2.4.3. Alloying

Alloying Mg with one or two elements produces various stable phases, having the properties to improve the thermodynamics of Mg/MgH_2 in Mg-based alloys. Alloy elements alter the reaction pathway and decrease the dehydriding enthalpy(ΔH),

which favours the dehydrogenation of hydrogen in Mg. [84] Examples of alloying metal elements include Aluminium, Silicon, Zinc, Zirconium, and Copper. Figure 2.11 illustrates the enthalpy diagram explaining the effect of alloying MgH_2 with a reactive additive to destabilise the hydride bound. Firstly, the pure hydride represented by AH_2 undergoes dehydrogenation to form $A + H_2$ with a relatively high enthalpy, resulting in a lower equilibrium hydrogen pressure, with a high temperature at 1 bar [T (1 bar)]. However, altering the chemical environment of AH_2 by alloying the first compound A with a second compound B will allow the dehydrogenation to proceed from $AH_2 + {}_xB$ to $AB_x + H_2$. Therefore, this reaction decreases enthalpy, though an increased equilibrium hydrogen pressure is observed. [85]

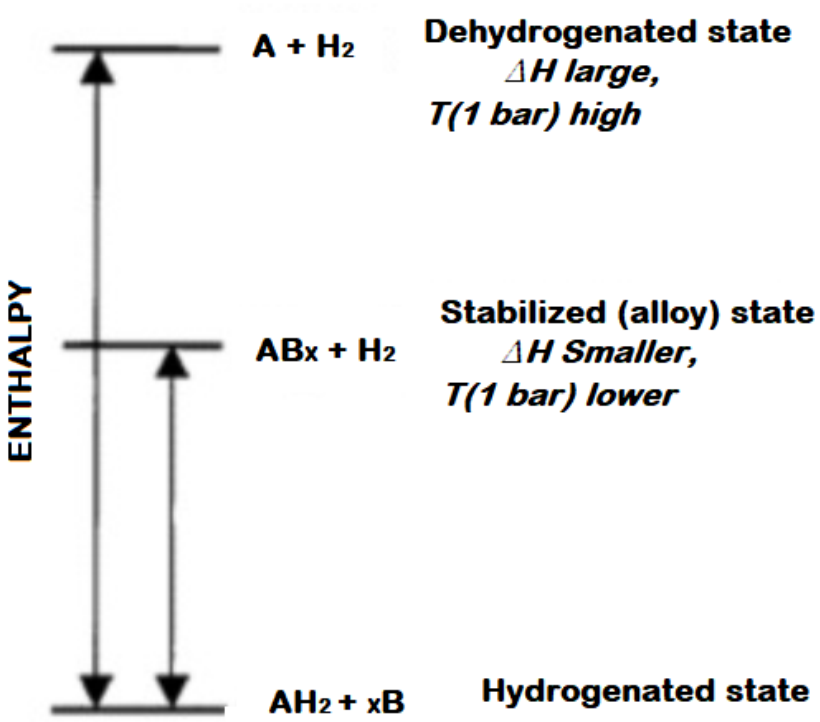

Figure 2. 11: Enthalpy diagram illustrating the alloy formation upon dehydrogenation. The addition of an alloying additive, B, reduces the enthalpy for dehydrogenation through the formation of Abx, adapted from [85]

2.5. Literature Background

2.5.1. Magnesium-based Materials with Zr/Ni-based nano-catalysts

Researchers [86–88] have widely investigated Ni nanoparticles as a catalyst in solid-state hydrogen storage to enhance the hydrogenation and dehydrogenation properties of Mg/MgH_2. Ni catalysts have a high affinity toward hydrogen, and they can break the H–H bond to facilitate the dissociation of hydrogen into the Mg matrix. Although, doping Ni alone with Mg/MgH_2 may result in particle agglomeration after several cycles – hydrogenation and dehydrogenation measurements. [89] Therefore, scientists have established that the catalyst activity of Ni is favoured as a multiphase-based catalyst. [86]

2.5.1.1. Doping Nickel with Zirconium

M. S. El-Eskandarany *et al*. [90–92] have reported a study of MgH_2/10wt.%$ZrNi_5$ by arc melting. The research group mechanically milled the composite for 50 hours. The hydrogenation was analysed at 275°C and released 5.3 wt.%H after 10 minutes. No significant degradation after 600 cycles 568 hours was registered. The hydrogen desorption capacity was recorded as 4.97 wt.%H. [90] The same group also have conducted a study on the catalyst effect of Zr_2Ni with MgH_2. The hydrogen desorption capacity was recorded as 6.2 wt.% H after approximately 12 minutes at 225 °C under 0.2 bar. [91]

To improve the sorption property of Mg/MgH_2, the research team have proposed a new heterogeneous catalytic agent, $ZrNi_5/Nb_2O_5$ [42] and $Zr_{70}Ni_{20}Pd_{10}$. [92] The authors have reported the absorption of 5wt.% H within 50 seconds, faster dehydrogenation of 6 wt.% H_2 within 3.8 min at 200 °C respectively. In a different study, M. S. El-Eskandarany *et al.* [93] have compared the sorption effect of the amorphous powder versus the big cubic of MgH_2/10wt.% Zr_2Ni. The metallic glassy Zr_2Ni powder's absorption rate was approximately 6 wt.% H at 250°C within 2.5 min. The big-cube nanocomposite resulted in a heterogeneous distribution of particles with slow absorption. [93] The catalytic effects of various $Zr_{(x)}Ni_{(y)}$ alloys used as additives to the Mg/MgH_2 system have also been reported by Z.Dehouche *et al*. [41] where the catalysts – $Zr_{47}Ni_{53}$ and Zr_9Ni_{11} were synthesised via an Arc melting technique. The composites MgH_2/10wt.%H $Zr_{47}Ni_{53}$ and Zr_9Ni_{11} catalysts resulted in a desorption rate of 5.37 wt.% H in 13 min, 5.88 wt.%H in 16 min at 250 °C respectively. The catalysts were activated

before being mechanically milled with MgH_2. The author stated that the activation process metamorphosed the alloys into fine powders and allowed them to form a more homogeneous catalyst particle distribution on the MgH_2 surface. In addition, the Mg cycling before the desorption and PCT analysis is beneficial, as it stabilises the desorption rates. [41]

Pighin, S.A. *et al*. [83] had reported a study on Zr_8Ni_{21} alloy, where the research group prepared the catalyst via Arc melting. The composite MgH_2/ 5wt.% Zr_8Ni_{21} was milled for 20 hours. The author had reported the importance of cycling the composite before carrying out the PCT analysis. In the cycling process, mechanical stress is produced by expansion and contraction, which allows for cracking and changes the surface extension and characteristics of the Mg particles. And this permits hydrogen to react with previously inaccessible material. Doping Mg/MgH_2 with Zr_8Ni_{21} enhanced the desorption rate by 5.9wt.% H in 4min at 300 ºC. [83] Molinas B. *et al*. [94] have reported a study on the Zr–Ni alloy as a catalyst with MgH_2. The authors have recorded a homogenous distribution of the alloy on the MgH_2 surface after 20 hours milling time. The MgH_2/10wt.% H ZrNi resulted in a dehydrogenation capacity of 5.3 and 5.6 wt.% at 304°C after 68 and 116 hours, respectively. At a plateau pressure at approximately 1 bar. [94]

C. Zhou *et al*. [95] have reported a study on the amorphous $Ti_{45}Cu_{41}Ni_9Zr_5$ alloy catalyst used as an additive for Mg/MgH_2. The authors have stated that the presence of the Ni and Zr ($Ti_{45}Cu_{41}Ni_9Zr_5$) slightly improved the hydrogen equilibrium pressure compared to the TiCu additive used alone – which absorbed approximately 3.3 wt.% H within 200 min at atmospheric ambient. [95] Jinjian Dong *et al*.[40] have published a study on the sorption property of the MgH_2/ 10wt.% $Zr_{0.67}Ni_{0.33}$. The authors have mechanically milled the powder for 50 hours. The research group reported the formation of ZrO_2 during the sample characterising. The powder oxidation was stated as a probability of slight leakage during the milling process via the SPEX high-pressure reactor and from exposure to powder to air during the analysis. However, the ZrO_2 phase was acknowledged as advantageous. It participated in the significant decrease in the particle size during the milling of the composite. The amorphous $Zr_{0.67}Ni_{0.33}$ catalyst particle sizes were recorded from 300 nm to 1 µm, and the composite average particle size was approximately 300 nm. The measured absorption capacity of the composite

MgH_2/ 10wt.% $Zr_{0.67}Ni_{0.33}$ was measured as 2.7 wt.% H at 275 °C in 20 minutes and 5.0 wt.% H at 325 °C in 4 minutes. [40]

2.5.1.2. Doping Nickel with Zirconium Oxide Catalyst

K.Tome *et al*.[39] have reported the advantages of doping Mg/MgH_2 with oxide catalysts. The authors have compared the sorption properties of composites MgH_2/5 wt.%Ni/5 wt.%ZrO_2, MgH_2/10 wt.%ZrO_2, and MgH_2/10 wt.%Ni. The composites were ball milled for 4 hours at a rotational speed of 240 rpm. The researchers have reported a homogenous dispersion of the ZrO_2 and Ni nanocatalysts into the MgH_2 matrix. Which was determined via the SEM analysis. As a result, a higher absorption capacity was achieved with the MgH_2/5 wt.%Ni/5 wt.%ZrO_2 – hydrogenation capacity of 6.10 wt.% at 310 °C. [39] The catalytic effects of ZrO_2 alloys used as additives to the Mg/MgH_2 system have also been reported by S. Hwang *et al*.[96] The research group reported the MgH_2/5 wt.% ZrO_2 absorbed approximately 2.96 wt.% H at ambient temperature in about 12 minutes.[96] B. Chen *et al*. [33] have also reported the advantage of milling MgH_2 with transition metal oxide. The authors have stated that ZrO_2 acts as a refining agent to decrease the MgH_2 activation energy and reduce the crystalline size during milling. As a result, the MgH_2/5wt.%ZrO_2 absorbed 2.96 wt.%H, at ambient temperature and 5.8 wt.%H at 150°C. [33]

2.5.1.3. Doping Nickel with Chloride Catalysts

Mao *et al*. [97] had revealed that doping MgH_2 with $NiCl_2$ catalyst released 5.17 wt.% H in 60 second at 300 °C and further decreased the activation energy for hydrogen desorption from 121.3 kJ/mol and 102.6 kJ/mol when compared to the two composites MgH_2/$CoCl_2$ and MgH_2/$NiCl_2$ consecutively. A different group Zhang *et al*. [98], have also reported the same study on MgH_2/$NiCl_2$ composite. The authors have stated that adding MgH_2 with a $NiCl_2$ catalyst decreases the particle size of MgH_2, which is advantageous to improve hydrogen sorption in metal hydride (MgH_2). However, doping MgH_2 with Nickel chloride for hydrogen storage property is not much explored in the literature compared to another group of catalysts such as metal Oxide. Galey *et al*. [30], [31] have reported a study where they compared doping Mg/MgH_2 with bis(tricyclo-hexyl phosphine)nickel (II) dichloride complex, $(NiCl_2(PCy_3)_2$. [30], [31] The

doping MgH_2 with 20NiCl and 20$NiCl_2$ released 5.2wt.% at 255°C, and 5.4 wt.% at 285°C of hydrogen respectively. The obtained results concluded that a larger percentage of Chlorine does not favour the hydrogenation and dehydrogenation properties of hydrogen in metal hydride.[31] Past studies demonstrate that the composition of dispersed Zr_xNi_y catalysts on the MgH_2 has the potential for the hydrogenation and dehydrogenation of Mg/MgH_2. The highly dispersed nickel on the surface of Mg/MgH_2 creates a homogeneous dispersion of the catalyst on the surface of the Mg/MgH_2, significantly enhancing hydrogen storage properties on the kinetics and thermodynamics of the Mg/MgH_2 system.

Additionally, past studies have demonstrated that doping nickel with two chlorine atoms increases the thermal stability of the complex. A poor percentage of nickel in the Mg/MgH_2 system results in lower decomposition kinetics of MgH_2. Therefore, keeping a good balance between the thermal stability of the complex provided, e.g., chlorine and the amount of nickel in the storage system, is crucial. From the information obtained from the literature, it is clear that there is still significant work on the evolution of the study of hydrogen storage with metal hydride. Therefore, the present study aims to develop a novel method to synthesise a catalyst that may enhance the sorption property of MgH_2.

Reader Guide

Chapter I: General Introduction

Chapter II: Literature

Chapter III: Methodology

Chapter IV: Establishing an Innovative Method for the Synthesis of ZrO_2/Ni Nanocatalyst for Improving the Sorption Property of MgH_2 in the Field of Solid-State Hydrogen Storage

20 hours milling time/ SPEX high energy ball mill MgH_2+10wt.%ZrO_2/Ni

Introduction Recap

Experimental

- Catalyst-ZrO_2/Ni synthesis
- Composite (MgH_2+10wt.%ZrO_2/Ni) ball mill: 5 hours via Planetary
- Characterisation

Results/ Discussion

- XRD
- SEM
- TPD
- Kinetics

Conclusion

References

Chapter V: Development of a Novel Method for the Fabrication of Nanostructured ZrO_2/Ni Catalyst to Enhance the Desorption Properties of MgH_2

5 hours milling time/ Planetary ball mill - MgH_2+10wt.%ZrO_2/Ni

Introduction Recap

Experimental

- Catalyst-ZrO_2/Ni synthesis
- Composite (MgH_2+10wt.%ZrO_2/Ni) ball mill: 20 hours via SPEX
- Characterisation

Results

- XRD
- SEM
- TPD

Discussion

Conclusion

References

Chapter VI: Comparing the Novel Catalysts ZrO_2/Ni and ZrO_2/$NiCl_2$ Storage Behaviour of Hydrogen Sorption Properties of MgH_2 Powder

5 hours milling time/ Planetary ball mill (ZrO_2/$NiCl_2$) catalyst

Introduction Recap

Experimental

- Catalyst-ZrO_2/Ni synthesis
- Composite (MgH_2+10wt.%ZrO_2/$NiCl_2$) ball mill: 5 hours via Planetary
- Characterisation

Results / Discussion

- XRD
- SEM
- Kinetics
- PCT

Conclusion

References

Chapter VII: General conclusion

References

Appendices

CHAPTER III: METHODOLOGY

This chapter covers the technical and theoretical tools used in the *present study* for the fabrication, characterisation and properties studies of Mg/MgH_2 for hydrogen storage, with and without the addition of catalysts. The instruments are detailed as follows:

- High-pressure reactor
- SPEX-high energy ball mill/ Planetary ball mills – for preparing the composite (Mg/MgH_2 commercial + Catalysts).
- XRD – X-ray diffraction D8 Advance Bruker: XRD 6000 with CuKα radiation, scan-lynxeye-5-100-35 minutes.
- SEM – The surface morphologies were studied using the scanning electron microscopic SEM SUPRA 35 VP EDAX to determine the material's microstructure.
- TEM **–** Transmission Electron Microscope studies were carried out on the sample using a model JE M-2100F microscope. The sample preparation consists of dissolving the powder in EtOH and drop cast onto holey carbon support film,3.05mm Diam. 300 Mesh copper grids.
- TPR – Temperature programmed desorption
- PCT – Pressure composition temperature

3.1. High-Pressure Reactor

The method for the catalyst fabrication in the *present study* is a novel approach only published in the past by the author of the *present study*. The catalyst was synthesised via the High-pressure Parr Series 5500 HPCL Compact Reactor with a 4836 temperature Controller. The high-pressure reactor enables it to carry a chemical reaction under elevated pressure (3000 psi _ 207 bar, 200 bar for CE/UKCA orders) and at a temperature (PTFE gasket for up to 350 °C) exceeding the boiling point of the reaction solvent. Furthermore, it is an ideal approach to run an experiment under an inert atmosphere and minimise the oxidation of the analysed solution whiles

producing nano-particles at the results. [99], [100] Figure 3.1. illustrate the schematic diagram of the high-pressure reactor.

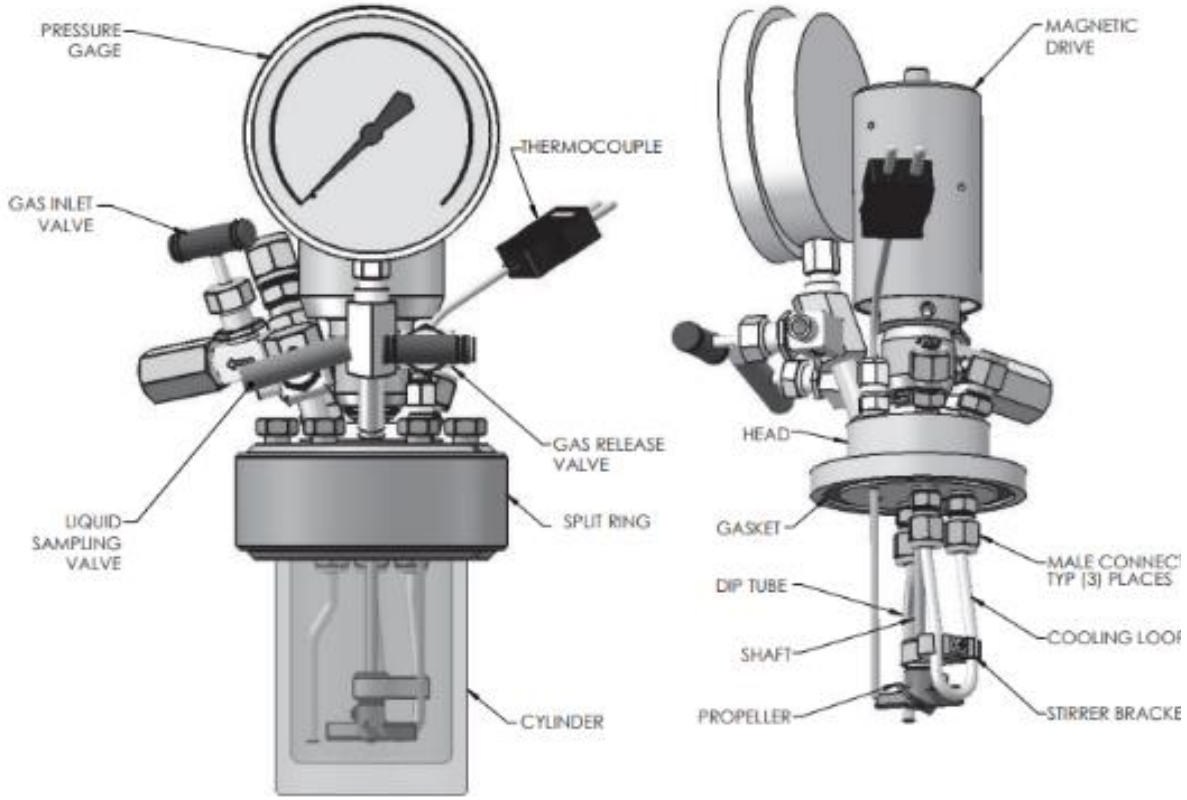

Figure 3. 1: Different part of the 5500 HPCL high-pressure reactor [99]

3.2. Operation Principle of the Ball Milling

Two different mill instruments were used in the present study. The powders were first milled via the high-energy ball mills SPEX Prep 8000. Due to numerous drawbacks, as listed below, this mill's instrument was later replaced by the Planetary ball mills-PM100.

3.2.1. SPEX High Energy Prep 8000-series Mixer/Mill

The powder grinding was via an 8001 Hardened Steel Vial Set. The SPEX Prep 8000-series Mixer/Mill, known as shaker mills or high-energy ball mills, presents high efficiency and can reduce samples to analytical fineness. This instrument is essential for blending powders, making emulsions, and performing mechanical alloying up to 0.2 - 10 grams of dry, brittle samples. [100] However, the SPEX high-energy ball mills come with numerous disadvantages. The steel vial is subject to contamination; it requires a long grinding time, over 20 hours, to result in a fine powder at a speed of 1725 RPM (115V) and 1425 RPM (230V).

Moreover, extra grinding time may be required to obtain fine particles, which may result in the powder's agglomeration. It is not an automated instrument, with no automatic stopping mode at the end of the analysis. Additionally, the vial is not inherently gas-tight and does not have a cooling system during the powder's milling to avoid overheating of the powder. [100]

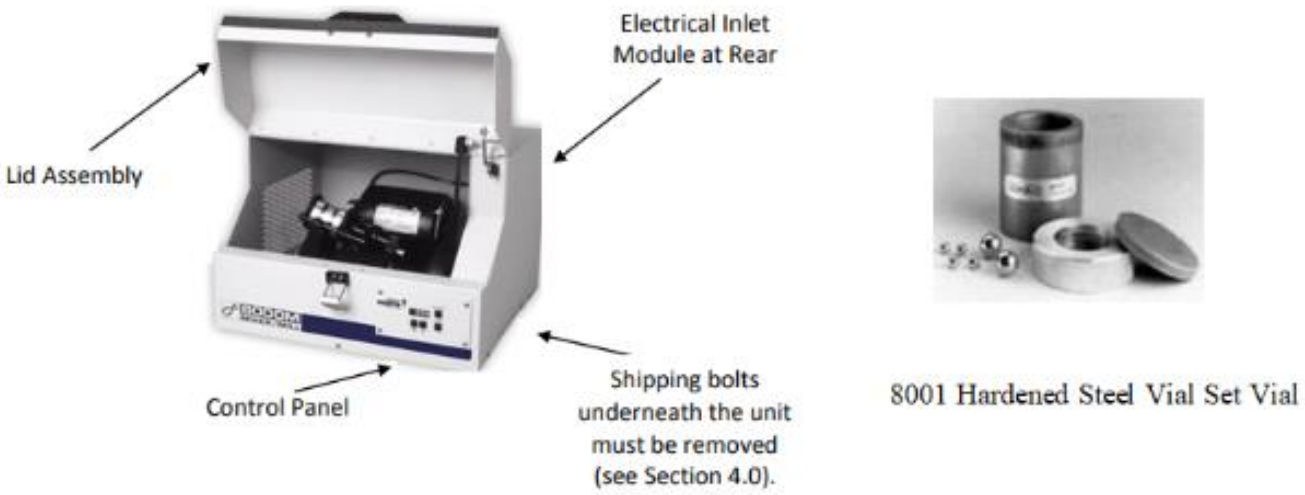

Figure 3. 2: Ball Milling: Spex CertiPrep 8000M mixer with 8001 Hardened Steel Vial Set

3.2.2. Planetary Ball Mill

The Planetary ball mill is one of the modern milling instruments that overcame the disadvantageous majority of the features listed above. The Planetary ball mills allow

a faster particle and crystallite size reduction at the nanoscale with homogeneous mixing distribution. The Planetary ball mills favour colloidal grinding and provide the energy input necessary for mechanical alloying. In addition, it has exceptionally high centrifugal forces, which result in very high pulverisation energy and, therefore, short grinding times. Planetary Ball Mills is the most used method in the literature as it speeds control and increased energy, allows reproducibility during experiments, and favours long-term. [101] Figure 3.2 (a) illustrates the planetary ball milling operation principle. There are two rotational movements taking place during the gridding of the powder. The planetary ball mill is automated and has a pause option to avoid overheating the powder and agglomerating. This instrument comes with the ZrO_2 gridding Jar, which favour the milling process of the powder prepared in the *present study*, as it limits the presence of impurities. [101]

Figure 3. 3: Planetary ball mills PM100 (a) Grinding jar and balls – made of (Zirconium oxide), (b) Aeration lids working under an inert atmosphere, (c) Slider to securely fixe the grinding jar with a clamping device.

3.2.3. Steps Taking Place During the Milling Process

The number of stages occurring during the milling of the powder, resulting in complex changes, are listed below.

Firstly, during the milling of MgH_2, there is a change in powder particle morphology taking place in the first few seconds, and the dissociation of the hydrogen molecules

occurs on the surface of the metal. The particles' fragmentation occurs within a few minutes. Some powder particles are heavily deformed, while the rest remain intact. The particle size distribution at this stage is quite broad. The average size reduction of MgH_2 nanocrystalline particles size ranges from an initial 9 nm to more than 100 nm. Secondly, the particle starts to alloys, where the aggregation of individual powder particles can be observed and increases their size. In the final stage, particles' intense fragmentation occurs, initially on the balls and the walls of the cylinder and then in the entire volume. The milled powder crystallite size remains constant after the optimal milling time. [102]

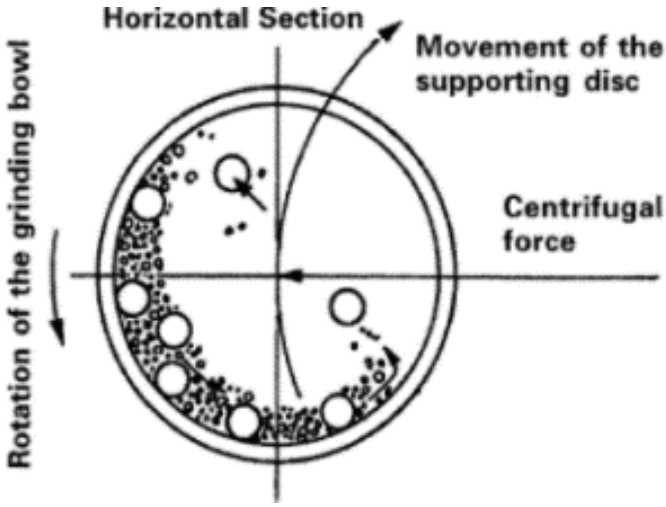

Figure 3. 4: Operational principle of the Planetary ball milling representing the schematic motion of the ball with the composites [102]

3.3. X-ray Diffraction

X-ray has high-energy light with a repeating period known as wavelength. The wavelength of an X-ray is similar to the distance between atoms in a crystal. Many tiny crystals are present in a material, each with a regular arrangement of atoms in space surrounded by a nucleus and cloud of electrons. During the exposition of the atomic planes (hkl) to an X-ray beam, the X-ray gets scattered by the regularly spaced atoms, and diffraction interference occurs, which Bragg's law may explain, refer to Figure 3. 5. [103] Von Laue had discovered the X-ray diffraction technique in 1912, and W.L.

Bragg had implemented it in 1915. Bragg's law defines the relationship between the diffraction angle and the spacing between the atoms, which can be explained by Equation 3.1.

$$n\lambda = 2d\ sin\theta \qquad Eq.3.1$$

Where n is the diffraction order, for first order n=1, λ is the wavelength of the X-ray – CuKα = 1.5406 Å, θ is the Bragg's angle in degrees, and d represents the distance between the atomic planes.

Referring to Figure 3. 5 (a), the diffraction interference allows measuring the distance between the atoms. There are two types of interference. When the waves align, the signal is amplified in contrastive interference, meaning that the second wave must travel a whole number of wavelengths. On the other end, destructive interference occurs when the waves are out of alignment; one-half of the wavelength travels on the incident side and one-half on the scattered side, yielding one additional wavelength. The angle between the incident and the scattered beam is called the 2-theta (2θ). The red triangle represents the angle at which diffraction occurs. [103], [104]

The Sherrer equation can measure the crystallite size of the X-ray diffraction peaks. Refer to Equation 3.2.

$$D = \frac{k.\lambda}{FWHM.cos\theta} \qquad Eq.3.2$$

Where *D* is the crystallite size (nm), *k* is the Scherrer's constant (0.94), *λ* is the wavelength of the X-ray source (0.15406 nm), *FWHM* is the full width at half maximum, and *θ* is the Bragg's angle in degree (peak position) half of 2θ.

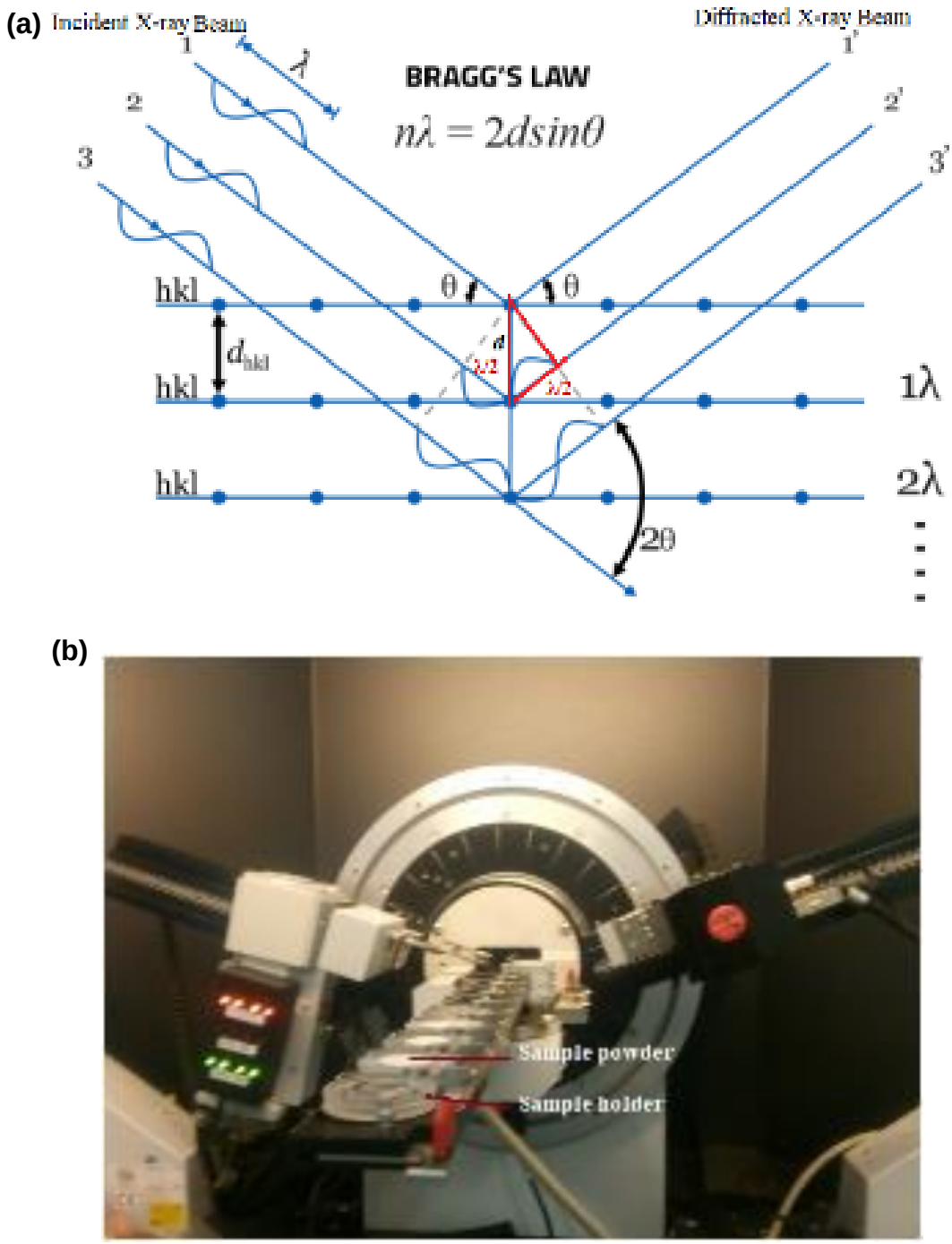

Figure 3. 5: Image adapted from [104] (a) Bragg's Law, b) x-ray-D8 Advance Bruker, illustrating the placement of the sample holder containing the sample.

3.4. Scanning Electron Microscopy (SEM)/ Transmission Electron Microscopic (TEM)

Scanning electron microscopy (SEM) allows studying the alloys' surface morphologies and chemical composition of the analysed powder. The SEM is incorporated with the Energy Dispersive X-ray spectroscopy (EDS) to study the sample elements analysis and identify the presence of impurities. In contrast, TEM analysis determines the surface morphologies of the composite on a nanometre scale.

3.4.1. General Principles of the SEM

In the *present study*, the analysis of the surface morphologies was via a "Field Emission Scanning Electron Microscope - (FESEM) (SUPRA 35VP, Zeiss, Germany)". The SEM process involves the focus of a high-energy electron beam ranging from 03 to 30 keV in a vacuum into a fine probe over the surface of the analysing sample. The resulting images are through different types of emitted electrons. The SEM system comes with four different detector systems. However, only two detectors are of interest in the *present study*. The Everhart-Thornley (ET) SE-detector for collecting SEs primarily, the in-lens SE-detector for short working distances, and the Back Scattered Electrons (BSEs) may contribute during the analysis via the SEs. The ImageJ software to determine the particle size of the analysed samples.

3.4.2. The Basic Principle of the Transition Electron Microscopic (TEM)

The structural features' analysis of the powders was via the Field emission high-resolution transmission electron microscopy (FE-HRTEM) model JEM-2100F. The Joel JEM2100F is a high-resolution TEM; it combines routine atomic resolution imaging of crystal lattices via coherent electron scattering or phase contrast (TEM) with incoherent electron scattering (or Z-contrast) in the scanning transmission electron microscopy (STEM) mode. This instrument is essential for ultrahigh resolution as it allows the analysis of particles in nano-scaled ranges. The Joel JEM2100F is a high-resolution TEM with attachments for XEDS analysis and a GIF TRIDIEM post-column energy filter to acquire energy-filtered images and diffraction. [105]

3.5. Temperature-Programmed Desorption – TPD

The dehydrogenation properties of the catalysts and composites in the *present study* were via temperature-programmed desorption (TPD). The TPD is a technique applied to study the desorption properties of hydrogen in a powder material. The main application involves heating the powder progressively under an inert gas while measuring the gas resulting from the desorption process as the temperature increases.

The samples analysed in the *present study* were at Lyon, Université Claude Bernard Lyon 1, CNRS, IRCELYON, F-69626 Villeurbanne, France, using the Thermo instrument TPDRO 1100 Series Thermo. This instrument can perform the reduction (RTP) and the oxidation (OTP) of temperature programs.

The calibration of the TPD/R/O-1100 apparatus was with the copper (II) Oxide (CuO). According to a well-known stoichiometry, the recommendation is to calibrate the instrument via a suitable pure sample that reacts with the probe gas. The calibration of the device is mainly dependent on the carrier flow rate. Furthermore, to have more accurate results, it is critical to calibrate the instrument at the same temperature rate at which the sample powder is to be analysed. [106]

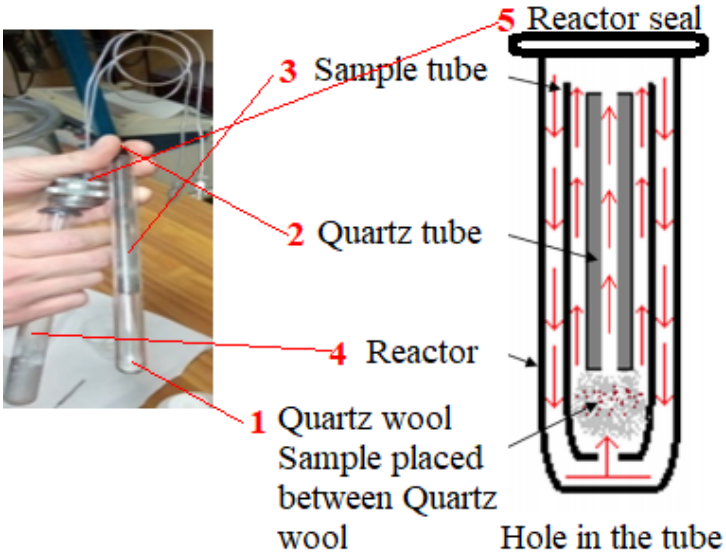

Figure 3. 6: TPD/R/O 1100 Series Thermo reactor parts

Figure 3.6. illustrate the TPD profiles. Firstly, the sample to be analysed is placed between two quartz wool to prevent the sample from failing inside the hole of the sample tube, which allows the gas circulation. Then the sample is inserted inside the sample tube. Secondly, a quartz tube is inserted inside the sample tube to maintain the wool at the bottom of the tube. The tube is inserted inside the reactor tube and sealed. The thermal conductivity works by having two parallel tubes containing gas and heating coils. When an analyte elutes from the column, the thermal conductivity of the eluent reduces, and a detectable signal of the analysed sample produces.

3.6. Manometric Gas Sorption Analyser

The fundamental properties of hydrogen storage materials characterisation were achieved by determining PCT (Pressure-Composition Temperature) relations, kinetic rates of absorption, and van ’t Hoff plots for the calculation of sorption enthalpies with the help of the Hiden Isochema IMI Series Manometric Gas Sorption Analyser. Refer to Chapter 2, section 1.2.2. for more detail on the van ’t Hoff plots. This instrument helps to investigate novel hydrogen storage materials using Sieverts’ Method. It can analyse samples up to pressures of 200 bar and at a temperate ranging from ambient up to approximately 500°C. [107]

Refer to Figure 3. 7 for the schematic to determine the amount of gas absorbed or desorbed by a sample via the manometric gas sorption measurements. The sorption measurement is fully automated and controls overall experimental parameters. [107]

The thermodynamics of the sample is determined by recording at least two isotherms for the same species at different temperatures. The temperature of the set of isotherms must be closely spaced to minimise the calculation error of the analysis. The isosteric state thermodynamic equation determines the differential enthalpy of adsorption, as shown in Eq.3.3.

$$\Delta H^{\theta} = R\,[\frac{\delta ln\hat{a}}{\partial\left(\frac{1}{T}\right)}]_n \qquad Eq.3.3$$

- *ΔH* is the isosteric enthalpy of adsorption
- *R* is the gas constant
- *T* is the temperature in K
- *n* is the number of moles of substance adsorbed by unit mass of adsorbate
- $\hat{a}$ is the ratio of absolute gas pressure and thermodynamic reference pressure – $P^{\theta} = 10^5$ *Pa or 101325 Pa*, for an ideal gas. Refer to Equation 3.4.

$$\hat{a} = \frac{P}{P^{\theta}} \qquad Eq. 3.4.$$

The relationship of the two pressure is analogous to the Clausius -Clapeyron equation, and a plot of $ln\hat{a}$ versus reciprocal temperature from which the differential enthalpy is found is therefore known as the Clausius-Clapeyron plot.

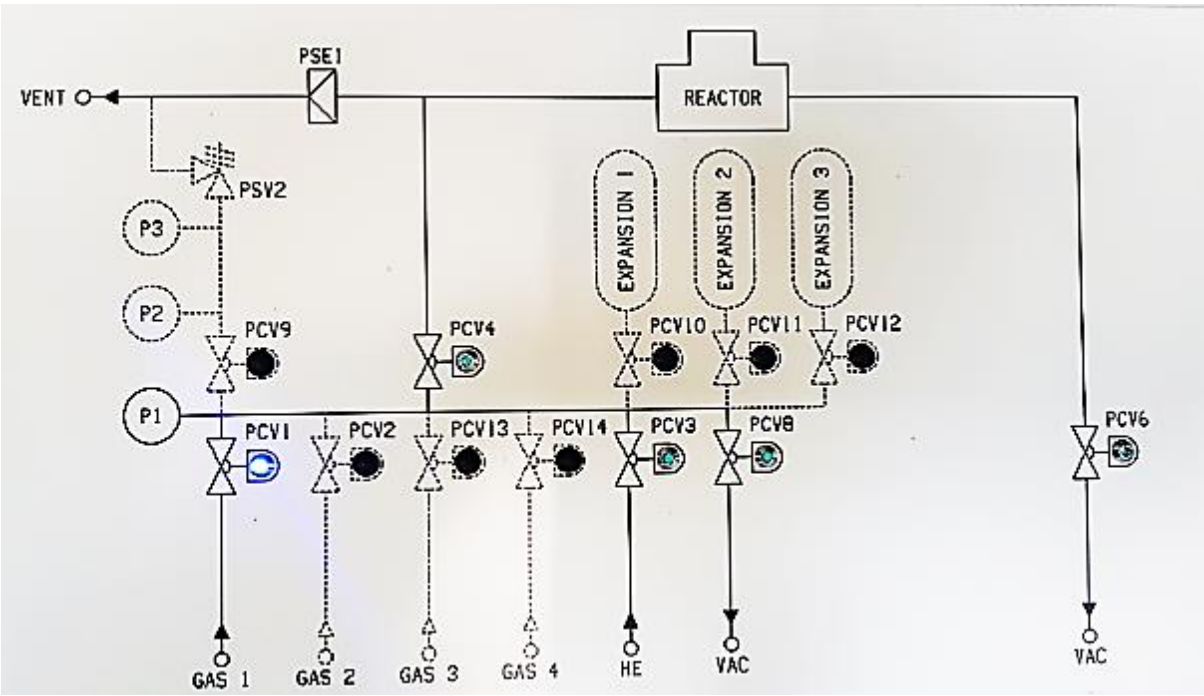

Figure 3. 7: Manometric analyser, showing the pressure dosing mode.

Before the experiment, the system is put under a vacuum to eliminate air in the dosing volume and reactor volume passages. PCV4, PCV6 and PCV8 open when the system is under vacuum. PCV4 is the connecting valve to the reactor, and PCV 6 and PCV8 are the vacuum valves to remove contaminated air and excesses purged gas in the reactor and out of the system, respectively. As the system finished vacuuming, all the opened valves closed. To start the sorption process, PCV 1 opens to purge a set volume of gas known as the initial dosing pressure (p1) into the system – dosing volume (V1). The connecting valve PCV4 reopens and purges the gas–final pressure (P2) into the reactor–reactor volume (V2). The addition of pressure induces step-by-step capacity changes. At each step, while the sample cell is closed, the added pressure increases absorption/desorption PCT by approximately 0.05–0.5 bar. The wait time was set for 15 minutes to stabilise the pressure. Afterwards, the alloy starts to absorb hydrogen at the set pressure till the pressure slowly reaches the point of the plateau. The amount of hydrogen stored in the hydride is automatically recorded. The PCT experimental procedure is further detailed by Debouche *et al*.[69]

Reader Guide

Chapter I: General Introduction

Chapter II: Literature

Chapter III: Methodology

Chapter IV: Establishing an Innovative Method for the Synthesis of ZrO_2/Ni Nanocatalyst for Improving the Sorption Property of MgH_2 in the Field of Solid-State Hydrogen Storage

20 hours milling time/ SPEX high energy ball mill MgH_2+10wt.%ZrO_2/Ni

Introduction Recap

Experimental

- Catalyst-ZrO_2/Ni synthesis
- Composite (MgH_2+10wt.%ZrO_2/Ni) ball mill: 5 hours via Planetary
- Characterisation

Results/ Discussion

- XRD
- SEM
- TPD
- Kinetics

Conclusion

References

Chapter V: Development of a Novel Method for the Fabrication of Nanostructured ZrO_2/Ni Catalyst to Enhance the Desorption Properties of MgH_2

5 hours milling time/ Planetary ball mill - MgH_2+10wt.%ZrO_2/Ni

Introduction Recap

Experimental

- Catalyst-ZrO_2/Ni synthesis
- Composite (MgH_2+10wt.%ZrO_2/Ni) ball mill: 20 hours via SPEX
- Characterisation

Results

- XRD
- SEM
- TPD

Discussion

Conclusion

References

Chapter VI: Comparing the Novel Catalysts ZrO_2/Ni and ZrO_2/$NiCl_2$ Storage Behaviour of Hydrogen Sorption Properties of MgH_2 Powder

5 hours milling time/ Planetary ball mill (ZrO_2/$NiCl_2$) catalyst

Introduction Recap

Experimental

- Catalyst-ZrO_2/Ni synthesis
- Composite (MgH_2+10wt.%ZrO_2/$NiCl_2$) ball mill: 5 hours via Planetary
- Characterisation

Results / Discussion

- XRD
- SEM
- Kinetics
- PCT

Conclusion

References

Chapter VII: General conclusion

References

Appendices

CHAPTER IV: ESTABLISHING AN INNOVATIVE METHOD FOR THE SYNTHESIS OF ZrO_2/Ni NANOCATALYST FOR IMPROVING THE SORPTION PROPERTY OF MgH_2 IN THE FIELD OF SOLID-STATE HYDROGEN STORAGE

***Method 1**: MgH_2/10wt.% ZrO_2/Ni - 20 hours milling time via the SPEX high energy mills*

This Chapter aims to establish a better approach for synthesising nanocatalysts that will significantly impact the hydrogen sorption properties of Mg/MgH2. There are five sections in this Chapter. First, the introduction explains the importance of doping Mg/MgH2 with a nanocatalyst. Second, the importance of ball milling and producing nano-size particles to enhance the kinetics and thermodynamics of hydrogen in Mg/MgH2 is highlighted. Last but not least, the method of synthesis and characterisation, the outcome and the summary of the *present study*.

N.B. Please note that throughout the text, the unmilled Magnesium Hydride (Mg/MgH_2) is also referred to as the "commercial MgH_2". Mg/MgH_2 is the medium where hydrogen is absorbed and desorbed.

4.1. Introduction

As mentioned in the literature in chapter II, Mg/MgH_2 is a potential hydride storage medium for hydrogen, mainly for automobile applications. MgH_2 is a low-cost material with high gravimetric and volumetric capacity, 7.6wt.% and 110g/l, respectively. [36] However, its practical application is still under development. MgH_2 has poor thermodynamic behaviour – high enthalpy value of (-74 kJ/mol) and entropy (-135 J/mol/K H_2).

Therefore its decomposition temperature is above 287°C, which results in poor hydrogenation and dehydrogenation kinetics. [108] Catalyst doping, nanosizing the

powder, and alloying are among the main approaches proposed in the literature to overcome the drawback of Mg/MgH_2. The nanosizing of the powder can be achieved via ball milling, where the particle size reduction creates a larger surface and more homogeneous catalyst distribution on the Mg surface. Doping the Mg/MgH_2 with the nano-catalyst reduces its activation energy (EaF) gap. Therefore this increases the hydrogenation and dehydrogenation rates. [109]

Pure metals, metal alloys, and metal oxide groups of catalysts have shown potential in past studies to improve the kinetics and thermodynamic properties of Mg/MgH_2. [39], [41], [42], [110] A small number of researchers in the literature [39] have published on the impact of ZrO_2/Ni catalysts on Mg/MgH_2. Most researchers focused their interest on the interaction of ZrO_2 with Mg/MgH_2 and the effect of doping the Zr/Ni-based catalyst with MgH_2. In the *present study* – Chapter IV, ZO_2/Ni catalysts are prepared via a novel sol-gel method and the composite MgH_2/10wt.% ZrO_2/Ni was ball milled for 20 hours via the SPEX high energy mills.

4.2. Material and Methods

In this section, the list of reactions used in *the present study* is detailed in Table 4. 1, based on their percentage purities and manufacturing. This section also provides more information on the properties of MgH_2.

4.2.1. List of all reagents used in the *present study*

The table below details the reagents used in *the present study* as highlighted in chapters 4, 5 and charter 6.

Table 4. 1: List of all reagents used in the *present study*

Reagent Name	Percentage Purities	Manufacturer
Nickel(II)Nitrate Hexahydrate	98%	Alfa Aesar
Zirconium (IV)Chloride	99.5+% trace metal basis	Alfa Aesar
Methanol	99%	Alfa Aesar
MgH2	99.99% trace metal basis	McPhy – La Motte-Fanjas

4.2.2. Mg/MgH_2 Characterisation

The commercial MgH_2 powder was used in the *present study* as the matrix where the hydrogen can be absorbed and desorbed. The Mg/MgH_2 used in the *present study* is the hydride magnesium purchased from McPhy – La Motte-Fanjas, France industry, provided by the University of Lyon, France. The obtained powder contained 94 wt.% Mg metal, with approximately 5wt.% MgO and $Mg(OH)_2$. Refer to Figure 4. 1 for the EDX image of the commercial MgH_2 obtained via SEM analysis.

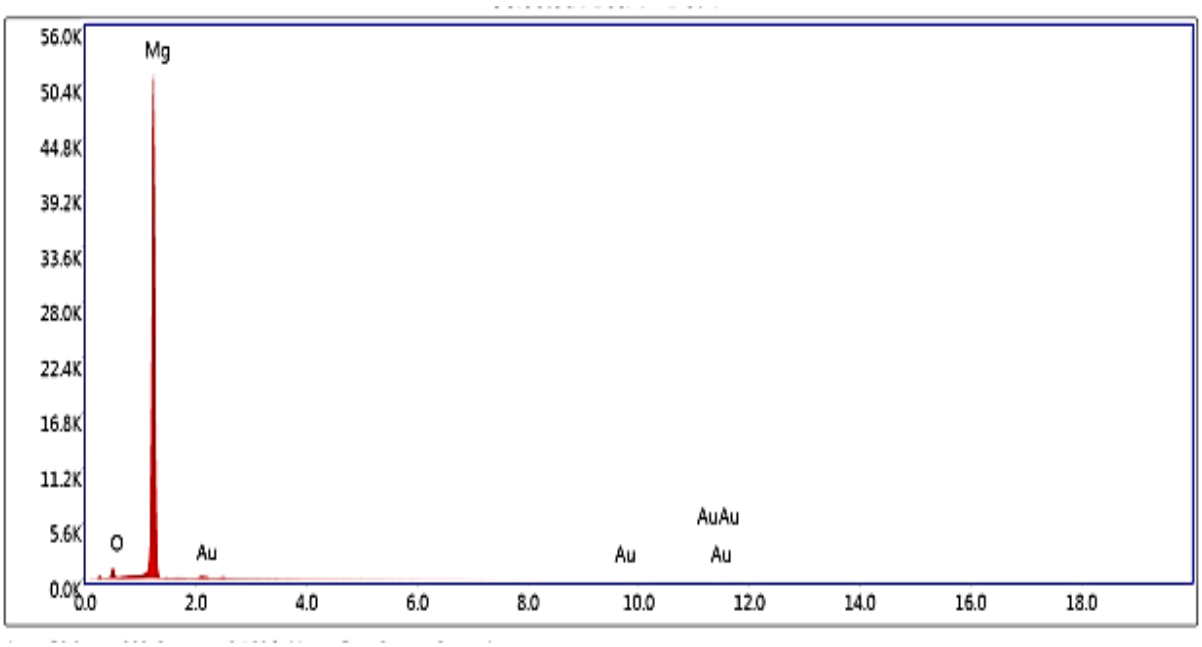

Figure 4. 1: The energy dispersive X-ray spectroscopy (EDX) of commercial MgH_2

The commercial MgH_2 was analysed according to the XRD and SEM analysis. Refer to section 4.2.3 of the present chapter IV below for further details on the analysis. The commercial MgH_2 has a hydrogen capacity of 7wt.%H, with a crystallite size of approximately 40nm and an average particle size ranging from 5-10µm, refer to Figure 4. 2 and Figure 4. 3.

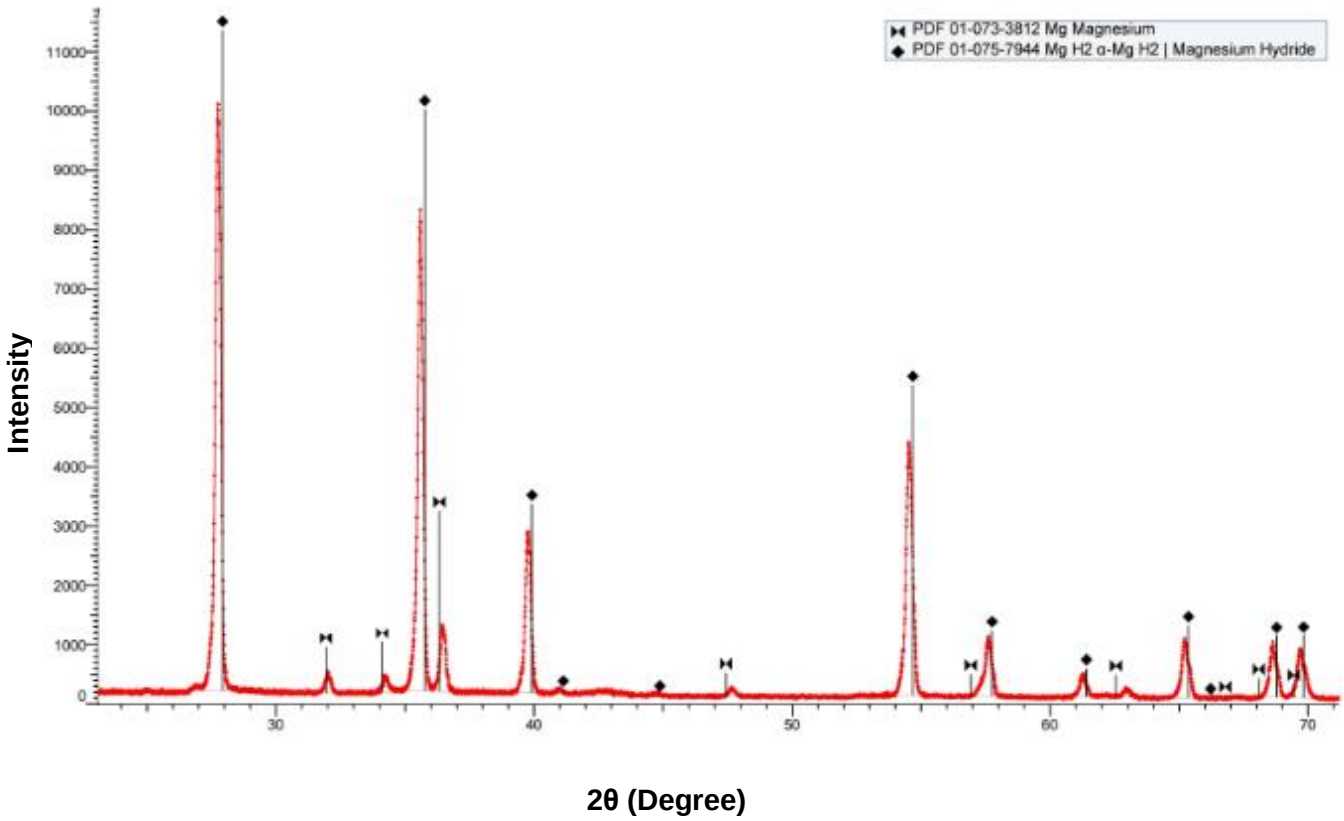

Figure 4. 2: The XRD patterns of the commercial MgH_2

Refer to Figure 4.4 for the TPD analysis of the commercial MgH_2 to determine its dehydrogenation properties. The commercial MgH_2 has a decomposition temperature of 419ºC with an activation energy of 239 kJ/mol H_2 and an enthalpy value of - 74 kJ/mol H_2.

(a)

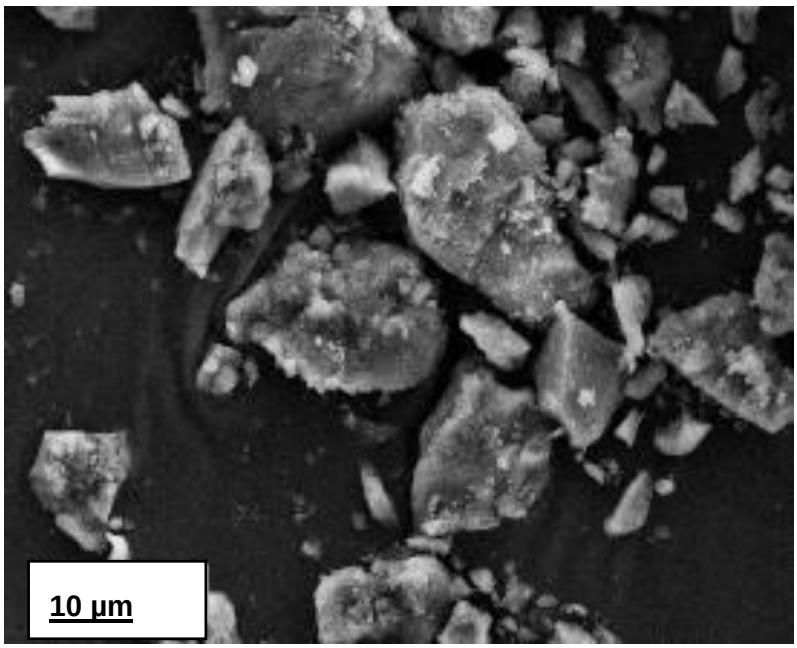

(b)

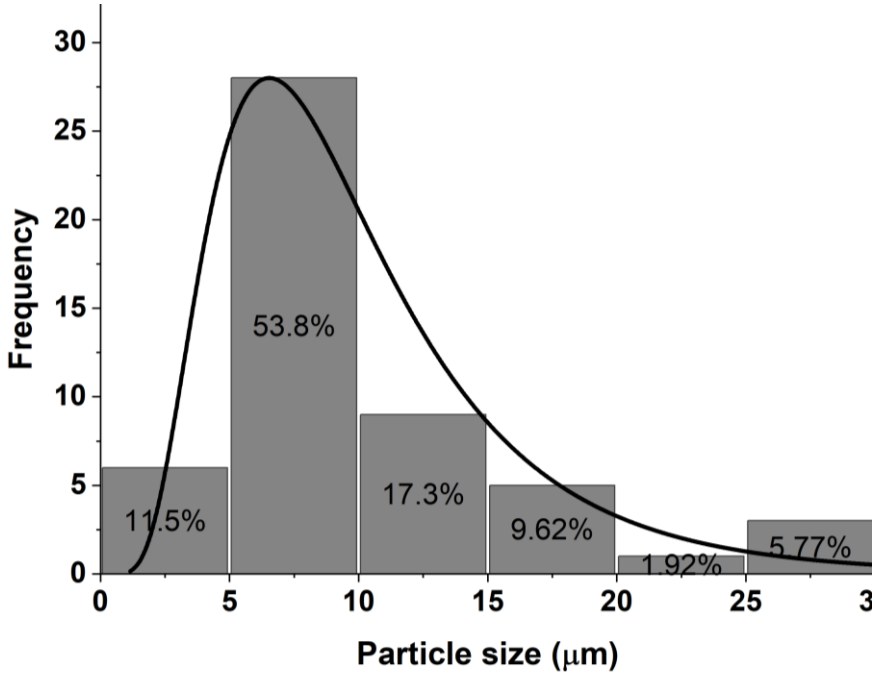

Figure 4. 3: (a) SEM image of the commercial MgH_2, (b) size distribution of the MgH_2 measure with image J software.

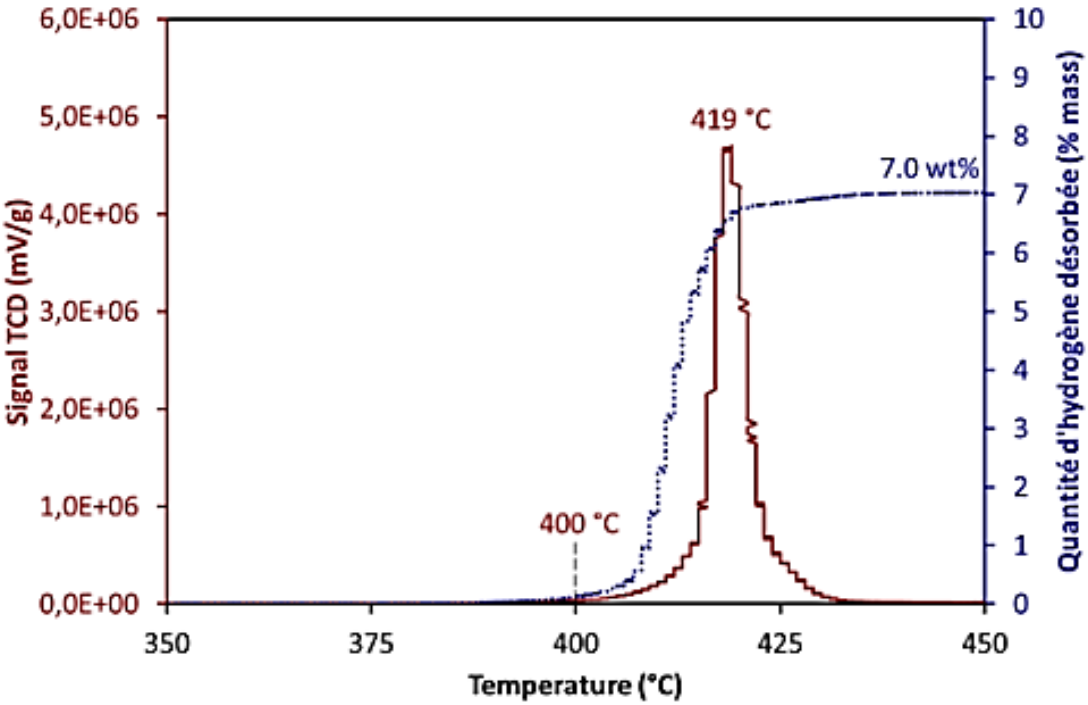

Figure 4. 4: TPD analysis of the MgH_2 commercial [106]

4.2.3. Catalyst ZrO_2/Ni Synthesis: High Pressure Reactor and Heat Treatment

The synthesis of the catalyst involves two steps.

The catalyst was prepared in the high-pressure PARR 5500 Series Compact Reactor from a mixture of $ZrCl_4$ fine white powder (starting material) with a 99.5+ metal basis and $Ni(NO_3)_2.6H_2O$ (98% green salt) provided by Alpha-Aesar and Sigma-Aldridge, respectively. Refer to Figure 4. 5 (a) step 1.

The precursor $ZrCl_4$ 0.99 wt/v.% and $Ni(NO_3)_2{\cdot}6H_2O$ 1.52 wt/v.% were dissolved at room temperature in 150 mL of methanol solvent and then were transferred into the reactor vessel (Type 316/austenitic chromium-nickel stainless steel containing molybdenum). The reactor was assembled and tightened vigorously to avoid the pressure drop of the hydrogen. The reactor vessel was purged with hydrogen for several minutes to flush out the air inside the reactor and refill it with hydrogen. The mixture was heated for 2 hours at 200 °C under hydrogen, at a starting pressure of 20 bar, whilst stirring at 60 revolutions per minute.

Refer to Figure 4. 5(b) step 2. The sample was cooled overnight; the supernatant was discarded, whilst the formed gel was dried overnight at room temperature. The sample was transferred into a u-shape tube, then into a heating furnace, where it was thoroughly dried when heat-treated at 350 °C for 5 hours and further cooled for 2 hours under the hydrogen flow at 0.6 bar.

4.2.3.1. Step 1: Catalyst synthesis (sol-gel formation)

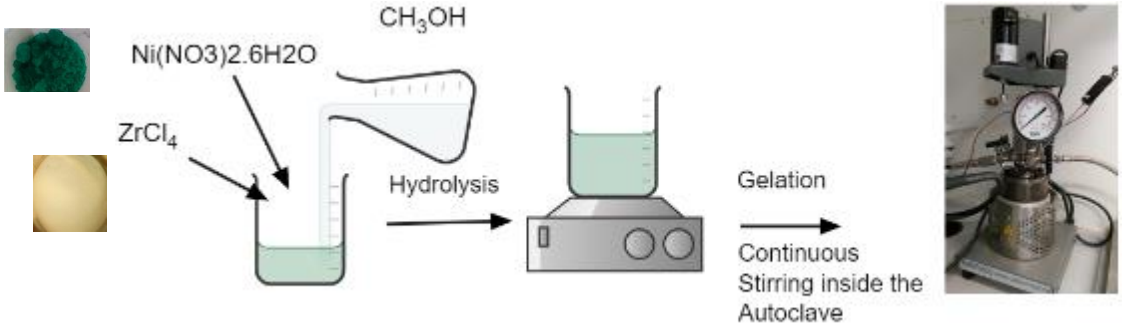

Figure 4. 5: Catalyst sol-gel formation in the high-pressure reactor PARR 5500 Series Compact Reactor, at 200 °C for 2 hours under hydrogen, at a starting pressure of 20 bar, 60 revolutions per minute

4.2.3.2. Step 2: Catalyst synthesis (powder calcination)

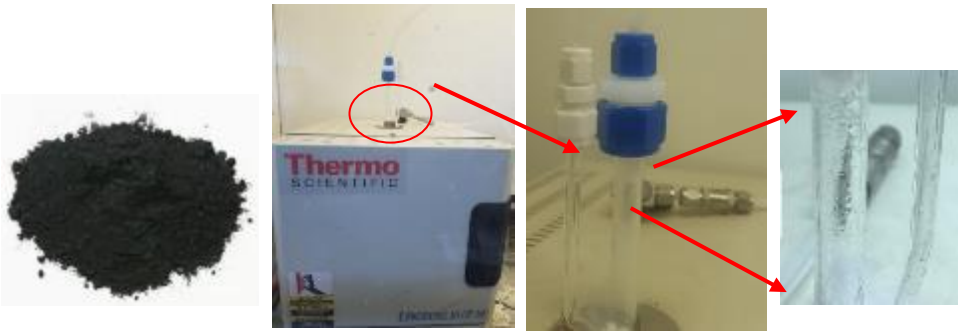

Figure 4. 6: Catalyst heat treatment (calcination) process, at 350 °C for 5 hours and further cooled for 2 h under the flow of hydrogen at 0.6 bar

4.2.4. Preparation of MgH_2-based Nanocomposite Powders: Ball Milling

The MgH_2/ ZrO_2/Ni composite was prepared under an inert Ar atmosphere via the Ball Milling: Spex Certi-Prep 8000M mixer. Two types of composites were prepared.

First, 10 wt.% of ZrO_2/Ni-based nano-catalyst was added to MgH_2 in a reactor vessel with Hardened Steel Vial Sets milling balls of 11mm diameter. The ball-to-powder mass ratio was 27:1. The reactor was sealed inside the glove box to prevent powder oxidation. The sample was milled for 20 hours at 1725 revolutions per minute. Subsequently, 10 wt.% of ZrO_2/Ni-based nano-catalyst was hydrogenated before being added to MgH_2. The mixture was milled under the same condition as mentioned above.

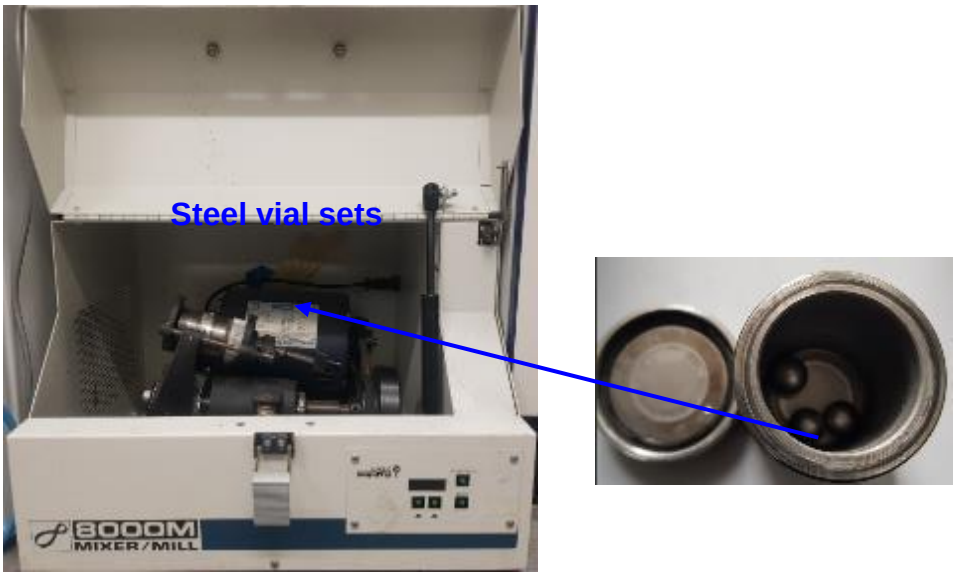

Figure 4. 7: Ball Milling: Spex Certi-Prep 8000M mixer set, reactor vessel with Hardened Steel Vial Sets milling balls of 11mm diameter

4.2.5. Sample Characterisations: XRD, SEM, TEM, and TPD

The properties of the synthesised catalyst and the formed composites were studied through XRD. The crystal structures of all samples were investigated by the XRD Bruker D8 Advance X-Ray Powder Diffractometer (XRD) with the CuKα (λ = 0.154 nm) radiation over the 2θ ranging from 20° to 80°. The instrument was calibrated with the

LaB6 NIST standard (660a). The specific surface area of the synthesised catalyst was measured with nitrogen gas (NOVAtouch LX1, USA) at a temperature of 77 Kelvin.

The surface morphologies were obtained with a field emission scanning electron microscope (FESEM) (SUPRA 35VP, Zeiss, Germany). Energy dispersive X-ray spectroscopy (EDS) was used for elemental analysis of the deposited layers. For the SEM analysis, the powder placed on a carbon tape was coated with a thin layer of gold and added through vacuum evaporation to prevent the sample from developing high conductivity and some charging effects during the analysis.

The TEM model JE M-2100F microscope was used for the structural features. The powder was suspended in EtOH and drop-cast onto holey carbon support film, Cu 200 mesh. The surface morphologies of the analysed powders were determined via the field emission scanning electron microscope (FESEM) (SUPRA 35VP, Zeiss, Germany). The images were collected using Gatan software.

4.2.6. The Hydrogenation and Dehydrogenation Behaviour and kinetic study

All the samples were handled in a glove box under a protective Ar atmosphere to prevent oxidation.

Temperature-programmed desorption (TPD) analyses were performed with a TPD/R/O-1100 apparatus from Thermo. The experiments were performed from ambient temperature to 500 °C at 2 °C min^{-1} under an Ar flow of 20 mL min^{-1}. The instrument was calibrated before the analyses by reducing different masses of copper (II) oxide to determine the samples' precise amount of hydrogen desorbed. The dehydrogenation properties of the composite were studied after the ZrO_2/Ni catalyst activation under 10 bar of hydrogen at 30 °C for 100 minutes.

The hydrogenation and dehydrogenation kinetics of hydrogen were measured with a Setaram volumetric apparatus model PCT Pro (version E & E). The samples were analysed at two different temperatures – 250 and 300 °C. Before starting the hydrogen absorption/desorption kinetics measurement, the powder was degassed and then heated at the selected temperatures and pressure of 250 °C/0.1 bar of H_2 and 300 °C under 10 bar of H_2, respectively.

4.3. Results and Discussion

The sample was analysed through XRD to quantify the crystalline phase compositions of the MgH_2 powder. The resulting peaks are related to the atomic structure of the analysed sample. The powder was placed in the sample holder and evenly distributed to avoid a high background and damage to the instrument. There are three phases detected, ZrO_2, $Ni_{0.99}Zr_{0.01}$ and Ni. It is visible from Figure 4.8 that the Ni phase was predominant after the 5 hours heat treatment at 350 °C. The sharp Bragg peaks indicate the precursor Ni powder and the phase of $Ni_{0.99}Zr_{0.01}$ at around 2θ of 44.5°, 51.8° and 76.2° (PDF file # 01-070-1849) and (PDF file # 01-072-2682) respectively. Additional broad peaks were identified at around 2θ of 30°, 50.2° and 60.5°, corresponding to the development of Zr_2O (PDF file #00-003-0640).

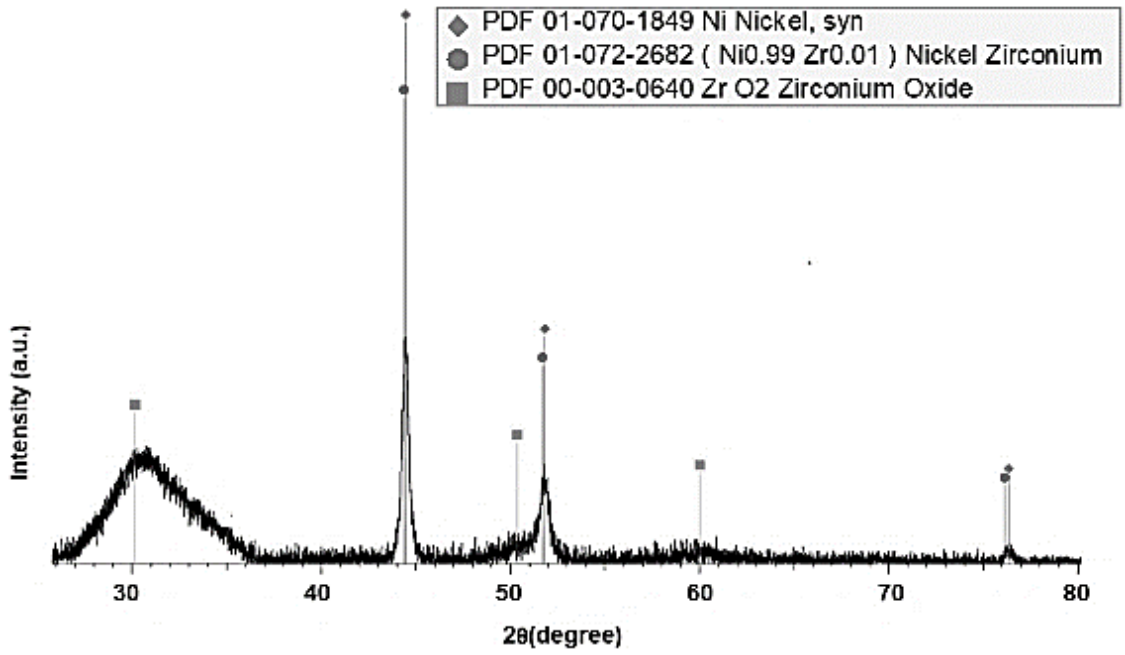

Figure 4. 8: Shows the X-ray diffraction pattern of catalyst ZrO_2/Ni after 5 hours heat treatment at 350ºC

4.3.1. Characterisation of the Nanocomposites

The dehydrogenation properties of the nanocomposites were determined by the means of temperature-programmed desorption (TPD). The hydrogenation properties

of composites were achieved by determining PCT (Pressure-Composition Temperature) and kinetic absorption rates with the help of a Manometric Gas Sorption Analyser.

4.3.1.1. Dehydrogenation study of composites -TPD analysis

Figure 4. 9. represents the temperature profiles of the MgH_2 decomposition, whilst Figure 4. 10. indicates the hydrogen capacity.

The first composite – MgH_2 + 10wt.% activated catalyst ZrO_2/Ni released 3wt.% of hydrogen in a wide range of desorption temperatures between 250 °C and 330 °C, the second composite MgH_2 + 10wt.% ZrO_2/Ni released a lower percentage of desorption temperature 1.8 wt.% of hydrogen in at 300 °C, and the last composite MgH_2 + 10wt.% ZrO_2/Ni (composite activated) released 3.8 wt.% in a range of 270 °C and 350 °C. It is worth noticing that the activation process plays a significant role in the sorption property of MgH_2. The importance of catalyst activation prior to doping with Mg/MgH_2 was also reported by Dehouche *et al*. [41] To metamorphose the alloys into a fine powder, which is beneficial to achieve a more homogenous distribution of the catalyst in the MgH_2 during the milling process. [41]

To evaluate the effect of temperature on the discharge characteristics of the sorption materials, the kinetics desorption rates of the MgH_2 of the three composites MgH_2 + 10wt.% activated catalyst ZrO_2/Ni, MgH_2 + 10wt.% ZrO_2/Ni, and MgH_2 + 10wt.% ZrO_2/Ni (composite activated) were calculated from the TPD curves of Figure 4.9 at a peak temperature of 326 °C, 336 °C and 327 °C, respectively.

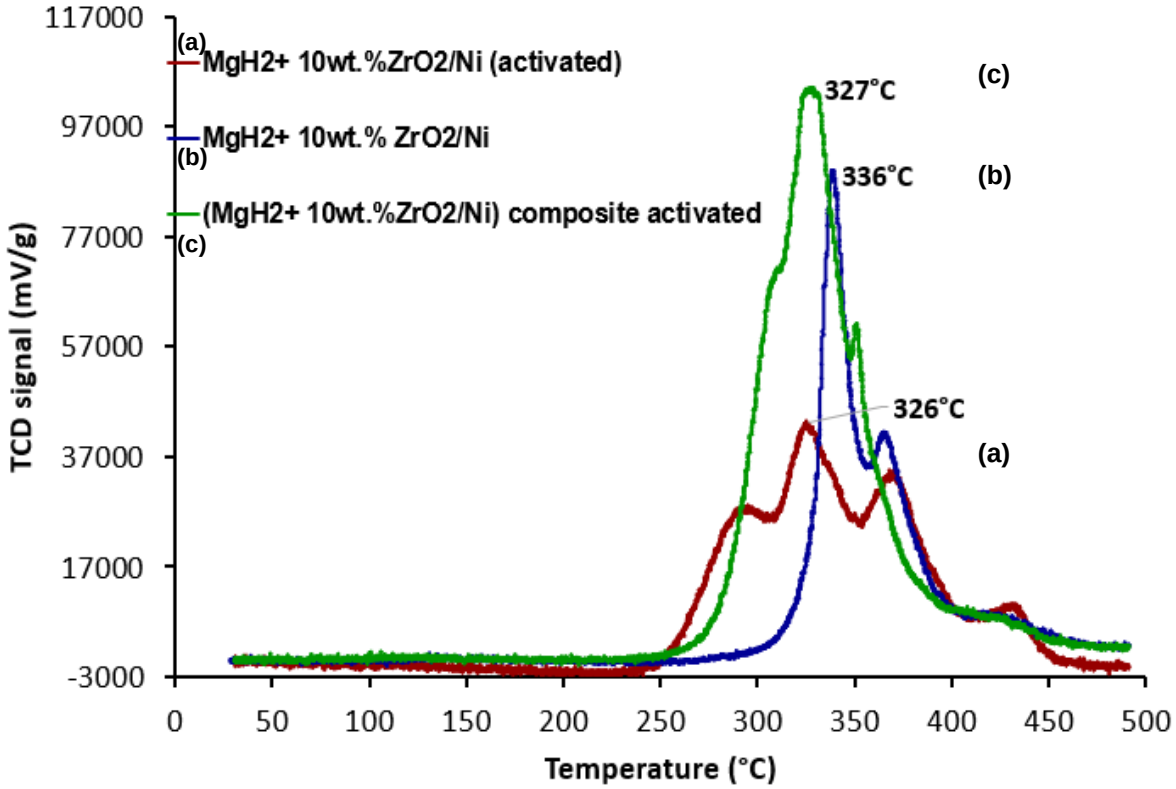

Figure 4. 9: The evolution of the temperature-programmed desorption (TPD) profile of MgH_2 + 10wt.% ZrO_2/Ni, MgH_2 + 10wt.% activated catalyst ZrO_2/Ni, and MgH_2 + 10wt.% ZrO_2/Ni (composite activated).

Experimental conditions: from ambient temperature to 500 °C under an Ar flow of 20 mL min^{-1} and at a heating rate of 2 °C min^{-1}.

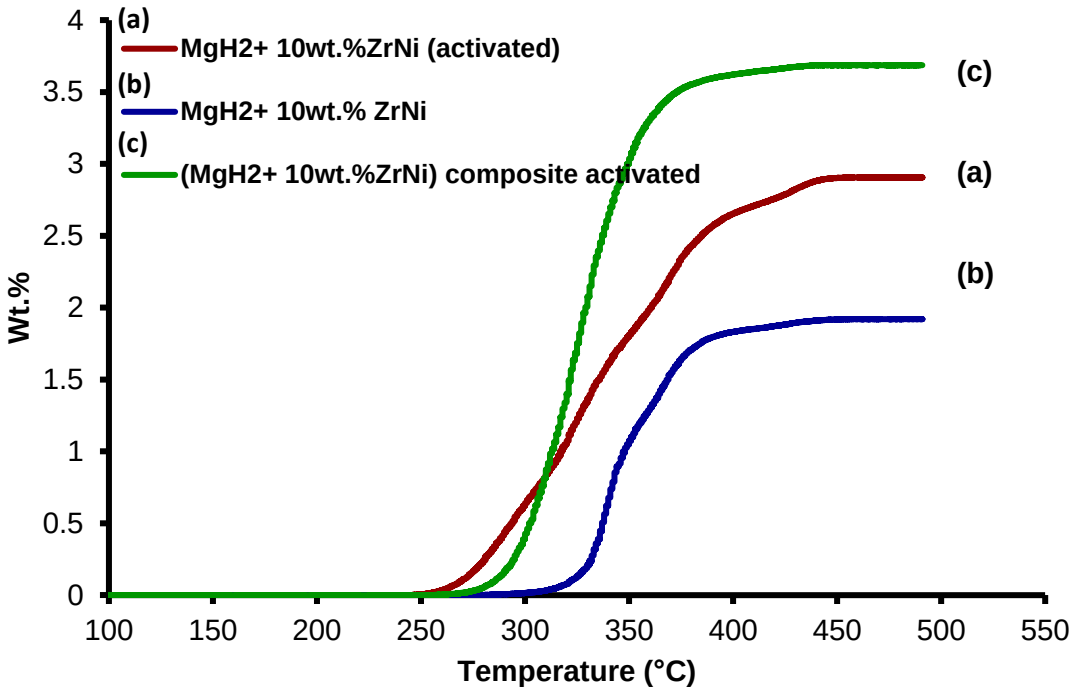

Figure 4. 10: Thermally programmed H_2 desorption capacity curves of studied powders—same experimental conditions as in Figure 4.9.

Table 4. 2: Desorption kinetic properties of MgH_2 + 10wt.% activated catalyst ZrO_2/Ni, MgH_2 + 10wt.% ZrO_2/Ni, and MgH_2 + 10wt.% ZrO_2/Ni (composite activated). The samples were analysed through a TPD at 500 °C under an Ar flow of 20 mL min^{-1} and a heating rate of 2 °C min^{-1}.

Composites (milled 20h)	Desorption wt.% H	Onset Desorption temp (°C)	Maximum Desorption temp (°C)
MgH_2 + 10wt.% activated catalyst ZrO_2/Ni	3	250	326
MgH_2 + 10wt.% ZrO_2/Ni	1.8	300	336
MgH_2 + 10wt.% ZrO_2/Ni (composite activated)	3.8	270	327

4.3.2. XRD Analysis of the Composites

Figure 4.11 (a) represent the XRD patterns of the composites – (1) MgH_2 + 10wt.% activated catalyst ZrO_2/Ni, (2) MgH_2 + 10wt.% ZrO_2/Ni (composite activated), (3) MgH_2 + 10wt. % ZrO_2/Ni. After 20-hours ball milling, the predominant peaks observed in the three composites were attributed to α-MgH_2 corresponding to the tetragonal phase (PDF#01-075-7944) coexisting with the β-MgH_2 (PDF#00-035-1185) are indicated by the Bragg's angle at 39.9º, 57.6º,64.9º. Referring to the first composite (1), the catalyst activation prior to the ball milling process resulted in the broader peaks of the β-MgH_2 phase with lower intensity. The broadening peaks suggest that the nanocrystalline phase formation occurs during milling.

The major Bragg's peaks were related to MgO at 2θ of 36.9º, 42.9º, 62.3º, and 74.7º (PDF#-1-074-4911). Additional phases were observed in the composite (3). A small mole fraction of the γ-MgH_2 (PDF#01-075-7945) orthorhombic metastable phase appeared at 32.9º, 36.3º, 67.2º and a small percentage of the β-Zr (PDF# 00—34-0657) coexisted with the α-MgH_2. Figure 4.11(b) is used as a reference material of the commercial Mg/MgH_2 and MgO to have a clear vision of where the oxide and MgH_2 Braggs peaks are located in the analysed composites MgH_2 + 10wt.% activated catalyst ZrO_2/Ni.

(a)

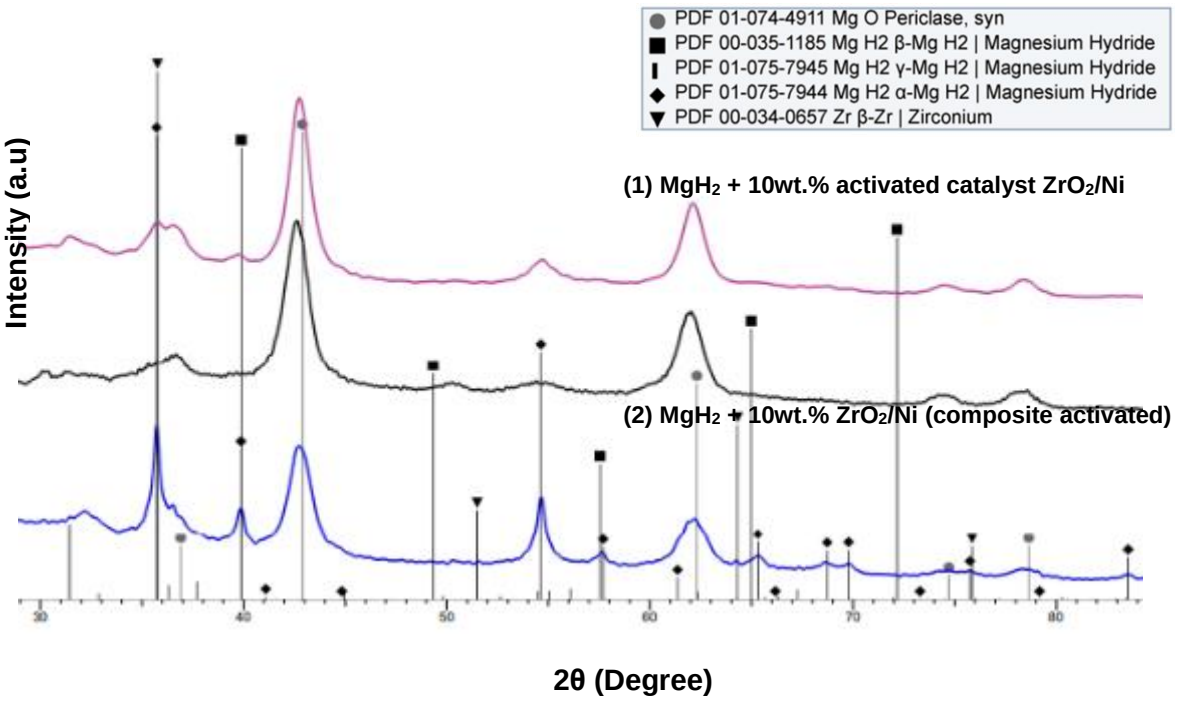

(b)

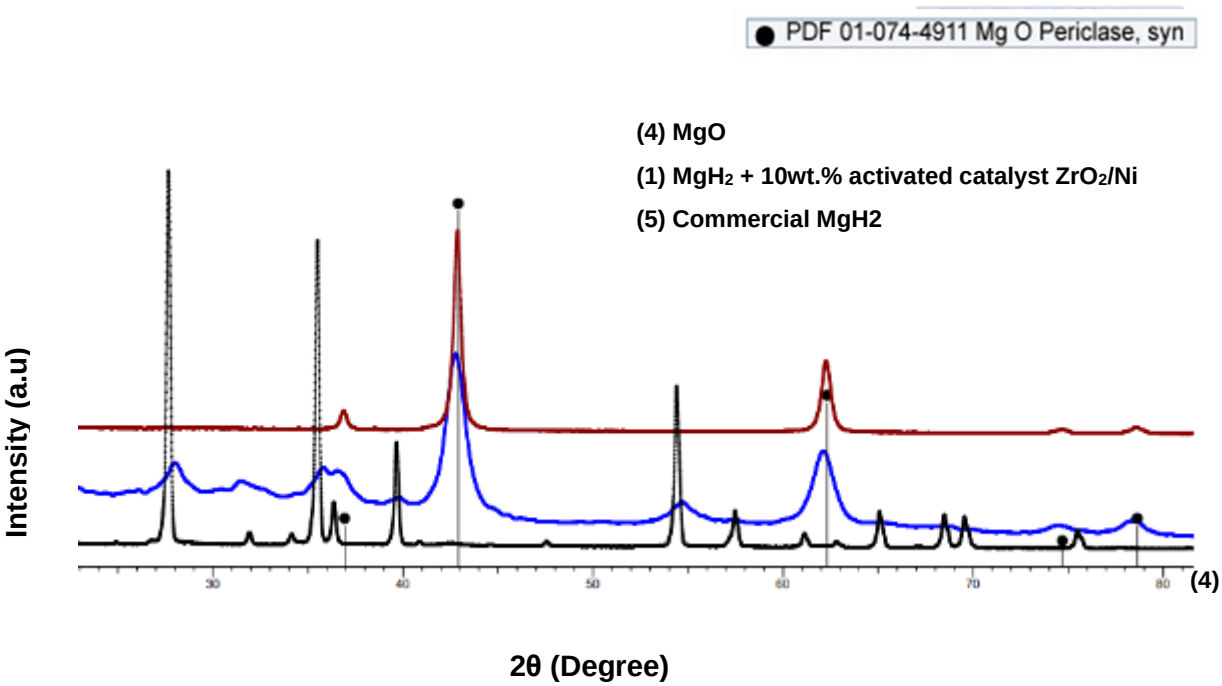

Figure 4. 11: (a) The XRD patterns of (1) MgH_2 + 10wt.% activated catalyst ZrO_2/Ni, (2) MgH_2 + 10wt.% ZrO_2/Ni (composite activated) and (3) MgH_2 + 10wt.% ZrO_2/Ni. (b) (4) MgO, (1) MgH_2 + 10wt.% activated catalyst ZrO_2/Ni, and (5) commercial MgH_2

4.3.3. Hydrogenation/ dehydrogenation behaviour – Kinetics

Based on the results obtained from the TPD analysis (Figure 4. 9.), the activation of the catalyst before the milling process with Mg/MgH_2 positively impacts the dehydrogenation behaviour of the MgH_2. Additionally, the sorption property of MgH_2 + 10wt.% activated catalyst ZrO_2/Ni was measured using a mass analyser to determine its kinetics and thermodynamics. The hydrogenation and dehydrogenation properties of the sample were analysed at two different temperatures.

Refer to Figure 4. 12. displays the kinetic plots of nanocomposite MgH_2 + 10wt.% activated catalyst ZrO_2/Ni obtained after 20 hours ball milled through the SPEX high energy ball mill. The nanocomposite powder absorbed 4.0 wt.% at 250ºC and 4.4 wt.% at 300ºC consecutively after approximately one minute. (Figure 4. 12. a, b). The obtained results proved that the catalyst prepared in *the present study* have an important impact on the hydrogenation of MgH_2 in term of decomposition temperature when compared to a previous study. [88] Refer to Table 4.3. El-Eskandarany *et al.* reported on the catalytic effect of nanocrystalline Zr_2Ni to improve the hydrogenation and dehydrogenation kinetics of MgH_2. The catalyst was prepared via an Arc melting method. 10wt% of Zr_2Ni with milled with MgH_2, via an high energy planetary ball mill - RETSCH, PM400 for 200 hours at 250 °C, 300 °C and 350 °C. MgH_2/10 wt.% Zr_2Ni powders only absorbed 4.9 wt.% at 325ºC after one minute. [88] Though the hydrogen was fully desorbed, at a desorption time of 300°C and 250°C, the desorption time too approximately 20 and 350 minutes, respectively.

Although the novel catalyst fabrication significantly impacts the sorption properties of MgH_2, more work is needed to improve the dehydrogenation behaviour of MgH_2 [39], [41], [111]. Tome *et al*. [39] published the same study on the MgH_2/5wt.%Ni5wt.%ZrO_2. The author used commercial Ni and ZrO_2 with a purity of 99.9% and a particle size between 20 -100 nm and 50 nm, respectively. The samples were ball milled for 4 hours through the planetary ball mill with a ball-to-powder weight ratio of 30:1. The composite MgH_2/5wt.%Ni5wt.%ZrO_2 released approximately 6.2 wt.% in approximately 10 min at 310°C. [39] Refer to Table 4. 3 for comparing the results of the *present study*.

Table 4. 3: Comparison of the kinetics data obtained in the *present study* to literature reports.

Sample (composites)	Temp (°C)	Abs (wt.%)	Time (min)	Des (wt.%)	Time (min)	B.M. time (h)	Reference
MgH_2 + 10wt.% activated catalyst ZrO_2/Ni	250	4.0	1.2	4.2	350	20h-SPEX (n.p)	*Present study*
MgH_2 + 10wt.% activated catalyst ZrO_2/Ni	300	4.4	0.5	4.7	20	20h-SPEX (n.p)	*Present study*
MgH_2-10% Zr_2Ni	325	4.9	1.7	5.1	10	150h PBM	Eskandarany *et.al* [88]
ZrO_2@Nb_2CTx/MgH_2	300	6.24	2.5	6.12	5	10h/ (p.i)	Lu *et.al* [111]
MgH_2/5wt.%Ni5wt.%ZrO_2	270	4.5	50	5.9	96	4h PBM	Tome *et al.* [39]
MgH2/5wt.%Ni5wt.%ZrO2	310	6.1	6	6.2	10	4h-PBM	Tome *et.al* [39]

Milling condition of the sample abbreviation

SPEX- composites milled using the high energy ball miler SPEX-8000

n.p- no pause during the milling of the sample

p.i. – the instrument was paused at intervals during the milling of the sample

PBM- composites milled using the Planetary ball mills

h- h milling time

(a) *Absorption of MgH_2 + 10wt.% activated catalyst ZrO_2/Ni*

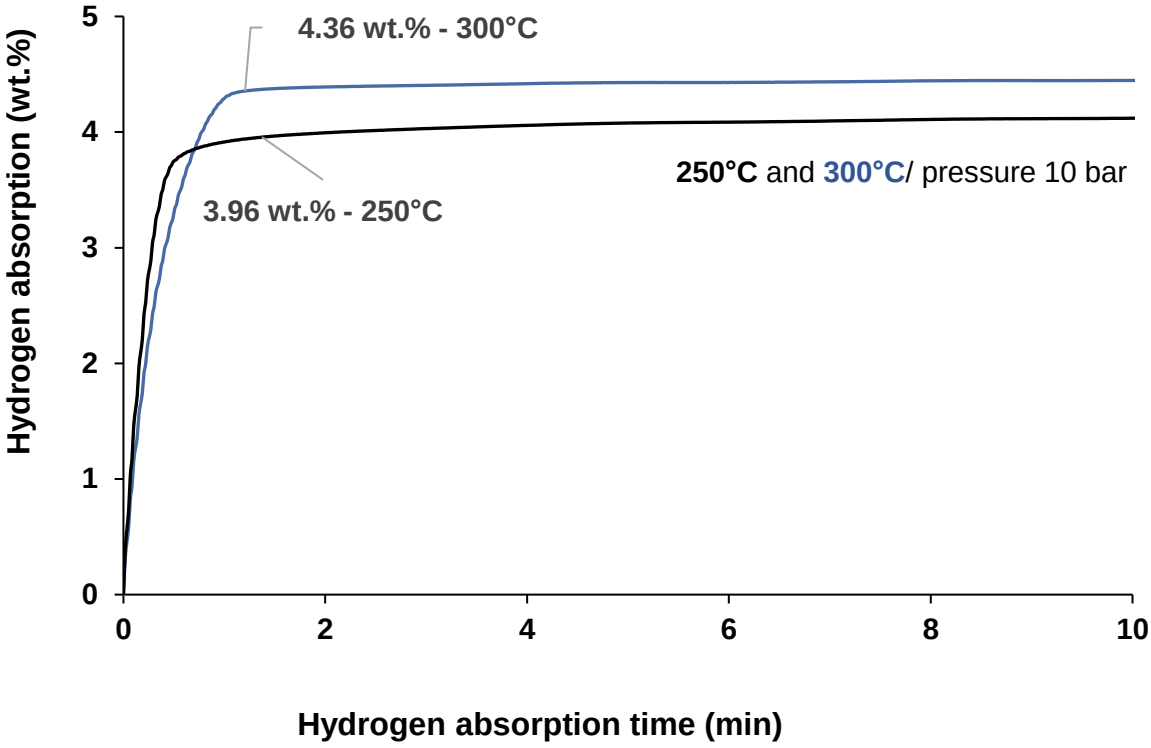

(b) Desorption of MgH_2 + 10wt.% activated catalyst ZrO_2/Ni at 300°C

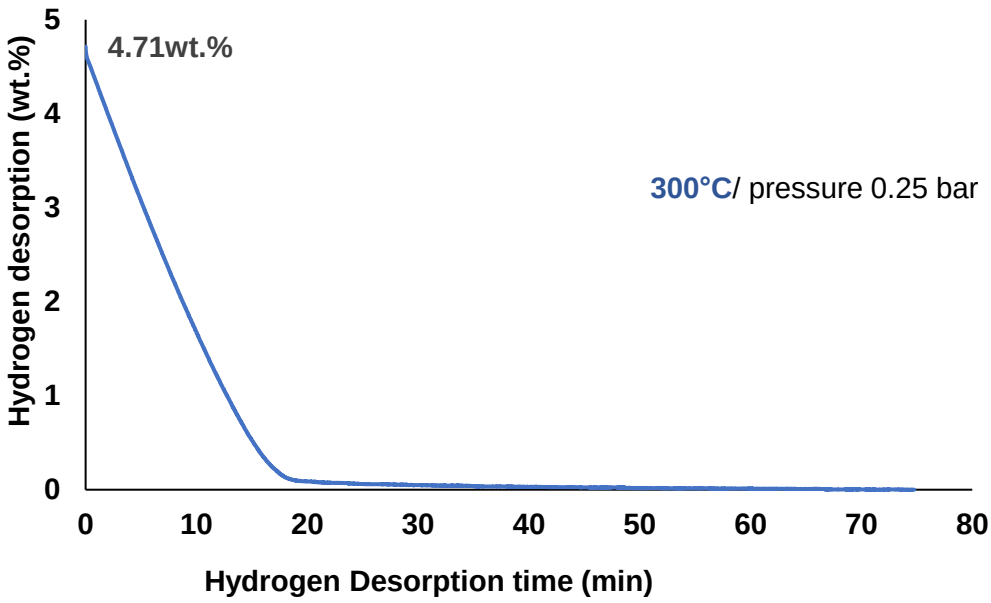

(c) Desorption at 250°C of MgH_2 + 10wt.% activated catalyst ZrO_2/Ni at 250°C

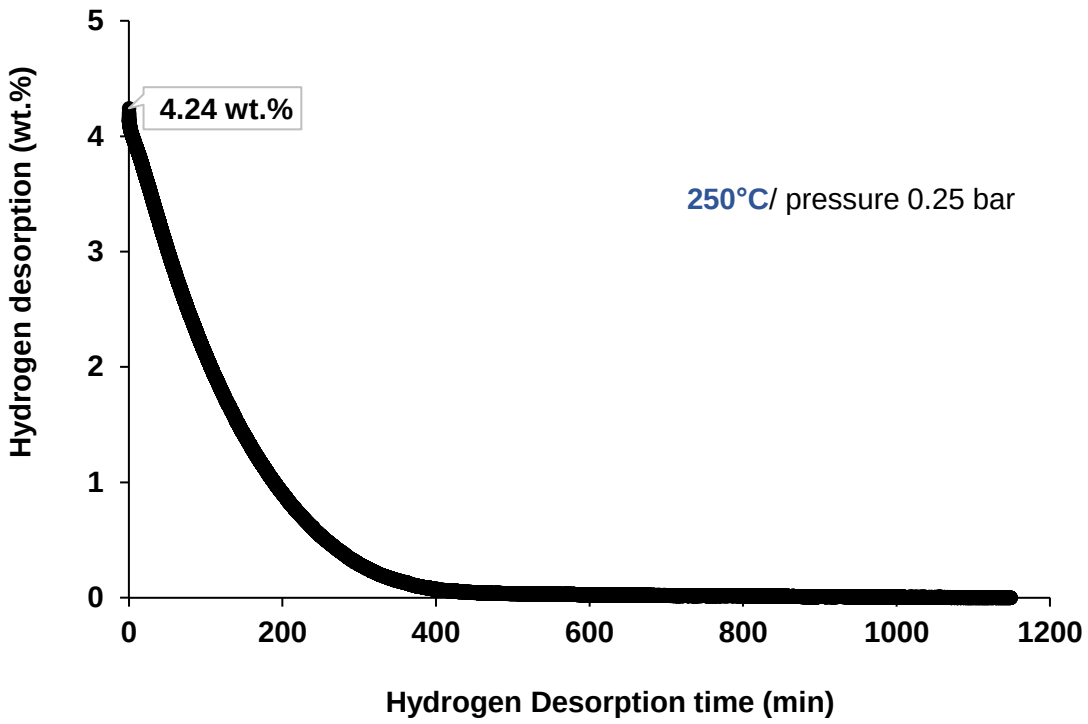

Figure 4. 12: (a) Absorption kinetics plots of MgH_2 + 10wt.% activated catalyst ZrO_2/Ni at 250°C and 300°C at 10 bar, (b) desorption kinetics plots of MgH_2 + 10wt.% activated catalyst ZrO_2/Ni at 250ºC and 300ºC 0.1 bar of H_2

The poor hydrogen storage properties may result from nanoparticle growth during milling. It is worth mentioning that the milling of the nano-powder in a large quantity when using a SPEX milling system comes with several disadvantages in terms of impurities and powder agglomeration. Long hour milling time without interval break leads to overheating powder and oxide formation. Researchers proposed 10 minutes pause interval between every 10 minutes of milling to prevent overheating, which may contribute to the agglomeration of the powder. [111]

The powder agglomeration was observed in the image obtained from the SEM analysis, as shown in Figure 4. 13. (a). The agglomeration of the powder contributed to the destruction of the nanoscale properties. The calculated particles size ranges from 2000 to 4000 nm; refer to Figure 4. 13. (b), and crystallite size of 34 nm (Figure 4.11(3)).

Researchers have suggested that a crystallite size of less than 20 nm contributes to compound stability, enhancing the absorption/ desorption of hydrogen in Mg/MgH_2. [59], [82], [112] Furthermore, this can be achieved with the Planetary ball mills. Referring to Figure 4. 13. (c), the composite's energy dispersive X-ray spectroscopy (EDX) shows approximately 19 % of oxide, 26 % of Mg, 3% of Ni and 27 % of zirconium. The rest of the detected peaks contributed from the powder contamination during the milling process and the SEM sample holder, such as Iron (Fe), copper (Cu), and chromium (Cr).

(a)

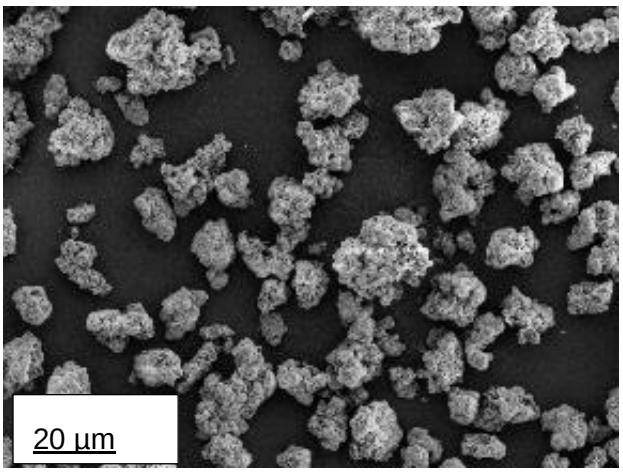

(b)

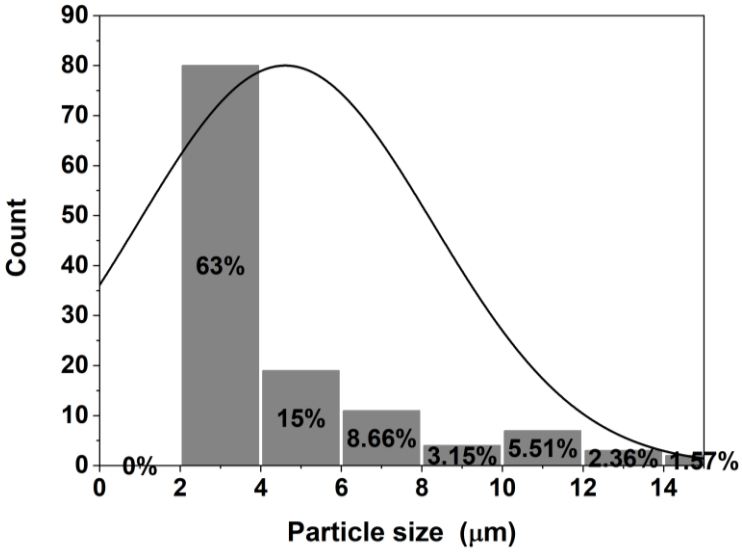

(c)

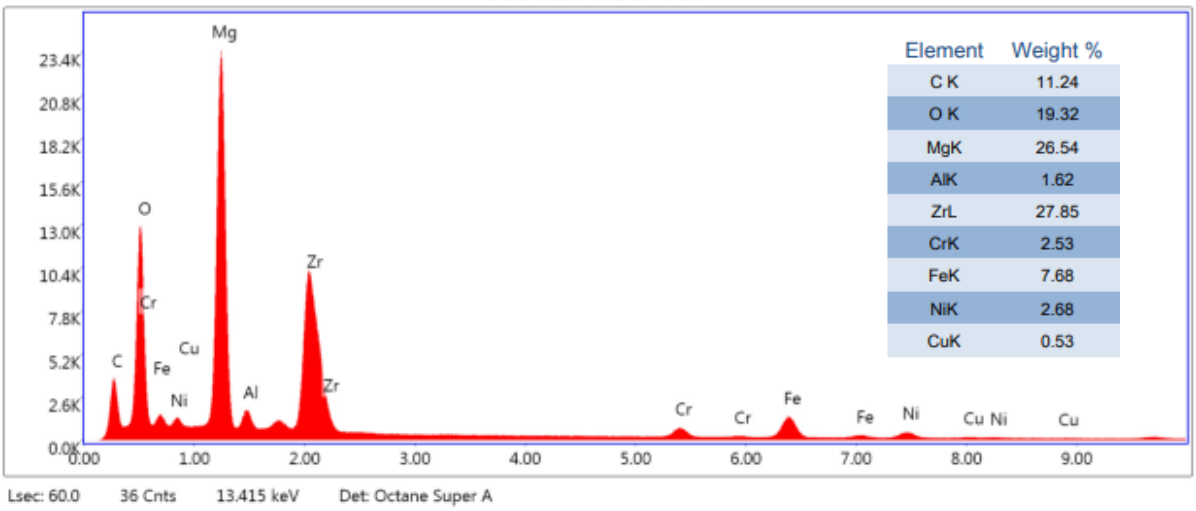

Figure 4. 13: (a) SEM micrograph of MgH_2 + 10wt.% activated catalyst ZrO_2/Ni based nano-catalyst after 20 h milling time under Ar (b) Histograms of particle size distribution measured by the SEM/ImageJ analysis (c) The energy dispersive X-ray spectrocopy (EDX) image analysis.

It is worth mentioning that the high-energy ball mill - SPEX selling vial does not have a lock system and the option to purge the air out of the vial before milling the sample. As expected, there is a relatively high percentage of oxide, which may result from different factors—exposing the powder during the characterisation analysis, and the milling system not having a properly adjusted compact lead. A high level of MgO is among the factors that contribute to the reduction in the rate of hydrogenation, which prevents the hydrogen from penetrating the molecules. The presence of MgO was also identified in the XRD pattern, as shown in Figure 4.11.

4.4. Conclusion

In the present study, a novel method was successfully established, which involves the synthesis of nano-sized catalysts ZrO_2/Ni through a high-pressure reactor, followed by a catalyst calcinated prior to being mechanically milled with MgH_2 to form the composite MgH_2/10wt%ZrO_2/Ni. The characterisation of the composite was via the XRD/ SEM/ TEM and PCT.

The approach demonstrated that activating such nano-catalysts before the milling process with MgH_2 offers promising perspectives. Although the developed method provides a faster and better system for the fabrication of nanomaterials, some significant improvements still need to be addressed regarding the milling technique. The milling of the powder via the SPEX ball mills resulted in particle agglomeration of the nanostructured composite MgH_2/10wt%ZrO_2/Ni mainly in the range of 2000 nm to 4000nm, as well as in a high level of impurities, and oxide formation, which significantly affected the absorption property of the MgH_2, 4.4wt.% at 250°C after 1 minute.

For future work, different approaches must be addressed to ameliorate the milling technique - such as reducing the milling time and implementing breaks intervals during the milling to avoid overheating the powder. Therefore, finding an automated milling instrument that favours the grinding of approximately one gram in an inert atmosphere can prevent agglomeration and oxidation of the powder.

Reader Guide

Chapter I: General Introduction

Chapter II: Literature

Chapter III: Methodology

Chapter IV: Establishing an Innovative Method for the Synthesis of ZrO_2/Ni Nanocatalyst for Improving the Sorption Property of MgH_2 in the Field of Solid-State Hydrogen Storage

20 hours milling time/ SPEX high energy ball mill MgH_2+10wt.%ZrO_2/Ni

Introduction Recap

Experimental

- Catalyst-ZrO_2/Ni synthesis
- Composite (MgH_2+10wt.%ZrO_2/Ni) ball mill: 5 hours via Planetary
- Characterisation

Results/ Discussion

- XRD
- SEM
- TPD
- Kinetics

Conclusion

References

Chapter V: Development of a Novel Method for the Fabrication of Nanostructured ZrO_2/Ni Catalyst to Enhance the Desorption Properties of MgH_2

5 hours milling time/ Planetary ball mill - MgH_2+10wt.%ZrO_2/Ni

Introduction Recap

Experimental

- Catalyst-ZrO_2/Ni synthesis
- Composite (MgH_2+10wt.%ZrO_2/Ni) ball mill: 20 hours via SPEX
- Characterisation

Results

- XRD
- SEM
- TPD

Discussion

Conclusion

References

Chapter VI: Comparing the Novel Catalysts ZrO_2/Ni and ZrO_2/$NiCl_2$ Storage Behaviour of Hydrogen Sorption Properties of MgH_2 Powder

5 hours milling time/ Planetary ball mill (ZrO_2/$NiCl_2$) catalyst

Introduction Recap

Experimental

- Catalyst-ZrO_2/Ni synthesis
- Composite (MgH_2+10wt.%ZrO_2/$NiCl_2$) ball mill: 5 hours via Planetary
- Characterisation

Results / Discussion

- XRD
- SEM
- Kinetics
- PCT

Conclusion

References

Chapter VII: General conclusion

References

Appendices

CHAPTER V: DEVELOPMENT OF A NOVEL METHOD FOR THE FABRICATION OF NANOSTRUCTURED ZrO_2/Ni CATALYST TO ENHANCE THE DESORPTION PROPERTIES OF MgH_2

Method 2: *MgH_2/10wt.% ZrO_2/Ni - 5 hours Ball milling through Planetary ball mills*

This Chapter is a publication of an article published in the Catalysts journal in July 2020. The published article addresses the problem of powder agglomeration and oxidation, likely to be the results of milling the MgH_2 composite via the High-pressure miller - SPEX. Significant concerns that resulted in poor hydrogenation/ dehydrogenation of hydrogen in the Mg/MgH_2,, as mentioned in the previous **Chapter IV,** are the focus of the present Chapter. Therefore, Chapter V offers an alternative milling system utilising the Planetary ball mills.

Gracia Shokano 1,, Zahir Dehouche 1,*,George Fern1,*, Basile Galey 2 and Georgeta Postole 2*
1 College of Engineering, Design and Physical Sciences, Brunel University London, Uxbridge UB8 3PH, U.K.
2 Univ Lyon, Université Claude Bernard Lyon 1, CNRS, IRCELYON, F-69626 Villeurbanne, France; basile.galey@ircelyon.univ-lyon1.fr (B.G.); georgeta.postole@ircelyon.univ-lyon1.fr (G.P.)

5.1. Introduction

The Mg/MgH_2 is one of the metal hydride systems that serve as a solid-state hydrogen storage system, captivating the attention of researchers due to its high and reversible volumetric, 110 g/L H_2, and gravimetric, 7.6 wt.% H_2, capacities. [113], [114] Despite these advantages, the Mg/MgH_2 system's practical applications have several drawbacks that limit its utilisation in automobiles. MgH_2 has an ionic phase with an Mg–H bond charge distribution of $Mg^{1.91+}$ $H^{0.26-}$. [60] The ionic structure contributes to its high thermodynamic stability of $\Delta H = \pm 75$ kJ/mol H_2 and entropy value of 130 J/mol/K. Therefore, the high stability results in an operating temperature above 350 °C. [115]

Moreover, the nanostructured Mg/MgH_2 suffers from poor hydrogenation and dehydrogenation kinetics at elevated temperatures. [30] Numerous factors contribute to the reduction in the rate of hydrogenation, which prevents the hydrogen from

penetrating the molecules. For example, the formation of MgO and magnesium hydroxide ($Mg(OH)_2$) on the surface of Mg may take place when exposing Mg to air. [116] The oxide layer on the surface of the Mg particles can be cracked or perforated during the activation of the metal or the ball milling preparation. [117] Activation consists of cycling and cooling the material in a vacuum atmosphere, and, as a result, the metal surface is exposed to hydrogen. [118]

The drawback of Mg/MgH_2 is still under investigation by researchers through different approaches, such as the reduction of the particle sizes during the ball milling process and the catalyst doping of metallic particles with varying fractions of catalytic agents. [118] Ni and Zr were reported to improve the dissociation of hydrogen at the Mg surface. [117] The metal oxides (ZrO_2, TiO_2) and the metastable phases ZrO_2/Ni have shown remarkable progress in past studies in enhancing the hydrogen storage properties of MgH_2. [28], [41], [61], [83], [91]

The present study proposes a novel method for fabricating a zirconium/nickel-based nanostructured catalyst. The catalyst fabrication is thru a modified sol-gel process. The synthesis is conducted in a compact high-pressure hydrogen reactor to produce nanostructured catalyst particles. Furthermore, it enhances the hydrogenation and dehydrogenation kinetics of the Mg/MgH_2 system.

5.2. Materials and Methods

5.2.1. Catalyst Synthesis: High Pressure Reactor and Heat Treatment

The catalyst was firstly prepared in the high-pressure PARR 5500 Series Compact Reactor from a mixture of the starting material of $ZrCl_4$ fine white powder with a 99.5+ metal basis and $Ni(NO_3)_2.6H_2O$ (98% green salt) provided by Alpha-Aesar and Sigma-Aldridge, respectively. The solution is 0.99 wt/v.% $ZrCl_4$ and 1.52 wt/v.% $Ni(NO_3)_2{\cdot}6H_2O$, dissolved at room temperature in 150 mL of methanol solvent, was transferred into the reactor vessel (Type 316/austenitic chromium-nickel stainless steel containing molybdenum). The reactor was assembled and tightened vigorously to avoid the pressure drop of the hydrogen. The reactor vessel was purged with hydrogen for several minutes to flush out the air inside the reactor and refill it with hydrogen. The mixture was heated for 2 hours at 200 °C under hydrogen, at a starting

pressure of 20 bar, whilst stirring at 60 revolutions per minute. The sample was cooled overnight; the supernatant was discarded, whilst the formed gel was dried overnight at room temperature. The sample was fully dried when heat-treated at 350 °C for 5 hours, and further cooled for 2 hours under the flow of hydrogen at 0.6 bar (Figure 5.1). The prepared catalyst was transferred to the glove box, purged with Ar, and then transferred into the reactor vessel for activation through a particulate system HPVA at 30 °C/10 bar.

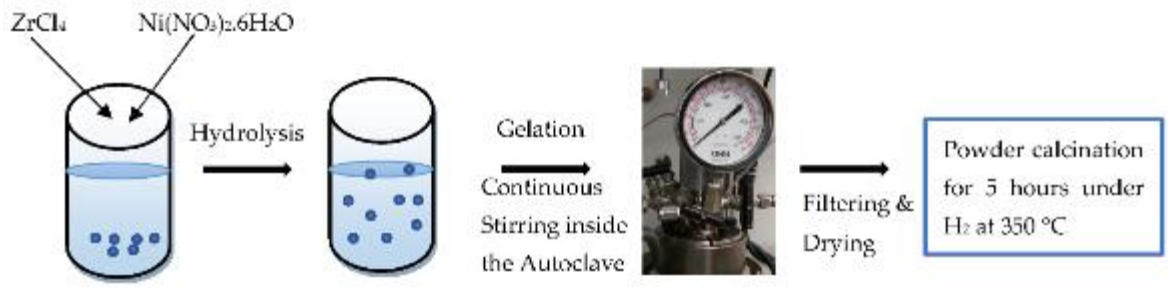

Figure 5. 1. The steps of synthesising the catalyst preparation**.**

5.2.2. Preparation of MgH_2-Based Nanocomposite Powders: Ball Milling

The MgH_2+10wt.%ZrO_2/Ni composite was prepared under an inert Ar atmosphere via the planetary ball mills using a PM100 apparatus from Retsch. 10 wt.% of the hydrogenated ZrO_2/Ni based nanocatalyst was added to MgH_2 in a reactor vessel with zirconium oxide (ZrO_2) milling balls of 1-mm diameter. The ball-to-powder mass ratio was 100:1. The reactor was hermetically sealed inside the glove box to prevent any oxidation of the powders. The sample was milled for 5 hours at 300 revolutions per minute. During the milling process, the ball's rotation in the mill was paused every 2 minutes and inverted every 5 minutes to prevent temperature increase in the milling cell. For comparison, MgH_2 was milled under the same conditions but without adding the catalyst.

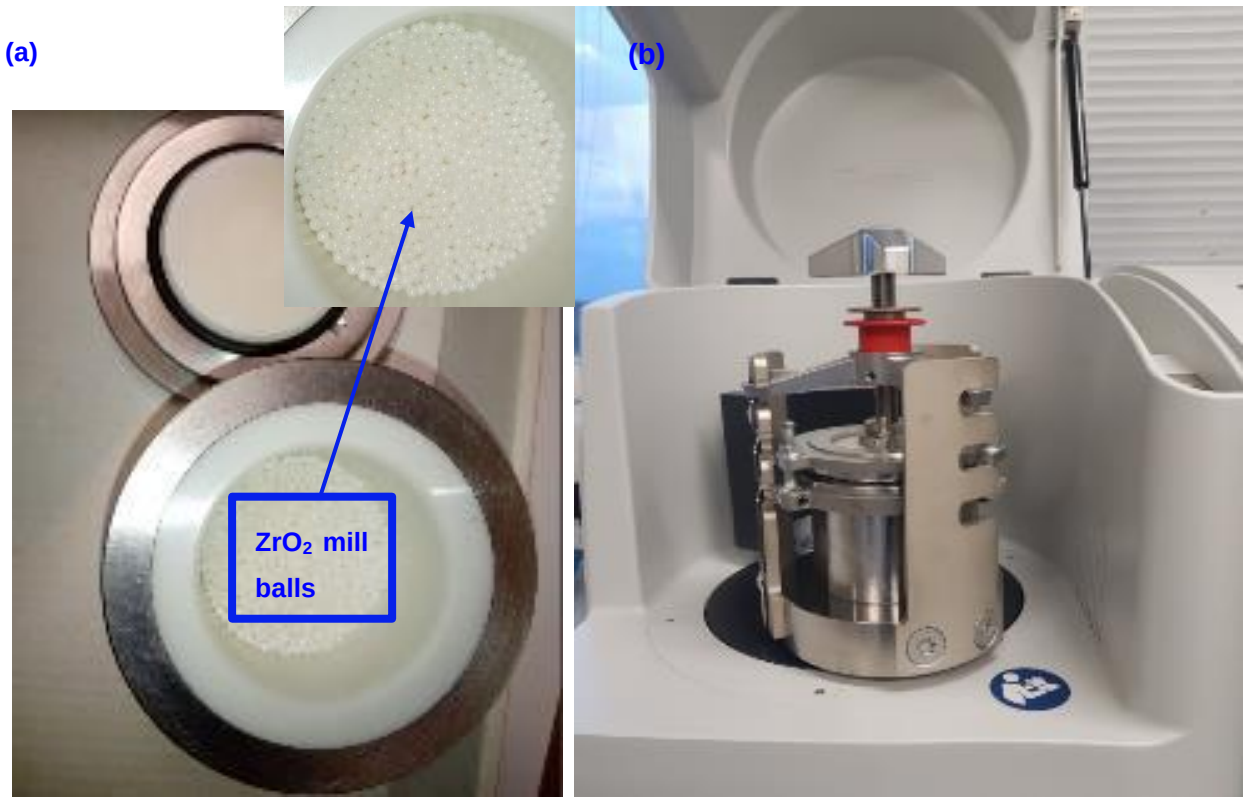

Figure 5. 2: (a) Reactor vessel with ZrO_2 milling balls of 1-mm diameter, (b) Planetary ball mills using a PM100 apparatus from Retsch

5.2.3. Sample Characterisations: XRD, SEM, and TEM

The properties of the synthesised catalyst and the formed composites were studied through X-ray diffraction (XRD). The crystal structures of all samples were investigated by the XRPD Bruker D8 Advance X-Ray Powder Diffractometer (XRPD) with the CuKα (λ = 0.154 nm) radiation over the 2θ ranging from 20° to 80°. The instrument was calibrated with the LaB6 NIST standard (660a). The specific surface area of the synthesised catalyst was measured with nitrogen gas (NOVAtouch LX1, USA) at a temperature of 77 Kelvin.

The surface morphologies were obtained with a field emission scanning electron microscope (FESEM) (SUPRA 35VP, Zeiss, Germany). Energy dispersive X-ray spectroscopy (EDS) was used for elemental analysis of the deposited layers. For the SEM analysis, the powder placed on a carbon tape was coated with a thin layer of gold and added through vacuum evaporation to prevent the sample from developing high conductivity and some charging effects during the analysis.

The TEM model JE M-2100F microscope was used for the structural features. The powder was suspended in EtOH and drop-cast onto holey carbon support film, Cu 200 mesh. The surface morphologies of the analysed powders were determined via the field emission scanning electron microscope (FESEM) (SUPRA 35VP, Zeiss, Germany). The images were collected using Gatan software.

5.2.4. The Dehydrogenation Behaviour: TPD

The dehydrogenation properties of the composite MgH_2/10 wt.% ZrO_2/Ni was studied after the ZrO_2/Ni catalyst activation under 10 bar of hydrogen at 30 °C for 100 minutes. Temperature-programmed desorption (TPD) analyses were performed with a TPD/R/O-1100 apparatus from Thermo. All the powder measurement and transfer were performed in a glove box under a protective Ar atmosphere to prevent oxidation. The experiments were performed from ambient temperature to 500 °C at 2 °C min^{-1} under an Ar flow of 20 mL min^{-1}. The instrument was calibrated before the analyses by reducing different masses of copper (II) oxide to determine the samples' precise amount of hydrogen desorbed.

5.3. Results

5.3.1. Characterisation of ZrO_2/Ni Catalyst: XRD and TEM

The zirconium nickel nanostructured catalyst was synthesised via a modified sol-gel method in a compact high-pressure hydrogen reactor and activated before being used as an additive to MgH_2. The catalyst preparation method used in the *present study* is further detailed in section 5.2. To fully characterise the catalyst after synthesis and activation, XRD, SEM-EDX and FE-HRTEM analytical methods were used. The results of the SEM-EDX are presented in section 5.3.3. Firstly, XRD was carried out to identify and quantify the crystalline phases in the synthesised ZrO_2/Ni-based catalyst powder prepared by the high-pressure reactor (Figure 5.1.).

It is visible from Figure 5. 3 that the Ni phase was predominant after the 5 hours heat treatment at 350 °C. The sharp Bragg peaks indicate the precursor Ni powder at around 2θ of 44.5°, 51.8° and 76.2° (PDF file # 01-070-1849). Additional broad peaks

were identified at around 2θ of 30° and 60.5°, corresponding to the development of Zr_2O (PDF file #01-071-6425).

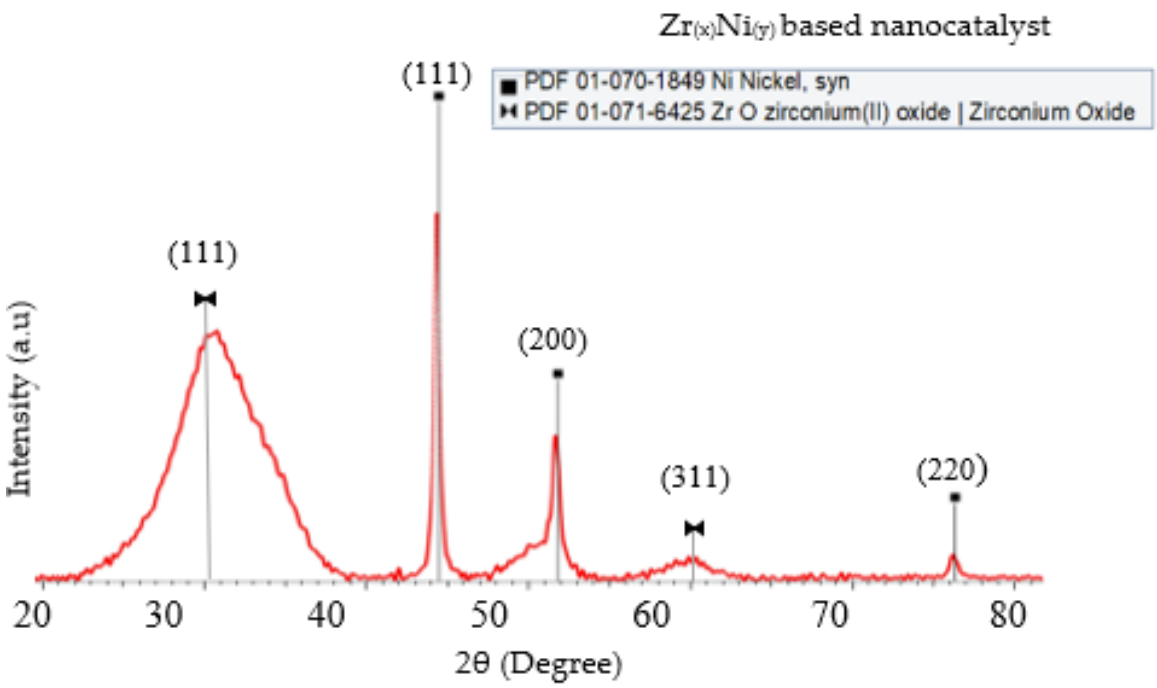

Figure 5. 3: The XRD patterns of ZrO2/Ni based nanocatalyst.

The crystallite size (d) was calculated using Scherrer's equation. Refer to Equation (1).

$$D = \frac{k.\lambda}{FWHM.cos\theta}, \qquad Eq.5.1$$

The catalyst particles' crystallite size D (nm) was calculated from the XRD results (Figure 5. 3). Where *D* is the crystallite size (nm), *k* is the Scherrer's constant (0.9), λ is the wavelength of the X-ray source (0.15406 nm), *FWHM* is the full width at half maximum, and θ is the peak position. The crystallite size of zirconium(II) oxide determined from 2θ = 30° was 2.8 nm, and Ni from the 2θ = 44.5° was 14.2 nm.

Lastly, FE-HRTEM analysis was performed to determine the surface morphologies of the catalyst ZrO_2/Ni and the nanocrystal structures (Figure 5.4.).

The Moire fringes with dissimilarity in the interplanar structure were identified. The powder consisted of nanocrystal structures corresponding to Zr and Ni, represented as zones I, II and III. The d spacing was determined in nm, and the XRD phases confirmed the identities of each characterised element. Zone I corresponds to the d spacing of 0.14 nm, determined as the Zr crystal (211) phase; zone II corresponds to the d spacing of 0.13 nm, determined as the Ni crystal (220) phase, as shown in Figure 5.4. c; zone III correlates to the d spacing of the 0.15 nm (311) phase, corresponding to the Zr_2O particle, as shown in Figure 5.4.d.

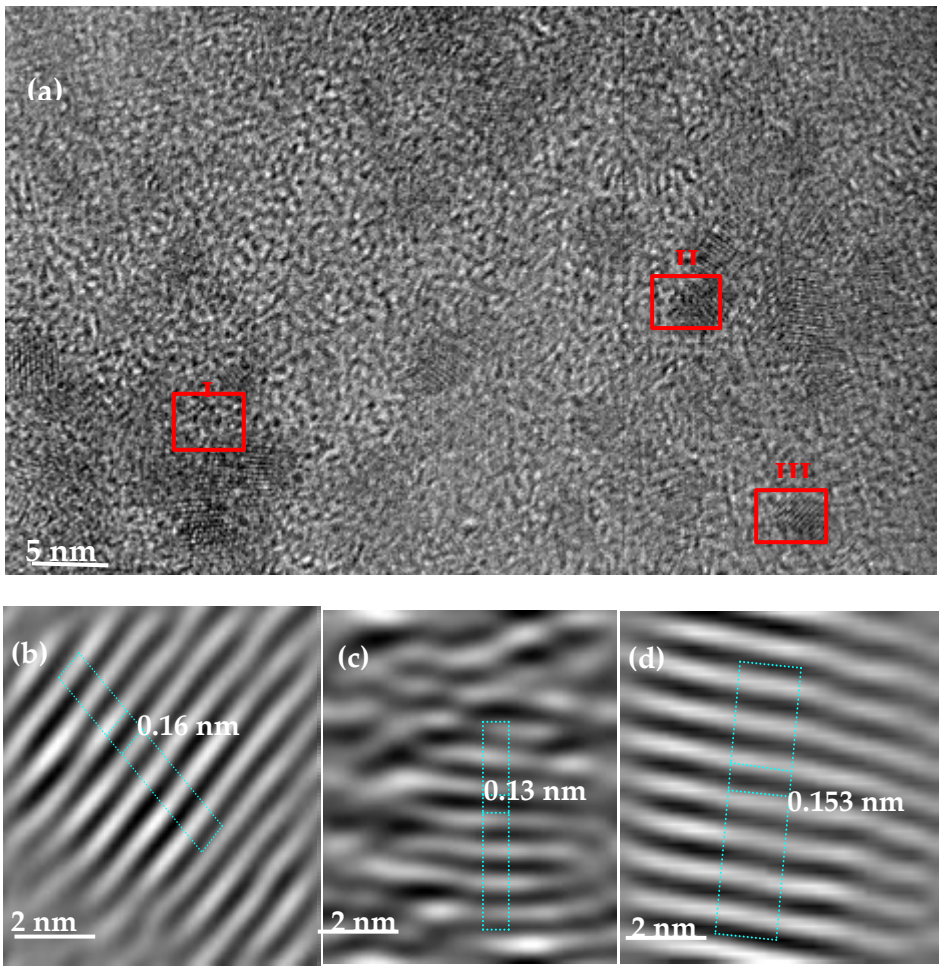

Figure 5. 4. Field emission high-resolution transmission electron microscopy (FE-HRTEM). (a) ZrO2/Ni nanocatalyst, (b) the lattice image of zone I; (c) the lattice image of zone II; (d) the lattice image of zone III.

5.3.2. Characterisation of MgH_2/10 wt.% ZrO_2/Ni Nanocomposite: TPD

After being activated under hydrogen, the ZrO_2/Ni catalyst was used as an additive in the Mg/MgH_2 system. The commercial MgH_2 was thus milled with 10 wt.% of ZrO_2/Ni for 5 hours, as detailed in section 5.2. The formed MgH_2/10 wt.% ZrO_2/Ni nanocomposite dehydrogenation properties were analysed via temperature-programmed desorption (TPD).

5.3.2.1. Dehydrogenation Properties of the Nanocomposite MgH_2/10 wt.% ZrO_2/Ni

To better understand how the ZrO_2/Ni catalyst impacts the dehydrogenation properties of MgH_2. The hydrogen release properties of the nanocomposite MgH_2/10 wt.% ZrO_2/Ni was compared with those of the as-received (un-milled MgH_2) and the milled MgH_2 - in similar conditions.

Figure 5. 5 represents the temperature profiles of the MgH_2 decomposition, whilst Figure 5. 6 indicates the hydrogen capacity. The milled MgH_2 released 6.74 wt.% of hydrogen in a wide range of desorption temperatures between 300 °C and 400 °C, which may be a result of a large particle size distribution.

It is worth noticing that the milled powder presents a significant decrease in the decomposition temperature. Compared with the as-received powder, which is directly related to the reduction in the particle sizes of MgH_2. The mean size of crystallites was approximately 34 nm for the milled MgH_2 versus approximately 213 nm for the as-received MgH_2 sample, as deduced from XRD analysis by the Rietveld method. The obtained result correlated with the findings reported in previous studies. [31], [119] The addition of 10 wt.% ZrO_2/Ni nanocatalyst to MgH_2 induced the onset hydrogen desorption temperature shift from 300 °C to a starting temperature below 210 °C. As observed for the nanocomposite MgH_2/10 wt.% ZrO_2/Ni, only 5.9 wt.% of hydrogen was released in a wide range of temperatures between 200 °C and 400 °C. This result was expected due to the high amount of additive used (10 wt.% of ZrO_2/Ni), which reduced the system's overall storage capacity.

Table .5. 1: Desorption kinetic properties of pure MgH_2 as-received (unmilled), MgH_2 (ball-milled 5 hours) and MgH_2/10 wt.% ZrO2/Ni. The samples were analysed via TPD, starting from room temperature to 500 °C, under an Ar flow of 20 mL min^{-1} and a heating rate of 2 °C min^{-1}.

Samples	Peak Desorption Temperature (°C)	Discharge Rate (H-wt.% min^{-1})	Discharge Capacity (H-wt.%)
MgH_2 as-received (un-milled)	418	1.51	7
MgH_2 (milled 5 hours)	328	0.17	6.7
MgH_2/10 wt.% ZrNi	232	0.07	5.9

Table 5.1 highlights the results of the novel catalyst effect achieved in the present study. The TPD results confirmed that adding ZrO_2/Ni to MgH_2 induced an essential shift towards the lower hydrogen desorption temperature. The MgH_2 as received (un-milled) powder resulted in a faster hydrogen release of 7 H_2-wt.% at onset temperature 400 °C/ peak temperature 418 °C and at a discharge rate of 1.51 H-wt.% min^{-1}. The MgH^2 milled for 5 hours resulted in a hydrogen release of 6.7 H_2-wt.% at onset temperature 300 °C/ peak temperature 328 °C and at a discharge rate of 0.17 H-wt.% min^{-1}. The nanostructured MgH_2 powder milled with MgH_2/10wt% ZrO_2Ni resulted in a faster hydrogen release—5.9 H_2-wt.% at onset temperature 210 °C/peak temperature 232 °C and at a discharge rate of 0.07 H-wt.% min^{-1}.

To evaluate the effect of temperature on the discharge characteristics of the sorption materials. The kinetic desorption rates of MgH_2 as-received (un-milled), MgH_2 (milled 5 hours) and MgH_2/10 wt.% ZrO_2/Ni (milled 5 hours) were calculated from the TPD curves of Figure 5.5, at peak desorption temperatures of 418 °C, 328 °C and 232 °C, respectively; these are shown in Figure 5.5 and 5.6.

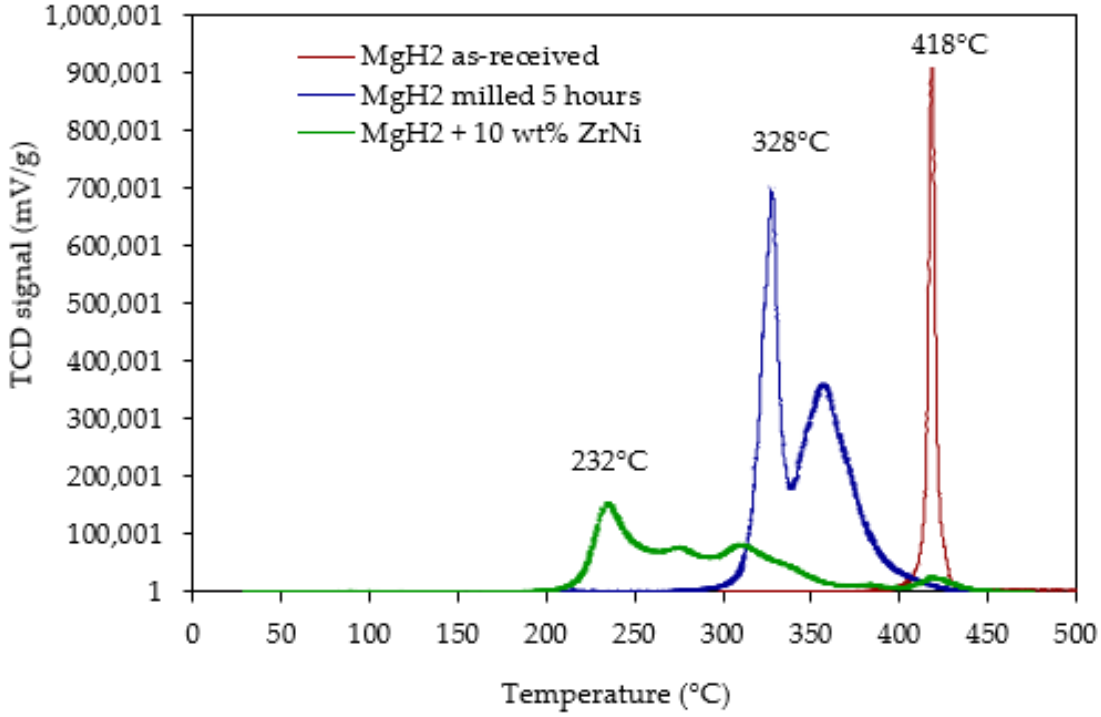

Figure 5. 5. The evolution of the temperature-programmed desorption (TPD) profile of as-received MgH_2 after milling without/with 10 wt.% ZrO2/Ni. Experimental conditions: from ambient temperature to 500 °C under an Ar flow of 20 mL min^{-1} and at a heating rate of 2 °C min^{-1}.

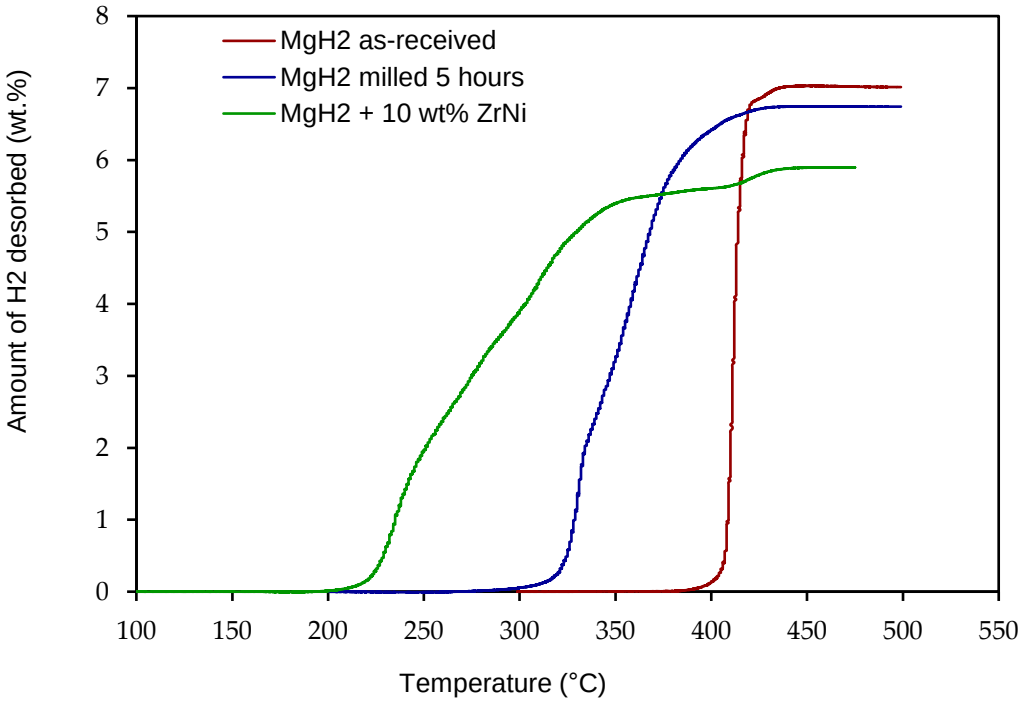

Figure 5. 6. Thermally programmed H_2 desorption capacity curves of studied powders. Same experimental conditions as given in Figure 3.

5.3.3. Characterisation of Crystal Structures: XRD, SEM, and TEM

XRD was carried out to quantify the compositions of the crystalline phases of the composite after the milling process with MgH_2 powder. The patterns of the composite MgH_2/10 wt.% ZrO_2/Ni was superimposed on the reference MgH_2 (un-milled) powder to reveal broadening in the diffracted line of the nanocomposite sample, which resulted from the grain refining of the powders during the planetary ball milling process (refer to Figure 5.7a). The composite powder obtained after 5 hours milling in an inert atmosphere consisted of the Bragg peaks β-MgH_2 (PDF file #: 00-012-0697) at 2θ of 27.95°, 35.74°, 39.86° and 54.62°; Ni (PDF file #: 00-001-1258) at 2θ of 44.37° and 51.60°; $Mg_{0.996}Zr_{0.004}$ (PDF file #: 01—71-9629) at 2θ of 32.23°, 34.42°, 36.67°, 47.88°, 57.480°, 63.13°, 67.45° and 68.75°. There was a small fraction of fcc-MgO observed at 2θ of 43.04°. The powder was mainly oxidised due to the sample preparation for the X-ray analysis handled outside the glove box, as shown in Figure 5.7b. However, a low amount of MgO was also revealed in the as-received MgH_2.

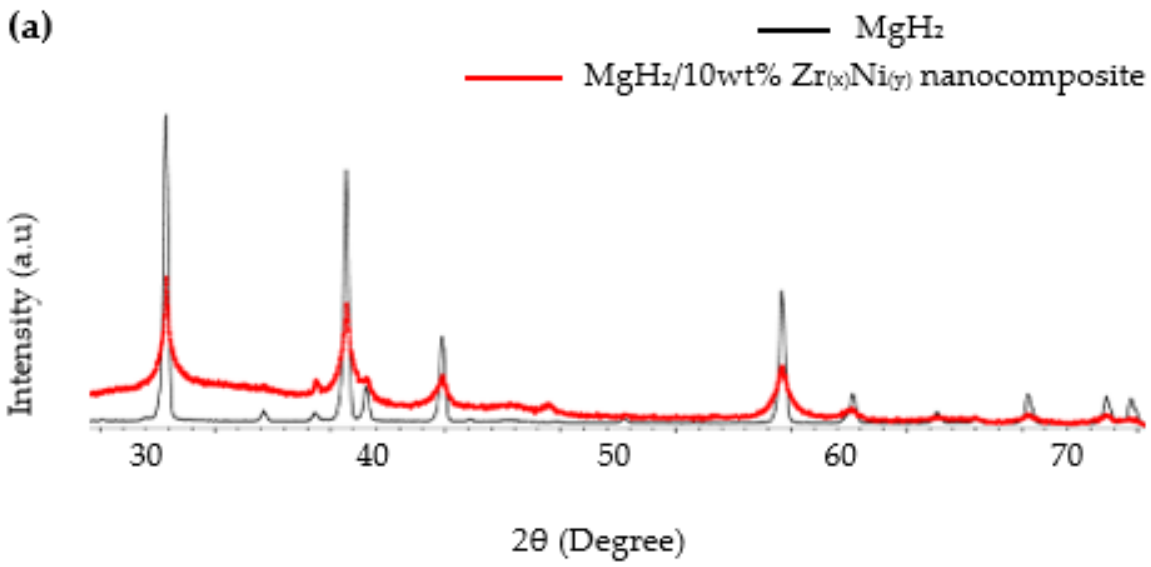

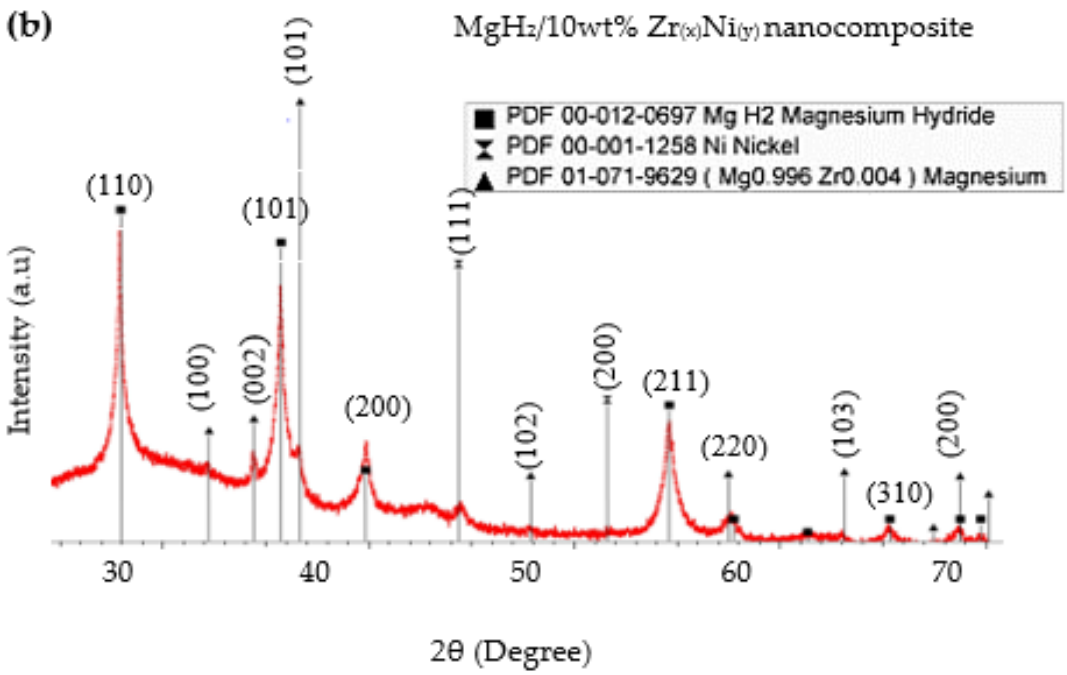

Figure 5. 7. The XRD patterns of (a) 10 wt.% ZrO_2/Ni nanocomposite in red and the un-milled MgH_2 used as reference in black and (b) MgH_2/10 wt.% ZrO_2/Ni nanocomposite to identify the crystal phase of each element.

The SEM determined the catalyst's distribution on the Mg's surface. Moreover, it was used to identify the size of the particles. There is a homogenous distribution of the catalyst particles, Zr and Ni, which can be distinguished from the SEM image, as seen in Figure 5. 8a. The SEM image of the milled MgH_2 powder used as a reference is shown in Figure 5. 8b. The SEM image of the nanocomposite MgH_2/10 wt.% ZrO_2/Ni (Figure 5. 8c) shows the distribution of the catalyst on the surface and edge of the MgH_2 matrix. The Zr particles are the white spots, with an average particle size of 10 nm in diameter, as shown in Figure 5. 8a. The obtained results correlate with the study reported by El-Eskandarany *et al*. [91], where the milled Zr_2Ni alloy powder agglomerated to form particle sizes of approximately 8 nm in diameter.

The average particle size of a Ni is 100 nm in diameter, as shown in Figure 5.9b. The wide range of MgH_2 particle size distribution of the composite MgH_2/10 wt.% ZrO_2/Ni is below 1000 nm, as shown in Figure 5.9c. Pighin *et al*. [83] reported a study of an MgH_2/10 wt.% Zr_8Ni_{21} alloy. They established that the white spots were the result of

the elastic collisions of the backscattered electrons with the heavy nuclei of zirconium, considering smaller particle sizes under 1000 nm, whereas the grey region, as shown in Figure 5. 8c, was reported to occur due to the light nuclei of MgH_2. [83]

Figure 5.8d shows the zoomed image of the MgH_2/10 wt.% ZrO_2/Ni nanocomposite, representing the catalyst aggregation on the surface MgH_2 matrix. The effect of powder aggregation was reported in a previous study as the result of the high concentration of Mg deposited at or near the edges of the catalyst. [120] Figure 5.8e represents the smooth surface of the matrix corresponding to MgO that formed while handling the powder outside the glove box.

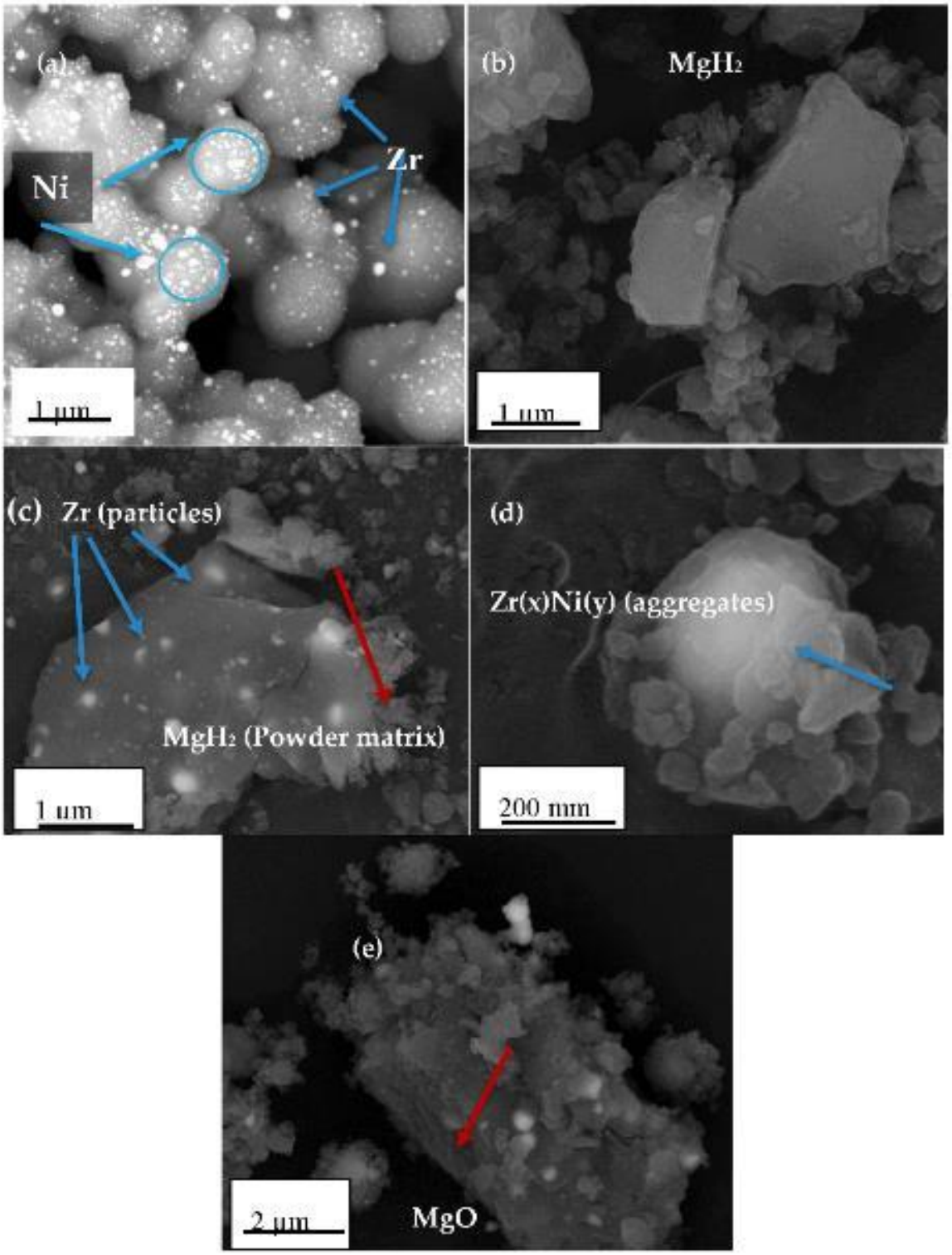

Figure 5. 8. SEM micrograph of (a) ZrO_2/Ni-based nano-catalyst after 5 hours heat treatment under hydrogen; (b) MgH_2 after 5 hours milling time under Ar, here used for reference; (c–e) MgH_2/10 wt.% ZrO_2/Ni nanocomposite. The homogeneous distributions of the ZrO_2/Ni on the MgH_2 surface are shown in (c). The enlarged image of the MgH_2/10 wt.% ZrO_2/Ni showing the aggregation of ZrO_2/Ni is represented in (d), and the presence of MgO is represented in (e).

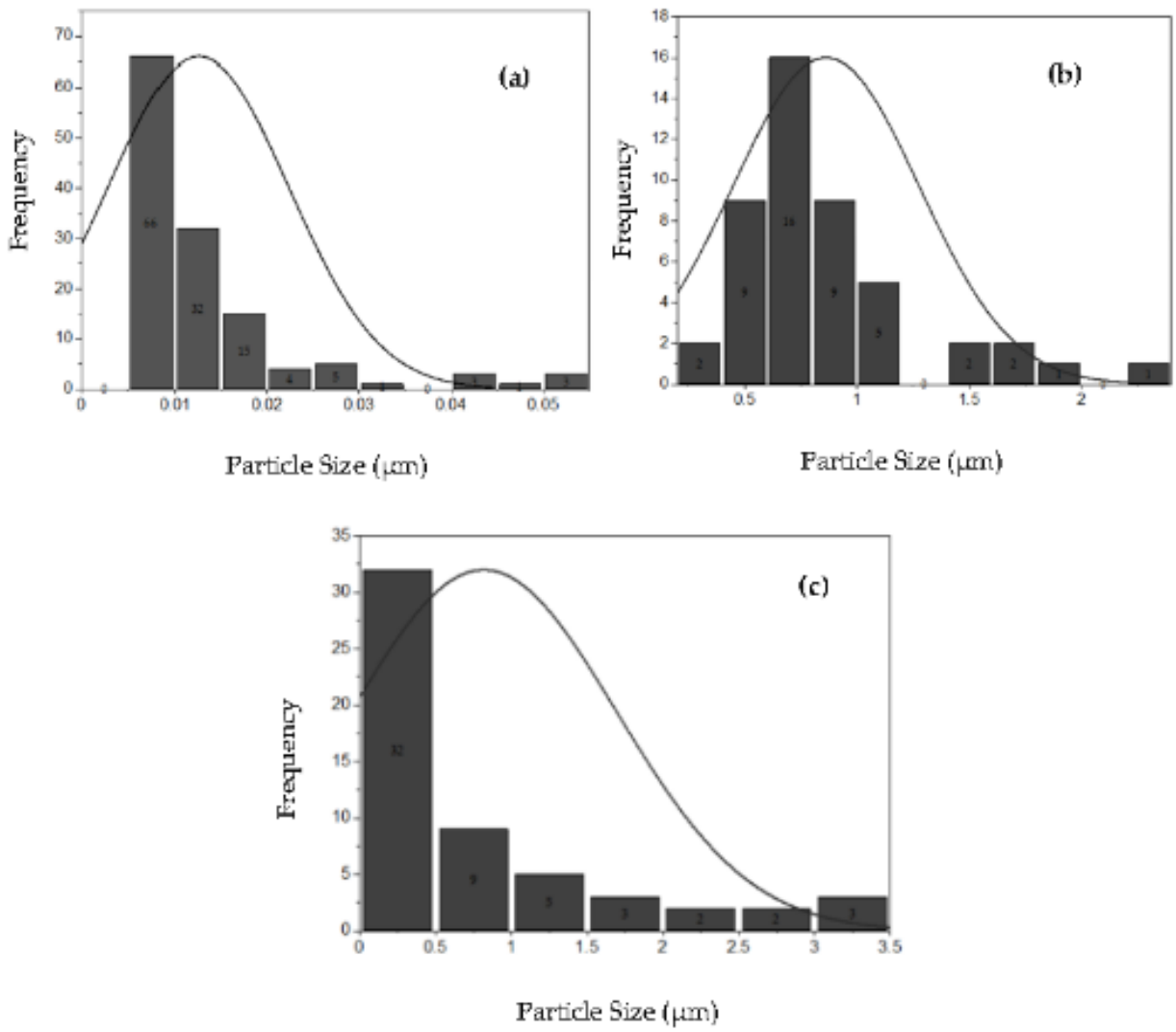

Figure 5. 9. Histograms of particle size distribution measured by the SEM/ImageJ analysis. (a) Zr; (b) Ni size distribution within the catalyst sample; (c) milled MgH_2 for 5 hours.

The EDX was used to confirm the presence of the analysed elements and impurities. Figure 5. 10a shows the activated ZrO_2/Ni-based nanocatalyst. The presence of impurities such as chlorine (Cl) came from the starting precursor material $ZrCl_4$ powder. Figure 5. 10b shows the presence of Mg in the milled MgH_2. Figure 5.10c shows the presence of Mg, Zr and Ni particles in the MgH_2/10 wt.% ZrO_2/Ni nanocomposite. The additional peaks are gold (Au) from the coating during the sample preparation of the SEM analysis; carbon (C) from the carbon tape; oxygen

(O) from preparing the sample outside the gloves box, and iron (Fe) from the reactor during the milling process.

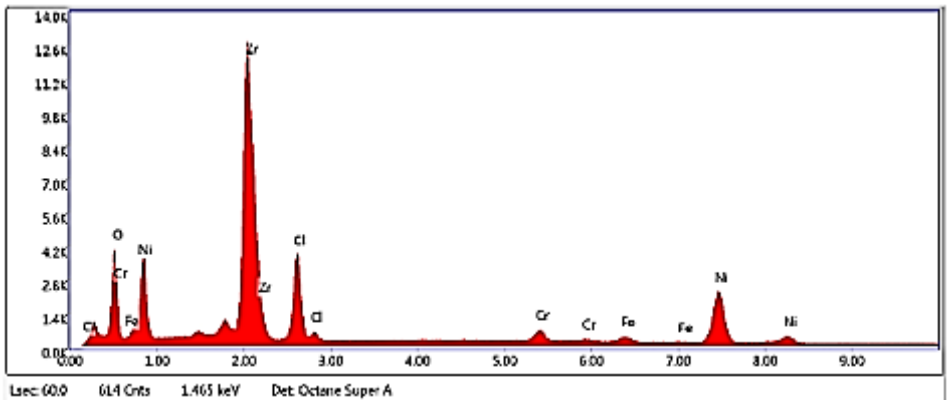

(**a**)

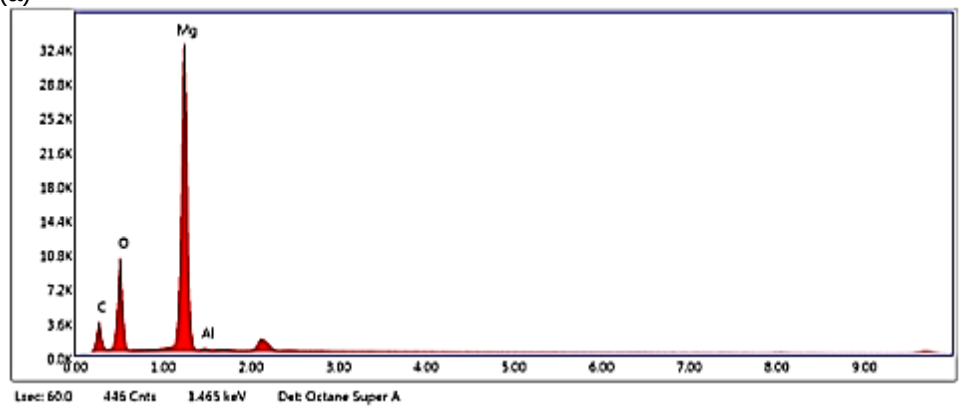

(**b**)

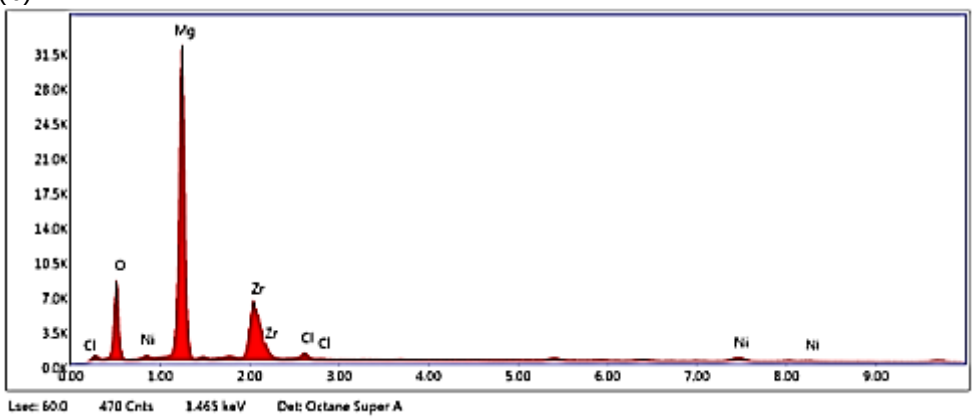

(**c**)

Figure 5. 10. The energy dispersive X-ray spectroscopy (EDX) of (a) ZrO_2/Ni nanocatalyst; (b) milled-MgH_2 as a reference; (c) MgH_2/10 wt.% ZrO_2/Ni nanocomposite.

The TEM analysis was performed to determine the surface morphologies of the composite MgH_2/10 wt.% ZrO_2/Ni on a nanometre scale and to understand the catalytic effect of ZrO_2/Ni on the dehydrogenation properties of MgH_2 powder. The TEM image of the composite can be seen in Figure 5. 11a, where the atomic array with a long-range ordered crystal structure is represented in the three zones. Zone I corresponds to the d-spacing of 1.63 nm in Figure 5.11b and correlates with the ($Mg_{0.996}Zr_{0.004}$) (110) phase. Zone II corresponds to the d-spacing of 2.58 nm, as shown in Figure 5. 11c, which correlates with the ($Mg_{0.996}Zr_{0.004}$) (002) phase. Zone III is confirmed by the d-spacing of 2.52 nm, as shown in Figure 5. 11d, which correlates with the nanocrystalline β-MgH_2 grain and is well-matched with the tetragonal-MgH_2 (101) phase.

In Figure 5. 12, the darker particles show the agglomeration of the metallic powder ZrO_2/Ni-based nanocatalyst on the surface of the MgH_2 matrix after milling with the catalyst. Ni particles are the dark grey elements covering the surface of the Mg matrix, and the small, darkest spots are the Zr particles. The agglomeration of the ZrO_2/Ni was also observed in a previous study, where a heterogeneous distribution catalyst on the surface of the MgH_2 powder was reported. [91]

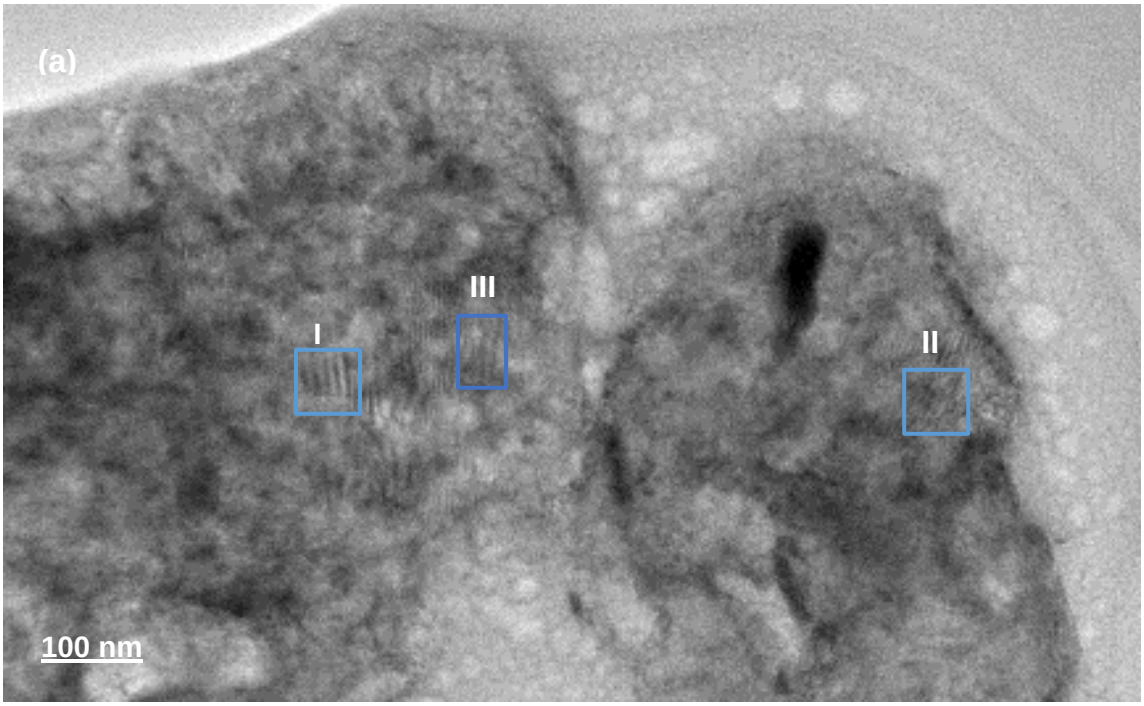

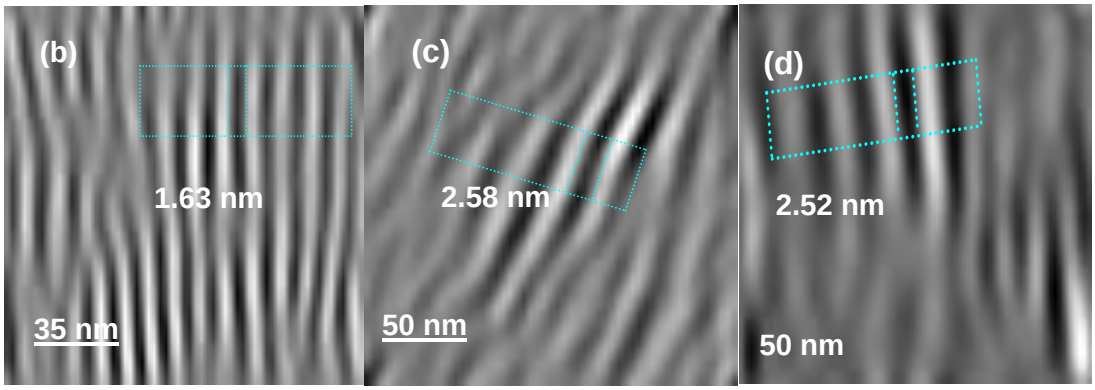

Figure 5. 11. Field emission high-resolution transmission electron microscopy (FE-HRTEM) of (a) MgH_2/10 wt.% ZrO_2/Ni nanocomposite; (b) the lattice image of zone I; (c) the lattice image of zone II; (d) the lattice image of zone III.

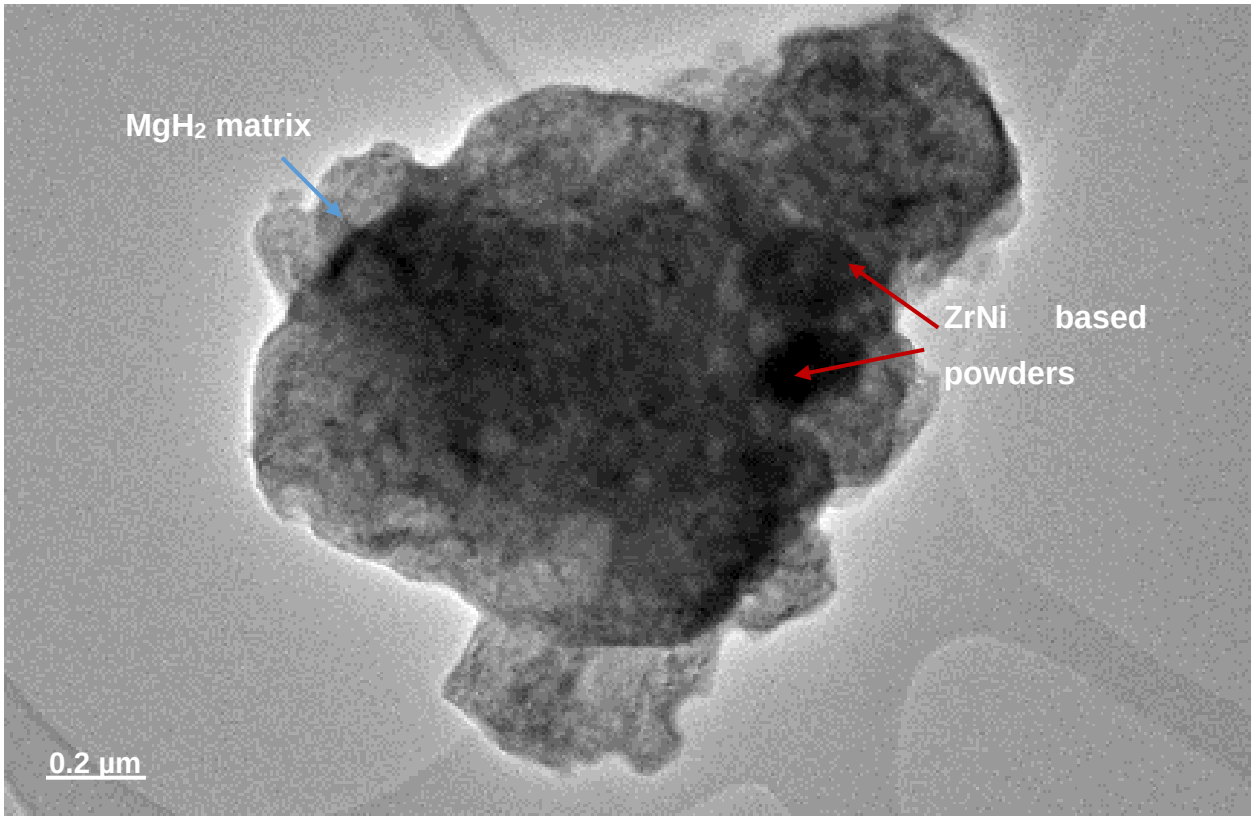

Figure 5. 12. TEM of the bright field image of MgH_2 powders milled with 10 wt.% ZrO_2/Ni, demonstrating the agglomeration of catalyst on the surface of the MgH_2 matrix after 5 hours milling time.

5.4. Discussion

In the aim to improve the kinetic and thermodynamic properties of the Mg/MgH_2 hydrogen storage system, ZrO_2/Ni catalyst was synthesised via a modified sol-gel method in a compact high-pressure hydrogen reactor and activated before being used as an additive to MgH_2. The TPD results confirmed that adding ZrO_2/Ni to MgH_2 induced an essential shift towards the lower hydrogen desorption temperature. This positive impact may be due to several factors.

First, the catalyst activation before the milling process with the MgH_2 metamorphosed the alloys into fine powders; as a result, this generated a more homogeneous catalyst distribution. [41] The SEM image analysis confirmed the grain size reduction of the current catalyst. The present study's reported size of the Zr particles agreed with several literature reports. [91] It was up to ten times smaller than Pighin *et al*.'s report [83] Although the SEM and TEM analyses confirmed that the catalyst is heterogeneously distributed, it aggregates with a high concentration at the surface and near the edges of the MgH_2 power. The TEM micrograph in Figure 5. 12a shows that the catalyst covered the surface of the MgH2 during the milling process. The efficiency of the ball milling procedure in dispersing the ZrO_2/Ni nanocatalyst on the MgH_2 was also reported by M. S. El-Eskandarany *et al*. [120] Additionally, because of the ductility differences between ZrO_2/Ni and MgH_2 particles, the efficiency of the MgH_2 ball milling preparation increases in the presence of the catalyst. [33], [121]

The combinative impact of MgH_2 crystal size reduction and ZrO_2/Ni nanocatalyst dispersion at the surface of MgH_2 particles dramatically enhances the dehydrogenation properties compared with pure-milled MgH2, as shown in

Figure 5. 5, and the results from the literature using different ZrO_2/Ni catalysts are listed in Table 5.1. This is likely due to the presence of ZrO_2 in the starting ZrO_2/Ni catalyst, as confirmed in the XRD analyses of Figure 5. 3. Indeed, ZrO_2 has been recognised as a transition metal oxide catalyst with the advantage of reducing the activation energy and the crystalline size during the ball milling process. [33], [40]

In addition, I.Yu. Zavaliy *et al*. [122] compared the hydrogenation of Zr_3V_3Ox to the $ZrV_2H_{4.9}$ catalysts and reported that the zirconium-based oxygen catalyst increased the hydrogen storage capacity. However, the presence of ZrO_2 in the

MgH_2+10wt.%ZrO_2/Ni composite does not explain the differences in results from the literature.

The XRD results presented in

Figure 5. 7 show the presence of a new $Mg_{0.996}Zr_{0.004}$ phase formed during the milling process; this phase may impact the thermodynamic properties of the Mg/MgH_2 system. In a previous study by Galey *et al*. [30], the presence of a $Mg_{0.992}Ni_{0.008}$ phase in an Mg/MgH_2 system doped with a Ni complex reduced the overall hydrogenation and dehydrogenation enthalpies of the formed composite from ±75 to ±65 kJ/mol H_2. The presence of the new phase is particularly remarkable as the destabilisation of MgH_2 is the main obstacle to overcome and allow the use of the Mg/MgH_2 system at moderate temperatures. Despite the critical number of studies devoted to the activation of MgH_2, very few researchers have successfully modified its thermodynamic properties.

Table .5. 2. Dehydrogenation properties of various ball milled MgH_2 nanocomposites in comparison to the results obtained in the *present study*.

Elements	Peak Desorption Temperature °C	H_2.wt.%	References
10 wt.% ZrO_2/Ni	232	5.9	*Present study*
10 wt.% $Zr_{0.67}Ni_{0.33}$	325	5.0	Dong *et al*. [40]
10 wt.% Zr_8Ni_{21}	300	5.9	Pighin *et al*. [83]
10 wt.% $ZrNi_5$	275	5.3	El-Eskandarany *et al*. [120]
10 wt.% Zr_9Ni_{11}	250	5.9	Dehouche *et al*. [41]

Although not studied here, the ZrO_2/Ni alloy is likewise expected to have a positive effect on the hydrogenation properties of the Mg/MgH_2 system. Undoubtedly, the presence of the nano-catalyst sites well dispersed on the Mg particles may allow for the splitting of the hydrogen molecules into hydrogen atoms and their adsorption, followed by the subsequent migration of hydrogen atoms onto the adjacent Mg surface via spillover and further surface diffusion. [91]

5.5. Conclusions

In summary, a novel approach was proposed for fabricating the catalyst ZrO_2/Ni by a high-pressure reactor, followed by a catalyst calcinated prior to being mechanically milled Via the planetary ball mills with MgH_2 powder to form the composite MgH_2/10wt%ZrO_2/Ni The approach demonstrates that mixing such nanocatalysts with MgH_2 via the ball milling process offers better perspectives. To fully characterise the catalyst after synthesis and activation, XRD, SEM-EDX and FE-HRTEM analytical methods were used.The developed method is a faster and more promising approach for the fabrication of catalysts. It is beneficial in terms of producing nanoparticle materials for improving the hydrogenation and dehydrogenation processes in future work.

The TPD results confirmed that adding ZrO_2/Ni to MgH_2 induced an essential shift towards the lower hydrogen desorption temperature. The nanocomposite MgH_2/10 wt.% ZrO_2/Ni resulted in a wide range of MgH_2 particle size distribution below 1000 nm. A faster hydrogen release of 5.9 wt.% at onset temperature 210 °C/peak temperature 232 °C was recorded, which is a novel achievement in the present study when compared to updated studies of solid-state hydrogen storage of MgH_2 with $Zr_{(x)}Ni_{(y)}$ based catalyst. However, a slightly lower hydrogen release is expected, due to the high amount of additive used (10 wt.% of ZrO_2/Ni), which reduced the system's overall storage capacity.

Therefore, there is work to be done to ameliorate the fabrication of the catalyst, such as conducting several experiments to find out if the presence of impurities such as chlorine has a positive or negative impact on improving the kinetic and thermodynamic properties of hydrogen storage.

Reader Guide

Chapter I: General Introduction

Chapter II: Literature

Chapter III: Methodology

Chapter IV: Establishing an Innovative Method for the Synthesis of ZrO_2/Ni Nanocatalyst for Improving the Sorption Property of MgH_2 in the Field of Solid-State Hydrogen Storage

20 hours milling time/ SPEX high energy ball mill MgH_2+10wt.%ZrO_2/Ni

Introduction Recap

Experimental

- Catalyst-ZrO_2/Ni synthesis
- Composite (MgH_2+10wt.%ZrO_2/Ni) ball mill: 5 hours via Planetary
- Characterisation

Results/ Discussion

- XRD
- SEM
- TPD
- Kinetics

Conclusion

References

Chapter V: Development of a Novel Method for the Fabrication of Nanostructured ZrO_2/Ni Catalyst to Enhance the Desorption Properties of MgH_2

5 hours milling time/ Planetary ball mill - MgH_2+10wt.%ZrO_2/Ni

Introduction Recap

Experimental

- Catalyst-ZrO_2/Ni synthesis
- Composite (MgH_2+10wt.%ZrO_2/Ni) ball mill: 20 hours via SPEX
- Characterisation

Results

- XRD
- SEM
- TPD

Discussion

Conclusion

References

Chapter VI: Comparing the Novel Catalysts ZrO_2/Ni and ZrO_2/$NiCl_2$ Storage Behaviour of Hydrogen Sorption Properties of MgH_2 Powder

5 hours milling time/ Planetary ball mill (ZrO_2/$NiCl_2$) catalyst

Introduction Recap

Experimental

- Catalyst-ZrO_2/Ni synthesis
- Composite (MgH_2+10wt.%ZrO_2/$NiCl_2$) ball mill: 5 hours via Planetary
- Characterisation

Results / Discussion

- XRD
- SEM
- Kinetics
- PCT

Conclusion

References

Chapter VII: General conclusion

References

Appendices

CHAPTER VI: COMPARING THE NOVEL CATALYSTS ZrO_2/Ni AND $ZrO_2/NiCl_2$ STORAGE BEHAVIOUR OF HYDROGEN SORPTION PROPERTIES OF MgH_2 POWDER

Method 3: *MgH_2+10wt.% ZrO_2/Ni and MgH_2+ 10wt.%$ZrO_2/NiCl_2$ - 5 hours milling time through Planetary ball mills*

From the results obtained in Chapter V, it is well established that the Planetary ball mills offer a practical approach for producing nanoparticle powders with minimum impurities. The present chapter focuses on the impact of oxide catalysts and nickel-chloride presence on the hydrogenation and dehydrogenation behaviour of Mg/MgH_2. In the current chapter, two heat treatment approaches are used to compare the effects of catalysts ZrO_2/Ni and $ZrO_2/NiCl_2$ storage behaviour on the hydrogen sorption properties of MgH_2 powder.

6.1. Introduction

Doping Mg with a nano-catalyst is one of the main approaches to improve the hydrogenation and dehydrogenation reaction of Mg/MgH_2. The catalyst acts as a gateway through which hydrogen can be released inside the Mg matrix. Refer to Figure 6. 1.

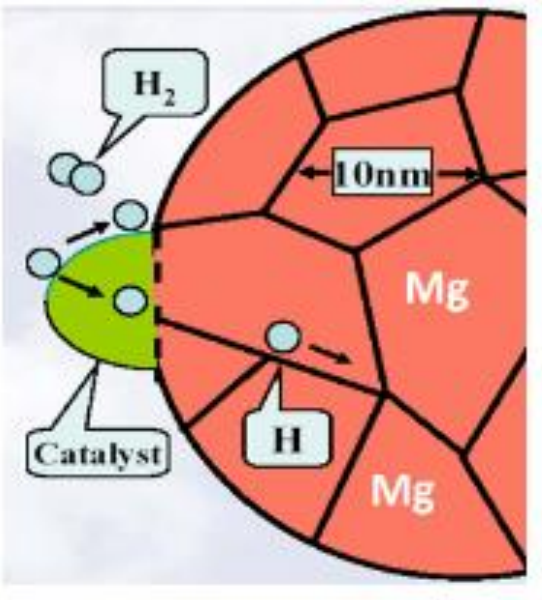

Figure 6. 1: Image illustrates the role of the catalyst at the surface of the Mg, acting as a gateway for the hydrogen.

Ni based catalyst has a high affinity toward hydrogen. Therefore, a Ni-based catalyst offers the potential to destabilise the Mg-H bond and facilitates the dissociation of hydrogen molecules in the Mg matrix. [71], [123] Zirconium oxide also comes with numerous advantages to improve metal hydride powder's absorption and desorption kinetics behaviour. Doping ZrO_2 with Mg/MgH_2 before milling help refines the grain size of Mg/MgH_2 particles and can allow the absorption/desorption of hydrogen at a lower temperature. [124] As stated in the introduction chapter I, a small group in the literature acknowledged that adding metal chloride in a Ni catalyst could benefit the hydrogen storage properties of the Mg/MgH_2. Recently Basil *et al*. [30], [31] have reported a study where the author compared the effect on the thermal stability of 20wt.% nickel hydride $[NiCl_2(P(C_6H_{11})_3)_2]$, and $NiHCl(P(C_6H_{11})_3)_2$ addition to MgH_2 consecutively. The presence of two chlorine atoms ($NiCl_2$) negatively impacted the decomposition kinetics of MgH_2, though the NiHCl improved the desorption rate by a peak temperature of 5.4wt.% of H_2 at 285°C. [30], [31]

From the results obtained in chapters IV and V, *the present study* proposes different approaches for the catalyst heat treatment to better understand if the presence of

chlorine in the catalyst has an advantage or disadvantage in term of hydrogenation/dehydrogenation behaviour of Mg/MgH_2.

6.2. Material and Method

Although reported in the previous study, detail of the experimental procedure in section 6.2.1.1 and section 6.2.1.3 is also reported in the present chapter to understand the work better. Refer to chapter IV for further details of the reagents used in *the present study.*

6.2.1. Synthesis of ZrO_2/Ni and $ZrO_2/NiCl_2$ nano-catalyst: High Pressure Reactor and Heat Treatment

The First step of the catalyst's synthesis and composite formation follows the same procedure as in previous chapter V, sections 5.2.1 and 5.2.2. In the present chapter, a brief description of the experiment is detailed.

6.2.1.1. Synthesis of ZrO_2/Ni nano-catalyst

Step 1: The catalyst (ZrO_2/Ni) was prepared in the high-pressure PARR 5500 Series Compact Reactor from a mixture of the starting material of $ZrCl_4$ fine white powder with a 99.5+ metal basis and $Ni(NO_3)_2.6H_2O$ (98% green salt) provided by Alpha-Aesar and Sigma-Aldridge, respectively. The mixture was heated for 2 hours at 200 °C under hydrogen, at a starting pressure of 20 bar, whilst stirring at 60 resolutions per minute. Refer to chapter V. for more details on the catalyst synthesis.

Step 2: The sample was thoroughly dried when heat-treated at 350 °C for 5 hours and further cooled for 2 hours under hydrogen flow at 0.6 bar. The prepared catalyst was transferred to the glove box and purged with Ar.

6.2.1.2. $ZrO_2/NiCl_2$ nano-catalyst

Step 1: The $ZrO_2/NiCl_2$ catalyst was prepared from the mixture of the starting material of $ZrCl_4$ fine white powder with a 99.5+ metal basis and $Ni(NO_3)_2.6H_2O$ (98%

green salt). The $ZrO_2/NiCl_2$ synthesis's first step follows the same procedure described in section 6.2.1.1 above.

Step 2: The sample was thoroughly dried when heat-treated at 350 °C for 5 hours and further cooled for 2 hours under 5%Hydrogen/95% Ar at 0.6 bar. The prepared catalyst was transferred to the glove box and purged with Ar.

6.2.2. Preparation of MgH_2-Based Nanocomposite Powders: Bal Milling

The composites MgH_2+10wt.%ZrO_2/Ni and MgH_2+10wt.%$ZrO_2/NiCl_2$ were prepared under an inert Ar atmosphere by the planetary ball mills using a PM100 apparatus from Retsch. 10 wt.% of the ZrO_2/Ni based nanocatalyst was added to MgH_2 in a reactor vessel with ZrO_2 milling balls of 1-mm diameter. The ball-to-powder mass ratio was 100:1. The sample was milled for 5 hours at a milling frequency of 300 revolutions per minute. The same procedure was repeated for preparing the MgH_2+10wt.%$ZrO_2/NiCl_2$ composite. Refer to the previous chapter V sections 5.2.1 and 5.2.2. for more details.

6.2.3. Sample Characterisation: XRD, SEM, and PCT

The structural characterisation of the synthesised catalyst and composites samples was carried out with a Bruker D8 Advance X-Ray Powder Diffractometer (XRPD) with the CuKα (λ = 0.154 nm) radiation over the 2θ ranging from 20° to 80°. The instrument was calibrated with the LaB6 NIST standard (660a). The diffraction patterns were analysed using the Topas software to determine the phase composition and crystallite mean size.

A field emission scanning electron microscope characterised the surface morphology of the prepared samples (FESEM) SUPRA 35VP, Zeiss, from Germany. Energy dispersive X-ray spectroscopy (EDS) was used for elemental analysis of the deposited layers.

For the SEM analysis, the powders were dispersed evenly on carbon tape. The sample was coated with a thin layer of gold and added through vacuum evaporation to prevent the sample from developing high conductivity and some charging effects during the analysis. The particle size of the sample was determined from the obtained SEM

image using the Image J software. The element in the samples was determined from the Energy-dispersive X-ray (EDX) analyses in parallel with SEM images.

The TEM model JE M-2100F microscope was used for the structural features. The powder was suspended in EtOH and drop-cast onto holey carbon support film, Cu 200 mesh. The surface morphologies of the analysed powders were determined via the field emission scanning electron microscope (FESEM) (SUPRA 35VP, Zeiss, Germany). The images were collected using Gatan software. Refer to Chapter III for more details on the characterisation instruments used in *the present study*.

6.2.4. Kinetic and Thermodynamic Analysis

The kinetic absorption rates and PCT measurement were determined via the Manometric Gas Sorption Analyzer.

The sample preparation was carried out inside the glove box under a protective Ar atmosphere to prevent powder oxidation. The sample was weighed inside the reactor, and four layers of quartz cotton were inserted and pushed gently. The sample's final weight and quartz were recorded before sealing the sample reactor. The sealed reactor was inserted into the instrument, as shown in Figure 6. 2(c), and the gasket was replaced to allow a firm seal of the device. Refer to Figure 6. 2(a) for the image of the sample reactor and cover.

At the start of the experiment, the sample was outgazed for 1 hour to remove unwanted particles and avoid the oxidation of Mg. The instrument was calibrated before use with palladium.

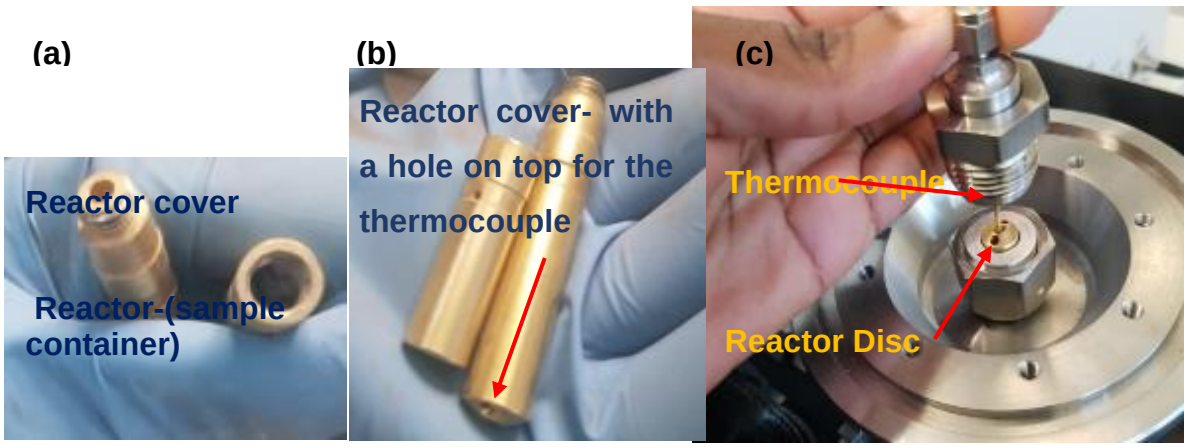

Figure 6. 2: Reactor part of the Manometer gas sorption analyser. (a) reactor and cover, (b) showing the hole to insert the thermocouple, (c) PCT instrument port, thermocouple and disc.

The hydrogen absorption was determined at different temperatures ranging from 200°C to 300°C at 8 and 10 bar to study the Kinetic and thermodynamics of the storage system. Whilst the PCT plots were selected in a pressure range starting from 0.25 bar to approximately 8 bar. Refer to experiment conditions listed below.

- Complex condition: Absorption at 300°C under 8 bar of H_2
- Complex condition: Absorption at 270°C under 8 bar of H_2
- Intermediate condition: Absorption at 250°C under 8 bar of H_2
- Moderate condition: Absorption at 230°C under 8 bar of H_2
- Moderate condition: Absorption at 200°C under 10 bar of H_2

The results of the PCT plots were used to calculate the thermodynamics - enthalpy and entropy of hydrogen absorption. The thermodynamics was determined with the Clausius Clapeyron interpolation software.

The kinetics plot of the composite was measured at a constant temperature three times in order to determine the certainty of the measurement; refer to Figure C. 6

6.3. Results and Discussion

The prepared catalysts were used as additive in the Mg/MgH_2 system. The commercial MgH_2 was thus milled with 10 wt.% of ZrO_2/Ni and 10wt.% $ZrO_2/NiCl_2$ for 5 hours, respectively.

6.3.1. Characterisation of ZrO_2/Ni, and $ZrO_2/NiCl_2$ Nano-catalyst

XRD was carried out to identify and quantify the crystalline phases present in the prepared catalysts. Figure 6. 3(b) represents the analysed ZrO_2/Ni nano-catalyst, where the ZrO_2 resulted a broad peak at 30.3°, 35.2°, 50.6°, 60.3°, 63.2°, and 74.7°, (PDF file # 01-071-4810), and Ni sharp Braggs peaks at 44.5°, 51.8°, and 76,4° (PDF file # 03-065-2865). The average crystallite size of the Ni and ZrO_2 was calculated with the Origin software, using Scherrer's equation – the crystallite size of ZrO_2 and Ni were approximately 5 nm and 23 nm respectively. The ZrO_2 and Ni peaks were also detected in the $ZrO_2/NiCl_2$ catalyst, as shown in Figure 6. 3 (a). Additional bragg peaks of nickel chloride were observed at 15.3°, 30.8º, 36.2º, 47.4º, 51.8º, 52.6º, 55.1º, 61.8º, 64.1º, 66.7º the (PDF file # 000-002-0765).

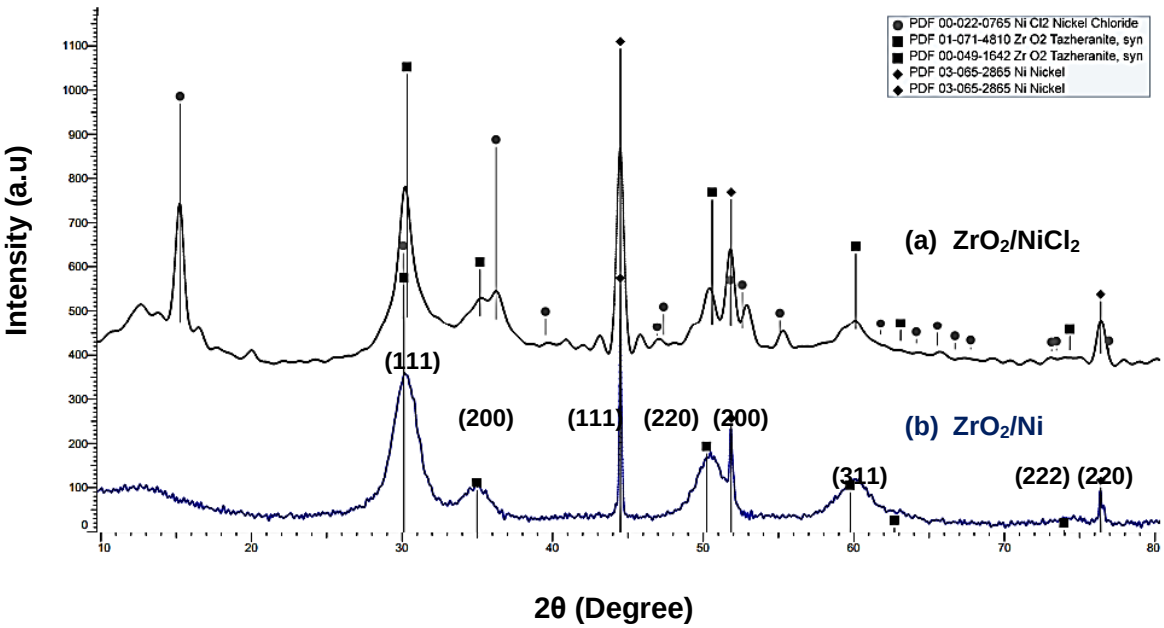

Figure 6. 3: The XRD patterns of (a) ZrO_2/Ni and (d) $ZrO_2/NiCl_2$ based nano-catalyst

6.3.2. Surface Morphologies of Synthesised Catalysts via the FE-HRTEM

The surface morphologies of the catalysts were determined via the FE-HRTEM. Figure 6. 4. correspond to the TEM image of ZrO_2/Ni. The powder consists of nanocrystal structures corresponding to Ni and ZrO_2 metallic powder, represented as zones I, II, III and IV, refer to Figure 6. 4.a. The d spacing was determined in nm, and the XRD phases confirmed the identities of each characterised element. Zone I, II and III correspond to the d spacing of 0.26 nm (200) phase, zone IV corresponds to the d spacing of 0.18 nm with a crystal phase at (220) corresponding to the Zr_2O particle, as shown in Figure 6. 4, b, c, d and e respectively. Though Zone III is determined as the Ni crystal 0.18nm (200) phase as shown in Figure 6. 4.e.

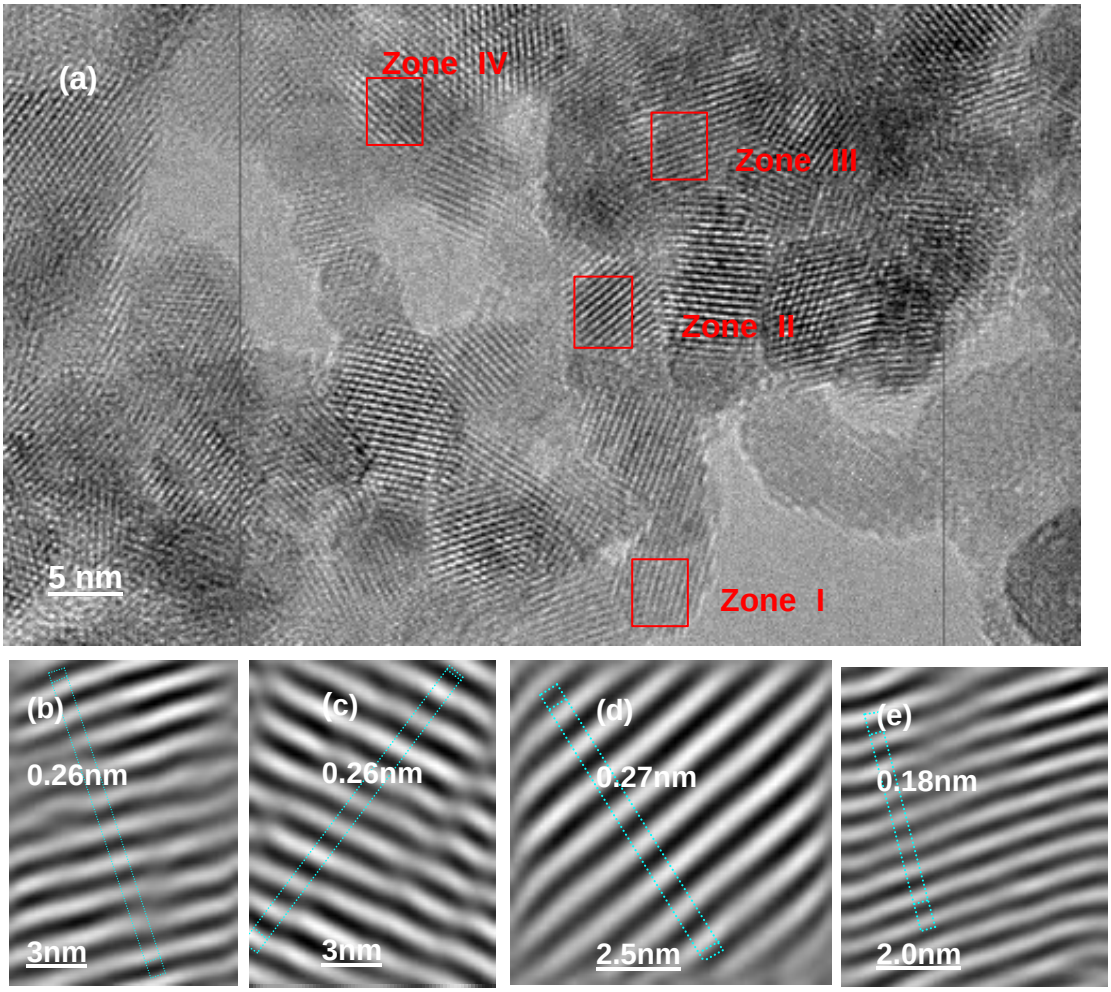

Figure 6. 4: Field emission high-resolution transmission electron microscopy (FE-HRTEM) of (**a**) ZrO_2/Ni catalyst; (**b**) the lattice image of zone I; (**c**) the lattice image of zone II; (**d**) the lattice image of zone III, the lattice image of zone IV

6.3.3. Characterisation of MgH_2+ 10wt.% ZrO_2/Ni and MgH_2+10wt.% ZrO_2/$NiCl_2$ Nanocomposites

The kinetic and PCT plots of the MgH_2+10wt.% ZrO_2/Ni and MgH_2+10wt.% ZrO_2/$NiCl_2$ Nanocomposites were obtained by the Manometric Gas Sorption Analyser.

6.3.3.1. Hydrogenation study – Kinetics

Figure 6. 5

The hydrogenation kinetics of MgH2+10wt.% ZrO2/Ni and MgH2+10wt.% ZrO2/NiCl2 samples are shown in Figure 6.5 (a) and 6.5 (b), respectively, and some hydrogenation kinetics data are summarised in Table 6.1. Doping MgH2 with ZrO2/Ni has resulted in a significant improvement in the hydrogenation kinetics. It is noticeable from the PCT curve of MgH2+10wt.% ZrO2/Ni. The sample absorbed 5.6 wt.%, 5.9 wt.%, 5.9 wt.%, 3.8wt.% and 0.9 wt.% at 300°C, 270ºC, 250ºC, 230°C and 200ºC consecutively after 1 minute. (Figure 6.5 a). The composite shows faster hydrogenation reactivity, especially at 300°C, the highest measured temperature, where the hydrogen absorption reached its maximum capacity of 5.6wt% after 30 seconds.

Figure 6. 5 (b) shows the absorption kinetics isotherms performed at 280ºC, 250ºC, and 235ºC for MgH_2+10wt.% ZrO_2/$NiCl_2$ Nanocomposites. In general, the synthesised nanocomposite powders showed good potential for absorbing hydrogen gas in a wide temperature range (230ºC – 300ºC).

Figure 6. 5. (a), after 1 minute, the nanocomposite powder absorbed 5.6 wt.%, 5.9 wt.%, 5.9 wt.%, 3.8wt.% and 0.9 wt.% at 300°C, 270ºC, 250ºC, 230°C and 200ºC consecutively. Whereas the composite MgH2+10wt.% ZrO_2/$NiCl_2$ studied at 280ºC, 250ºC, and 235ºC resulted to the hydrogen absorption 5.4 wt.%, 4.0 wt.% and 3.7 wt.%, respectively, as shown in Figure 6.5(b). The increased time of hydrogen gas uptakes results in a significant improvement in hydrogen absorption.

After two minutes, the uptake was recorded as 5.8 wt.%, 4.5 wt.% and 4.0 wt.% at 280ºC, 250ºC, and 235ºC respectively, refer to Figure 6.5(b). Although the nanocomposite MgH_2/10wt.% ZrO_2/$NiCl_2$ showed significant improvement after 2 minutes; increasing the absorption time did not lead to a remarkable increase in

hydrogen absorption compared to MgH_2+10wt.% ZrO_2/Ni. The sample reaches its saturation point after 10 minutes at 6.1 wt.%, 5.3 wt.%, 4.3 wt.% at 280ºC, 250ºC, and 235ºC respectively, refer to Figure 6.5.(b). The hydrogen absorption with MgH_2+10 wt.% of ZrO_2/Ni exceeds of that reported by Tome *et al*. [39]. Refer to Table 6.1.

(a) Kinetic plot of nanocomposite MgH_2/10 wt.% ZrO_2/Ni

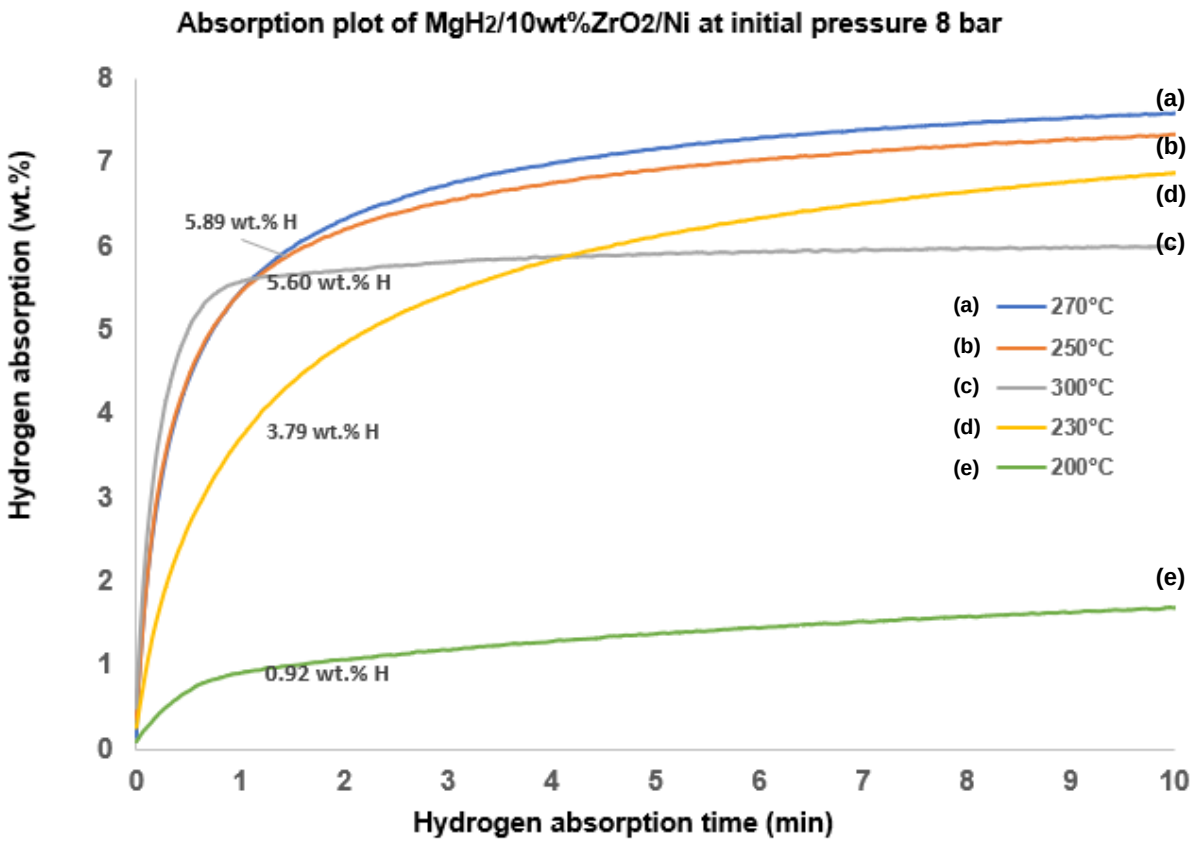

(b) Kinetic plot of nanocomposite MgH_2/10 wt.% Ni/Cl_2ZrO_2

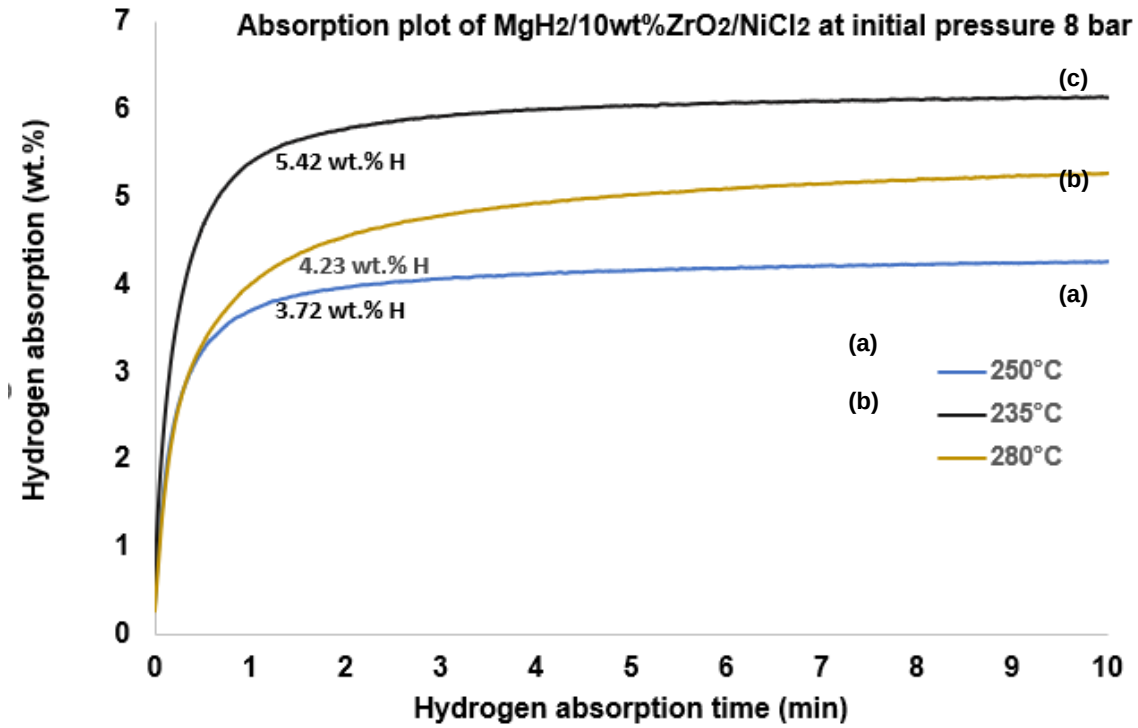

Figure 6. 5: (a) Absorption kinetics plots of MgH_2/10 wt.% ZrO_2/Ni at 300ºC, 270ºC, 250ºC and 200°C. (b) Absorption kinetics plots of MgH_2/10 wt.% ZrO_2lNiCl_2 at 280ºC, 250ºC and 235ºC.

Referring to Table 6.1. it is worth noting that the catalyst ZrO_2/Ni offers promising outcomes for the hydrogenation and dehydrogenation properties of MgH_2 compared to the ZrO_2/$NiCl_2$. The presence of a high percentage of chlorine negatively impacts the sorption property of Mg/MgH_2. Basil *et al*. also reported the negative impact of chlorine. [30], [31]

Table.6. 1: Absorption kinetics properties of different Mg/MgH_2 composites milled for 5 hours. (Recorded at different temperatures).

Samples	Temp (°C)	Abs rate after 1 min(wt.%H)	Abs cap (wt.%H)	References
	200	0.9	1.9	*Present study*
	230	3.7	7.0	*Present study*

MgH_2/10wt.% ZrO_2/Ni	250	5.4	7.3	*Present study*
	270	5.5	7.6	*Present study*
	300	5.6	6.0	*Present study*
MgH_2/10wt.%ZrO_2/Cl_2	235	3.7	4.3	*Present study*
	250	4.0	5.3	*Present study*
	280	5.4	6.1	*Present study*
MgH_2/$Zr_{0.67}Ni_{0.33}$	250	4.2	4.5	Dong *et al*., [40]
$ZrNi_5$/Nb_2O_5	300	3.0	6.7	El-Eskandarany *et al*, [42]
MgH_2+5 wt.%Ni+5 wt.% ZrO_2	310	5.6	6.8	Tome *et al*, [39]
MgH_2+5 wt.%Ni+5 wt.% ZrO_2	270	3.5	4.5	Tome *et al*, [39]

Abbreviation

Abs- absorption

Abs cap- absorption capacity

Table 6.1. illustrate the comparison of the results obtained in the present study to the literature data. In the study reported by Dong et al. [40], MgH_2/ 10wt.% $Zr_{0.67}Ni_{0.33}$ was mechanically milled for 50 hours. The powder was oxidized, forming ZrO_2. The absorption capacity of the composite MgH_2/ 10wt.% $Zr_{0.67}Ni0._{33}$ was measured as 2.7 wt.% H at 275 °C in 20 minutes and 5.0 wt.% H at 325 °C in 4 minutes.[40]

In the study reported by K.Tome *et al*.[39] on the sorption properties of composites MgH_2/5 wt.%Ni/5 wt.%ZrO_2, the composites were ball milled for 4 hours at a rotational speed of 240 rpm. As a result, a higher absorption capacity was achieved with the MgH_2/5 wt.%Ni/5 wt.%ZrO_2 – hydrogenation capacity of 6.10 wt.% H at 310 °C and at 270 °C, the absorption capacities was 4.49 wt.%H. [39]

Whereas, in the present work, the MgH_2/10wt.% ZrO_2/Ni milled for 5 hours via the planetarium ball milled, resulted in a hydrogen abortion of 7.0 wt.%H, 7.3 wt.%H, 7.6 wt.%H, and 6.0 wt.%H at 230°C, 250°C, 270°C, and 300°C respectively.

6.3.3.2. Hydrogenation study – thermodynamic PCT- Enthalpy

The Pressure–composition isotherms and thermodynamics (PCT) of the analysed nanocomposite were studied at different temperatures (Figure 6.6). Table 6.2.

represents the isothermal absorption properties resulting from the PCT curves as presented in Figure 6.6(a), and Figure 6.6(b). The results show that the intermetallic powder significantly increased the absorption plateau pressure of the Mg/MgH_2. It is reported in the literature that elevating the sorption plateau pressures is crucial to obtain the ideal material that can absorb and desorbs hydrogen at lower temperatures. [41] Similarly, elevated sorption plateau pressures relate to faster hydrogen discharge. Hydrogen absorption PCT isotherms given in Figures 6.6 (a) and 6.6. (b), where the Mg-nanocomposites (MgH_2/10wt.% ZrO_2/Ni) were analysed at 300°C, 270ºC, 250ºC and 230 ºC and the Mg-nanocomposites (MgH_2/10wt.% ZrO_2/$NiCl_2$) at 285ºC, 270ºC, and 250 ºC respectively. The resulting curves were obtained from a range of temperatures and pressures, from 0.07 to 2.2 bar. The information on the characterisation of the PCT data summarised in Table 6.2 shows the maximum hydrogen content of the mild composite MgH_2/10wt.% ZrO_2/Ni at approximately 7.5 wt.5 H. However, a lower absorption plateau pressure of 0.95 bar was resulted. Refer to Figure 6.6 (a). The obtained results show that doping MgH_2 with 10wt.% ZrO_2/Ni may result in a reduction in the hydrogen storage capacity. Refer to Figure 6.6.

(a) PCT plot of nanocomposite MgH_2+10 wt.% ZrO_2/Ni

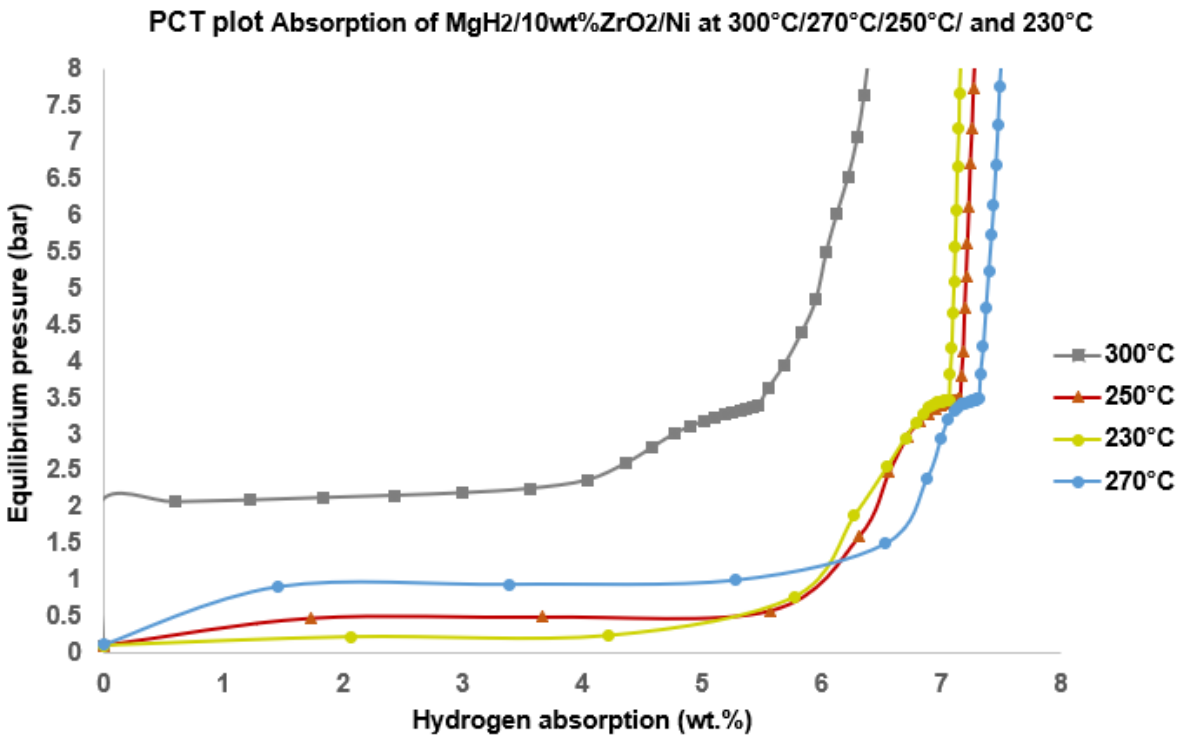

(b) PCT plot of nanocomposite MgH_2/10 wt.% ZrO_2/$NiCl_2$

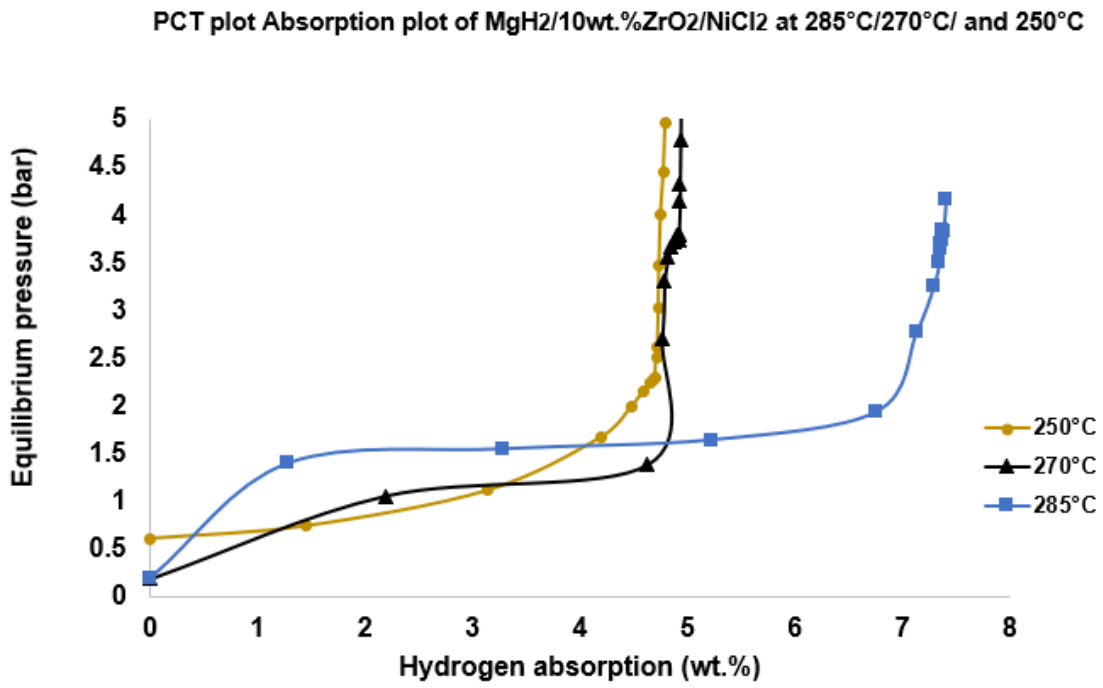

Figure 6. 6: (a) Pressure–composition isotherms of Mg-nanocomposites (MgH_2/10wt.% ZrO_2/Ni) at 300°C, 270ºC, 250ºC and 230 ºC. (b)Pressure–composition isotherms of Mg-nanocomposites (MgH_2/10wt.% ZrO_2/$NiCl_2$) at 285ºC, 270ºC, and 250 ºC.

Table.6. 2: Isothermal sorption properties of ball-milled nanocomposites analysed at different temperatures

Samples	Temperature (◦C)	Absorption plateau pressure (bar)	Maximum H (wt.%)	References
MgH_2/10wt.% ZrO_2/Ni	230	0.25	7.2	*Present study*
	250	0.49	7.3	*Present study*
	270	0.95	7.5	*Present study*
	300	2.2	6.4	*Present study*
MgH_2/10wt.% ZrO_2/$NiCl_2$	235	1.06	4.8	*Present study*
	250	1.06	4.9	*Present study*
	285	1.5	7.4	*Present study*
$MgH_2/Zr_{0.67}Ni_{0.33}$	340	0.6	6.4	[40]
$MgH_2/Zr_{0.67}Ni_{0.33}$	300	0.2	6.2	[40]

Abbreviation

Abs- absorption

Abs cap- absorption capacity

Table 6.2 illustrate the absorption plateau pressure over the hydrogen absorption obtained at different temperature. The plateau pressure of the sample absorbed at different temperatures in the present study is compared to the results reported by Dong *et al*., [40]. The authors reported a hydrogen absorption of $MgH_2/Zr_{0.67}Ni_{0.33}$ at a plateau pressure of 0.2 bar at 5.8wt.% H, and of 0.07 bar at 6.1 wt.% H at a temperature of 300 °C and 250 °C respectively. Whereas in the present study, MgH_2/10wt.% ZrO_2/Ni resulted in hydrogen absorption at a plateau pressure of 2.2 bar at 6.4 wt.%H and 0.49 bar at 7.3 wt.%H at 300 °C and 250 °C consecutively.

6.3.3.3. Thermodynamic plot – Enthalpy (ΔH) / Entropy (ΔS)

The hydrogenation of ΔH and ΔS of nanocomposites MgH_2/10 wt.% of ZrO_2/Ni and MgH_2/10wt.% $ZrO_2/NiCl_2$ was obtained from the PCT curve to predict the plateau pressure level, which is related to the temperature by van't Hoff's law. Refer to Equation 6.1. [69]

$$ln\left(\frac{P_{eq}}{P_o}\right) = \frac{\Delta H}{RT} - \frac{\Delta S}{R} \qquad Eq.6.1$$

Where *ΔH* is the slope of the graph of the hydrogen gas pressure (ln [Pressure/bar]) over the general operating temperature (1000/T (K^{-1}). The *ΔS* is the Y-intercept, representing the entropy of hydrogen gas lost during the hydrogenation process, R is the ideal gas constant = 8.3145 J/K/mol, P_{eq} is the equilibrium pressure (bar) and P_o is the atmospheric pressure (bar).

The thermodynamics of the sample was determined by recording at least two isotherms for the composites MgH_2/10 wt.% of ZrO_2/Ni at 300°C, 270°C, 250°C and 230°C and 285°C, 270°C and 250°C temperatures respectively. The temperatures of the set of isotherms were closely spaced to minimise the calculation error of the analysis. The enthalpy of adsorption was determined from the generated Clausius-Clapeyron plot. This plot determined the relations of the absolute gas pressure and thermodynamic reference pressure over the reciprocal temperature from which the

differential enthalpy is identified. Refer to Equation 6.2. for the Clausius-Clapeyron. [107]

$$\Delta H^{\theta} = R\,[\frac{\delta ln\hat{a}}{\partial\left(\frac{1}{T}\right)}]_n \qquad Eq.6.2$$

Where ΔH^{θ} is the isosteric enthalpy of adsorption, *R* is the gas constant, *T* is the temperature in K, *n* is the number of moles of substance adsorbed by unit mass of adsorbate, $\hat{a}$ is the ratio of absolute gas pressure and thermodynamic reference pressure – *P'= 10*^{5} *Pa or 101325 Pa*, for an ideal gas. Refer to Equation 6.3.

$$\hat{a} = \frac{P}{P^{\theta}} \qquad Eq.6.3.$$

Figure 6.7 illustrates van't Hoff's law, applied at the MgH_2. Figure 6.7. (a) present the PCT curve to predict the plateau pressure level, where the composite MgH_2/10 wt.% of ZrO_2/Ni heated at different temperatures 300°C, 270°C, 250°C and 230°C. Figure 6.7 (b) corresponds to the same composite heated at 285°C, 270°C and 250°C.

Please see below the details of the obtained results. The PCT plot of the MgH_2/10 wt.% of ZrO_2/Ni resulted in a significant thermodynamic improvement in enthalpy value, which is approximately 20% when compared to the commercial MgH_2 – enthalpy value of 74.7 kJ/mol, and an entropy value of 130 J K^{-1} mol^{-1} and kinetic barrier Ea = 160 kJ/mol. [58] The obtained enthalpy is a crucial thermodynamic parameter; it gives the formation of the amount of energy loss during the reaction- as the absorption of MgH_2 is an exothermic reaction.

Figure 6. 7.(a). The thermodynamics data of nanocomposites MgH_2/10 wt.% of ZrO_2/Ni - 4 interpolated isothermal series at 300°C, 270°C, 250°C and 230°C.

R^2 = .995

Enthalpy of adsorption = -61.88 ± 3.05 kJ/mol

Entropy of adsorption = -114.375 ± 5.718 J/mol/K

Mean temperature (|T|) = 262.50°C: 230.01°C ≤ |T| ≤ 299.99°C

Figure 6. 7.(b). The thermodynamics data of nanocomposites MgH_2/10 wt.% of ZrO_2/Ni - 3 interpolated isothermal series at 285°C, 270°C and 250°C.

R^2 = 0.997

Enthalpy of adsorption = -57.17 ± 3.13 kJ/mol

Entropy of adsorption = -107.144 ± 5.970 J/mol/K

Mean temperature (|T|) = 251.67°C: 235°C ≤ |T| ≤ 270°C

(a)The thermodynamics data of nanocomposites MgH_2/10 wt.% of ZrO_2/Ni - 4 interpolated isothermal series at 300°C, 270°C, 250°C and 230°C

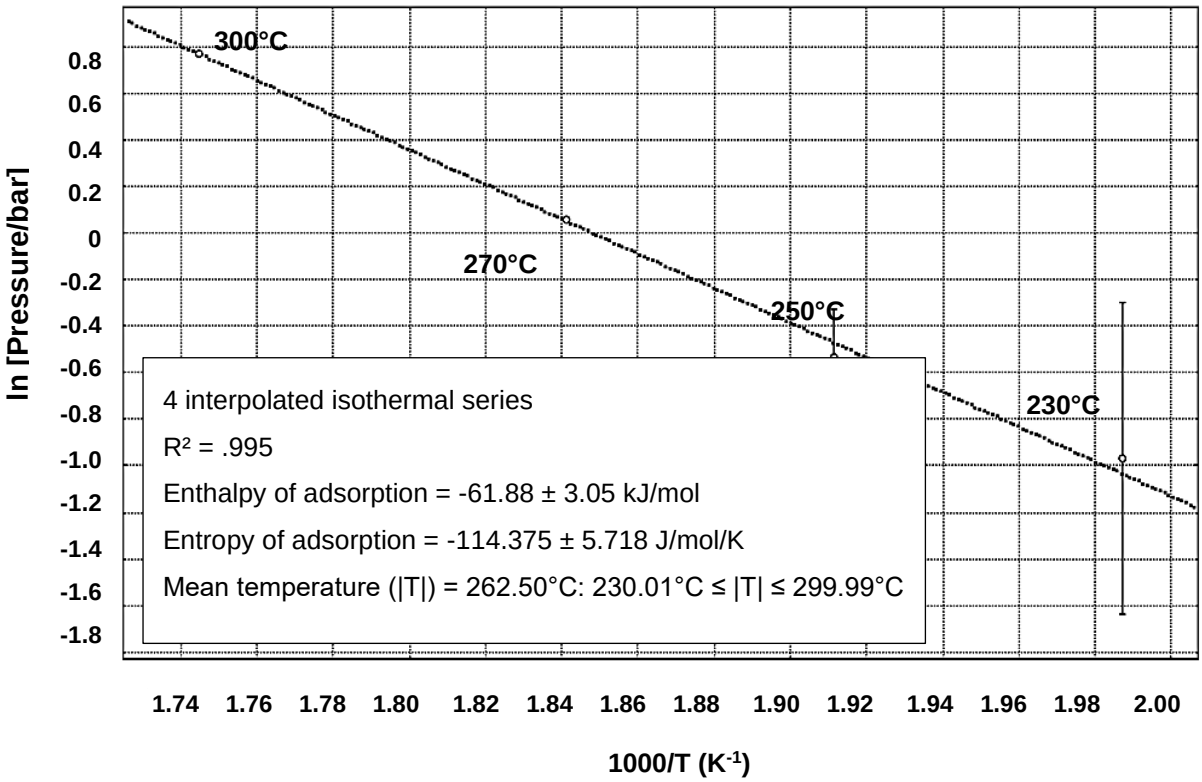

Figure 6.7: (a) Thermodynamic plot of MgH_2/10 wt.% of ZrO_2/Ni at 300°C, 270°C, 250°C and 230°C determination by the Clausius Clapeyron interpolation log.

(b)The thermodynamics data of nanocomposites MgH_2/10 wt.% of ZrO_2/Ni - 3 interpolated isothermal series at 285°C, 270°C and 235°C

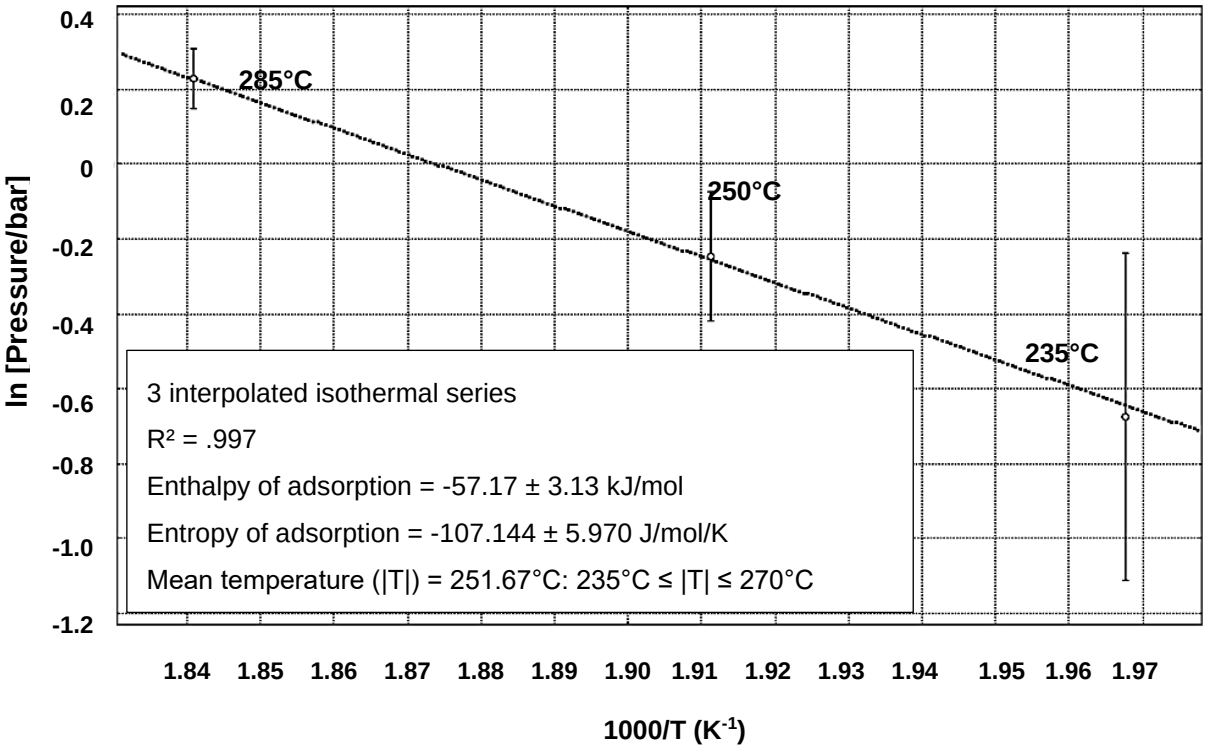

Figure 6. 7:(b) Thermodynamic determination by the Clausius Clapeyron interpolation log. Plot of MgH_2/10 wt.% of ZrO_2/Ni at 285°C, 250°C and 235°C.

The PCT plot of the MgH_2/10 wt.% of ZrO_2/Ni resulted in a significant thermodynamic improvement in enthalpy value, which is approximately 20% when compared to the commercial MgH_2 – enthalpy value of 74.7 kJ/mol, and an entropy value of 130 J K^{-1} mol^{-1} and kinetic barrier Ea = 160 kJ/mol. [58]

Whist the thermodynamics data of nanocomposites MgH_2/10 wt.% of ZrO_2/$NiCl_2$ resulted to:

- R^2 = 1.000,
- Enthalpy of adsorption = -69.74 kJ/mol,
- Entropy of adsorption = -127.957 J/mol/K,

- Mean temperature (|T|) = 282.50°C: 280°C ≤ |T| ≤ 285°C.

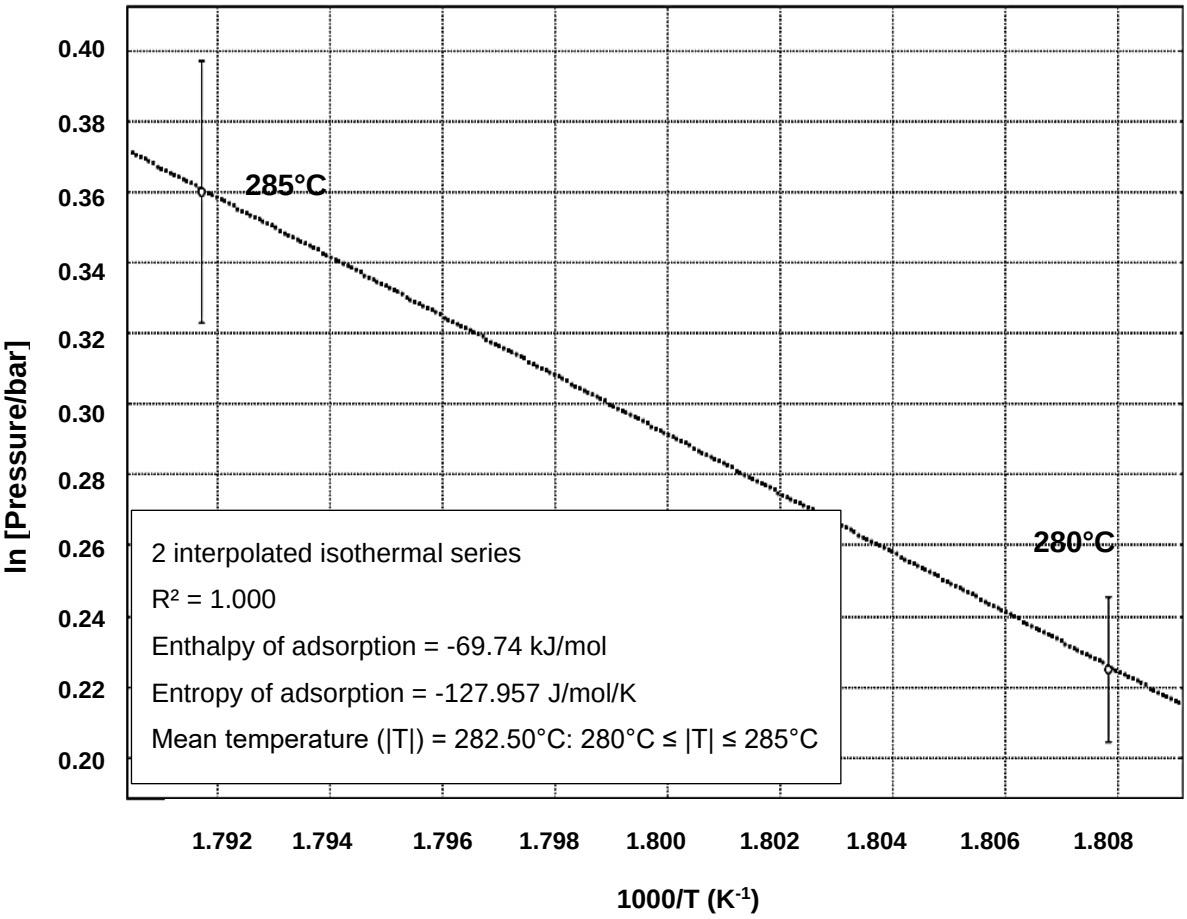

Figure 6. 8: Thermodynamic determination by the Clausius Clapeyron interpolation log. Plot of MgH_2+10 wt.% of $ZrO_2/NiCl_2$ at 280°C and 285°C

The obtained enthalpy (ΔH) value of the composite MgH_2+10 wt.% of ZrO_2/Ni is not only approximately 15% smaller or similar than the ΔH of MgH_2 -74.5kJ/mol H_2 [109], [125], but it is also lower to the study reported by Dong *et al*. [40] MgH_2 + $Zr_{0.67}Ni_{0.33}$ ΔH=-63.40 kJ/mol H_2, Tome *et al*. [39] MgH_2+5 wt. %Ni+5 wt.%ZrO_2 ΔH= -70.5 kJ/mol H_2. Refer to Table 6.3.

Table.6. 3: Thermodynamic results resulted for the PCT plots, compared to literature data.

Sample	ΔH (kJ/mol)	References
MgH_2	−74.5	[125–127]

	–72.29	
MgH_2/10wt.% ZrO_2/Ni	–57.17±3.13	*Present study*
	-61.88 ± 3.05	*Present study*
MgH_2/10wt.% ZrO_2/$NiCl_2$	-69.74 kJ/mol	*Present study*
MgH_2 doped with 10 wt.% $ZrNi_5$	−72.85	[128]
MgH_2+5 wt.%Ni+5 wt.%ZrO_2	−70.5	[39]
MgH_2/$Zr_{0.67}Ni_{0.33}$	-63.40	[40]

6.3.4 XRD analysis of the composites

It is readily apparent that peaks in the XRD pattern of the composite - MgH_2/10 wt.% of ZrO_2/Ni are rather broadened than those of the MgH_2/10 wt.% of ZrO_2/$NiCl_2$, with an average crystallite size of approximately 20 nm and 34 nm respectively. This observation was recently reported by Basil *et al*.[30] The peak broadening was a result of a slightly high concentration of Ni in the MgH_2 lattice during the milling process. The author added that the elevated concentration of chlorine has a negative impact on the Mg, as the chlorine creates a layer on the surface of the MgH_2, which may have obstructed the dissolution of Ni on the Mg matrix. [30]

After 5 hours of ball milling, the predominant peaks observed in the two composites were attributed to the tetragonal α-MgH_2 (PDF#01-075-7944) coexisting with the hexagonal β-MgH_2 (PDF#00-035-1185) indicated by the Bragg's angle at 27.9, 39.9º, 57.6º,64.9º. additional Braggs' lines corresponding to $Mg_{0.996}Zr_{0.004}$ (PDF#01-071-9629) were observed at 32.2°, 34.4°, 36.7°, 47.9°, 63.1°, 67.5°, 68.7°, 70.1° and 72.6°. And the $Ni_{0.99}Zr_{0.01}$(PDF#01-072-2682) at angles 44.3° and 51.7°. Some oxide elements were observed at 2θ of 42.7º and 52.6º attributed to MgO (PDF# 01-080-4185). A small mole fraction of the γ-MgH_2 (PDF#01-075-7945) orthorhombic metastable phase appeared at 39.9º and 52.6º.

The formation of metastable γ-MgH_2 hydride coexisting with the stable nanocrystalline β-MgH_2 was previously reported by Varin *et al*. [82] The formation of metastable γ-phase implies the destabilisation of the β- MgH_2 phase. Moreover, the metastable γ-phase reduces the hydrogen desorption temperature of MgH_2 hydride. [82]

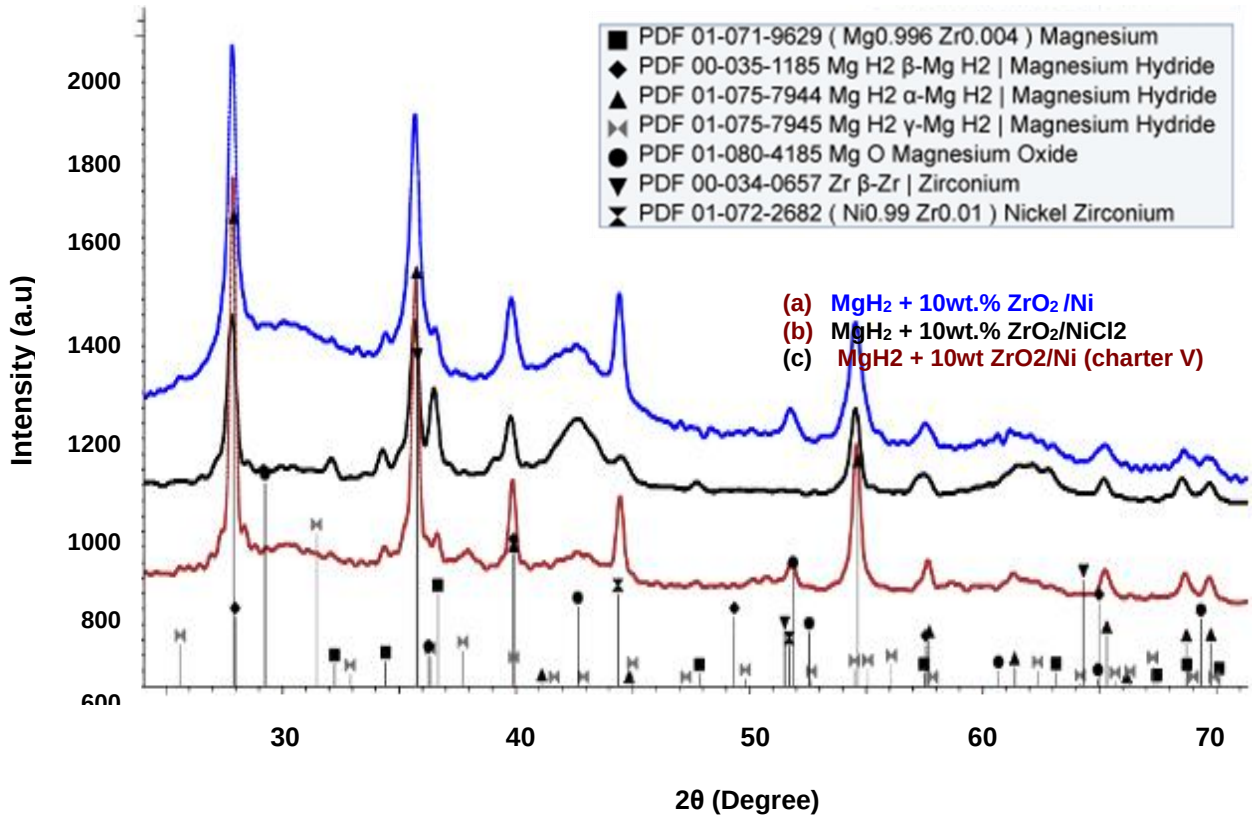

Figure 6. 9: The XRD image of nanocomposite (a) MgH_2+10wt.% ZrO_2/Ni, (b) MgH_2+10wt.% $ZrO_2/NiCl_2$ (c) MgH_2 +$ZrO_2/NiCl_2$ reported in chapter V as reference.

Referring to Figure 6.11, the elemental mapping of the composite MgH_2+ZrO_2/Ni recorded by energy dispersive spectrometer (EDS) reveals a uniform dispersion of the catalysts ZrO_2/Ni among the MgH_2 particles after the mechanical milling of 5 hours. Based on the SEM images, most of the particles are spherical, with slightly rough surfaces, and some have irregular shapes, as shown in Figures 6.10a, and 6.10b. And Figures 6.10c, and 6.10d show the catalyst aggregates on the MgH_2 surface. The calculated particle determined from the SEM image ranges from 200 to 800 nm, refer to Figure 6.12, the histogram plot obtained from image J and Origin software. The size of the particle correlates with previous literature data. [40] However, some large particles are still present in the composite, indicating a bi-modal particle size distribution of the MgH_2+ ZrO_2/Ni composite.

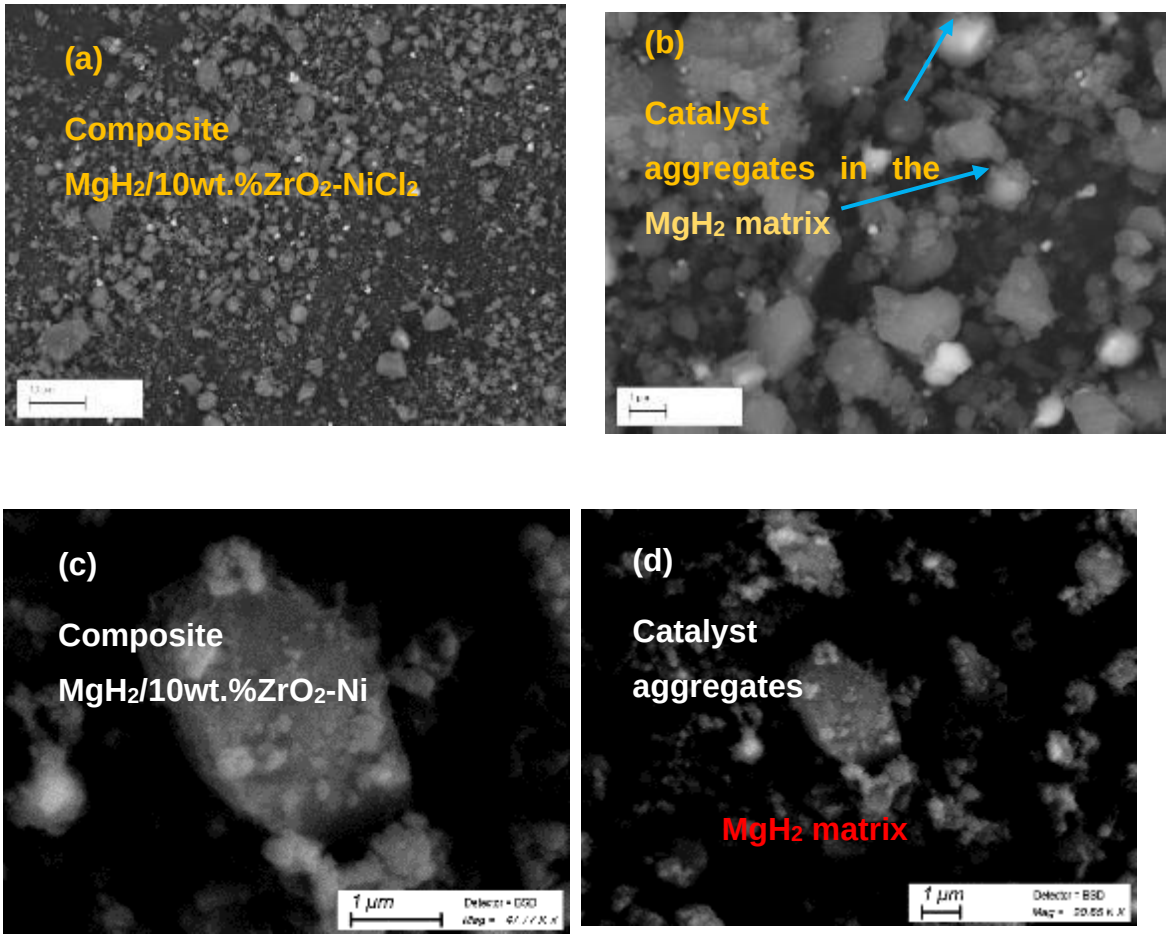

Figure 6. 10: SEM image of (a) composite MgH_2+ZrO_2/$NiCl_2$, (b) imagine showing the catalyst ZrO_2/$NiCl_2$ aggregation in MgH_2, (c) composite MgH_2+ZrO_2/Ni, (d) SEM image showing the catalyst ZrO_2/Ni on the surface of the MgH_2 matrix

It is more likely that the grain refinement has resulted from the presence of ZrO_2. This hypothesis was previously reported by Dong *et al.* [40], where the author reported a study on the advantage of the hydrogen sorption kinetics and thermodynamics when doping Mg/MgH_2 with amorphous $Zr_{0.67}Ni_{0.33}$, containing nano-ZrO_2. [40]

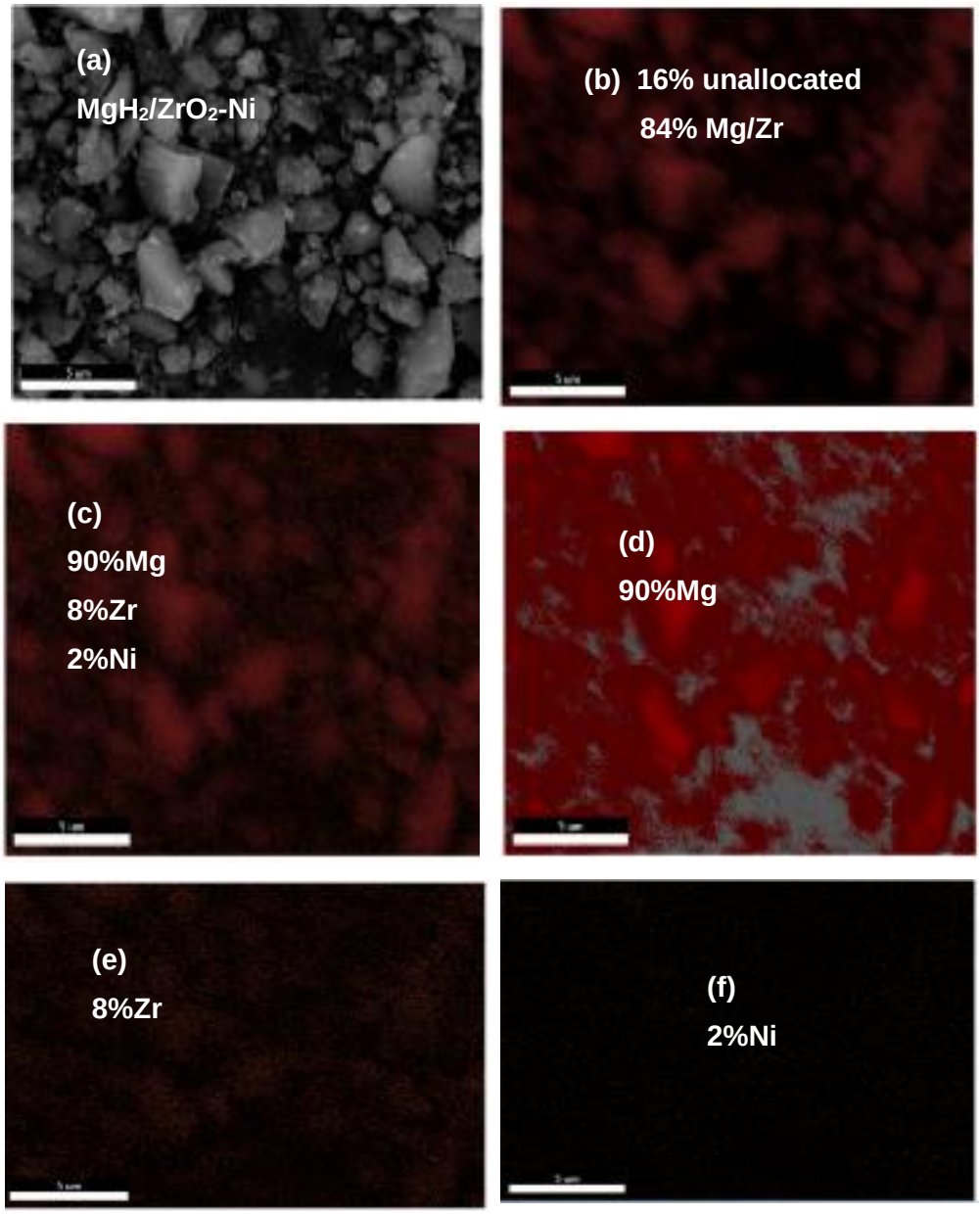

Figure 6. 11: EDX element mapping of composites MgH_2 + ZrO_2/Ni particle distribution

Figure 6. 10 shows the homogeneous particle distribution of the catalyst in the Mg. There is approximately 90 % Mg and 8 % of zirconium. The poor percentage of Ni may result from some of Ni being dissolved into MgH_2 during milling.

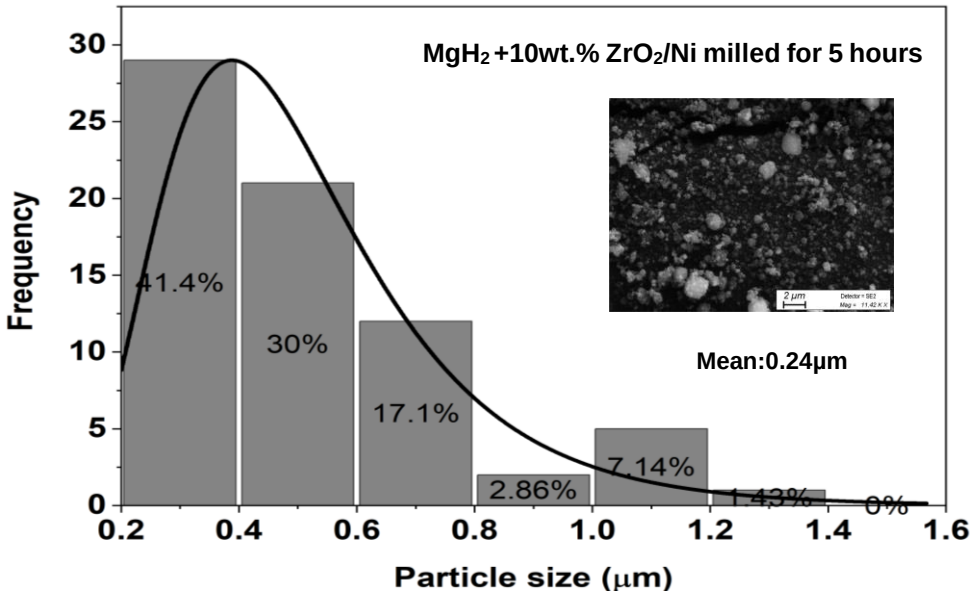

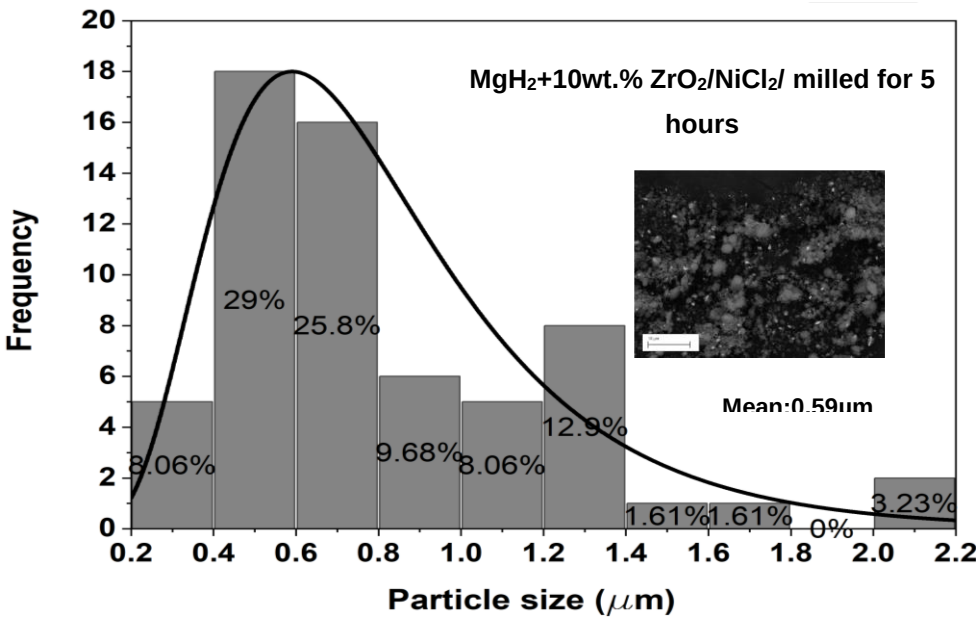

Figure 6. 12: Histograms of particle size distribution measured by the SEM/ImageJ analysis. (a) 5 hours ball milled MgH_2 +10wt.% ZrO_2/Ni average particle size 0.24 µm, and (b) composite MgH_2+10wt.% ZrO_2/$NiCl_2$ average particle size 0.59 µm.

The EDX was used to confirm the presence of the analysed elements and impurities. The presence of impurities such as gold (Au) comes from the coating of the powder during the sample preparation of the SEM analysis, carbon (C) from the carbon tape,

and oxygen (O) from preparing the sample outside the gloves box. Refer to Figure 6. 13.

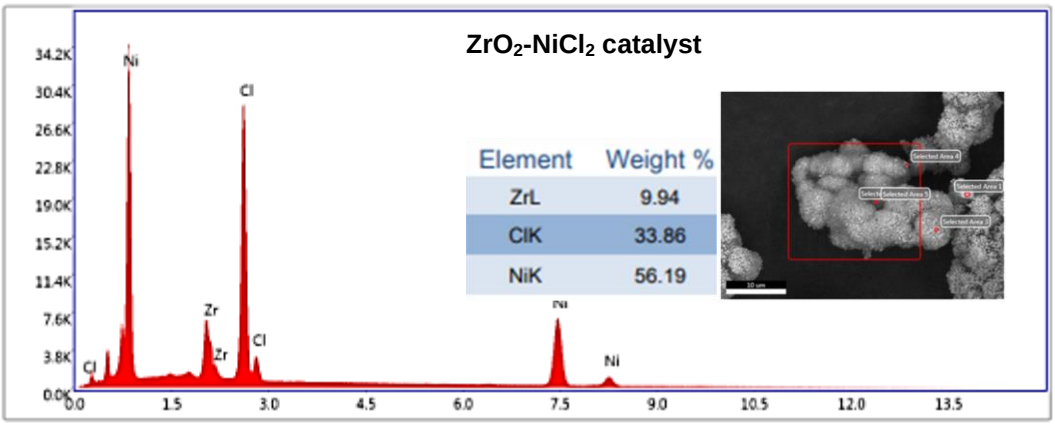

Figure 6. 13: The energy dispersive X-ray spectroscopy (EDX) of $ZrO_2/NiCl_2$ nano-catalyst after 5 hours heat treatment at 35°C under 95%Ar/H_2

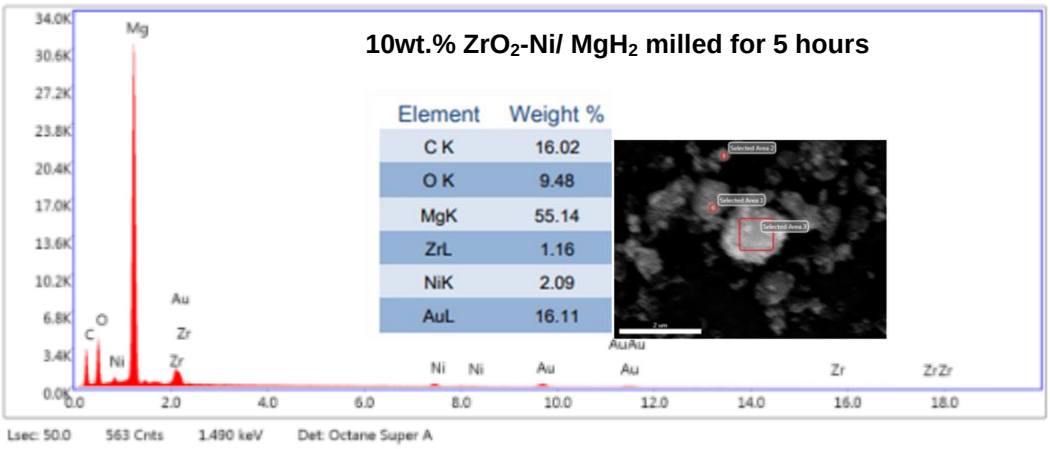

Figure 6. 14: The energy dispersive X-ray spectroscopy (EDX) of MgH_2/ ZrO_2/Ni after 5 hours milling

After establishing the best approach from the catalyst preparation, the TEM analysis was only reported for the composite MgH_2+ 10 wt.% ZrO_2/Ni. Figure 6. 15 (b) shows the bright phase representing the Mg/MgH_2, and the dot dark and field in the image are the catalyst. Refer to Figure 6. 15a., the HRTEM image mainly consists of an

amorphous matrix with some crystalline features whose lattice fringes correspond to the planes (102) d=0.19nm for Mg0.996Zr0.004 (Zone I), and (111) d=0.20nm for Ni0.99Zr phase (Zone II).

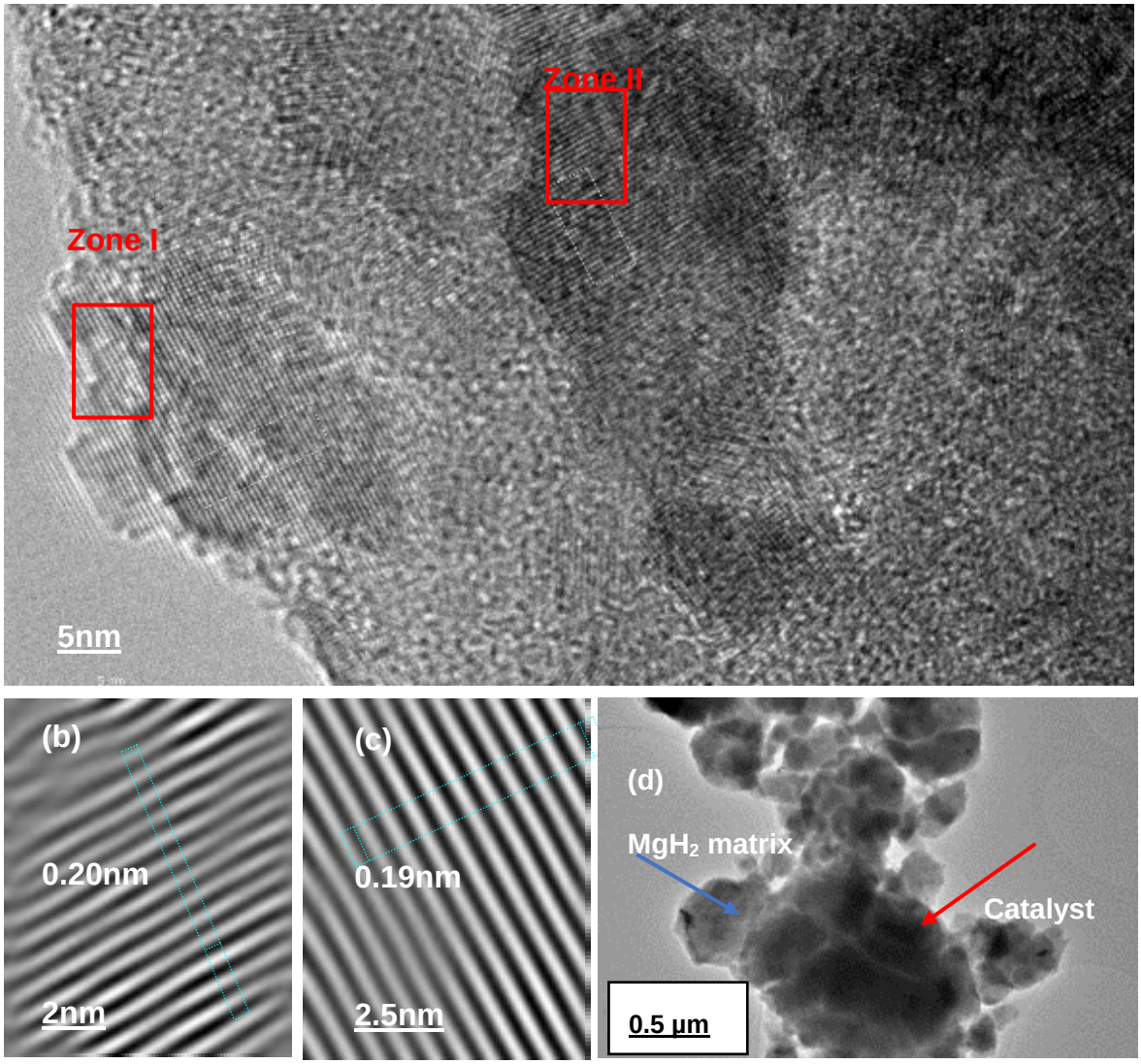

Figure 6. 15: Field emission high-resolution transmission electron microscopy (FE-HRTEM) of (**a**) MgH_2/10 wt.% ZrO_2/Ni nanocomposite; (**b**) the lattice image of zone I; (**c**) the lattice image of zone II; (d) TEM of the bright field image of MgH_2 powders milled with 10 wt.% ZrO_2-Ni, demonstrating the agglomeration of catalyst on the surface of the MgH_2 matrix after 5 hours milling time.

The significant improvement in the hydrogen desorption properties was likely due to the impact of the highly dispersed catalyst on the surface of the Mg/MgH_2 system and

the reduction in particle size during the ball milling process and the formation of $Mg_{0.996}Zr_{0.004}$ phase during the milling process as stated in the previous study. [21]

6.4. Conclusion

In *the present study*, the catalyst ZrO_2/Ni and $ZrO_2/NiCl_2$ have been successfully synthesised in a high-pressure reactor via a novel method. Both catalysts were analysed followed by a catalyst calcinated and characterised to determine their importance in hydrogen sorption properties with MgH_2 after 5 hours milling process via the planetary ball mills. The structure morphology of the analysed catalyst via XRD, SEM-EDX and FE-HRTEM analytical methods were used shows the broadening of the ZrO_2/Ni nanocatalyst, indicating the reduction in the particle size on the nanometric scale.

The nanocomposites MgH_2 powder milled with 10 wt.% of ZrO_2/Ni have a high percentage of hydrogen, 5.4 wt.% at 250ºC with a fast kinetic of hydrogen uptake at 1 minute, and a maximum absorption capacity of 7.3 wt.% was achieved in less than 10 minutes. The presence of chlorine seems to form a layer that blocked the surface of the MgH_2. The composite MgH_2/10wt.% $ZrO_2/NiCl_2$ shows moderate improvement of hydrogen uptake, 4.0 wt.% at 250ºC, with a maximum uptake of 5.3wt.%, which may be due to the presence of a high percentage of chloride catalyst on the surface of the Mg/MgH_2. The ZrO_2/Ni nanocatalyst synthesised via a novel method in *the present study* significantly decreased the enthalpy value of -57.17KJ/mol which is approximately 20% when compared to the commercial MgH_2. The decrease in enthalpy explains the destabilisation of the Mg, which decreased the absorption temperature to approximately 230°C.

The PCT plot of the MgH_2/10 wt.% of ZrO_2/Ni resulted in significant thermodynamic improvement, with a faster hydrogen release of 5.9 wt.% at onset temperature 210 °C/peak temperature 232 °C. The observed significant improvement in the hydrogen sorption properties may be due to the impact of the highly dispersed catalyst on the surface of the Mg/MgH_2 system as well as due to the reduction in particle size during the ball milling process and the formation of $Mg_{0.996}Zr_{0.004}$ phase during the milling process. Furthermore, the significant reduction in particle size and homogenous

distribution of the catalyst in the MgH_2 was probably the result of the catalyst activation prior to the milling process with the MgH_2.

The present study established a practical approach to synthesising nanostructure catalysts that significantly enhance the sorption property of the Mg/MgH_2.

Reader Guide

Chapter I: General Introduction

Chapter II: Literature

Chapter III: Methodology

Chapter IV: Establishing an Innovative Method for the Synthesis of ZrO_2/Ni Nanocatalyst for Improving the Sorption Property of MgH_2 in the Field of Solid-State Hydrogen Storage

20 hours milling time/ SPEX high energy ball mill MgH_2+10wt.%ZrO_2/Ni

Introduction Recap

Experimental

- Catalyst-ZrO_2/Ni synthesis
- Composite (MgH_2+10wt.%ZrO_2/Ni) ball mill: 5 hours via Planetary
- Characterisation

Results/ Discussion

- XRD
- SEM
- TPD
- Kinetics

Conclusion

References

Chapter V: Development of a Novel Method for the Fabrication of Nanostructured ZrO_2/Ni Catalyst to Enhance the Desorption Properties of MgH_2

5 hours milling time/ Planetary ball mill - MgH_2+10wt.%ZrO_2/Ni

Introduction Recap

Experimental

- Catalyst-ZrO_2/Ni synthesis
- Composite (MgH_2+10wt.%ZrO_2/Ni) ball mill: 20 hours via SPEX
- Characterisation

Results

- XRD
- SEM
- TPD

Discussion

Conclusion

References

Chapter VI: Comparing the Novel Catalysts ZrO_2/Ni and ZrO_2/$NiCl_2$ Storage Behaviour of Hydrogen Sorption Properties of MgH_2 Powder

5 hours milling time/ Planetary ball mill (ZrO_2/$NiCl_2$) catalyst

Introduction Recap

Experimental

- Catalyst-ZrO_2/Ni synthesis
- Composite (MgH_2+10wt.%ZrO_2/$NiCl_2$) ball mill: 5 hours via Planetary
- Characterisation

Results / Discussion

- XRD
- SEM
- Kinetics
- PCT

Conclusion

References

Chapter VII: General conclusion

References

Appendices

CHAPTER VII: GENERAL CONCLUSION

7.1. Work Summury

The aim of *the present study*'s was to develop an innovative method of synthesising a nanocatalyst that will significantly impact the sorption properties of the Mg/MgH_2. The catalyst was synthesised via a modified sol-gel method in a high-pressure reactor and heat treated at 350°C for 5 hours. *The present study* is grouped into three studies named **Method 1(p85), Method 2(p104) and Method 3(p127).** For the analysis technique, the XRD, TEM and SEM-EDX characterised the synthesised catalysts and composites to determine the microstructure of the powder. The desorption characteristic of the nanocomposite was determined via TPD. The hydrogenation and dehydrogenation properties of hydrogen storage materials in the MgH_2 were measured from the PCT plots and kinetic plots with the help of a Manometric Gas Sorption Analyser.

Method 1: "*Synthesis of ZrO_2/Ni Nanocatalyst".* The first method aimed to establish the methodology of the catalyst synthesis. Two different approaches were established. ***Step 1 - High-Pressure Reactor/ and Catalyst Activation.*** ZrO_2/Ni was synthesised via the high-pressure reactor at 200°C for 2 hours under hydrogen. The supernatant was dried, then calcinated under the flow of hydrogen at 350°C for 5hours before being mechanically milled with the commercial Mg/MgH_2 for 20 hours under Ar in a SPEX High-Energy Ball Mill**. *Step 2 – Ball Milling - SPEX High-Energy Ball Mill.*** Following the same procedures as in step 1, the synthesised catalyst was activated under hydrogen before being mechanically milled with the MgH_2 for 20hours under Ar in a SPEX High-Energy Ball Mill**.** The outcome of the experiment from **(Method 1)** shows that the milling of the powder via the SPEX ball mills resulted in particle agglomeration mainly in the range of 2000 to 4000nm, and a high level of impurities, and oxide formation, which significantly affected the sorption property of MgH_2, 4.4wt.% at 250°C after 1 minute.

Method 2: "*Synthesis of ZrO_2/Ni Nanocatalyst. High-pressure reactor, Catalyst Activation, and Ball Milling - Planetary Ball Mill PM 100".* The second method aimed to find alternative approaches to overcome the problem of oxidation and powder

agglomeration, which significantly impacted the sorption property of Mg/MgH_2, resulting from method 1. Therefore, a more advanced milling system - Planetary Ball Mill PM 100 - with zirconium oxide (ZrO_2) milling balls of 1-mm diameter was implemented from the milling of the composite. The activated ZrO_2/Ni catalyst was mechanically milled with the Mg/MgH_2 for 5 hours under Ar in a Planetary Ball Mill PM 100. As a result, the nanostructured MgH_2 powder milled with 10 wt.% of ZrO_2/Ni-based nanocatalyst resulted in a wide range of MgH_2 particle size distribution below 1000 nm. A faster hydrogen release of 5.9 wt.%-H at onset temperature 210 °C/peak temperature 232 °C was recorded.

Method 3: After establishing the methodology for synthesising the catalyst, this section aims to identify the impact of chlorine on the catalyst. The sorption properties of catalyst $ZrO_2/NiCl_2$ are to be compared to the ZrO_2/Ni in terms of hydrogenation/ dehydrogenation sorption properties in Mg/MgH_2.

$ZrO_2/NiCl_2$ was synthesised via the high-pressure reactor and calcinated under 95% Ar /5%hydrogen flow before being mechanically milled with the Mg/MgH_2 for 5 hours under Ar in a Planetary Ball Mill PM 100. The results show that nanocomposites MgH_2/10 wt.% of ZrO_2/Ni have a significant capacity of storing hydrogen 5.4 wt.% at 250ºC with a fast kinetic of hydrogen uptake at one minute. Whereas the composite MgH_2/10wt.% $ZrO_2/NiCl_2$ shows moderate improvement of hydrogen uptake, 4.0 wt.% at 250ºC, which may be due to a high percentage of Chloride catalyst on the surface of the Mg/MgH_2. The PCT plot of the MgH_2/10 wt.% of ZrO_2/Ni resulted in significant thermodynamic improvement, with the enthalpy value of -57.17KJ/mol, approximately 20% when compared to the commercial MgH_2.

7.2. Further Work

There is work to be done to determine the full impact of the synthesised catalyst: Such as – increasing the percentage ratio of the catalyst to be milled with MgH_2. - Increasing the percentage ratio of nickel- over chlorine as nickel is known as an active species at the surface of the Mg/MgH_2 particles.

- To determine the sorption property of the synthesised ZrO_2 and Ni separately for reference to the alloys ZrO_2/Ni.

- To determine the hysteresis of hydrogen absorption/desorption, to see if the synthesised catalyst may produce a flat plateau and low hysteresis, which may be associated with significant hydrogenation and dehydrogenation sorption property of MgH_2.

- To determine the cycle life of the catalyst, as according to the DOE's criterion set for hydrogen storage materials, the hydrogen kinetics and the absorption/desorption properties of the metal hydride should not degrade after undergoing approximately 1000 cycles.

Reader Guide

Chapter I: General Introduction

Chapter II: Literature

Chapter III: Methodology

Chapter IV: Establishing an Innovative Method for the Synthesis of ZrO_2/Ni Nanocatalyst for Improving the Sorption Property of MgH_2 in the Field of Solid-State Hydrogen Storage

20 hours milling time/ SPEX high energy ball mill MgH_2+10wt.%ZrO_2/Ni

Introduction Recap

Experimental

- Catalyst-ZrO_2/Ni synthesis
- Composite (MgH_2+10wt.%ZrO_2/Ni) ball mill: 5 hours via Planetary
- Characterisation

Results/ Discussion

- XRD
- SEM
- TPD
- Kinetics

Conclusion

References

Chapter V: Development of a Novel Method for the Fabrication of Nanostructured ZrO_2/Ni Catalyst to Enhance the Desorption Properties of MgH_2

5 hours milling time/ Planetary ball mill - MgH_2+10wt.%ZrO_2/Ni

Introduction Recap

Experimental

- Catalyst-ZrO_2/Ni synthesis
- Composite (MgH_2+10wt.%ZrO_2/Ni) ball mill: 20 hours via SPEX
- Characterisation

Results

- XRD
- SEM
- TPD

Discussion

Conclusion

References

Chapter VI: Comparing the Novel Catalysts ZrO_2/Ni and ZrO_2/$NiCl_2$ Storage Behaviour of Hydrogen Sorption Properties of MgH_2 Powder

5 hours milling time/ Planetary ball mill (ZrO_2/$NiCl_2$) catalyst

Introduction Recap

Experimental

- Catalyst-ZrO_2/Ni synthesis
- Composite (MgH_2+10wt.%ZrO_2/$NiCl_2$) ball mill: 5 hours via Planetary
- Characterisation

Results / Discussion

- XRD
- SEM
- Kinetics
- PCT

Conclusion

References

Chapter VII: General conclusion

References

Appendices

REFERENCES

[1] BP Energy Outlook 2018, “2018 BP Energy Outlook 2018 BP Energy Outlook,” p. 125, 2018, doi: 10.1088/1757-899X/342/1/012091.

[2] U.S Deparment of Energy, “DOE Technical Targets for Onboard Hydrogen Storage for Light-Duty Vehicles | Department of Energy,” *Energy.gov*, no. August 2009. pp. 1–23, 2017, doi: https://energy.gov/eere/fuelcells/doe-technical-targets-onboard-hydrogen-storage-light-duty-vehicles.

[3] T. Sinigaglia, F. Lewiski, M. E. Santos Martins, and J. C. Mairesse Siluk, “Production, storage, fuel stations of hydrogen and its utilization in automotive applications-a review,” *Int. J. Hydrogen Energy*, vol. 42, no. 39, pp. 24597–24611, 2017, doi: 10.1016/j.ijhydene.2017.08.063.

[4] G. Interest, “Fossil fuels made up 79 % of 2021 US primary energy consumption,” pp. 2020–2021, 2021.

[5] OGJ Editors, “BP Energy Outlook: Global energy demand to grow 30% to 2035,” *Oil & Gas Journal*. 2017, [Online]. Available: https://www.ogj.com/general-interest/article/17288577/bp-energy-outlook-global-energy-demand-to-grow-30-to-2035.

[6] P. Modi and K. F. Aguey-Zinsou, “Room Temperature Metal Hydrides for Stationary and Heat Storage Applications: A Review,” *Front. Energy Res.*, vol. 9, no. April, pp. 1–25, 2021, doi: 10.3389/fenrg.2021.616115.

[7] BP, “Statistical Review of World Energy globally consistent data on world energy markets and authoritative publications in the field of energy,” *BP Energy Outlook*, vol. 70, pp. 8–20, 2021.

[8] L. E. Klebanoff and J. O. Keller, “Erratum: 5 years of hydrogen storage research in the U.S. DOE Metal Hydride Center of Excellence (MHCoE) (International Journal of Hydrogen Energy (2013) 38 (4533-4576)),” *Int. J. Hydrogen Energy*, vol. 38, no. 19, p. 8022, 2013, doi: 10.1016/j.ijhydene.2013.04.105.

[9] P. Preuster, A. Alekseev, and P. Wasserscheid, “Hydrogen storage technologies for future energy systems,” *Annu. Rev. Chem. Biomol. Eng.*, vol. 8, pp. 445–471, 2017, doi: 10.1146/annurev-chembioeng-060816-101334.

[10] M. S. Javed, T. Ma, J. Jurasz, and M. Y. Amin, “Solar and wind power generation systems with pumped hydro storage: Review and future perspectives,” *Renew. Energy*, vol. 148, pp. 176–192, 2020, doi: 10.1016/j.renene.2019.11.157.

[11] M. Mahmoud, M. Ramadan, A. G. Olabi, K. Pullen, and S. Naher, “A review of mechanical energy storage systems combined with wind and solar applications,” *Energy Convers. Manag.*, vol. 210, no. March, p. 112670, 2020, doi: 10.1016/j.enconman.2020.112670.

[12] J. O. Abe, A. P. I. Popoola, E. Ajenifuja, and O. M. Popoola, “Hydrogen energy, economy and storage: Review and recommendation,” *Int. J. Hydrogen Energy*, vol. 44, no. 29, pp. 15072–15086, 2019, doi: 10.1016/j.ijhydene.2019.04.068.

[13] K. T. Møller, T. R. Jensen, E. Akiba, and H. wen Li, “Hydrogen - A sustainable energy carrier,” *Prog. Nat. Sci. Mater. Int.*, vol. 27, no. 1, pp. 34–40, 2017, doi: 10.1016/j.pnsc.2016.12.014.

[14] H. Barthelemy, M. Weber, and F. Barbier, “Hydrogen storage: Recent improvements and industrial perspectives,” *Int. J. Hydrogen Energy*, vol. 42, no. 11, pp. 7254–7262, 2017, doi: 10.1016/j.ijhydene.2016.03.178.

[15] N. A. A. Rusman and M. Dahari, “ScienceDirect A review on the current progress of metal hydrides material for solid-state hydrogen storage applications,” *Int. J. Hydrogen Energy*, vol. 41, no. 28, pp. 12108–12126, 2016, doi: 10.1016/j.ijhydene.2016.05.244.

[16] J. Zhang, S. Yan, and H. Qu, “Recent progress in magnesium hydride modified through catalysis and nanoconfinement,” *Int. J. Hydrogen Energy*, vol. 43, no. 3, pp. 1545–1565, 2018, doi: 10.1016/j.ijhydene.2017.11.135.

[17] A. Züttel, A. Remhof, A. Borgschulte, and O. Friedrichs, “Hydrogen: The future energy carrier,” *Philos. Trans. R. Soc. A Math. Phys. Eng. Sci.*, vol. 368, no. 1923, pp. 3329–3342, 2010, doi: 10.1098/rsta.2010.0113.

[18] W. Liu *et al.*, “materials relying on H2 physisorption, high-pressure cylinders and cooling systems are required to store H2 making them not convenient for automotive applications,” *Diam. Relat. Mater.*, 2017, doi: 10.1016/j.diamond.2017.12.003.

[19] F. Zhang, P. Zhao, M. Niu, and J. Maddy, “ScienceDirect The survey of key technologies in hydrogen energy storage,” *Int. J. Hydrogen Energy*, vol. 41, no. 33, pp. 14535–14552, 2016, doi: 10.1016/j.ijhydene.2016.05.293.

[20] J. Ren, N. M. Musyoka, H. W. Langmi, M. Mathe, and S. Liao, “ScienceDirect Current research trends and perspectives on materials-based hydrogen storage solutions : A critical review,” *Int. J. Hydrogen Energy*, vol. 42, no. 1, pp. 289–311, 2016, doi: 10.1016/j.ijhydene.2016.11.195.

[21] G. Shokano, Z. Dehouche, B. Galey, and G. Postole, “Desorption Properties of MgH 2,” no. x, 2020.

[22] Y. Shimizu, M. Otowaki, K. Shirai, and M. Ohyanagi, “Consistency between the experimental formation entropy of MgH2 and the spectroscopic entropy based on the third law of thermodynamics,” *J. Alloys Compd.*, vol. 811, p. 152062, 2019, doi: 10.1016/j.jallcom.2019.152062.

[23] T. Sadhasivam, H. T. Kim, S. Jung, S. H. Roh, J. H. Park, and H. Y. Jung, “Dimensional effects of nanostructured Mg/MgH2for hydrogen storage applications: A review,” *Renew. Sustain. Energy Rev.*, vol. 72, no. November 2015, pp. 523–534, 2017, doi: 10.1016/j.rser.2017.01.107.

[24] L. Zhou, “Progress and problems in hydrogen storage methods,” *Renew. Sustain. Energy Rev.*, vol. 9, no. 4, pp. 395–408, 2005, doi: 10.1016/j.rser.2004.05.005.

[25] M. Latroche, “Structural and thermodynamic properties of metallic hydrides used for energy storage,” *J. Phys. Chem. Solids*, vol. 65, no. 2–3, pp. 517–522, 2004, doi: 10.1016/j.jpcs.2003.08.037.

[26] F. C. Ruiz, E. B. Castro, S. G. Real, H. A. Peretti, A. Visintin, and W. E. Triaca, “Electrochemical characterization of AB2alloys used for negative electrodes in Ni/MH batteries,” *Int. J. Hydrogen Energy*, vol. 33, no. 13, pp. 3576–3580, 2008, doi: 10.1016/j.ijhydene.2007.12.019.

[27] E. Diagram and G. Features, “The Ni-Zr (Nickel-Zirconium) System,” vol. 5, no. 2, pp. 144–145, 1984.

[28] J. Nei, K. Young, R. Regmi, G. Lawes, S. O. Salley, and K. Y. S. Ng, “Gaseous phase hydrogen storage and electrochemical properties of Zr8Ni21, Zr7Ni10, Zr9Ni11, and ZrNi metal hydride alloys,” *Int. J. Hydrogen Energy*, vol. 37, no. 21, pp. 16042–16055, 2012, doi: 10.1016/j.ijhydene.2012.08.024.

[29] J. Nei, K. Young, S. O. Salley, and K. Y. S. Ng, “Effects of annealing on Zr8Ni19X2(X = Ni, Mg, Al, Sc, V, Mn, Co, Sn, La, and Hf): Hydrogen storage and electrochemical properties,” *Int. J. Hydrogen Energy*, vol. 37, no. 10, pp. 8418–8427, 2012, doi: 10.1016/j.ijhydene.2012.02.066.

[30] B. Galey, A. Auroux, S. Sabo-Etienne, S. Dhaher, M. Grellier, and G. Postole, “Improved hydrogen storage properties of Mg/MgH2 thanks to the addition of nickel hydride complex precursors,” *Int. J. Hydrogen Energy*, vol. 44, no. 54, pp. 28848–28862, 2019, doi: 10.1016/j.ijhydene.2019.09.127.

[31] B. Galey, A. Auroux, S. Sabo-Etienne, M. Grellier, and G. Postole, “Enhancing hydrogen storage properties of the Mg/MgH2 system by the addition of bis(tricyclohexylphosphine)nickel(II) dichloride,” *Int. J. Hydrogen Energy*, vol. 44, no. 23, pp. 11939–11952, 2019, doi: 10.1016/j.ijhydene.2019.03.114.

[32] H. B. Milling, T. Czujko, and E. E. Oleszek, “New Aspects of MgH 2 Morphological and Structural,” 2020.

[33] B. H. Chen, Y. S. Chuang, and C. K. Chen, “Improving the hydrogenation properties of MgH2 at room temperature by doping with nano-size ZrO2 catalyst,” *Journal of Alloys and Compounds*, vol. 655. pp. 21–27, 2016, doi: 10.1016/j.jallcom.2015.09.163.

[34] Office-of-Energy-Efficiency-&-Renewable-Energy, “Materials-Based Hydrogen Storage | Department of Energy,” *Department of Energy*, no. 1. p. n/a-n/a, 2015, [Online]. Available: https://www.energy.gov/eere/fuelcells/hydrogen-storage%0Ahttp://energy.gov/eere/fuelcells/hydrogen-storage%0Ahttp://energy.gov/eere/fuelcells/materials-based-hydrogen-storage.

[35] X. Zhang *et al.*, “Synthesis of magnesium nanoparticles with superior hydrogen storage properties by acetylene plasma metal reaction,” *Int. J. Hydrogen Energy*, 2011, doi: 10.1016/j.ijhydene.2010.12.052.

[36] F. Leardini, J. R. Ares, J. F. Fernández, J. Bodega, and C. Sánchez, “An investigation on the thermodynamics and kinetics of magnesium hydride decomposition based on isotope effects,” *Int. J. Hydrogen Energy*, vol. 36, no. 14, pp. 8351–8357, 2011, doi: 10.1016/j.ijhydene.2011.04.069.

[37] 3and Gang Chen Vincent Be´rube´1,*, y, Gregg Radtke2, Mildred Dresselhaus1, “Size effects on the hydrogen storage properties ofnanostructured metal hydrides: A review,” vol. 31, no. 1, pp. 637–663, 2007.

[38] J. M. Hemming *et al.*, “Changes to lung surfactant monolayers upon exposure to gas phase ozone observed using X-ray and neutron reflectivity,” *Environ. Sci. Atmos.*, no. 2, pp. 753–760, 2022, doi: 10.1039/d2ea00032f.

[39] K. C. Tome *et al.*, “Remarkable catalytic effect of Ni and ZrO2 nanoparticles on the hydrogen sorption properties of MgH2,” *Int. J. Hydrogen Energy*, vol. 47, no. 7, pp. 4716–4724, 2022, doi: 10.1016/j.ijhydene.2021.11.102.

[40] J. Dong, S. Panda, W. Zhu, J. Zou, and W. Ding, “Enhanced hydrogen sorption properties of MgH2 when doped with mechanically alloyed amorphous Zr0·67Ni0.33 particles,” *Int. J. Hydrogen Energy*, vol. 45, no. 52, pp. 28144–28153, 2020, doi: 10.1016/j.ijhydene.2020.03.119.

[41] Z. Dehouche, H. A. Peretti, S. Hamoudi, Y. Yoo, and K. Belkacemi, “Effect of activated alloys on hydrogen discharge kinetics of MgH2nanocrystals,” *J. Alloys Compd.*, vol. 455, no. 1–2, pp. 432–439, 2008, doi: 10.1016/j.jallcom.2007.01.138.

[42] M. S. El-Eskandarany, M. Banyan, and F. Al-Ajmi, “Synergistic effect of new ZrNi5/Nb2O5 catalytic agent on storage behavior of nanocrystalline MgH2 powders,” *Catalysts*, vol. 9, no. 4, pp. 7–10, 2019, doi: 10.3390/catal9040306.

[43] U.S. DRIVE Partnership, “Hydrogen Storage Tech Team Roadmap,” no. July, 2017, [Online]. Available: https://www.energy.gov/sites/prod/files/2017/08/f36/hstt_roadmap_July2017.pdf.

[44] Y. Sun, C. Shen, Q. Lai, W. Liu, D. W. Wang, and K. F. Aguey-Zinsou, “Tailoring magnesium based materials for hydrogen storage through synthesis: Current state of the art,” *Energy Storage Mater.*, vol. 10, no. October 2016, pp. 168–198, 2018, doi: 10.1016/j.ensm.2017.01.010.

[45] L. Grinberga and J. Kleperis, “Composite Nanomaterials for Hydrogen Technologies,” vol. 2, no. June 2014, 2011, doi: 10.5772/14231.

[46] C. Tong, *Introduction to Materials for Advanced Energy Systems*. 2019.

[47] Q. Lai *et al.*, “Hydrogen Storage Materials for Mobile and Stationary Applications: Current State of the Art,” *ChemSusChem*, vol. 8, no. 17, pp. 2789–2825, 2015, doi: 10.1002/cssc.201500231.

[48] C. Lang, Y. Jia, and X. Yao, “Recent advances in liquid-phase chemical hydrogen storage,” *Energy Storage Mater.*, vol. 26, no. November 2019, pp. 290–312, 2020, doi: 10.1016/j.ensm.2020.01.010.

[49] A. Züttel, P. Wenger, S. Rentsch, P. Sudan, P. Mauron, and C. Emmenegger, “LiBH4 a new hydrogen storage material,” *J. Power Sources*, vol. 118, no. 1–2, pp. 1–7, 2003, doi: 10.1016/S0378-7753(03)00054-5.

[50] N. Zafirah, A. Khalim, Z. Yaakob, and K. Long, “ScienceDirect The kinetics of lightweight solid-state hydrogen storage materials : A review,” *Int. J. Hydrogen Energy*, vol. 41, no. 30, pp. 13131–13151, 2016, doi: 10.1016/j.ijhydene.2016.05.169.

[51] B. T. K. A. Hoang and D. M. Antonelli, “Exploiting the Kubas Interaction in the Design of Hydrogen Storage Materials,” vol. 4, pp. 1787–1800, 2015, doi: 10.1002/adma.200802832.

[52] C. V. J. Skipper, A. Hamaed, D. M. Antonelli, and N. Kaltsoyannis, “The Kubas interaction in M(ii) (M = Ti, V, Cr) hydrazine-based hydrogen storage materials: A DFT study,” *Dalt. Trans.*, vol. 41, no. 28, pp. 8515–8523, 2012, doi: 10.1039/c2dt30383c.

[53] K. Bohmhammel, U. Wolf, G. Wolf, and E. Königsberger, “Thermodynamic optimization of the system magnesium-hydrogen,” *Thermochim. Acta*, vol. 337, no. 1–2, pp. 195–199, 1999, doi: 10.1016/s0040-6031(99)00235-x.

[54] F. Guo, K. Namba, H. Miyaoka, A. Jain, and T. Ichikawa, “Hydrogen storage behavior of TiFe alloy activated by different methods,” *Mater. Lett. X*, vol. 9, p. 100061, 2021, doi: 10.1016/j.mlblux.2021.100061.

[55] G. Liang, J. Huot, and R. Schulz, “Hydrogen storage properties of the mechanically alloyed LaNi5-based materials,” *J. Alloys Compd.*, vol. 320, no. 1, pp. 133–139, 2001, doi: 10.1016/S0925-8388(01)00929-X.

[56] Y. Cao *et al.*, “Potential application of metal-organic frameworks (MOFs) for hydrogen storage: Simulation by artificial intelligent techniques,” *Int. J. Hydrogen Energy*, vol. 46, no. 73, pp. 36336–36347, 2021, doi: 10.1016/j.ijhydene.2021.08.167.

[57] L. Wang, A. Rawal, M. Z. Quadir, and K. F. Aguey-Zinsou, “Nanoconfined lithium aluminium hydride (LiAlH4) and hydrogen reversibility,” *Int. J. Hydrogen Energy*, vol. 42, no. 20, pp. 14144–14153, 2017, doi: 10.1016/j.ijhydene.2017.04.104.

[58] X. X. Zhang, Y. Liu, X. X. Zhang, J. Hu, M. Gao, and H. Pan, “Empowering hydrogen storage performance of MgH2 by nanoengineering and nanocatalysis,” *Mater. Today Nano*, vol. 9, p. 100064, 2019, doi: 10.1016/j.mtnano.2019.100064.

[59] P. Vajeeston *et al.*, “Structural stability and pressure-induced phase transitions in MgH2,” *Phys. Rev. B - Condens. Matter Mater. Phys.*, vol. 73, no. 22, 2006, doi: 10.1103/PhysRevB.73.224102.

[60] Y. Wang and Y. Wang, “Recent advances in additive-enhanced magnesium hydride for hydrogen storage,” *Prog. Nat. Sci. Mater. Int.*, vol. 27, no. 1, pp. 41–49, 2017, doi: 10.1016/j.pnsc.2016.12.016.

[61] I. P. Jain, C. Lal, and A. Jain, “Hydrogen storage in Mg: A most promising material,” *Int. J. Hydrogen Energy*, vol. 35, no. 10, pp. 5133–5144, 2010, doi: 10.1016/j.ijhydene.2009.08.088.

[62] M. Bortz, B. Bertheville, G. Böttger, and K. Yvon, “Structure of the high pressure phase λ-MgH2 by neutron powder diffraction,” *J. Alloys Compd.*, vol. 287, no. 1–2, pp. 4–6, 1999, doi: 10.1016/S0925-8388(99)00028-6.

[63] V. V. Bhat, A. Rougier, L. Aymard, X. Darok, G. Nazri, and J. M. Tarascon, “Catalytic activity of oxides and halides on hydrogen storage of MgH2,” *J. Power Sources*, vol. 159, no. 1 SPEC. ISS., pp. 107–110, 2006, doi: 10.1016/j.jpowsour.2006.04.059.

[64] J. Zhang, S. Yan, L. P. Yu, X. J. Zhou, T. Zhou, and P. Peng, “Enhanced hydrogen storage properties and mechanisms of magnesium hydride modified by transition metal dissolved magnesium oxides,” *Int. J. Hydrogen Energy*, vol. 3, pp. 21864–21873, 2018, doi: 10.1016/j.ijhydene.2018.10.017.

[65] A. Züttel, “Materials for hydrogen storage,” *Mater. Today*, vol. 6, no. 9, pp. 24–33, 2003, doi: 10.1016/S1369-7021(03)00922-2.

[66] Y. Kitagawa and K. Tanabe, “Development of a kinetic model of hydrogen absorption and desorption in magnesium and analysis of the rate-determining step,” *Chem. Phys. Lett.*, vol. 699, pp. 132–138, 2018, doi: 10.1016/j.cplett.2018.03.036.

[67] T. G. Manivasagam, K. Kiraz, and P. H. L. Notten, “Electrochemical and optical properties of magnesium-alloy hydrides reviewed,” *Crystals*, vol. 2, no. 4, pp. 1410–1433, 2012, doi: 10.3390/cryst2041410.

[68] M. Martin, C. Gommel, C. Borkhart, and E. Fromm, “Absorption and desorption kinetics of hydrogen storage alloys,” *J. Alloys Compd.*, vol. 238, no. 1–2, pp. 193–201, 1996, doi: 10.1016/0925-8388(96)02217-7.

[69] Z. Dehouche, N. Grimard, F. Laurencelle, J. Goyette, and T. K. Bose, “Hydride alloys properties investigations for hydrogen sorption compressor,” *J. Alloys Compd.*, vol. 399, no. 1–2, pp. 224–236, 2005, doi: 10.1016/j.jallcom.2005.01.029.

[70] H. Wang, H. J. Lin, W. T. Cai, L. Z. Ouyang, and M. Zhu, “Tuning kinetics and thermodynamics of hydrogen storage in light metal element based systems e A review of recent progress,” *J. Alloys Compd.*, vol. 658, pp. 280–300, 2016, doi: 10.1016/j.jallcom.2015.10.090.

[71] L. shuai XIE, J. shan LI, T. bang ZHANG, and H. chao KOU, “Role of milling time and Ni content on dehydrogenation behavior of MgH2/Ni composite,” *Trans. Nonferrous Met. Soc. China (English Ed.*, vol. 27, no. 3, pp. 569–577, 2017, doi: 10.1016/S1003-6326(17)60063-3.

[72] A. Jain, S. Agarwal, and T. Ichikawa, “Catalytic tuning of sorption kinetics of lightweight hydrides: A review of the materials and mechanism,” *Catalysts*, vol. 8, no. 12, 2018, doi: 10.3390/catal8120651.

[73] J. Li, B. Li, H. Shao, W. Li, and H. Lin, “Catalysis and downsizing in Mg-based hydrogen storage materials,” *Catalysts*, vol. 8, no. 2, 2018, doi: 10.3390/catal8020089.

[74] S. K. Parayil, R. J. Psota, and R. T. Koodali, “Modulating the textural properties and photocatalytic hydrogen production activity of TiO2 by high temperature supercritical drying,” *Int. J. Hydrogen Energy*, vol. 38, no. 25, pp. 10215–10225, 2013, doi: 10.1016/j.ijhydene.2013.06.015.

[75] P. Pluengphon, T. Bovornratanaraks, P. Tsuppayakorn-aek, U. Pinsook, and B. Inceesungvorn, “High-pressure phases induce H-vacancy diffusion kinetics in TM-doped MgH2: Ab initio study for hydrogen storage improvement,” *Int. J. Hydrogen Energy*, vol. 44, no. 39, pp. 21948–21954, 2019, doi: 10.1016/j.ijhydene.2019.06.066.

[76] M. S. El-Eskandarany, E. Shaban, N. Ali, F. Aldakheel, and A. Alkandary, “In-situ catalyzation approach for enhancing the hydrogenation/dehydrogenation kinetics of MgH2 powders with Ni particles,” *Sci. Rep.*, vol. 6, no. June, pp. 1–13, 2016, doi: 10.1038/srep37335.

[77] Y. Fu *et al.*, “Effect of in-situ formed Mg2Ni/Mg2NiH4 compounds on hydrogen storage performance of MgH2,” *Int. J. Hydrogen Energy*, vol. 45, no. 52, pp. 28154–28162, 2020, doi: 10.1016/j.ijhydene.2020.03.089.

[78] M. V. Lototskyy, V. A. Yartys, B. G. Pollet, and R. C. Bowman, “Metal hydride hydrogen compressors: A review,” *Int. J. Hydrogen Energy*, vol. 39, no. 11, pp. 5818–5851, 2014, doi: 10.1016/j.ijhydene.2014.01.158.

[79] V. K. Sharma and E. Anil Kumar, “Metal hydrides for energy applications – classification, PCI characterisation and simulation,” *Int. J. Energy Res.*, vol. 41, no. 7, pp. 901–923, 2017, doi: 10.1002/er.3668.

[80] S. Suda, “Metal hydrides,” *Int. J. Hydrogen Energy*, vol. 12, no. 5, pp. 323–331, 1987, doi: 10.1016/0360-3199(87)90057-7.

[81] A. Zaluska, L. Zaluski, and J. O. Ström-Olsen, “Synergy of hydrogen sorption in ball-milled hydrides of Mg and Mg2Ni,” *J. Alloys Compd.*, vol. 289, no. 1–2, pp. 197–206, 1999, doi: 10.1016/S0166-0462(99)00013-7.

[82] R. A. Varin, T. Czujko, and Z. Wronski, “Particle size, grain size and γ-MgH2 effects on the desorption properties of nanocrystalline commercial magnesium hydride processed by controlled mechanical milling,” *Nanotechnology*, vol. 17, no. 15, pp. 3856–3865, 2006, doi: 10.1088/0957-4484/17/15/041.

[83] S. A. Pighin, G. Capurso, S. Lo Russo, and H. A. Peretti, “Hydrogen sorption kinetics of magnesium hydride enhanced by the addition of Zr8Ni21 alloy,” *J. Alloys Compd.*, 2012, doi: 10.1016/j.jallcom.2012.03.100.

[84] L. Ouyang *et al.*, “Magnesium-based hydrogen storage compounds: A review,” *J. Alloys Compd.*, vol. 832, p. 154865, 2020, doi: 10.1016/j.jallcom.2020.154865.

[85] J. J. Vajo, T. T. Salguero, A. F. Gross, S. L. Skeith, and G. L. Olson, “Thermodynamic destabilization and reaction kinetics in light metal hydride systems,” *J. Alloys Compd.*, vol. 446–447, pp. 409–414, 2007, doi: 10.1016/j.jallcom.2007.02.080.

[86] Z. Jia *et al.*, “Boron nitride supported nickel nanoparticles as catalyst for enhancing the hydrogen storage properties of MgH2,” *J. Alloys Compd.*, vol. 927, p. 166853, 2022, doi: 10.1016/j.jallcom.2022.166853.

[87] I. Journal, H. Energy, and P. Chemistry, “Multiple hydriding:dehydriding of Zr 0[91 Ni 9[87 alloy ^{3}.”

[88] M. S. El-Eskandarany, H. Al-Matrouk, E. Shaban, and A. Al-Duweesh, “Superior catalytic effect of nanocrystalline big-cube Zr2Ni metastable phase for improving the hydrogen sorption/desorption kinetics and cyclability of MgH2 powders,” *Energy*, vol. 91, pp. 274–282, 2015, doi: 10.1016/j.energy.2015.07.135.

[89] D. Khan, J. Zou, X. Zeng, and W. Ding, “Hydrogen storage properties of nanocrystalline Mg2Ni prepared from compressed 2MgH2–Ni powder,” *Int. J. Hydrogen Energy*, vol. 43, no. 49, pp. 22391–22400, 2018, doi: 10.1016/j.ijhydene.2018.10.055.

[90] M. S. El-Eskandarany *et al.*, “te MgH2/10 wt% ZrNi5 powders,” *Mater. Today Energy*, vol. 3, pp. 60–71, 2017, doi: 10.1016/j.mtener.2016.12.002.

[91] M. S. El-eskandarany, F. Al-ajmi, and M. Banyan, “Mechanically-Induced Catalyzation of MgH 2 Powders with Zr 2 Ni-Ball Milling Media,” 2019.

[92] M. S. El-Eskandarany, “Metallic glassy Zr70Ni20Pd10powders for improving the hydrogenation/dehydrogenation behavior of MgH2,” *Sci. Rep.*, vol. 6, no. December 2015, pp. 1–13, 2016, doi: 10.1038/srep26936.

[93] M. S. El-Eskandarany *et al.*, “Amorphous-versus big cube- Zr2Ni for improving the kinetics of hydrogenation/dehydrogenation behaviors for MgH2powders,” *Mater. Chem. Phys.*, vol. 203, no. September, pp. 17–26, 2018, doi: 10.1016/j.matchemphys.2017.09.046.

[94] B. Molinas *et al.*, “Scaled-up production of a promising Mg-based hydride for hydrogen storage,” *Int. J. Hydrogen Energy*, 2009, doi: 10.1016/j.ijhydene.2008.09.076.

[95] C. Zhou *et al.*, “Amorphous TiCu-Based Additives for Improving Hydrogen Storage Properties of Magnesium Hydride,” *ACS Appl. Mater. Interfaces*, vol. 11, no. 42, pp. 38868–38879, 2019, doi: 10.1021/acsami.9b16076.

[96] S. J. Hwang and Y. S. Chuang, “Enhanced hydrogen storage properties of MgH2 co-catalyzed with zirconium oxide and single-walled carbon nanotubes,” *J. Alloys Compd.*, vol. 664, pp. 284–290, 2016, doi: 10.1016/j.jallcom.2015.12.243.

[97] J. Mao, Z. Guo, X. Yu, H. Liu, Z. Wu, and J. Ni, “Enhanced hydrogen sorption properties of Ni and Co-catalyzed MgH2,” *Int. J. Hydrogen Energy*, vol. 35, no. 10, pp. 4569–4575, 2010, doi: 10.1016/j.ijhydene.2010.02.107.

[98] J. Zhang, H. Qu, S. Yan, L. R. Yin, and D. W. Zhou, “Dehydrogenation properties and mechanisms of MgH2-NiCl2 and MgH2-NiCl2-graphene hydrogen storage composites,” *Met. Mater. Int.*, vol. 23, no. 4, pp. 831–837, 2017, doi: 10.1007/s12540-017-6793-7.

[99] O. I. Manual, “Compact Mini Bench Top Reactors.”

[100] “8000M MIXER/MILL ® OPERATING MANUAL,” 2010. [Online]. Available: www.spexsampleprep.com.

[101] “An expert guide to neutral-to-analysis size reduction and homogenization in the laboratory The Art of Milling 2,” 2017.

[102] “High energy ball milling process for nanomaterial synthesis.”

[103] A. A. Bunaciu, E. gabriela Udriştioiu, and H. Y. Aboul-Enein, “X-Ray Diffraction: Instrumentation and Applications,” *Critical Reviews in Analytical Chemistry*, vol. 45, no. 4. Taylor and Francis Ltd., pp. 289–299, Oct. 02, 2015, doi: 10.1080/10408347.2014.949616.

[104] “VEQTER Residual Stress Experts X-ray Diffraction Technique.” [Online]. Available: www.veqter.co.uk.

[105] F. Specifications *et al.*, “JEM-2100 Electron Microscope | Products | JEOL Ltd.” pp. 14–16, 2020, [Online]. Available: https://www.jeol.co.jp/en/products/detail/JEM-2100.html.

[106] B. Galey, “complexes de métaux de transition pour le stockage solide de l ’ hydrogène To cite this version : HAL Id : tel-02657258 Développement de poudres à base de MgH 2 et de complexes de métaux de transition pour le stockage solide de l ’ hydrogène,” 2020.

[107] H. Isochema, “IMI Systems User Manual,” vol. 44, no. 0, 2011.

[108] Q. Luo *et al.*, “Thermodynamics and kinetics of phase transformation in rare earth–magnesium alloys: A critical review,” *J. Mater. Sci. Technol.*, vol. 44, pp. 171–190, 2020, doi: 10.1016/j.jmst.2020.01.022.

[109] Q. Li *et al.*, “Thermodynamics and kinetics of hydriding and dehydriding reactions in Mg-based hydrogen storage materials,” *J. Magnes. Alloy.*, vol. 9, no. 6, pp. 1922–1941, 2021, doi: 10.1016/j.jma.2021.10.002.

[110] Z. Dehouche, T. Klassen, W. Oelerich, J. Goyette, T. K. Bose, and R. Schulz, “C ycling and thermal stability of nanostructured MgH 2 –Cr 2 O 3 composite for hydrogen storage,” vol. 347, pp. 319–323, 2002.

[111] H. Lu, J. Li, Y. Lu, and T. Xie, “ScienceDirect ZrO 2 @ Nb 2 CT x composite as the efficient catalyst for Mg / MgH 2 based reversible hydrogen storage material,” vol. 7, 2022.

[112] R. A. Varin, T. Czujko, E. B. Wasmund, and Z. S. Wronski, “Catalytic effects of various forms of nickel on the synthesis rate and hydrogen desorption properties of nanocrystalline magnesium hydride (MgH2) synthesized by controlled reactive mechanical milling (CRMM),” *J. Alloys Compd.*, vol. 432, no. 1–2, pp. 217–231, 2007, doi: 10.1016/j.jallcom.2006.05.129.

[113] S. F. Matar, “Intermetallic hydrides: A review with ab initio aspects,” *Prog. Solid State Chem.*, vol. 38, no. 1–4, pp. 1–37, 2010, doi: 10.1016/j.progsolidstchem.2010.08.003.

[114] M. S. El-Eskandarany, S. A. Ahmed, and E. Shaban, “Metallic Glassy V45Zr20Ni20Cu10Al3Pd2 Alloy Powders for Superior Hydrogenation/Dehydrogenation Kinetics of MgH2,” *Mater. Today Proc.*, vol. 5, no. 5, pp. 13718–13725, 2018, doi: 10.1016/j.matpr.2018.02.010.

[115] M. El Khatabi, S. Naji, M. Bhihi, A. Benyoussef, A. El Kenz, and M. Loulidi, “Effects of double substitution on MgH2 hydrogen storage properties: An Ab initio studEl Khatabi, M. et al. (2018) ‘Effects of double substitution on MgH2 hydrogen storage properties: An Ab initio study’, Journal of Alloys and Compounds. Elsevier B.V, 743,” *J. Alloys Compd.*, vol. 743, pp. 666–671, 2018, doi: 10.1016/j.jallcom.2017.11.083.

[116] J. O. S.-O. A.Zaluska, L.Zaluski, “Nanocrystalline magnesium for hydrogen storge.” J. Alloys Compd., pp. 217–225, 1999.

[117] L. Zaluski, A. Zaluska, and J. O. Ström-Olsen, “Hydrogen absorption in nanocrystalline Mg2Ni formed by mechanical alloying,” *J. Alloys Compd.*, vol. 217, no. 2, pp. 245–249, 1995, doi: 10.1016/0925-8388(94)01348-9.

[118] A. Zaluska and L. Zaluski, “Nanocrystalline magnesium for hydrogen storage ¨,” vol. 288, pp. 217–225, 1999.

[119] Q. Zhang *et al.*, “Improved hydrogen storage properties of MgH2 with Ni-based compounds,” *Int. J. Hydrogen Energy*, vol. 42, no. 38, pp. 24247–24255, 2017, doi: 10.1016/j.ijhydene.2017.07.220.

[120] M. S. El-eskandarany, E. Shaban, H. Al-matrouk, and M. Behbehani, “Structure , morphology and hydrogen storage kinetics of nanocomposite MgH 2 / 10 wt % ZrNi 5 powders,” no. November, 2017, doi: 10.1016/j.mtener.2016.12.002.

[121] B. Galey, A. Auroux, S. Sabo-Etienne, M. Grellier, S. Dhaher, and G. Postole, “Impact of the addition of poly-dihydrogen ruthenium precursor complexes on the hydrogen storage properties of the Mg/MgH2 system,” *Sustain. Energy Fuels*, vol. 2, no. 10, pp. 2335–2344, 2018, doi: 10.1039/c8se00170g.

[122] I.Yu. Zavaliy, “Effect of oxygen content on hydrogen storage capacity of Zr-based h-phases,” vol. 291, pp. 102–109, 1999.

[123] R. A. Varin, T. Czujko, E. B. Wasmund, and Z. S. Wronski, “Hydrogen desorption properties of MgH2 nanocomposites with nano-oxides and Inco micrometric- and nanometric-Ni,” *J. Alloys Compd.*, vol. 446–447, pp. 63–66, 2007, doi: 10.1016/j.jallcom.2006.10.134.

[124] L. Zeng, T. Kimura, S. Hino, H. Miyaoka, T. Ichikawa, and Y. Kojima, “Improvement of hydrogenation and dehydrogenation kinetics on MgH 2 by the catalytic effect of ZrO 2,” *Appl. Mech. Mater.*, vol. 117–119, pp. 1195–1198, 2012, doi: 10.4028/www.scientific.net/AMM.117-119.1195.

[125] K. J. Jeon *et al.*, “Air-stable magnesium nanocomposites provide rapid and high-capacity hydrogen storage without using heavy-metal catalysts,” *Nat. Mater.*, 2011, doi: 10.1038/nmat2978.

[126] Q. Luo, J. Li, B. Li, B. Liu, H. Shao, and Q. Li, “Kinetics in Mg-based hydrogen storage materials: Enhancement and mechanism,” *J. Magnes. Alloy.*, vol. 7, no. 1, pp. 58–71, 2019, doi: 10.1016/j.jma.2018.12.001.

[127] C. N. C. Hitam, M. A. A. Aziz, A. H. Ruhaimi, and M. R. Taib, “Magnesium-based alloys for solid-state hydrogen storage applications: A review,” *Int. J. Hydrogen Energy*, vol. 46, no. 60, pp. 31067–31083, 2021, doi: 10.1016/j.ijhydene.2021.03.153.

[128] M. S. El-Eskandarany *et al.*, “Structure, morphology and hydrogen storage kinetics of nanocomposite MgH2/10 wt% ZrNi5 powders,” *Mater. Today Energy*, vol. 3, no. November, pp. 60–71, 2017, doi: 10.1016/j.mtener.2016.12.002.

Reader Guide

Chapter I: General Introduction

Chapter II: Literature

Chapter III: Methodology

Chapter IV: Establishing an Innovative Method for the Synthesis of ZrO_2/Ni Nanocatalyst for Improving the Sorption Property of MgH_2 in the Field of Solid-State Hydrogen Storage

20 hours milling time/ SPEX high energy ball mill MgH_2+10wt.%ZrO_2/Ni

Introduction Recap

Experimental

- Catalyst-ZrO_2/Ni synthesis
- Composite (MgH_2+10wt.%ZrO_2/Ni) ball mill: 5 hours via Planetary
- Characterisation

Results/ Discussion

- XRD
- SEM
- TPD
- Kinetics

Conclusion

References

Chapter V: Development of a Novel Method for the Fabrication of Nanostructured ZrO_2/Ni Catalyst to Enhance the Desorption Properties of MgH_2

5 hours milling time/ Planetary ball mill - MgH_2+10wt.%ZrO_2/Ni

Introduction Recap

Experimental

- Catalyst-ZrO_2/Ni synthesis
- Composite (MgH_2+10wt.%ZrO_2/Ni) ball mill: 20 hours via SPEX
- Characterisation

Results

- XRD
- SEM
- TPD

Discussion

Conclusion

References

Chapter VI: Comparing the Novel Catalysts ZrO_2/Ni and ZrO_2/$NiCl_2$ Storage Behaviour of Hydrogen Sorption Properties of MgH_2 Powder

5 hours milling time/ Planetary ball mill (ZrO_2/$NiCl_2$) catalyst

Introduction Recap

Experimental

- Catalyst-ZrO_2/Ni synthesis
- Composite (MgH_2+10wt.%ZrO_2/$NiCl_2$) ball mill: 5 hours via Planetary
- Characterisation

Results / Discussion

- XRD
- SEM
- Kinetics
- PCT

Conclusion

References

Chapter VII: General conclusion

References

Appendices

APPENDICES

Appendix (A): Steps to assemble and disassemble the High-Pressure Reactor

Assembling the high-pressure reactor

- A and B were inserted in the vessel containing the salt mixture,
- D was firmly attached to avoid the escape of the build-up pressure during the reaction,
- E is added to secure the reactor.
- The assembled reactor is then placed in the reactor furnace, as shown in Figure A,2.

Disassembling the high-pressure reactor

- E, D, (A.B) were opened consecutively to disassemble the high-pressure reactor.
- The solution in C was transferred to a beaker; the vessel was rinsed with 20 ml of methanol to recover the remaining sol-gel formed.

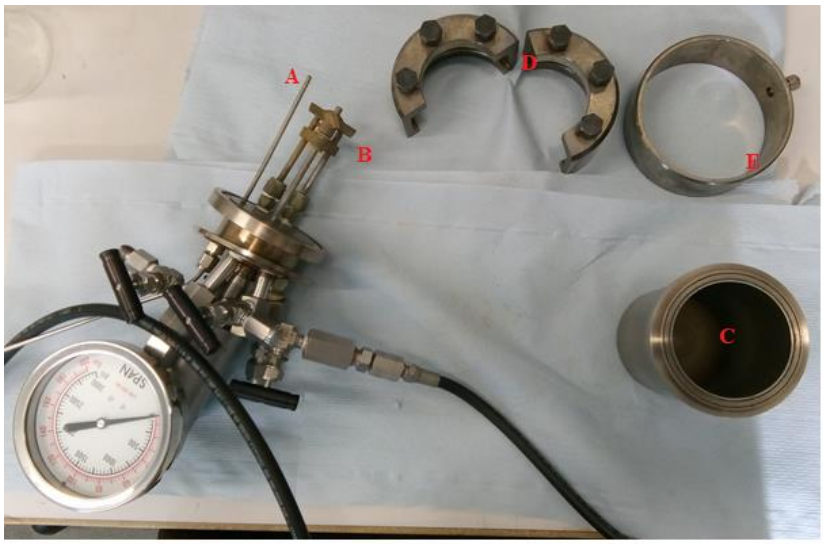

Figure A. 1: Steps for assembling the pressure reactor

Operation of the high-pressure reactor for the catalyst synthesis

- 1 is the magnetic clutch
- 2 the stirrer
- The thermocouple was connected by connecting the silver and the copper tail from the heat controller to the head of the reactor,
- 3 the main valve of the hydrogen cylinder was opened,
- 6 is the inlet hydrogen valve to the pressure reactor
- 7 is the outlet valve of the pressure reactor from 8 was opened,
- 4, the first control valve was opened, and 5, the second control valve of the hydrogen cylinder was to remove the unwanted contaminated air in the system.
- Valve 7 was closed as the pressure increased to 20 bar from the pressure gouge, the hydrogen valves were closed consecutively in 5, 4, and 3, and then valve 6 was closed.
- The temperature was set, and the stirrer was turned on via controller box 9.

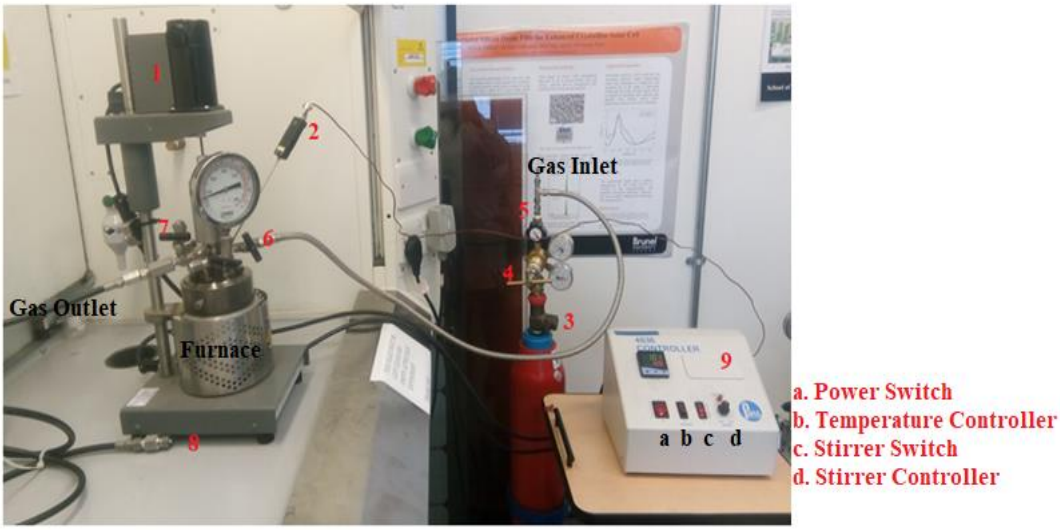

Figure A. 2: Steps procedures for the synthesis of MgH_2. Zr_9Ni

Appendix (B): Details on Experimental Method

At the very start of the present study, the focus was to alloy the Mg with the catalyst in the high-pressure reactor before milling.

For this approach, the salts Mg (NO3)2 · 6H2O + ZrCl4, + Ni(NO3)2 · 6H2O were used from the starting material without requiring further purification. The salts were dissolved in methanol and heated in a high-pressure reactor.

Refer to Table B.1 below for the difference in salts and powder colour before and after heat treatment.

Table B. 1: Difference in colour of the catalyst and composites before and after heat treatment

 **Starting material $Mg(NO_3)_2 \cdot 6H_2O$**	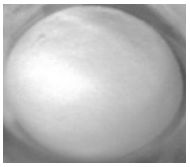 **Starting material $ZrCl_4$**	 **Starting material $Ni(NO_3)_2 \cdot 6H_2O$**
Mg $(NO_3)_2 \cdot 6H_2O$ + $ZrCl_4$, + $Ni(NO_3)_2 \cdot 6H_2O$ in Methanol. Weight before heat treatment = 2.68g Weight after heat treatment = 2.20g	 Before heat treatment 2 hours run in pressure reactor at 200ºC, 20 bar	 After 5 hours heat treatment 5 hours run at 300ºC under Hydrogen
$ZrCl_4$, Ni $(NO_3)_2 \cdot 6H_2O$ in Methanol. Weight before calcination = 0.59g Weight after heat treatment =0.36g	 Before heat treatment	 After 5 hours heat treatment

	2 hours run in pressure reactor at 200ºC, 20 bar	5 hours run at 300ºC in autoclave under Hydrogen
$Mg(NO_3)_2 \cdot 6H_2O$, $ZrCl_4$, $Ni(NO_3)_2 \cdot 6H_2O$ in Methanol. Weight after calcination = 0.35g	 Before heat treatment 2 hours run in pressure reactor at 100ºC,20 bar	 After 5 hours heat treatment 5 hours run at 300ºC in autoclave under Hydrogen
$Mg(NO_3)_2 \cdot 6H_2O$ + Zr/Ni based nano-catalyst powder) in Methanol. Weight before calcination = 0.48g Weight after calcination =0.36g	 After 5 hours heat treatment 5 hours run at 300ºC in autoclave under Hydrogen	

Appendix (C): Supplementary Datas

First Mg/g/MgH_2 powder provided for the present study

The composite MgH_2+ 10wt.%ZrO_2/Ni temperature stability was analysed by Thermogravimetric Analysis (TGA) with a TG Discovery from TA Instruments. The analyses were performed from ambient to 450 °C under an argon flow of 25 mL/min and at a heating rate of 2 °C/min. The sample to be analysed was added into a Hermetic aluminium pan with a pinhole. The sample transfer was performed into the glove box to prevent oxidation.

The three peaks were generated for the Mg/MgH_2 at a decomposition temperature of 362°C, 387°C, and 410°C, implying contamination and powder oxidation. Whilst the decomposition temperature of MgH_2+ 10wt.%ZrO_2/Ni started at 200°C and reached its peak point at 268°C, which is significantly lower compared to the peak temperature (364°C) of the as-milled MgH_2 recently reported in the literature [39] Refer to Figure C1.

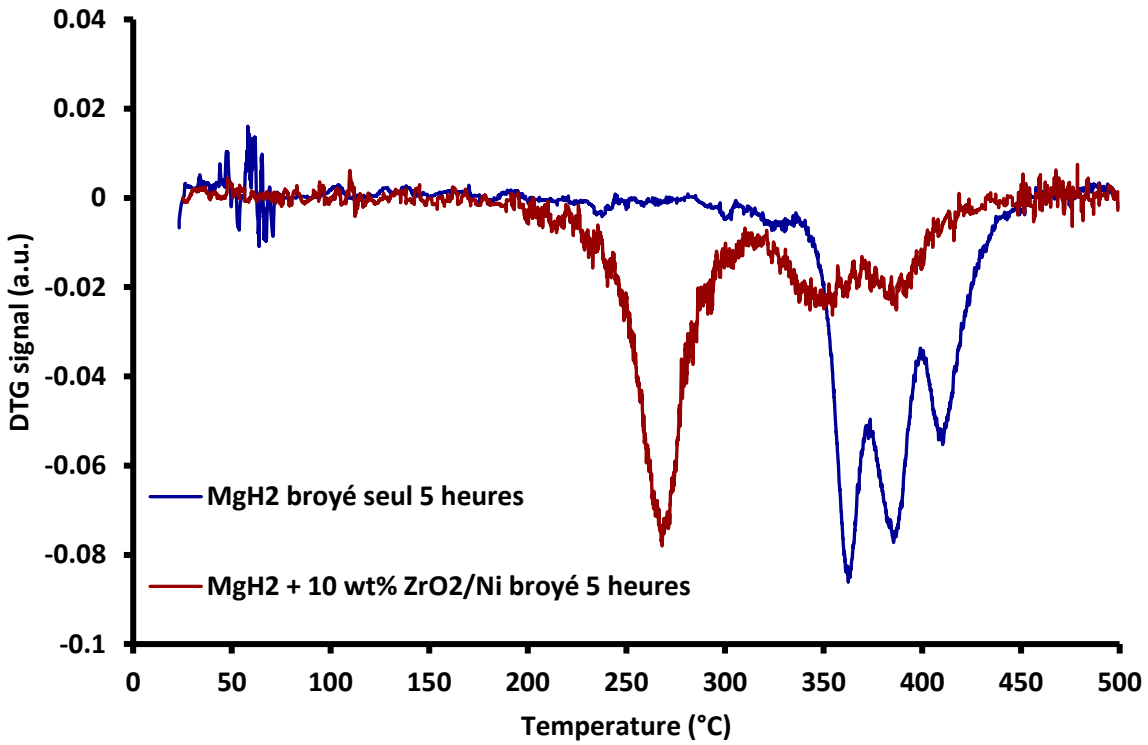

Figure C. 1: Thermogravimetric analysis - DTG signal over the temperature of Mg/MgH_2 and MgH_2+ 10wt.%ZrO_2/Ni obtained after 5 hours milling time. Sample heated from ambient to 450 °C under an argon flow of 25 mL/min and at a heating rate of 2 °C/min.

XRD analysis of Ni, ZrO_2 powders prepared by the high-pressure reactor

XRD was carried out to identify crystalline phases present in the Ni, ZrO_2 powders prepared by the high-pressure reactor respectively. Figure C.2 and C.3. shows the XDR patterns of Ni, and ZrO_2 after 5-hours heat treatment at 350°C respectively.

Refer to Figure C.2. ZrO_2 shows broads Braggs peaks at around 2θ of 30.1°, 34.9°, 50.2°, and 59.7° (PDF file # 00-049-1642), and Zr at 34.8, and 50.0° corresponding to the (PDF file # 01-079-9867). Whilst Ni resulted to sharp Braggs peaks at around 2θ of 44.5°, 51.8°, 76.4°, 92.9°, and 98.4° (PDF file # 03-065-2865. (Figure C.3.)

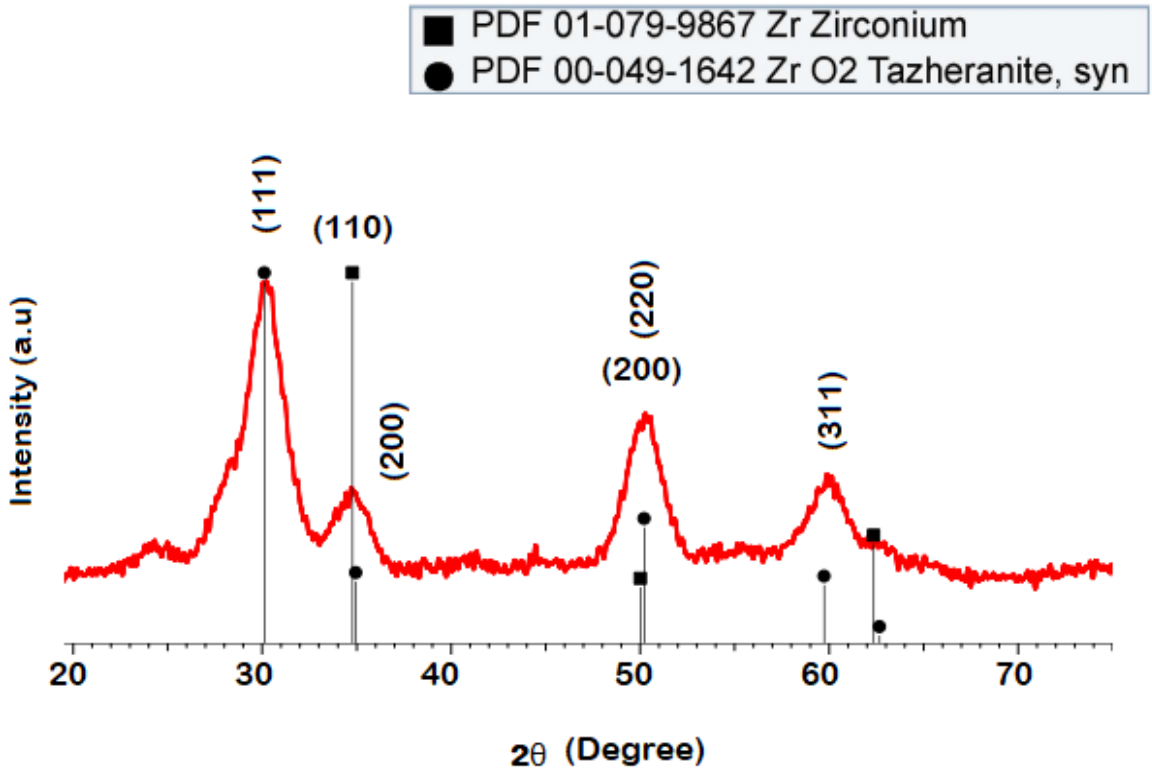

Figure C. 2: ZrO_2 catalyst prepared in the high-pressure reactor

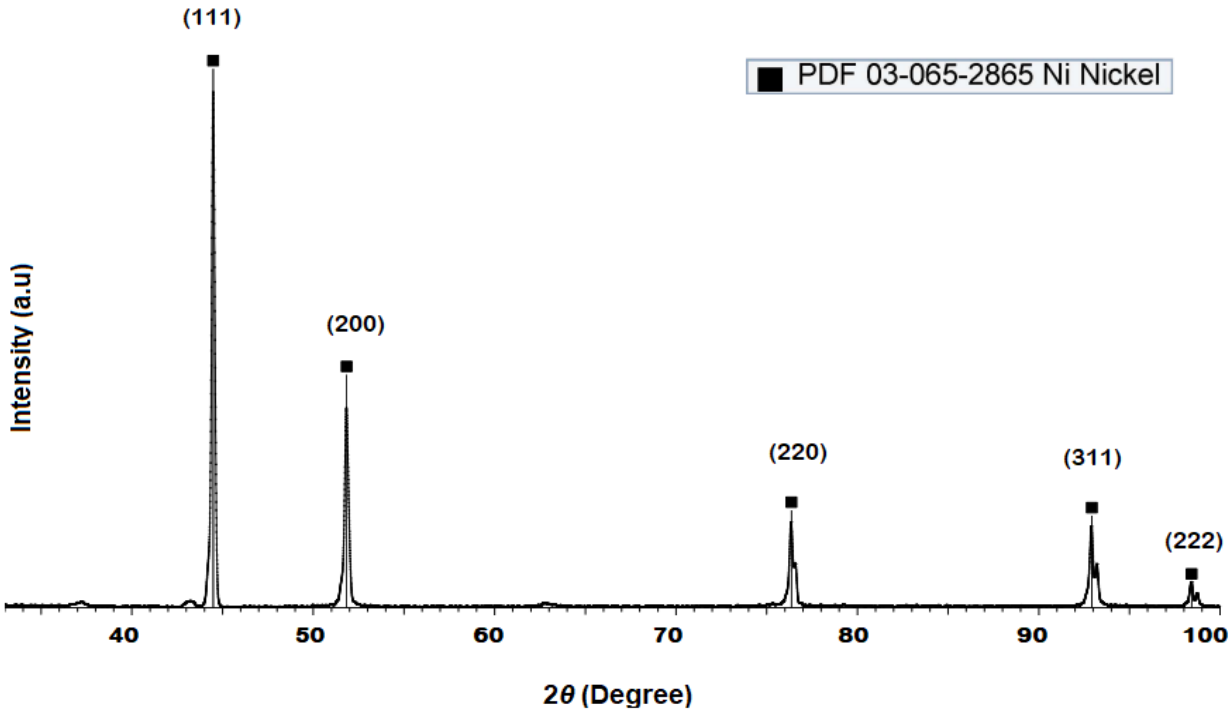

Figure C. 3: Nickel nano powder catalyst prepared in the high-pressure reactor

EDX analysis of Ni, ZrO_2 powders prepared by the high-pressure reactor, after 5 hours ball mill with MgH_2

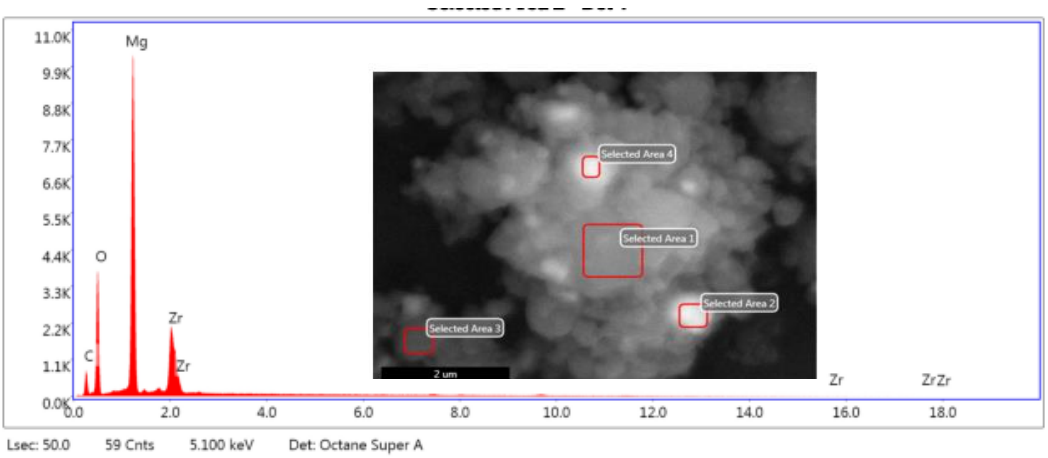

eZAF Smart Quant Results

Element	Weight %	Atomic %	Net Int.	Error %	Kratio	Z	A	F
C K	15.01	25.69	122.66	11.70	0.0272	1.1244	0.1613	1.0000
O K	31.28	40.19	884.37	9.08	0.0841	1.0766	0.2496	1.0000
MgK	35.51	30.02	3121.71	5.00	0.2250	0.9950	0.6359	1.0015
ZrL	18.20	4.10	714.23	3.29	0.1231	0.7493	0.9034	0.9994

Figure C. 4: The energy dispersive X-ray spectroscopy (EDX) of MgH_2/ ZrO_2 after 5 hours milling

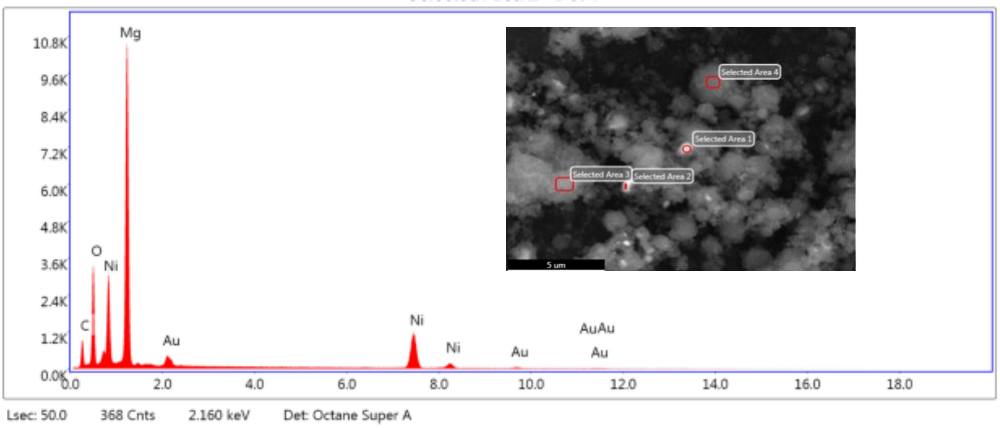

eZAF Smart Quant Results

Element	Weight %	Atomic %	Net Int.	Error %	Kratio	Z	A	F
C K	16.78	30.92	202.60	10.51	0.0344	1.1360	0.1803	1.0000
O K	17.76	24.58	829.70	8.47	0.0602	1.0881	0.3117	1.0000
MgK	38.56	35.11	3317.53	6.63	0.1826	1.0061	0.4705	1.0003
AuM	2.86	0.32	114.08	9.16	0.0211	0.6409	1.1339	1.0173
NiK	24.04	9.06	686.07	2.86	0.2064	0.8399	1.0065	1.0156

Figure C. 5: The energy dispersive X-ray spectroscopy (EDX) of MgH_2/Ni after 5 hours milling

Absorption kinetics plots of MgH_2/10 wt.% ZrO_2/Ni

The absorption kinetics plots of MgH_2/10 wt.% ZrO2/Ni was measured at a constant temperature three times in order to determine the certainty of the measurement.

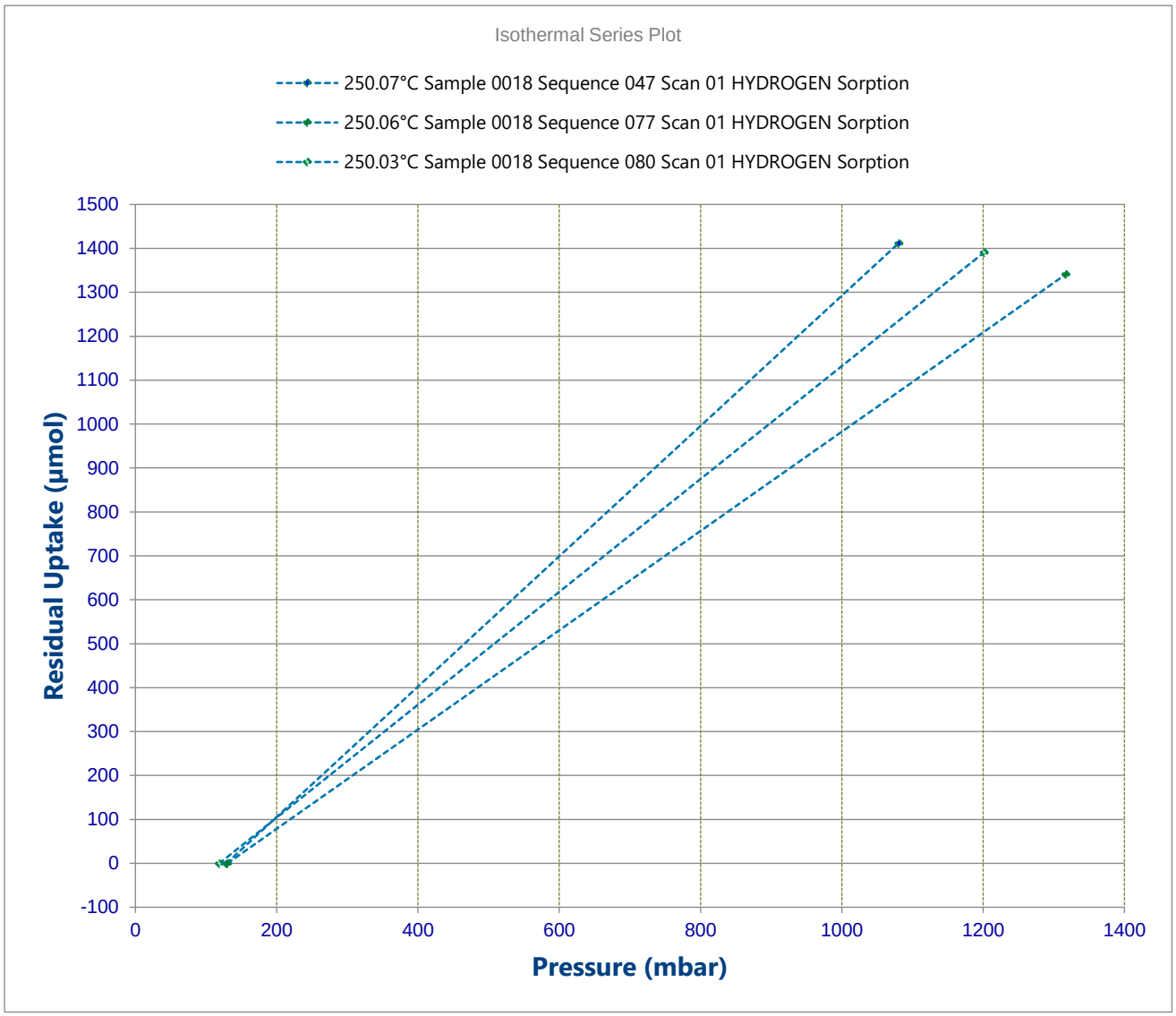

Figure C. 6: Absorption kinetics plots of MgH_2/10 wt.% ZrO_2/Ni at 250°C

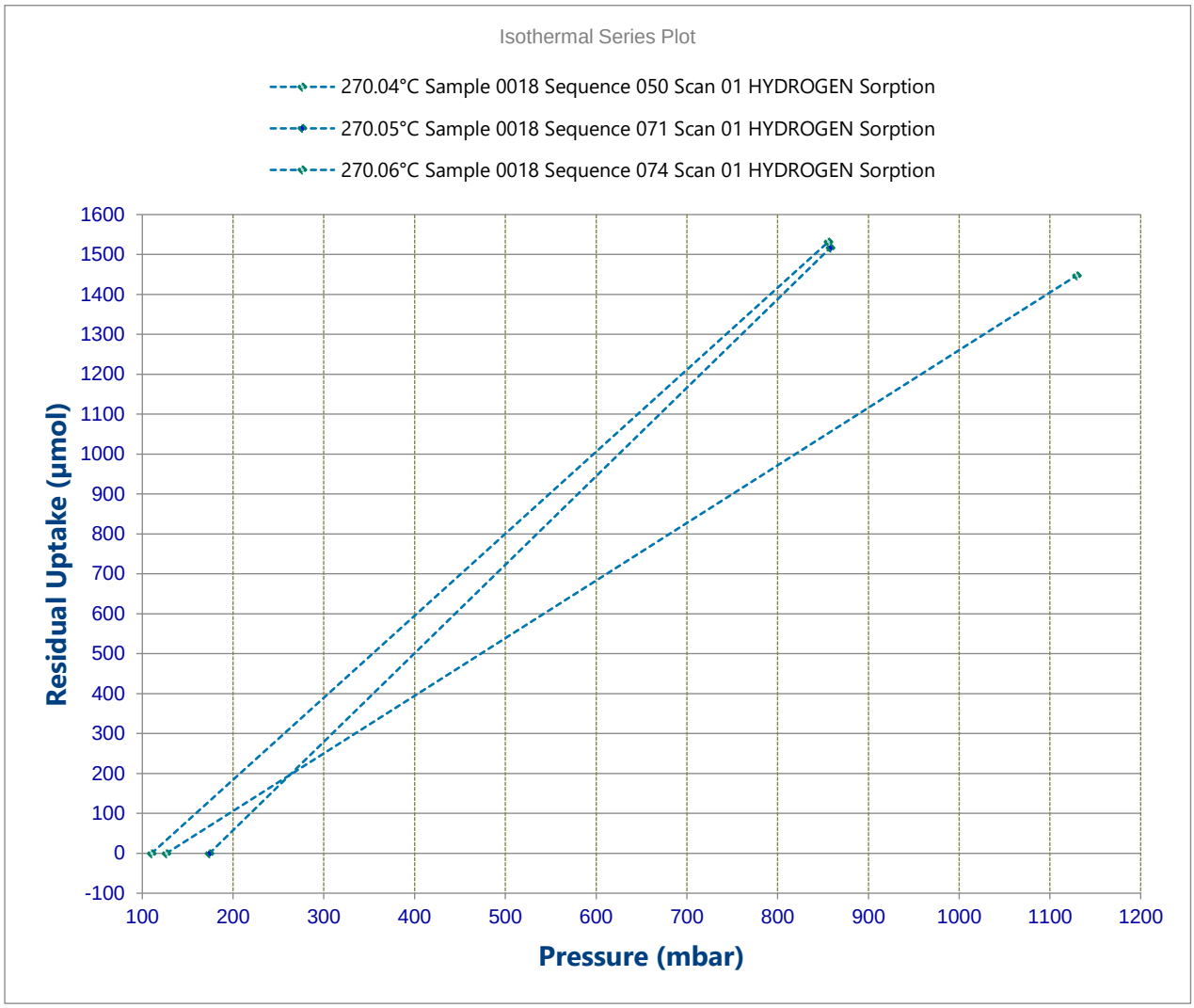

Figure C. 7: Absorption kinetics plots of MgH_2/10 wt.% ZrO_2/Ni 270°C